Electrochemical-Thermal Modeling of Lithium-ion Batteries

by

Mehrdad Mastali Majdabadi Kohneh

A thesis
presented to the University of Waterloo
in fulfillment of the
thesis requirement for the degree of
Doctor of Philosophy
in
Mechanical Engineering

Waterloo, Ontario, Canada, 2016

AUTHOR'S DECLARATION

I hereby declare that I am the sole author of this thesis. This is a true copy of the thesis, including any required final revisions, as accepted by my examiners.

I understand that my thesis may be made electronically available to the public.

Abstract

Incorporating lithium-ion (Li-ion) batteries as an energy storage system in electric devices including electric vehicles brings about new challenges. In fact, the design of Li-ion batteries has to be optimized depending on each application specifications to improve the performance and safety of battery operation under each application and at the same time prevent the batteries from quick degradation. As a result, accurate models capable of predicting the behavior of Li-ion batteries under various operating conditions are necessary. Therefore, the main objective of this research is to develop a battery model that includes thermal heating and is suitable for large-sized prismatic cells used in electric vehicles.

This works starts with developing a dual-extended Kalman filter based on an equivalent circuit model for the battery. The dual-extended Kalman filter simultaneously estimates the dynamic internal resistance and state of the charge of the battery. However, the estimated parameters are only the fitted values to the experimental data and may be non-physical. In addition, this filter is only valid for the operating conditions that it is validated against via experimental data. To overcome these issues, physics-based electrochemical models for Li-ion batteries are subsequently considered.

One drawback of physics-based models is their high computational cost. In this work, two simplified one-dimensional physics-based models capable of predicting the output voltage of coin cells with less than 2.5% maximum error compared to the full-order model are developed. These models reduce the simulation computational time more than one order of magnitude. In addition to computational time, the accuracy of the physico-chemical model parameter estimates is a concern for physics-based models. Therefore, commercial $LiFePO_4$ (LFP) and graphite electrodes are precisely modelled and characterized by fitting experimental data at different charge/discharge rates (C/5 to 5C). The temperature dependency of the kinetic and transport properties of LFP and graphite electrodes is also estimated by fitting experimental data at various temperatures (10 ºC, 23 ºC, 35 ºC, and 45 ºC).

Since the spatial current and temperature variations in the large-sized prismatic cells are significant, one-dimensional models cannot be used for the modeling of these prismatic cells. In this work, a resistor network methodology is utilized to combine the one-dimensional models into a

three-dimensional multi-layer model. The developed model is verified by comparing the simulated temperatures at the surface of the prismatic cell (consist of LFP as the positive and graphite as the negative electrode) to experimental data at different charge/discharge rates (1C, 2C, 3C, and 5C). Using the developed model the effect of tab size and location, and the current collector thickness, on the electrochemical characteristics of large-sized batteries is evaluated. It is shown that transferring tabs from the edges and the same side (common commercial design) to the center and opposite sides of the cell, and extending them as much as possible in width, lowers the non-uniformity variation in electrochemical current generation.

Acknowledgements

I would like to express my sincere gratitude to Prof. Fraser and Prof. Fowler, for their constant guidance and support during the course of this research. I would also like to thank Dr. Siamak Farhad, Mohammad Farkhondeh, Dr. Ehsan Samadani and Satyam Panchal for providing assistance and constructive feedbacks. Last but not least, my special gratitude to my family for all their encouragement and support during these years.

Dedication

In memory of my brother Peiman …

Table of Contents

List of Figures

List of Tables

Nomenclature

a	slope of the linear current-voltage relation, S m^{-2}
a_k	specific surface area of the k^{th} LFP particle bin, m^{-1}
b	y-intercept of the linear current-voltage relation, A m^{-2}
c_e	electrolyte concentration, mol m^{-3}
c_e^0	initial electrolyte concentration, mol m^{-3}
$c_{s,k}$	Li concentration inside the k^{th} LFP particle bin, mol m^{-3}
$c_{s,k}^0$	initial Li concentration inside the k^{th} LFP particle bin, mol m^{-3}
c_s^{max}	maximum Li concentration in the LFP particles, mol m^{-3}
d_k	vector of outputs in k^{th} time step
e_k	independent, zero-mean, Gaussian noise in the measurement model of Kalman filter
$f(.)$	process model function for the states
$g(.)$	measurement model function
h	hysteresis state
i_k	current of the battery in k^{th} time step
i_k^0	exchange current density of the k^{th} active particle bin, A m^{-2}
i_f^0	exchange current density of Li foil counter electrode based on a 1 M reference concentration, referred to the counter electrode area, A m^{-2}
$i_{n,k}$	reaction current density at the surface of the k^{th} active particle bin, A m^{-2}
j_n	electrochemical current generation (normal current density), A m^{-2}
k^0	electrochemical reaction constant, mol m^{-2} s^{-1} (mol m^{-3})$^{-1.5}$
k	thermal conductivity, W m^{-1} K^{-1}
n	unit normal vector
p	polynomial coefficients of the electrolyte concentration in the separator
q	polynomial coefficients of the electrolyte concentration in the cathode
$\dot{q}_{gen}$	heat generation per unit volume, W m^{-3}
$\dot{q}_{conv}$	convective heat transfer per unit surface area, W m^{-2}
$\dot{q}_{rad}$	radiative heat transfer per unit surface area, W m^{-2}
r_k	independent, zero-mean, Gaussian noise in the process model of Kalman filter
r_k	radial distance from the center of the k^{th} active particle bin, m
s	polynomial coefficients of the electrolyte potential in the cathode
sgn	sign function
t	time, s
t_+^0	Li^+ transference number
u_k	vector of inputs in k^{th} time step
v_k	independent, zero-mean, Gaussian noise in the measurement model of Kalman filter
w_k	independent, zero-mean, Gaussian noise in the process model of Kalman filter
x	distance from the negative current collector/anode interface inside the cell, m
$x_{c,a}$	arbitrary point inside the cathode, m

x_k	vector of states in k^{th} time step
y_k	vector of outputs in k^{th} time step
y_k	mole fraction of the Li concentration in the k^{th} active particle bin
A	surface are, m^2
C	Arrhenius equation constant
C_n	nominal capacity of the battery
C_p	specific heat, J kg^{-1} K^{-1}
$\mathcal{D}$	solid-state binary diffusion coefficient, m^2 s^{-1}
D_e	electrolyte diffusion coefficient, m^2 s^{-1}
$\mathbb{E}$	expectation operator
E^a	Activation energy, J mol^{-1}
F	Faraday's constant, 96,487 C mol^{-1}
I	current of the battery and identity matrix
I_{app}	total current applied to the prismatic cell, A
I_i	current flows in the positive current collector/tab interface, A
L	component thickness, m
L_k	Kalman gain matrix in k^{th} time step
M	hysteresis
M	an arbitrary large number
P_e	covariance matrix of process noise
P_r	covariance matrix of measurement noise
P_v	covariance matrix of measurement noise
P_w	covariance matrix of process noise
R^+	internal resistance of the battery during discharging
R^-	internal resistance of the battery during charging
R	universal gas constant, 8.314 J mol^{-1} K^{-1}
R_c	contact resistance between the electrodes and current collectors, Ω m^2
R_{eq}	equivalent Ohmic resistance of the cell, Ω m^2
$R_{p,k}$	radius of the k^{th} active particle bin, m
T	temperature, K
U_k	OCP of the k^{th} active particle bin vs. Li, V
V	volume of a specific component, m^3
V_{cell}	operating voltage of the cell, V
V_k	terminal voltage of the battery in k^{th} time step
α_k	thermodynamic factor of the k^{th} active particle bin
β	charge-transfer coefficient of the electrode
γ	tuning factor in hysteresis state model
γ	Bruggeman exponent, 1.5
δ	arbitrary small number
ε	component porosity
ε_k	volume fraction of the k^{th} active particle bin per unit volume of the electrode
ε_t	total volume of the electrode active material per unit volume of the electrode

η_i	coulombic efficiency of the battery
η_k	surface overpotential of the k^{th} active particle bin, V
θ_k	vector of parameters in k^{th} time step
κ	ionic conductivity of the electrolyte, S m^{-1}
ρ	density, kg m^{-3}
σ	bulk electronic conductivity, S m^{-1}
ϕ_s	electrical potential of the electrode, V
ϕ_e	electrical potential of the electrolyte, V
Δt	time step
Φ	electrical potential of the current collectors, V

Subscript:

a	anode
amb	ambient
c	cathode
cc	current collector
f	lithium foil
lay	active material layers (electrodes plus separator)
$layer$	a particular layer of the battery
par	parallel
s	separator
ser	series
$surf$	surface of the prismatic cell
Al	aluminum
Cu	copper
G	graphite electrode
Li	Lithium foil
LFP	LFP electrode
NT	negative tab
PT	positive tab
X	along the X-axis
Y	along the Y-axis
Z	along the Z-axis

Superscript:

avg	averaged value
c	charge
d	discharge
eff	effective value
P	pressure

Chapter 1 Introduction

Electric vehicles (EV) and plug-in hybrid electric vehicles (PHEV) present the best solution to reduce the level of pollutants in the atmosphere being produced by the transportation sector. These vehicles also reduce the dependency on petroleum [1]. Since lithium-ion (Li-ion) batteries produce zero emissions, offer flexibility of operation, and have high energy and power densities, they are more popular than other types of rechargeable batteries [2].

Li-ion batteries offer lower cost compared to nickel-metal hydride (NiMH) batteries, which are widely used in hybrid electric vehicles (HEV). Moreover, these batteries typically produce a greater voltage, about 3.6 V, than NiMH batteries, about 1.2 V [2]. Therefore, a NiMH battery pack can be replaced by a Li-ion battery pack with one-third of the battery cells. Reducing the number of cells in turn increases reliability due to the battery structure. In a battery pack, the components are usually connected in series, and failure of one component can deactivate the whole module. In addition, the energy density of Li-ion batteries is as much as two times that of the NiMH batteries' density. Their power density is also two to three times of NiMHs' density. Thus, Li-ions are more efficient than NiMHs [2]. These advantages make Li-ion batteries more viable candidates as energy storage systems in electric vehicles. However, incorporating these batteries introduces new challenges which require attention and lead to an important area of research.

The main issues arising from the commercial usage of Li-ion batteries in electric vehicles are safety, cost, and poor temperature performance. These are all connected to the battery thermal management. Therefore, employing Li-ion batteries as an energy storage system necessitates more studies of their thermal characteristics. In this work, the numerical simulation of Li-ion batteries is considered. In addition, the effect of tab locations on the performance and electrochemical characteristics of the battery is evaluated.

1.1 Lithium-Ion Batteries

Thermal behavior of Li-ion batteries is highly affected by their properties, including the positive and negative electrode materials, thickness of different cell layers, and electrolyte characteristics. Therefore, in this section some general information about Li-ion batteries and their characteristics are provided [3–5]. These batteries are categorized as rechargeable batteries and are composed of a number of cells. Every cell includes negative and positive electrodes whose constructive materials are made of lithium insertion compounds. In these batteries, lithium ions move from negative to positive electrode during discharging and from positive to negative electrode during charging period. They are also referred to as rocking chair batteries, as the ions are rocking between the positive and negative electrodes.

The pros and cons of Li-ion batteries compared to the other batteries are listed in Table 1-1. The high specific energy and energy density of Li-ion batteries, their long cycle life, and wide range of operating temperature make them a prominent choice for electric vehicles. Higher energy density and specific energy enable manufacturers to equip vehicles with smaller and lighter battery packs without compromising the driving range. On the other hand, Li-ion batteries have some drawbacks like the sensitivity to high temperature, which affects the rate of degradation and the safety of batteries.

Table 1-1: Advantages and disadvantages of Li-ion batteries [3]

Advantages	Disadvantages
Sealed cells; no maintenance required	Moderate initial cost
Long cycle life	Degrades at high temperature
Broad temperature range of operation	Need for protective circuitry
Long shelf life	Capacity loss or thermal runaway when over-charged
Low self-discharge rate	Venting and possible thermal runaway when crushed
Rapid charge capability	Cylindrical designs typically offer lower power density than NiCd or NiMH
High rate and high power discharge capability	
High coulombic and energy efficiency	
High specific energy and energy density	
No memory effect	

Li-ion battery cells usually have five different layers, namely: the negative current collector, negative electrode (anode), separator, positive electrode (cathode), and positive current collector (Figure 1-1). The positive electrode's material is typically a metal oxide with a layered ($LiCoO_2$), tunneled ($LiMn_2O_2$), or olivine structure ($LiFePO_4$). The negative electrode's material is typically a graphite carbon with a layered structure. In addition, Li-ion batteries' electrodes have a porous structure to increase reaction surface area which, in turn, increases the current for a fixed amount of active material in the electrode. The porous structure also reduces the distance between the electrolyte and active material in the solid phase and distributes the reaction across the electrode width.

Both electrodes are connected to highly conductive metals (current collectors) for exchanging the current with an external circuit. It should be mentioned that copper and aluminum current collectors are usually employed in Li-ion batteries as negative and positive current collectors, respectively. Positive and negative electrodes are separated by a medium called the separator. A separator is a very thin sheet of micro-porous plastic that allows the lithium ions to pass through. The separator and electrodes are immersed in a solution called electrolyte. The electrolyte conducts the ions between the electrodes but is an electric insulator. This makes the electrons flow through the external circuit. Due to the high voltage of Li-ion batteries, aqueous solutions may be electrolyzed, and non-aqueous solutions are typically utilized as the electrolyte. In this case, the electrolyte is usually a concentrated solution of lithium salts, such as $LiPF_6$ in an organic solvent.

1.1.1 Insertion Process

In a Li-ion cell, the active materials in both electrodes behave as a host for the lithium content of the battery. The lithium ions can be removed from or inserted into the active material particles without significant structural change to the host. This exchange process forms the basis of Li-ion batteries. During the charging process, lithium ions are removed from the active site in the positive electrode and inserted into the negative electrode (Figure 1-1). In Figure 1-1, $LiMO_2$ is a metal oxide material used in the positive electrode and C is a carbonaceous material used in the negative electrode. In the

discharge process, lithium ions travel through the electrolyte from the negative to positive electrode. The electrochemical reactions are also in the following form:

Positive electrode reaction: $LiMO_2 \underset{\text{Discharge}}{\overset{\text{Charge}}{\rightleftharpoons}} Li_{1-x}MO_2 + xLi^+ + xe^-$

Negative electrode reaction: $C + xLi^+ + xe^- \underset{\text{Discharge}}{\overset{\text{Charge}}{\rightleftharpoons}} Li_xC$

Overall reaction: $LiMO_2 + C \underset{\text{Discharge}}{\overset{\text{Charge}}{\rightleftharpoons}} Li_xC + Li_{1-x}MO_2$

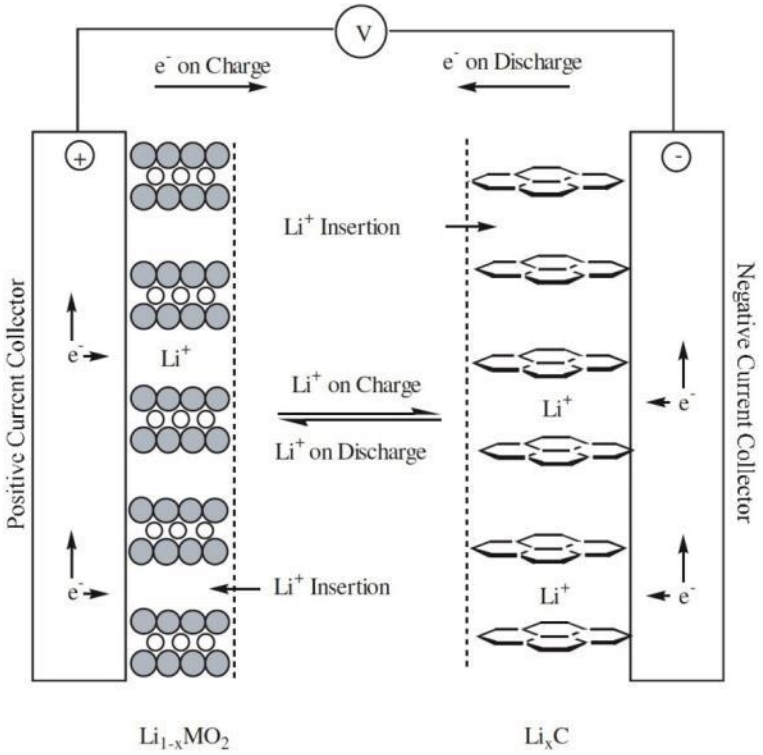

Figure 1-1: Schematic of the electrochemical process in Li-ion cells [3].

1.1.2 Positive Electrode Materials

Different chemical materials such as $LiCoO_2$, $LiMn_2O_2$, and $LiFePO_4$ can be used in the positive electrode. These materials must satisfy a series of requirements to be suitable choices for Li-ion batteries. One of these requirements is the capability of accepting a large amount of lithium in order to produce high capacity batteries. In addition, when high-working voltage and energy density are

required, the material should support the exchange reactions at high potential. Exchanging the lithium ions during the charging and discharging also should not affect their material structure. In the following, a review of the four most common materials for the positive electrodes and their characteristics are presented.

- Lithium Cobalt Oxide ($LiCoO_2$): This material has a layered structure and lithium ions are inserted between the layers of cobalt oxide. Although this chemistry supports high specific energy, its specific power is limited. Furthermore, it cannot be charged or discharged at a current higher than its standard value. Forcing these batteries to charge or discharge quickly causes overheating and undue stress.
- Lithium Manganese Oxide ($LiMn_2O_2$): This material has a three-dimensional spinel structure, which induces lower internal resistance and improves current handling. It also has high thermal stability and safety, but limited life cycle and calendar life. In addition, the capacity of a $LiMn_2O_2$ battery is roughly one-third lower than the capacity of a $LiCoO_2$ battery.
- Lithium Iron Phosphate ($LiFePO_4$): This material, which is shortly named LFP, has a tunneled structure and offers good electrochemical performance with low internal resistance. The main benefits of this material are enhanced safety, tolerant to abuse, good thermal stability, long cycle life, and high current rating. However, this material has lower voltage, thus reducing the specific energy. Also, their performance is reduced in low temperatures. Finally, high storage temperatures shorten their service life.
- Lithium Nickel Manganese Cobalt Oxide ($LiNiMnCoO_2$): This material, which is shortly named NMC, has high specific power or high specific energy, but not both. The secret of NMC lies in combining the manganese and nickel. Since nickel has high specific energy but low stability, and manganese has low internal resistance and low specific energy due to its spinel structure, combining these two materials brings out the best in each.

Figure 1-2 summarizes the performance of the batteries with the discussed positive electrode material.

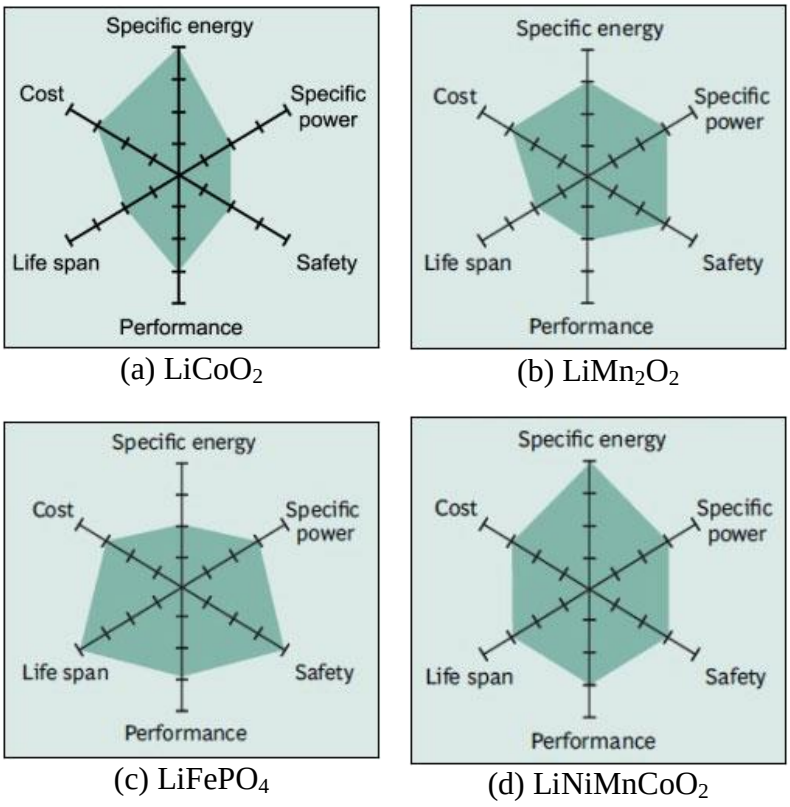

Figure 1-2: Characteristics of the common Li-ion batteries (based on [4,6]).

1.1.3 Large Li-Ion Batteries

The most basic unit of batteries is the cell that contains five layers: the negative current collector, negative electrode, separator, positive electrode, and positive current collector (Figure 1-1). Battery cells are assembled in different forms, such as cylindrical and prismatic, depending upon the application. The cylindrical types provide good mechanical stability and ease of manufacturing; while prismatic ones satisfy the demand for thinner sizes, lower manufacturing costs, and better heat transfer characteristics. In practice, prismatic cells are primarily used for electric powertrains within PHEVs and HEVs.

Since using batteries in electric vehicles requires more power compared to consumer electronic devices, the battery stacks are integrated into the modules and then into the battery packs (Figure 1-3). In the process of integrating stacks into a pack, many electrical, thermal, and

mechanical issues must be considered [7]. As a result, battery modules and packs are equipped with several additional components to increase their performance and safety. The potential, current, and temperature sensors and the stack balancing devices are some of the augmented components in modules. Similarly, a temperature and state of charge (SOC)[1] management system, module balancing devices, and communication modules to other parts of the vehicle are some of the components used in a pack.

Figure 1-3: Schematic depiction of the progress from cell to pack.

1.2 Motivation

Although Li-ion batteries are well-suited for electric vehicles, they have not yet been widely incorporated. This is mainly due to the safety problem, cost (related to cycle and calendar life), and low temperature performance of these batteries, which are mostly related to the thermal effects [8]. Electrochemical behavior of batteries is another factor that limits the performance and decreases the useful life of the battery. In addition, moving toward PHEVs necessitates employing larger battery packs. Thus, more attention is needed to reduce the cost and improve the safety and performance of batteries. Most of the reported researches are focused on finding electrode materials with higher specific energy, power, and cycle life [9–11], and the electrochemical-thermal effects are not well studied. This presents a significant gap in the knowledge of manufacturers and developers to design and fabricate safe and reliable batteries for EVs and PHEVs. In fact, the electrochemical and thermal patterns affect important characteristics of the battery, including the capacity and power fade,

[1] The SOC measures the level of the energy in the battery and is usually expressed as a percentage. When the SOC is 100%, it means the battery is fully charged. Similarly, when the SOC is 0%, it means the battery is fully discharged.

thermal runaway, and cold temperature performance [12]. These issues are briefly discussed in the rest of this section.

Capacity and power fade. —Capacity fade of Li-ion batteries occurs because of the loss of active materials needed for cycling. Power fade is also due to an increase in the internal resistance of the battery, resulting in the decrease of the operating voltage. For almost all of the cathode chemistries, the high operating temperature speeds up the aging process [13,14]. However, depending on the chemistry, this effect may be weaker or stronger. Higher temperatures also increase the rate of aging during battery storage. Therefore, the battery temperature is a critical parameter for studying the capacity and power fades. Moreover, the electrochemical behavior of Li-ion batteries highly affects their aging rate. Higher operating rates and higher change of SOC resulted from non-uniform electrochemical reaction distribution on the surface of the battery yield to higher degradation rate of batteries. As a result, studying the battery electrochemical reaction rate distribution is a key factor in design of a more durable battery.

Thermal runaway. —This process occurs when high temperatures trigger exothermic reactions. Exothermic reactions, in turn, increase the temperature further, potentially triggering more reactions. In this situation, the lack of a thermal management strategy can rapidly increase the internal temperature of the battery and lead to destructive results. When the battery temperature reaches 90-120 ºC, the metastable part of the SEI film[2] decomposes exothermically. As the SEI layer decomposes, the resistance of the electrochemical reaction is reduced and the negative electrode material reacts more with the electrolyte; as a result, more heat is produced. The positive electrode may also react with the electrolyte either directly or through the released oxygen due to the high temperature, around 180 ºC. In addition, the melting of the separator can occur at temperatures around 140 ºC. This leads the battery to short circuit and more heat generation [15,16].

[2] Solid-electrolyte interface (SEI) is a passivation layer that forms especially on the surface of the negative electrode (and to a less degree on the positive electrode as well) due to the reaction with electrolyte. This layer adds a resistance for the reaction to occur. Moreover, the composition of this layer may change depending upon the electrode potential, and the film dissolves and reforms as the cell is cycled.

In general, once a portion of the battery reaches a critical temperature, the exothermic reactions begin. By starting these reactions, more exothermic reactions are triggered, causing thermal runaway. This situation can be quite dangerous and result in the battery explosion, especially for the large battery packs. Therefore, different scenarios to prevent any possible chain of exothermic reactions must be considered in the battery design and an effective thermal management system (BTMS) should be incorporated. This system should carefully dissipate the heat generated inside the battery to prevent the likelihood of thermal runaway.

Low temperature performance. —The performance of Li-ion batteries is reduced as their operating temperature decreases [17]. The charging performance of Li-ion batteries is sensitive to the lower temperatures due to the irreversible lithium plating on the negative electrode; hence, charging at the lower temperatures should be limited [18]. It is also argued in [18], that the reduced battery performance at lower temperatures is mainly related to the poor charge transfer at the electrode/electrolyte interface rather than the poor ionic electrolyte conductivity and low solid diffusions. This issue is important for electric vehicles, especially during vehicle startup in cold ambient temperatures. To prevent the described problem, the BTMSs may employ battery-heating strategies to elevate the pack temperature at the vehicle startup.

In summary, the performance and safety of Li-ion batteries are highly influenced by their temperature distribution and their electrochemical behavior. As a result, researchers have been investigating the effect of different parameters such as battery design and operating conditions on the electrochemical reaction and temperature distributions in batteries using the available numerical and experimental methods. Obviously, full experimental characterization of Li-ion batteries gives the most accurate results, with the drawback of requiring several hundred hours of testing. On the other hand, electrochemical-thermal models can provide a fast and reliable tool to predict the behavior of Li-ion batteries especially in the process of design and development. These well-developed models can even be incorporated into the vehicle powertrain simulators to resemble the behavior of Li-ion batteries as energy storage systems. In this way, without spending much time and expense, the electrochemical-thermal response of batteries are tested in the simulated environment of vehicles.

The one-dimensional battery model presented by Newman et al. [19–21] predicts the behavior of small battery cells very well, but cannot accurately simulate large cells involving non-uniform potential, current, and temperature distributions. This inaccuracy in large cell modeling leads to a larger error, when being utilized to estimate battery variables on the volume of multi-layer batteries [22,23]. Therefore, in the absence of a comprehensive model to account for imbalanced distributions on the surface of large-sized batteries and between different battery layers, this study develops a electrochemical-thermal model that simulates the behavior of large-sized multi-layer batteries based on fundamental electrochemical and thermal equations. In addition, to be able to use the model for the dynamic charge and discharge studies as well as studying large-sized multi-layer batteries when they are assembled in modules or even packs, the computational efficiency is improved for faster convergence of the model.

1.3 Objective

In general, the main issues in utilizing Li-ion batteries especially for electric vehicles are related to the thermal effects. The battery design and its associated thermal management system must keep the battery temperature in a certain range. They must also maintain the temperature distribution inside the batteries uniform. In addition to the thermal issues, some more problems such as higher degradation rates occur due to the non-uniform electrochemical reaction distribution inside the batteries. These problems can be addressed by making battery current and potential distributions more uniform. An efficient way to gain knowledge about the electrochemical reaction rate and temperature distributions inside the battery and study the effective parameters on them is through the battery modeling. Given the battery model, one can optimize the battery design as well as test different operating parameters and thermal management strategies. However, in the literature the developed models are usually applicable to small coin cells introducing significant errors when are used for large-sized Li-ion battery simulations. In addition, the models developed for large-sized batteries are not considering the electrochemical and multi-layer details of prismatic cells leading to inaccuracy in their predictions. Finally, the proposed models in the literature are not computationally

efficient for dynamic modeling of prismatic cells when assembled in vehicles' battery pack or even module. Therefore, the main objective of this study is as follows:

Objective: To develop a high fidelity computationally efficient battery model suitable for design of large-sized prismatic cells considering both electrochemical and thermal effects.

This objective is expressed in more detail, as follows:

- *Develop a model for simulating the electrochemical-thermal behavior of Li-ion batteries:* This model should predict the temperature, potential, current, and electrochemical variable distributions in the battery. In order to calculate all these variables, however, a large number of equations have to be solved simultaneously leading to the high model computational cost. Therefore, the appropriate methods to reduce the model computational complexity should be utilized.
- *Parametric studies using the developed model:* The developed electrochemical-thermal model can be used to analyze the effect of different parameters on the electrochemical and thermal characteristics of batteries. These parameters may include charge/discharge rates and geometric design of the battery cells. With this type of studies, their design can be optimized, contributing to a more uniform electrochemical reaction and temperature distributions.
- *Validate the developed model with experimental data:* The developed model should be validated against the experiment results for the operating voltage of the battery and the temperature distribution on the surface of the battery. This validation assures that the model is correctly developed and can be used in different studies such as battery design.

1.4 Thesis Outline

The remainder of this thesis is organized as follows:

- Chapter 2 presents the literature on studying the electrochemical and thermal characteristics of the batteries with the main emphasis on the battery modeling approaches. In this chapter, first, the heat generation in Li-ion batteries and the approaches to measure and calculate this

heat generation is presented. Thereafter, the numerical and analytical methods used in the literature for modeling the batteries in different scales both thermally and electrochemically are reviewed.

- Chapter 3 introduces an extended and a dual extended Kalman filter for estimating the SOC of Li-ion batteries. The internal resistance of the battery, which can be used for calculating the battery heat generation, is also estimated in the developed filters. These filters can therefore be added to a general model including a heat conservation equation to even estimate the thermal response of the battery. However, as seen in the thesis, this method is not followed since the estimated parameters may be non-physical and be only useful for a specified battery. Moreover, the prediction ability of this method is limited and cannot be effectively be used for parametric studies and battery design. Therefore, more physical electrochemical methods are used in the next chapters. It should be mentioned that although Kalman filtering is not followed in the rest of the thesis, reviewing this method and its included models brings about unique insights regarding battery modeling, and internal battery states and parameters; hence, this method is not excluded from the thesis.
- Chapter 4 discusses the one-dimensional mathematical modeling of Li-ion batteries. The simulation results are compared against the reported experimental data in the literature showing the accuracy of the model in a broad range of operating rates. However, due to the complexity of the one-dimensional electrochemical model, the simulation time is high and the model cannot be effectively used for the large-sized prismatic cell modeling. Therefore, a simplifying method reducing the computational time is introduced and validated against the full-order model predictions.
- Chapter 5 first introduces a new simplifying method for fast simulation of one-dimensional electrochemical models. The results of this new method are compared with the full-order model predictions to show the accuracy of the proposed simplifying method. Afterwards, this chapter explains how to convert the simplified one-dimensional electrochemical models to a

three-dimensional model for the large-sized batteries. The advantages of the proposed approach compared to the others suggested in the literatures are then discussed.

- Chapter 6 uses the developed three-dimensional electrochemical model to study the effect of current collectors' thickness, and tab location and size on the electrochemical performance of Li-ion batteries. Some modifications to improve the uniformity of the electrochemical reaction rates on the surface of the current collectors are suggested. As it is mentioned in this chapter improving the uniformity of the electrochemical reactions reduces the battery aging and leads to design of more durable batteries.
- Chapter 7 estimates the electrochemical and thermal parameters of the electrode materials studied in this thesis (graphite as the negative electrode and $LiFePO_4$ as the positive electrode). A series of experiments are fist designed and performed on the electrode materials. Thereafter, the full-order one-dimensional electrochemical model is used to fit the experimental data and estimate the required parameters. Especially, the temperature dependence of electrochemical reaction kinetic at the surface of active particles and transport properties inside the active particles are characterized in this chapter.
- Chapter 8 uses the results obtained in the previous chapters and develops an electrochemical-thermal model for large-sized multi-layer prismatic Li-ion batteries. The three-dimensional model developed in Chapter 5 is extended to include multi-layer feature of the prismatic cell. The parameters obtained in Chapter 7 are also used in the model to describe the behavior of the electrode materials. The simulation results of the developed model are compared against the experimental results for the output voltage and temperature distribution on the surface of the prismatic cell showing the accuracy of the model.
- Chapter 9 summarizes the main conclusions and contributions of the work presented in this thesis, and presents some directions for future work.

Chapter 2 Background and literature review

Thermal analysis of Li-ion batteries has received considerable attention in the literature. Three different approaches are used to extend the studies in this area: analytical, experimental, and numerical approaches. The problem of battery thermal behavior was briefly introduced in the previous chapter. In this chapter, the methods presented to solve this problem are reviewed with a focus on numerical approaches. Moreover, the limitations of the extended studies are discussed, and some constructive suggestions are provided. This chapter is divided into four sections as follow. In Section 2.1, the models presented for the battery heat generation rate are discussed. In Section 2.2, the experimental techniques utilized to measure the heat generation rate in Li-ion batteries are addressed. Then, in Section 2.3, analytical methods are presented. Section 2.4 describes the utilization of heat generation models in thermal modeling. It also shows the importance of three-dimensional modeling and reviews different levels of thermal modeling.

2.1 Heat Generation in Battery Cells

During the operation, batteries produce heat due to the electrochemical reactions, phase changes, mixing effects, and resistance of the cell layers. Furthermore, the movement of the electrons inside the current collectors is a source of heat generation, which becomes more important in the case of a larger size battery. Since understanding the battery heat generation is critical in thermal studies, a review of the heat generation models is provided in this section.

Bernardi et al. [24] used the energy balance equation to derive a general estimation of battery thermal characteristics. The temperature was assumed to be constant across the cell, and pressure effects were considered negligible. In this work, the electrochemical reaction, charge transfer, phase change, and enthalpy of mixing were contributed to the heat generation rate of the battery, $\dot{Q}$, and the following expression was achieved

$$\dot{Q} = -IT\frac{dU^{avg}}{dT} + (IU^{avg} - IV) + mixing\ terms + phase\ change\ term, \qquad (2\text{-}1)$$

where I is the total current of the cell, T is the temperature of the cell, U^{avg} is the average open circuit potential (OCP)[3] evaluated at the average value of SOC along the battery cell, and V is the potential of the cell. Detailed equations of the mixing and phase change terms can be found in [24]. In Equation (2-1), the first term accounts for the reversible heat generation and is produced due to the entropy of electrochemical reactions. The second term accounts for overpotential caused by Ohmic losses, charge transfer overpotential at the solid/electrolyte interface, and mass transfer limitations. The reversible heat generation can be endothermic or exothermic, depending upon the entropy of reaction and whether the battery is being charged or discharged; the irreversible heat generation is always exothermic.

Although the method presented by Bernardi et al. is a general thermal model, the constructive elements of the heat of mixing term were not explicitly developed. In the developed equation (Equation (2.1)), the mixing term can be thought of as a correction to the dependence of the involved terms on the average SOC, rather than local values in the electrodes. However, more explicit expressions for this term are required. Rao and Newman [25] attempted to develop a thermal model that considers the effect of concentration variation across the electrode by locally determining the OCP. They showed that the calculation of the OCP, as an average quantity, introduces some errors to the rate of heat generation; it is better to locally determine the OCP through the following equation:

$$\dot{Q} = -\int a i_n U dv - IV, \qquad (2\text{-}2)$$

where the integral is taken over the cell volume, a is the surface area per unit volume of the porous electrodes, i_n is the interfacial current density and is positive for anodic and negative for cathodic reactions, U is the local OCP of the reactions. In fact, by relating the OCP to the local concentration of the lithium, they accounted for contribution of heat of mixing resulting from concentration variation across the electrode. However, they ignored the contribution of other mixing effects.

[3] The OCP is the electronic potential difference between the positive and negative electrodes when the battery is disconnected form the external circuit. This parameter is measured in voltage.

The model developed by Rao and Newman improves the heat generation prediction; however, it still treats the heat of mixing inconsistently. Thomas and Newman [26] showed that treating the heat of mixing inconsistently can cause a wrong prediction of the heat generation in some cases. This is because the components of heat of mixing may have the same magnitude, but opposite signs. Therefore, the better way is to add them to the heat generation equation at the same time.

Thomas and Newman developed a model to explicitly incorporate different components of mixing heat into the heat generation equation. They reported the final form of heat generation equation as

$$\dot{Q} = (IU^{avg} - IV) - IT\frac{\partial U^{avg}}{\partial T} - \sum_k \Delta H_k^{avg} r_k - \int \sum_j \sum_i \left(\bar{H}_{ij} - \bar{H}_{ij}^{avg}\right)\frac{\partial c_{ij}}{\partial t} dv\,, \qquad (2\text{-}3)$$

where the first summation is over k chemical reactions, ΔH_k^{avg} is the enthalpy of reactions evaluated at the volume-average composition in the cell, and r_k is the rate of chemical reactions. Furthermore, the integral is taken over the cell volume, the summation inside the integral is taken over all species$i$ in phase j, $\bar{H}_{ij}$ is the partial molar enthalpy, and c_{ij} is the concentration of species i and is a function of position and time. In Equation (2-3), the third term on the right hand side is the heat change by any chemical reaction inside the battery and the last term is the heat of mixing; then, the heat of reaction and mixing are separated.

It is worth mentioning here that the heat of mixing is the direct result of using insertion compounds in electrodes as well as utilizing the porous structures for them. The former causes variation of the lithium concentration inside the solid particles while the latter leads to a non-uniform reaction rate across the electrode, and thus non-uniform lithium concentration in the solid phase and electrolyte. As a result, there are four components for heat of mixing: across the electrodes because of the non-uniform reaction and current distribution, across the electrolyte due to the finite mass transfer, within the solid particles due to the insertion, and within the electrolyte-filled pores of the porous electrodes because of the occurrence of electrochemical reactions only at the solid/electrolyte interface. Thomas and Newman explicitly expressed each of them by integrating the last term of Equation (2-3) over the appropriate phase and location. In addition, the heat of mixing is the only

term that contributes even after the current is interrupted, since the concentration gradients developed during the battery operation relax and cause the heat to be released or absorbed.

In the literature, both experimental and numerical investigations are used to estimate the battery heat generation. However, some terms such as entropic heat generation need to be measured experimentally. These experimental measurements then are directly applied to the numerical thermal models. Therefore, in the next section, the experimental methods utilized to measure the battery heat generation are reviewed and it is explained how entropic heat is obtained from the experimental measurements.

2.2 Heat Generation Measurements

In this section, two main subjects are covered: the measurement of total battery heat generation and entropic heat generation. The purpose of this section is to provide an introduction to the experimental measurement techniques in Li-ion battery studies. The measured values in these experiments can be used to validate theoretical models as well as increase the understanding about the nature of the heat generation process in these batteries. In addition, the measured entropic heat generation is used as an input to the thermal models.

2.2.1 Total Battery Heat Generation

The primary experimental methods to measure total battery heat generations are accelerated-rate calorimetry (ARC) [27–29] and isothermal heat conduction calorimetry (IHC) [26,30–32]. In the ARC method, the battery temperature change is captured and the following relation is used to calculate the heat generation of the battery:

$$\dot{Q} = MC_P \frac{dT}{dt} + hA\left(T_{surf} - T_{amb}\right), \tag{2-4}$$

where M is the total mass of the battery, T is the battery temperature, C_P is the battery heat capacity, T_{surf} is the surface temperature, T_{amb} is the calorimeter temperature, and hA is the calorimetric constant. The calorimetric constant is estimated using a high conductive material in the exact shape and size of the battery. Since the heat generation of this piece is zero, when it is placed in the

calorimeter and tested under different conditions, it gives the calorimetric constant determined by Equation (2-4). In the IHC method, the battery temperature is always kept constant during the experiments by incorporating liquid or metal heat sinks. Therefore, all the heat dissipated to the sink represents the battery heat generation.

Most of the reported works have been conducted on small cells and under low charge/discharge rates (i.e., 0.1 C to 1 C) [12]. In high operating rates, the battery is rapidly warmed up and heat storage term becomes more important; therefore, accurate estimation of the heat capacity is critical. In addition, in these rates, the concentration gradients developed inside the battery can change the local heat generation. For large batteries, the temperature variation inside the battery is more critical and makes the experimental procedure more complicated. Although the published works in this area are discrepant, their highlighted points can be summarized as [12]:

- Heat generation rate increases with the discharge rate.
- In higher discharge rates, by increasing the depth of discharge (DOD)[4] (which changes the internal resistance), the heat generation increases. Moreover, the increment profile depends upon the relative magnitude of entropic and overpotential heat.
- Effect of environment temperature has rarely been studied. Since the temperature affects the battery behavior, and especially, improves the battery mass transport and kinetics, increasing the environment temperature is expected to reduce the battery heat generation.

2.2.2 Entropic Heat Generation

The reversible heat generation is an important part of the total heat. Neglecting this term may introduce large errors in the thermal consideration of batteries especially in lower charge/discharge rates where the overpotential heat is comparatively small. This heat is also important for larger charge/discharge rates. In a comparative study on reported heat generation data [12], the reversible heat generation was indicated to have the same order of magnitude as overpotential heat generation

[4] The DOD is the inverse of SOC and while one increases the other one decreases.

at the moderately high C-rate[5] (1C). In addition, transient behavior of the total heat is largely affected by the this heat and it was stated that the oscillations observed in the battery heat generation originated from this source term [26,29,31].

To add this term to the thermal models, the value of entropic heat generation has to be estimated experimentally. Several methods were utilized to obtain the entropic heat generation. The most usual method is measuring the OCP variation with temperature at a fixed SOC [26–29,31,32]. However, because of some problems with this method, such as long time to reach the steady OCP, other calorimeter-based methods were developed. In these methods, irreversible heat is assumed to be unchanged during the charging and discharging periods. Therefore, if the collected discharging heat, q_{dis}, is subtracted from the charging heat, q_{cha}, the reversible heat, q_{rev}, can be calculated as

$$q_{rev} = \frac{q_{dis} - q_{cha}}{2}. \tag{2-5}$$

This method of calculation is shown [31] to result in the same predictions as measuring the OCP as a function of temperature with a fixed SOC. However, Hong et al. [27] observed sensitivity to the rate of charge/discharge, which may cause some inaccuracies. The other method is based on subtracting the irreversible heat from the total heat. In this case, irreversible heat is estimated using the OCP and voltage of the battery during the operation [33]. More details on this heat source and its sign during charge and discharge periods can be found in [29,33].

2.3 Analytical Methods

Since the battery geometry and heat generation models are fairly complex and their simplification causes unrealistic predictions, not much attention is paid to the analytical methods. Newman and Tiedemann [34] modeled the batteries by assuming the constant heat generation rate and constant temperature at the boundaries. The transient three-dimensional heat conduction in a block was solved using the separation of variables method. Accordingly, the battery thermal aspect ratios

[5] The C-rate is a measure for the current of a battery cell which is scaled to the nominal capacity of a cell stated by the manufacturer at reference conditions. A current of 1C means that the battery cell is ideally charged or discharged in one hour, C/2 in two hours and 2C in half an hour.

defined as $L_x/L_y\left(k_y/k_x\right)^{1/2}$ and $L_x/L_z(k_z/k_x)^{1/2}$, are found to be important in the process of heat dissipation.

As an extension to the work done by Newman and Tiedemann, Taheri and Bahrami [35] investigated the transient three-dimensional heat conduction in a block resembling a Li-ion battery stack. In this case, the heat conduction equation was analytically solved by integral transform techniques [36]. Transient heat generation and convective boundary conditions were also considered. In this study, Equation (2-7) and experimental measurements were used to estimate the heat generation rate. The entropic heat generation term was ignored and heat generation was assumed to be independent of battery temperature. Finally, they reported temperature increase under different discharge rate and convective heat transfer coefficients. They suggested utilizing the battery up to 90% DOD in order to prevent the sudden temperature rise at the end of discharge. However, the analytical scheme requires a lot of simplifications to make this method applicable. In general, the main approach for studying Li-ion batteries is the use of numerical simulations.

2.4 Numerical Simulations

Several numerical simulations have been conducted to study the thermal behavior of Li-ion batteries. These simulations range from modeling a single cell to complicated models for large battery packs. In all these works, the temperature distribution inside the battery is calculated by the heat equation described as follows:

$$\rho C_P \frac{\partial T}{\partial t} = \nabla(k\nabla T) + \dot{q}, \tag{2-6}$$

where the term on the left hand side is the heat stored in the battery, and the terms on the right hand side are respectively heat conduction and the volumetric heat generation rate. In numerical methods, the battery simulation domain is discretized to small volumes; then, the temperature distribution is obtained by solving Equation (2-6) for each volume using appropriate boundary conditions.

In the process of simulation, many different assumptions have been made, resulting in several modeling approaches in the papers. Therefore, the thermal modeling of Li-ion batteries can be divided according to different criteria as listed below:

- *Methodology to predict the heat generation rate inside Li-ion batteries:* In general, the heat generation rate can be estimated using experimental measurements or electrochemical models.
- *Size of the battery cell:* While small cell simulation has been studied in many papers, only a few have considered the effect of battery size on thermal behavior.
- *Scale of modeling:* The modeling of Li-ion batteries can be conducted on different scales, from just a single cell to a full battery containing many cell layers.

In the rest of this section, a review of published papers on thermal modeling of Li-ion batteries is presented. In addition, the main features of these studies are highlighted, and more physical insight for the modeling of Li-ion batteries is provided.

2.4.1 Heat Generation Rate Prediction

As pointed out above, experimental measurements and electrochemical models are employed to calculate the heat generation rate of Li-ion batteries. In experiment-based methods, the reviewed papers [35,37–44] utilized the simplified form of Equation (2-1) as follows:

$$\dot{Q} = -IT\frac{dU^{avg}}{dT} + (IU^{avg} - IV). \tag{2-7}$$

In Equation (2-7), the heat of mixing is neglected. The required data to calculate the entropic and overpotential heats are gathered from experimental tests. In this approach, the only connection between the thermal field and electrochemical heat generation rate is through the entropic heat, which is the product of temperature and IdU^{avg}/dT.

To calculate the irreversible heat generation, some researchers [35,37–39] used the OCP and operating voltage curves; others [40–44] utilized an equivalent circuit model which relates the OCP and operating voltage via the battery internal resistance, R_{int} (Figure 2-1). In the latter case, the

model is similar to ones used in the state estimation of the batteries [45,46] and usually has the following form:

$$U^{avg} - V = R_{int} I. \tag{2-8}$$

After approximating the internal resistance using the experimental data, the Ohmic heat generation can be calculated by $R_{int} I^2$.

Battery internal resistance has been approximated using different equivalent circuits. For example, Kim et al. [41] employed the simplest equivalent circuit model (Figure 2-1(a)) and a cubic polynomial to describe the internal resistance as a function of DOD. The polynomial coefficients were determined by curve fitting to the experimental data obtained for different charge/discharge rates. In order to improve the predictions of equivalent circuit model, Sun et al. [42] employed a more complicated equivalent circuit (Figure 2-1(b)). In this case, the internal resistance is estimated by

$$R_{int} = R_1 + R_2(1 - e^{-t/CR_2}). \tag{2-9}$$

In this study, battery resistances, R_1 and R_2, and capacitance, C, used to calculate irreversible heat generation of the battery as a function of temperature, DOD, and charge/discharge rate.

The researchers that estimate heat generation using experimental measurements usually use the data from one temperature and ignore the variation of the battery properties by temperature. However, the battery transport properties are all temperature dependent and affect the irreversible heat generation. In addition, the electrochemical reaction coefficients, which influence the contribution of reactions to irreversible heat generation, are also a function of temperature.

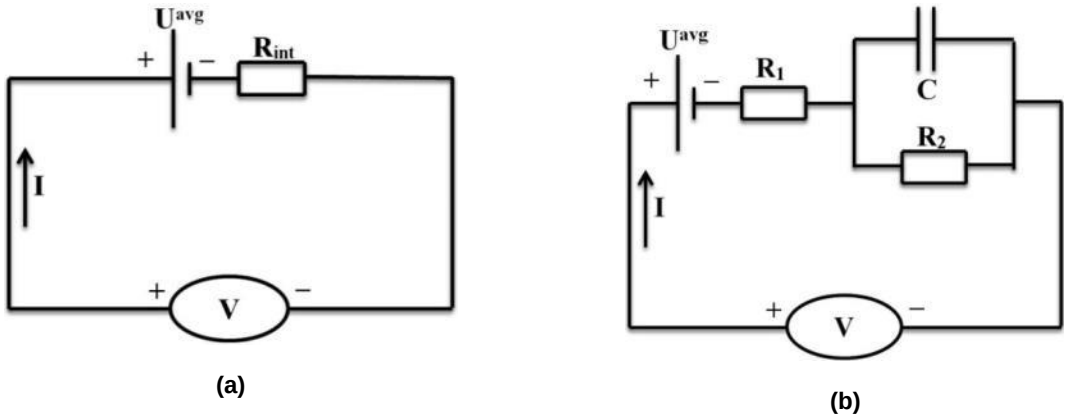

Figure 2-1: Equivalent circuit models of the battery (based on [42,46]).

Pals and Newman [17] studied the effects of temperature variation on the performance and heat generation rate of Li-ion batteries. In their study, the electrolyte conductivity and solid-phase diffusion coefficient are exponentially related to temperature; hence, any increase in temperature improves the transport of lithium ions. This improvement consequently decreases the heat generation rate of the battery in higher temperatures. Srinivasan and Wang [47] also compared the heat generation predictions of isothermal and non-isothermal models. They observed a large error (about 40%) in isothermal predictions at high C-rates. They concluded that ignoring temperature dependency of the battery properties may introduce a significant error to the heat generation predictions and more attention should be given to considering and measuring these properties.

As another approach, the heat generation of Li-ion batteries can be predicted via detailed electrochemical models. This approach yields a strong connection between the temperature field and heat generation. In this approach, one way of calculating the heat generation rate is utilizing the average cell overpotential [17,22,48,49]; the other option took advantage of detailed electrochemical information [23,47,50–53]. In the former case, a simplified form of the Bernardi and Newman [24] energy balance equation (Equation (2-7)) is used, while in the latter case the expressions presented by Rao and Newman [25] (Equation (2-2)), Gu and Wang [54] or Thomas and Newman [26] are incorporated (Equation (2-3)). These equations and the pros and cons of each one are explained in detail in Section 2.1.

Finally, as another part of heat generation calculations, the importance of the entropic heat can be discussed. In the literature, this term is treated as constant [37–39,50], a function of SOC [23,26,40–43,47,53], or even neglected [17,22,49,51,52]. Srinivasan and Wang [47] evaluated the effect of this heat and showed its importance at all C-rates. Thomas and Newman [26] also observed that the variation of the total heat generation rate as a function of SOC is dictated by the entropic heat. Moreover, this term is important even in the applications such as HEVs wherein the battery is alternatively charged and discharged about a relatively fixed SOC. Wang et al. [51,52] ignored entropic heat under this condition because of its reversibility. However, Bandhauer et al. [12] discussed that due to heat accumulation during multiple cycles, the entropic heat should be included even in HEV applications.

2.4.2 One-Dimensional Versus Two or Three-Dimensional Modeling

In simulating the thermal behavior of Li-ion batteries, some researchers just used one-dimensional models [17,19,20,25,26,49,51,53,54], whereas others moved toward incorporating the two or three-dimensional models [16,22,23,37–40,47,50,55]. In the case of one-dimensional models, the variation of battery variables in the directions parallel to the current collectors is ignored. This assumption is valid for small coin cells where the current and potential on current collectors are almost constant. However, in the case of large capacity Li-ion batteries, ignoring the non-uniformities in distribution of battery variables is not acceptable. These non-uniformities grow even more when large batteries operate at high C-rates.

Evans et al. [37,38,50], Chen et al. [39], and Yeow et al. [43] considered the three-dimensional distribution of temperature in the battery. In their models, the heat generation was constant over the volume of the battery, and three-dimensional temperature distribution was obtained with only applied boundary conditions. Srinivasan and Wang [47] used a two-dimensional model to analyze the Li-ion cells and concluded that the temperature variation across a cell is negligible even at high C-rates. They also found the non-uniformity in electrochemical and thermal variable distributions becomes an important factor when operating rate increases. However, the method used in this work was fully solving the electrochemical and thermal equations. This method is computationally very

intensive and is not employed for three-dimensional modeling. Other researchers used simplified models to do simulations in a reasonable time frame.

Some researchers [40–42,55] assumed the current only flows in the perpendicular direction to battery layers (Figure 2-2). Based on this assumption, they calculated the two-dimensional potential and current density distributions on the large-sized battery. In these calculations, only Ohm's law, charge conservation on the electrodes, and polarization characteristics of the battery were used. Although this method is computationally fast, it requires many experiments to characterize the internal resistance of the battery as a function of temperature and DOD, making the model hard to develop. In addition, this model can be used just for studying the battery under different operating conditions. Any study about the effect of different battery parameters on the thermal behaviors is not achievable by this type of modeling.

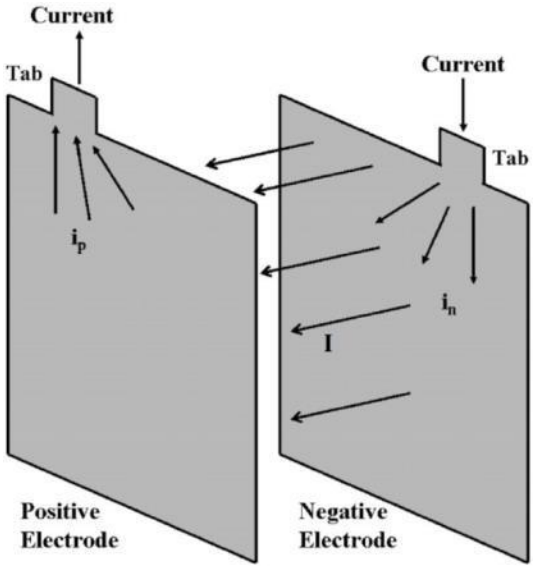

Figure 2-2: Schematic diagram of the current flow in a battery cell (based on [55]).

Kim et al. [23] developed a three-dimensional model for Li-ion cells by dividing the battery into three subdomains, namely: particle domain, electrode domain, and cell domain (Figure 2-3). The particle domain deals with solid-phase particles in the positive and negative electrodes and concerns the diffusion inside the particles as well as the reaction at the particle surface. The electrode domain includes diffusion and current flow in the electrodes and electrolyte. Finally, the cell domain is

utilized for the electrical and thermal behavior calculations of the battery. The current and temperature distributions over the cell are calculated in this domain. Three domains are decoupled and solved separately in this method, but the physics between them is still coupled by the inter-domain information exchange.

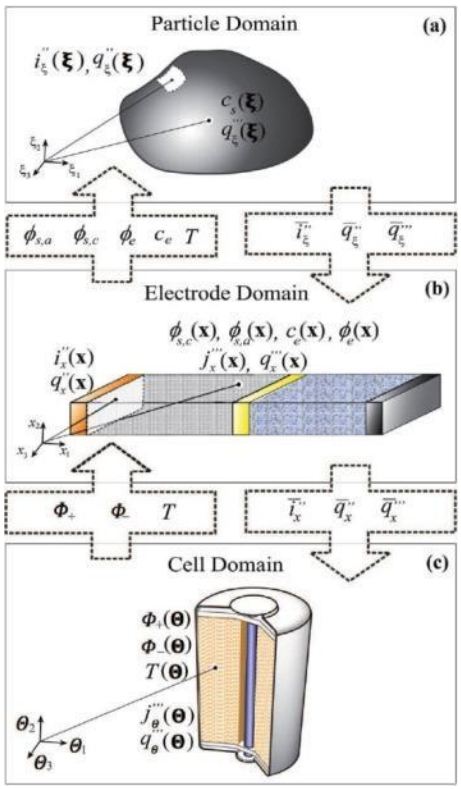

Figure 2-3: Summary of the model developed by Kim et al. [23].

Finally, Gerver and Meyers [22] presented a three-dimensional electrochemical-thermal battery model simulating coupled thermal and electrochemical phenomena in Li-ion batteries simultaneously. They modeled the current collectors with a network of resistors connected to the other current collector via a number of electrochemical resistors. The electrochemical resistors were also nonlinear curve fittings to the one-dimensional electrochemical models derived from the basic electrochemical equations of the battery. Combining the electrochemical resistors and two-dimensional resistor networks and solving the subsequent equations determined the battery variables in three dimensions.

2.4.3 Different Scales of Modeling

Battery simulation has been conducted in different scales, namely: cells, stacks, modules, and packs. Many researchers [17,19,20,23,25,26,47,52,56] investigated the thermal behavior of Li-ion batteries only for a single cell. Compared to work done in the cell scale, fewer studies have been conducted on other battery scales. In these studies, different approaches have been taken to move from single cell to a stack of cells. Kim et al. in [40,41] employed the method described in [55] and dealt with the stack as an equivalent circuit (Figure 2-1). The output voltage of the battery was fitted to the experimental data by optimizing the internal resistance coefficients. However, in this works, the detail of the layered structure of stacks has not been considered and hence the temperature distribution inside the stack is not accessible. On the other hand, due to the thermally accumulative behavior of these multi-layer cells, the maximum temperature occurs in the middle of the stack. As a result, this model needs to be improved to accurately capture the thermal behavior of the battery.

Pals and Newman [49] modeled a stack by placing different numbers of the battery cells side by side. The temperature gradient across the stack was modeled by assuming a constant temperature in each cell but variable from cell to cell (Figure 2-4). The results revealed that by increasing the stack thickness the temperature of the battery increases and its profile gets steeper. Moreover, they found out that since heat is generated more in the regions with lower temperature, the process of heat generation tends to flatten the temperature profile. Therefore, considering the uniform heat generation across the stack, causes a wrong temperature prediction as in some papers, such as [34,35,40,41,43].

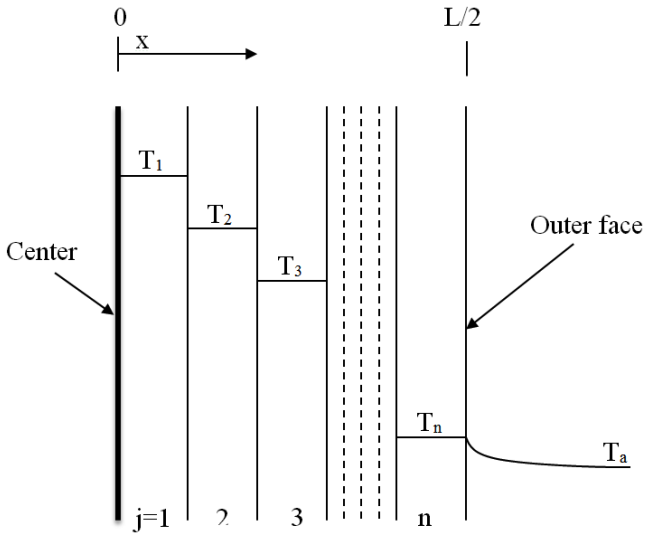

Figure 2-4: Schematic diagram of one-half of a stack [49].

Although the developed model by Pals and Newman provides some insight in thermal modeling of multi-layer cells, it does not consider the current distribution between their layers. It is expected that the layers located in the middle, rise in temperature, thus allowing more current to pass. To address current distribution between the cells, Gerver and Meyers [22] connected all cells and solved the entire system simultaneously. In this model, since the cells are parallel, the current entering a current collector can go into either the cell on the left or on the right (Figure 2-5). The reported results showed that the current of the cells in the middle of the stack increases with time, while for the outer cells the current drastically decreases.

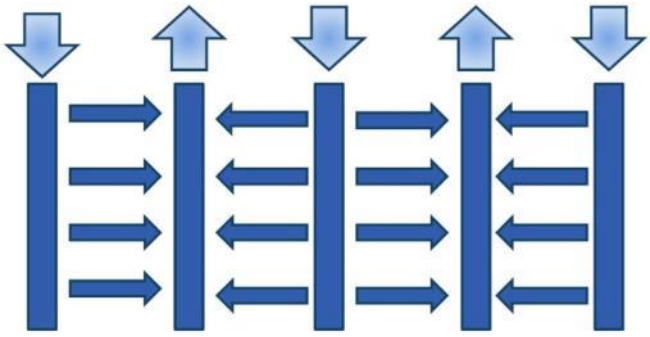

Figure 2-5: Diagram of current flow in the stack [22].

In published papers, almost no one has simulated battery modules or packs in detail. For example, Smith and Wang [51] simply modeled a battery pack using 72 series connected cells, where the final voltage was calculated by multiplying the voltage of a single cell by 72. The same holds true for the works reported by Evans et al. [37,38,50], Chen et al. [39], and Karimi and Li [44] where the battery pack is treated using a series of connected cells. In these types of works, Yeow et al. [43] considered more detail and conducted a study of a battery system consisting of three stacks. The stacks were connected by aluminum cooling fins that conducted generated heat in stacks to the cold plates located at the sides. In fact, the fins functioned as a thermal bridge between the stacks and cold plate. This simulation predicted the temperature at the surface of the stacks, but the temperature variation inside the stacks was ignored.

Finally, Sun et al. [42] developed a three-dimensional decoupled battery pack model to estimate the temperature distribution on a single stack as well as across the battery pack. The battery pack included 40 stacks, cooling plates, and lower and upper cooling ducts. This model consisted of a three-dimensional battery pack submodel, an equivalent circuit submodel, a one-dimensional transient battery network thermal submodel, and a three-dimensional battery stack thermal submodel. Many details were included in this model, but the temperature variation was still calculated at the surface of the stacks and no insight was provided inside the stacks.

In summary, in spite of a large number of papers regarding the thermal modeling of batteries, few models with electrochemical details are reported. These detail models have usually been used only in single cell modeling. In larger scales, the researchers utilized mostly the simplified models that can track temperature at the surface of the batteries. However, the temperature of the inner layers may exceed the maximum limit, while the surface temperature is still in the allowed range. As a result, developing a detailed battery model capable of simulating large-sized multi-layer cells in a reasonable time is necessary. Due to these advantages, this model can also be utilized in modeling of battery modules and packs.

Chapter 3 Kalman Filtering

The following section is based on previously published work by Mastali, M., Vazquez-Arenas, J., Fraser, R., Fowler, M., Afshar, S., and Stevens, M.

Journal of Power Sources 2013, 239: 294-307 [46].

"**Battery state of the charge estimation using Kalman filtering**"

This thesis author specific contribution to this paper was to develop the model, conduct the simulations, prepare all the graphics and results, prepare the final manuscript and reviewer edits with direction from the project supervisors who were co-authors. All authors reviewed the manuscript.

Reproduced with the permission from Elsevier.

3.1 Introduction

One of the most important battery control and monitoring parameters is the state of charge (SOC) of the battery, since it determines the amount of energy available and thus the range of the vehicle under all electrical or electrical assist operation. Therefore, correct estimation of the SOC of the battery has become crucial in the manufacture of Battery Electric (BEV), Plug-in Hybrid Electric (PHEV), and Hybrid Electric Vehicles (HEV). These vehicles experience a dynamic power demand profile, with peaks in power draw as well as a wide range of SOC change [57].

Methods to estimate SOC in small electronic devices have been implemented for several years [58]. However, different requirements are demanded by the batteries in the vehicles, whereby relying on these methods may be totally inaccurate for vehicle purposes. Plett [59] compared battery applications for portable electronic devices and EVs against those utilized in HEVs, concluding that the latter one is much more demanding than the other two applications in terms of battery usage. The parameters used for this comparative study were the maximum rate of the charge and discharge, duty cycle, accuracy needed to estimate the SOC, and lifetime of the battery. It was concluded that for all the aforementioned parameters, the HEV environment involves more challenges when the battery

management systems (BMS) are engaged. Particularly, SOC estimation within the accuracy range demanded for the HEVs presents a serious challenge for the BMSs.

For this reason, the objective of this chapter is to solve the described problem by developing a robust Kalman filtering method to estimate the SOC of commercial batteries implemented in HEV and PHEV. In addition, we provide a more complete description for implementing the Kalman filter in order to make it more accessible to a greater number of battery researchers. By comparing the noise parameters used in Kalman filtering of two cylindrical and prismatic $LiFePO_4$ batteries, some physical descriptions are also provided to explain the reason behind the difference between the values of these parameters.

3.1.1 Background

Some research has been carried out to develop methods capable of estimating the SOC of the batteries for vehicle applications [60–69]. In the most recent published work Andre et al. have fitted a Kalman filter and support vector machine (SVM) algorithm to NMC cathode cells. Piller et al. have published an extensive review of different methods applied to determine the SOC [70]. To this concern, the most frequent methods for SOC estimation utilized are summarized below, and include:

1. coulomb counting,
2. open circuit voltage (OCV) estimation,
3. electrochemical impedance spectroscopy (EIS), and
4. filtering.

Among these, coulomb counting is the most common used for small electronic devices. This method employs a very simple and intuitive principle entailing that the number of electrons transferred to the battery during the charge period are equal to the number of electrons transferred from the battery during the discharge period. This can be formulated as

$$SOC = SOC_0 + \frac{1}{C_n}\int (I_{batt} - I_{loss})dt \tag{3-1}$$

where SOC_0 is initial SOC, C_n is the nominal capacity of the battery in As, I_{batt} is the discharging (positive) or charging (negative) current of the battery in A, and I_{loss} is the current consumed by the loss reactions in A.

However, the coulomb counting method presents two main problems. First, the charging current supplied by an external power source is not totally used, and thus calculations of the I_{loss} are required. This calculation is not straightforward, and it may introduce a considerable error in the lack of a precise determination [70]. Second, an accurate measurement of the current is crucial in this technique, whereby more expensive sensors are required. In general, two different types of sensors are used: Hall Effect and current shunt sensors. A Hall Effect sensor measures the magnetic field around a wire and then estimates the current through it by using Ampere's law. On the other hand, the current shunt sensor is a very small resistance used in series with the circuit to measure the voltage drop. Ohm's law is subsequently used to calculate the current flow in the wire. Although the current shunt sensors provide more precise current measurements, the Hall Effect sensors are easier to install. However, none of them can provide accurately measurements for SOC estimation via coulomb counting. Therefore, a better method needs to be applied for these purposes. In portable devices recalibration of the SOC estimation often requires complete discharge of the battery that has degradation impacts on cells, as well as being impractical in vehicle applications.

The OCV estimation is a method regularly used for SOC prediction. It relies on the fact that under open circuit conditions (i.e. current equals zero), the measured voltage can be related to the battery SOC using the OCV diagram. Figure 3-1 shows the OCV diagram of a battery fabricated with $LiFePO_4$ cathodes. However, the use of this method leads to some problems in SOC estimation. The OCV-SOC relation highly depends on the chemistry, temperature, and state of the health (SOH) of the battery. As battery ages, the OCV diagram changes slightly, whence its use for SOC estimation turns out to be inaccurate. In Li-ion technology the discharge performance is 'flat' with limited change in voltage over a wide range of SOC making estimation of SOC difficulty. The prediction of this dynamic change is especially difficult as a result of the complex duty profile and environment within the HEV and PHEV. In addition, the OCV is also affected by temperature, and a single OCV diagram cannot be utilized to account for different temperatures. It is worth to highlight

from Figure 3-1 that for the SOC range between 10-90%, wherein the HEV and PHEV mostly operate, the OCV changes approximately by 0.2 V. Consequently, a small inaccuracy in the voltage measurement yields a large error in SOC estimations.

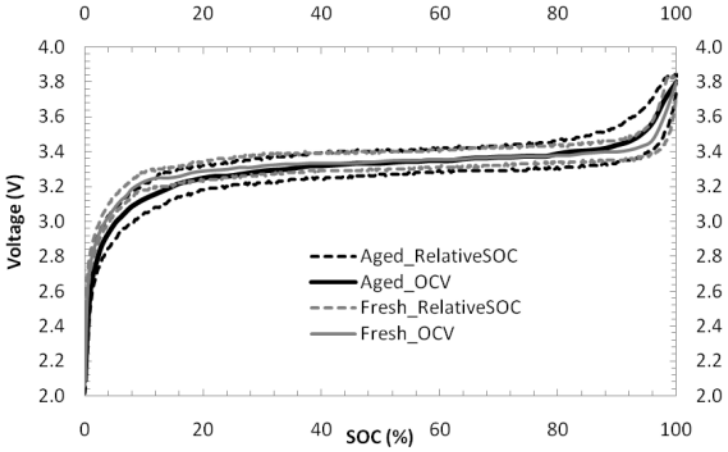

Figure 3-1: Open-circuit voltage for fresh and aged batteries as a function of state-of-charge [71].

The third technique studied in this thesis is the Electrochemical Impedance Spectroscopy (EIS). Considerable research has been devoted in this area in order to estimate SOC and SOH. Further details of the SOC measurement in batteries through EIS can be consulted in reference [72]. The basis of this technique is considering that the electrochemical resistance can be separated into the electrical impedance and mass transfer resistance. Electrochemical impedance spectroscopy (EIS) is applied through the measurement of the system response to a periodic small amplitude ac signal. This allows for examination of various electrode processes such as the ionic transfer and electrons transfer. Of interest to this study is that when the SOC decreases, the contribution of the resistance associated with diffusion phenomena becomes higher, and the Nyquist plot exhibits a 45º linear-slope. Figure 3-2 exhibits the Nyquist plot of a Li-ion battery for different SOCs. In spite of the large number of papers published on this subject [72–75], this method is rarely used as the SOC estimator. This stems from the fact that the instrumentation is complex and expensive. Moreover, the measurement is highly affected by the localized electrode temperature and aging of the electrode materials. Hence, this method is typically used for quality control and to a limited extent to provide

information about the SOH in academic studies rather than a practical measure of SOC. Please refer to [76], for further information concerning impedance measurements for Li-ion batteries.

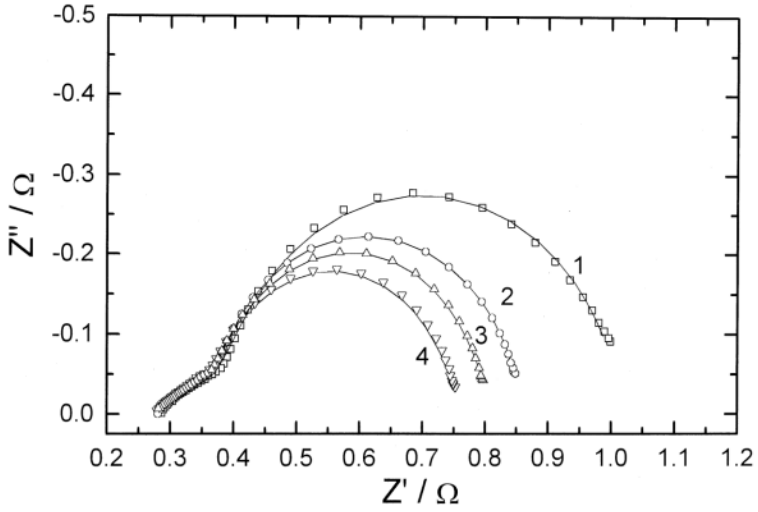

Figure 3-2: Impedance spectra of lithium-ion battery at SOC≃0 (1),0.14 (2),0.28 (3),0.42 (4) [74].

Recently, adaptive methods including fuzzy logic, neural networks, adaptive observers, and Kalman filters are widely used to estimate SOC [77]. Among these techniques, the Kalman filtering seems to be very promising [60–69]. In practice, it filters the input and output signals of the system to accurately predict the dynamic state of the system. Since the equations of this filter involve basic matrix operations, it can be easily implemented on a Digital-Signal-Processing (DSP) chips, making it valuable from a practical point of view. One of the advantages of Kalman filtering is providing the error bound for each estimated state [59]. In addition, this method can be utilized for parameter estimation, whereby the system identification and state estimation can be implemented at the same time.

Although Kalman filtering has lately received considerable attention [60–69], some gaps are still observed in this area. To this concern, the effect of battery type on the parameters of the Kalman filter has not been assessed yet, whereby only one battery chemistry and geometry are typically analyzed in each study. In this work, two different geometries of Li-ion batteries (cylindrical and prismatic) are considered, and by comparing the covariance noise parameters of the Kalman filters, some physical insights are discussed considering the magnitude of these values. Moreover, a good

comparison over the different equivalent circuits of the battery and their impact on the accuracy of the Kalman filtering is provided. Both methods, extended and dual extended Kalman filters are described in detail, in order to expedite their implementation for practical applications in HEV or PHEV.

3.2 Battery experiment

A comparison of the performance of different proposed methods utilized to estimate SOC is carried out through experimental data. To this concern, an experimental setup for testing batteries containing $LiFePO_4$ cathodes was designed to collect the data. This was developed in such a way that simulates driving conditions for real HEV and is also a scaled-down adaptation of a HEV powertrain. The experimental setup contains three major components: the battery, regenerative source (which simulates the regenerative braking of a real vehicle), and a load box (which simulates the motor). The schematic diagram of the test stand is shown in Figure 3-3.

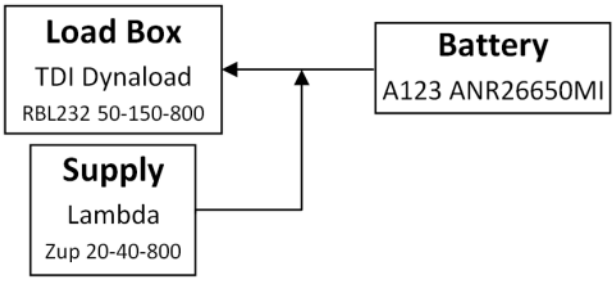

Figure 3-3: Battery testing apparatus [78].

The batteries tested in the facility, shown in Figure 3-3, were A123 cylindrical 26650 Li-ion batteries [79]. These batteries are commonly used in HEV, contain cathodes of $LiFePO_4$ and present a nominal voltage of 3.8 V. Moreover, they can provide a maximum continuous current of 60 A, or up to 120 A for peak currents during 10 s. The load box mounted on the test stand is a TDI Dynaload RBL232 50-150-800. This part was added to the test stand to resemble the behavior of an electric motor that initiates the load on the batteries. A Lambda ZUP 20-40-800 model AC/DC power source was integrated with the setup to charge the cells. The Lambda ZUP 20-40-800 model was selected based on its compatibility with the recharge requirements for the A123 Li-ion batteries. This setup

was also equipped with a controller which is able to read the desired drive cycles and then drive the experimental setup according to the drive cycle's power demand data. Further details about this test setup can be found in [78].

In order to mimic the environment of the batteries in a HEV, the batteries were dynamically subjected to a series of charge and discharge cycles. Figure 3-4 shows the current profile, whose duration was longer than 45,000 s. Positive current represents discharge from the battery and negative current is charging the cells. For better appreciation, the charging periods of the last cycles are expanded in the inset shown on the right part of the figure. The cycling of the batteries is started with a pre-test run at very slow charge and discharge rates, to position the battery at the same initial SOC. Then, the battery went through a series of high rate charge and discharges. The discharge process is designed to occur at maximum discharge current of 60 A. During this time, the cell was partially discharged (almost to 55% SOC). After 20,000 s, the depth of discharge (DOD) was gradually lowered for each discharge period such that at the end of the test the DOD of the last discharge period was around 5%. Furthermore, the charging process was comprised of two regions: the first part was a constant charging current (10 A) followed by a period of a constant voltage (3.8 V) until the current reached zero. This type of charge profile commencing around 19,000 s was chosen to ensure that the battery reached the 100% SOC at the end of each charging process. The experimental data were used to identify the parameters of the battery model described in Section 3.3, and to predict the SOC described in Section 3.4.

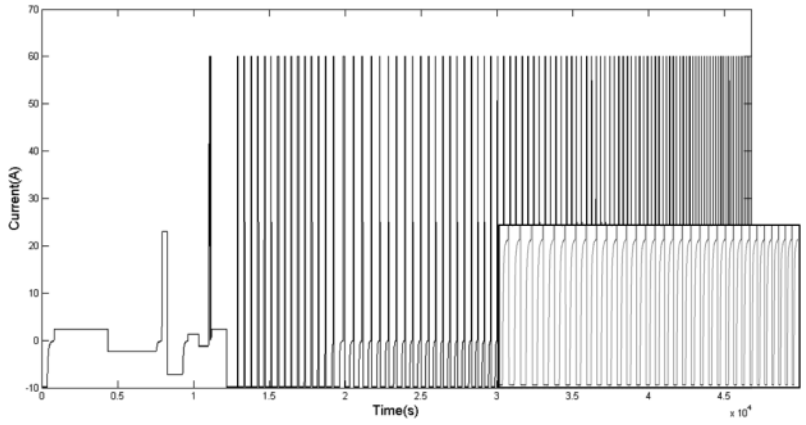

Figure 3-4: Current profile of the battery during the dynamic test which resembles the HEVs environment.

3.3 Model development

Two sets of equations are required to estimate SOC using a Kalman filtering signal processing technique, as discussed in Section 3.4. The first set is called the 'process model' where a discrete form of the coulomb counting equation (Equation (3-1)) is commonly used. The second set is called 'measurement model' and is utilized to correct the error of the process model estimation, and to reduce the uncertainty. This model should provide a correct relation between the states, inputs, and outputs of the system. In this paper, the state of the system is SOC, the input of the system is measured current, i, and the output is terminal voltage, V. The measurement model has the form of $V_k = f(SOC_k, i_k, \theta_k)$; where θ is the parameters of the model and subscript k shows the k^{th} time step. This section describes the measurement models, and is intended to find an appropriate measurement model for being used in the Kalman filtering process, as well as its parameters. Parameters for the measurement models can be classified in two categories: the fixed and varying parameters. They are explained in detail in the following paragraphs. It is worth mentioning that there is another approach to account for the behavior of a Li-ion battery through modeling. In this approach, physics based models such as the single particle (SP) model or any other type of electrochemical reduced models are considered [80,81]. However, the use of this type of models is beyond the scope of this work and generally involves much more computational time and effort.

Both types of parameters use the OCV diagram of the battery to relate the SOC of the battery to its voltage under load. They add or subtract some terms such as voltage drop across the battery with the aim of equalizing the terminal voltage, e.g. current flow to OCV relation. Therefore, the first requirement of the model is to calculate the OCV of the battery as a function of SOC. The easiest way to obtain this relation is to charge and discharge the battery at very slow rates to the cell's voltage limits prescribed by the manufacturer. In practice, the OCV is the average of the charge and discharge curves. Figure 3-5 shows the charge, OCV and discharge curves of A123 battery used for the tests. To obtain these curves, the battery was charged and discharged at 0.2C rate, and the OCV was calculated from the obtained curves.

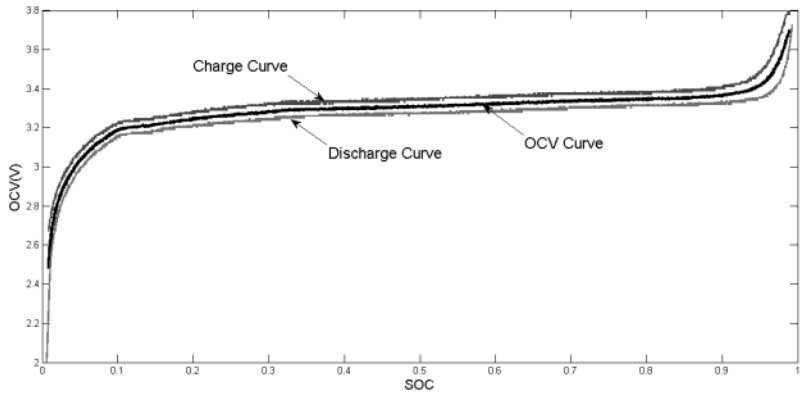

Figure 3-5: Charge, OCV, and discharge curves of A123 battery.

3.3.1 Fixed-parameter model

Two types of models will be considered in this category: simple model, and zero-sate hysteresis model [45].

3.3.1.1 Simple model

In the simple model, the terminal voltage of the battery is estimated using a very simple model depicted in Figure 3-6. This model can be formulated as

$$V_k = OCV(SOC_k) - Ri_k \tag{3-2}$$

It should be noted that the resistance in the Equation (3-2) depends on whether the battery is being charged or discharged and different values of R for charging and discharging is replaced in it [45].

To identify the parameters of the simple model, the off-line identification using Least Squares Estimation (LSE) theory is employed since the parameters are constant, and the model is linear with respect to the parameters. Thus, the first step is to form the overvoltage vector and current matrix as described below:

$$Y = \begin{bmatrix} V_1 - OCV(SOC_1) \\ V_2 - OCV(SOC_2) \\ \vdots \\ V_n - OCV(SOC_n) \end{bmatrix}, \quad H = \begin{bmatrix} i_1^+ & i_1^- \\ i_2^+ & i_2^- \\ \vdots & \vdots \\ i_n^+ & i_n^- \end{bmatrix}$$

where the i_k^+ equals i_k if $i_k > 0$, the battery is discharging, and i_k^- equals i_k if $i_k < 0$, the battery is charging, otherwise they are zero. By introducing Y and H into the Equation (3-2), it has the form $Y = H\hat{R}$, where $\hat{R} = [R^+, R^-]^T$ is the unknown vector of parameters. In this vector, R^+ and R^- denote internal resistance of the battery during discharge and charge periods, respectively. Using the known Y and H, the unknown vector can be calculated by LSE method as $\hat{R} = (H^T H)^{-1} H^T Y$. The simple model is completely defined when the constant $\hat{R}$ vector and the lookup table for OCV as a function of SOC are estimated and plugged in the Equation (3-2).

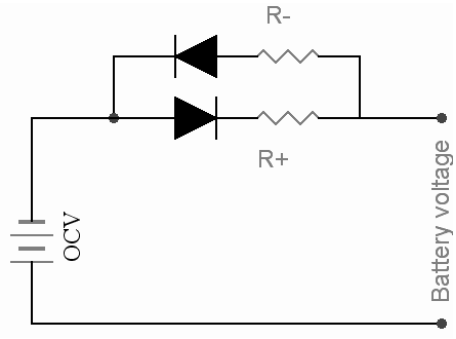

Figure 3-6: Circuit of simple model, R+ and R- are charge and discharge resistances, respectively.

Figure 3-7 shows the result of the simple model, simulating the voltage profile for a single cycle. As observed, a good quality fit is obtained between the measured and predicted voltage, except for the region of constant voltage at the end of the cycle. This deviation is probably due to the hysteresis effect that is not incorporated in the simple model.

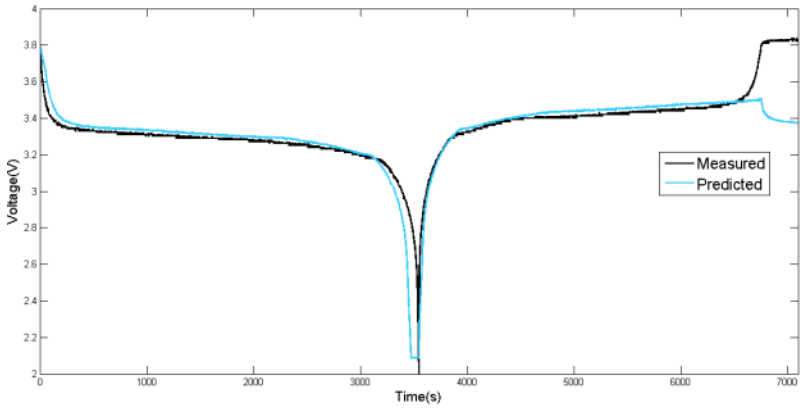

Figure 3-7: Simple model voltage prediction for a single cycle.

3.3.1.2 Zero-state hysteresis model

The hysteresis is a characteristic of a system where by changing the current course from charge to discharge, the output voltage of the cell does not trace back along the same voltage profile. This behavior of the system can be quantified by utilizing Figure 3-5. The difference between the charging and discharging curves divided by two, all minus the effect of the voltage drop due internal resistance (Ri_k), and the result is taken as the hysteresis effect. The magnitude of the hysteresis is shown in Figure 3-8 as a function of the SOC.

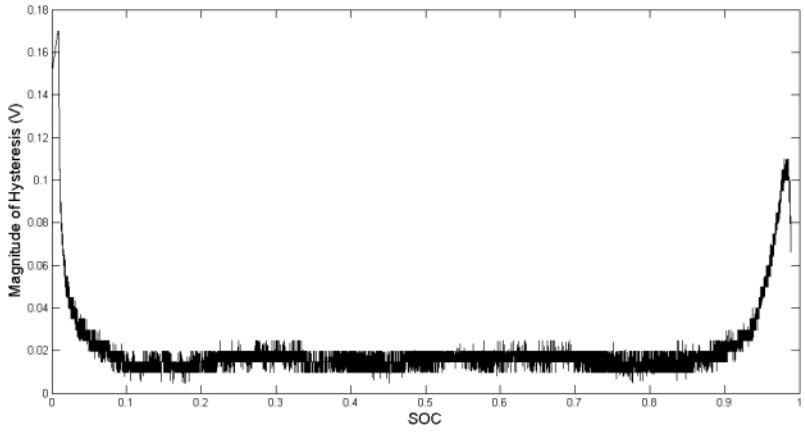

Figure 3-8: Magnitude of the difference between charge and discharge OCV a function of SOC (i.e. magnitude of the hysteresis).

It can be seen from Figure 3-8 that the hysteresis is almost constant in most of the SOCs and is less than 1% of the overall cell voltage. Therefore, it is reasonable to consider the hysteresis as a constant parameter in the measurement model and use the following form called zero-state hysteresis model.

$$V_k = OCV(SOC_k) - Ri_k - s_k M \tag{3-3}$$

where the parameter M is the hysteresis and s_k depends on the direction of the current and has adjustable memory during the rest period. The parameter s_k is defined as

$$s_k = \begin{cases} 1, & i_k > \varepsilon, \\ -1, & i_k < -\varepsilon, \\ s_{k-1}, & |i_k| \le \varepsilon. \end{cases}$$

where the ε is a small positive constant number.

Similarly as the simple model, LSE theory is used to identify the parameters since they are constant and the model is linear with respect to the parameters. The vector Y and matrix H are defined as

$$Y = \begin{bmatrix} V_1 - OCV(SOC_1) \\ V_2 - OCV(SOC_2) \\ \vdots \\ V_n - OCV(SOC_n) \end{bmatrix}, \quad H = \begin{bmatrix} i_1^+ & i_1^- & s_1 \\ i_2^+ & i_2^- & s_2 \\ \vdots & \vdots & \vdots \\ i_n^+ & i_n^- & s_n \end{bmatrix}$$

and then the parameter vector ($\theta = [R^+, R^-, M]^T$) is obtained as described for the simple model. The result for a single cycle of this model is shown in Figure 3-9. Evidently, this model predicts better the battery voltage during the last portion of the cycle than the simple model. However, the result shown in Figure 3-9 is just for one cycle (e.g. first one). An appropriate model should regenerate the output of the battery for all current inputs, but this cannot be precisely addressed when constant parameters are used in the model. Thus, in order to tackle the dynamics of the system with different input currents, a model allowing the variation of the parameters needs to be developed.

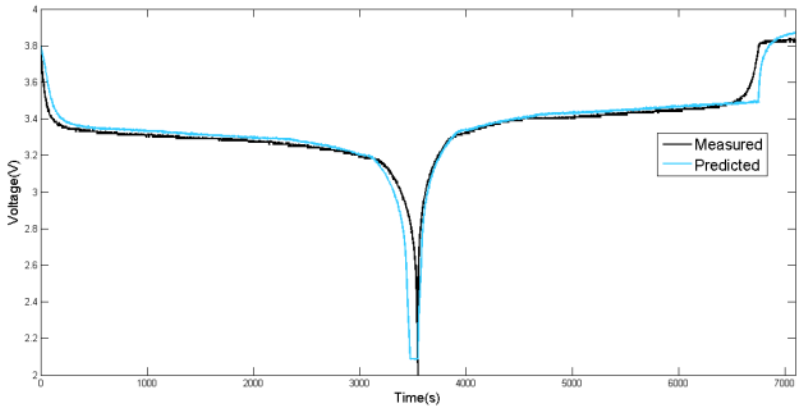

Figure 3-9: Zero-state hysteresis model voltage prediction for a single cycle.

3.3.2 Varying-parameter model

By using the zero-state model, the prediction of the battery voltage improves considerably, yet it is not adequate to simulate the behavior of the battery under dynamic environments like HEV and PHEV. In addition, the zero-state model cannot detect the slow variation of the hysteresis while changing the current direction. It just fluctuates between the positive and negative values of the

identified hysteresis constant. Consequently, it is desired to add the hysteresis of the battery as another state of the system. Augmenting the hysteresis with the SOC in the state vector and estimating both OCV and SOC using a Kalman filtering approach addresses the discussed problems of the zero-state model. In this work, the hysteresis-state model proposed by Plett [45] is used according to the following formulation:

$$\frac{dh(SOC,t)}{dSOC} = \gamma sgn(\dot{SOC})\left(M(SOC,\dot{SOC}) - h(SOC,t)\right) \tag{3-4}$$

where $M(SOC,\dot{SOC})$ is the maximum polarization due to battery hysteresis as function of SOC and its rate of change. Moreover, $M(SOC,\dot{SOC})$ has the positive value during charging and negative during discharging. Equation (3-4) relates the rate of the hysteresis change to its distance from M. This form of equation results in an exponential decay of hysteresis to the major loop. The term γ is a tuning factor and controls the rate of decay. Finally, the term $sgn(SOC)$ has a stabilizing effect on the model. By using this type of hysteresis, the output of the model yields

$$V_k = OCV(SOC_k) - Ri_k + h_k \tag{3-5}$$

The simulation of the battery voltage by the hysteresis-state model is reported in Figure 3-10 for one cycle. A comparison of Figure 3-10 with Figure 3-7 and Figure 3-9 reveals that the hysteresis-state model presents a better prediction of the battery voltage over the simple and zero-state hysteresis models. Additionally, a very good quality can be observed over the entire range of voltage when this model is used. Figure 3-11 compares the capability of the hysteresis-state and zero-state hysteresis model to predict the output voltage of the battery under a dynamic environment. As previously mentioned, constant parameters restrict the capabilities of the zero-state hysteresis model to accurately predict the output voltage. Despite this, the hysteresis-state model shows an acceptable performance regardless of the dynamics of the system.

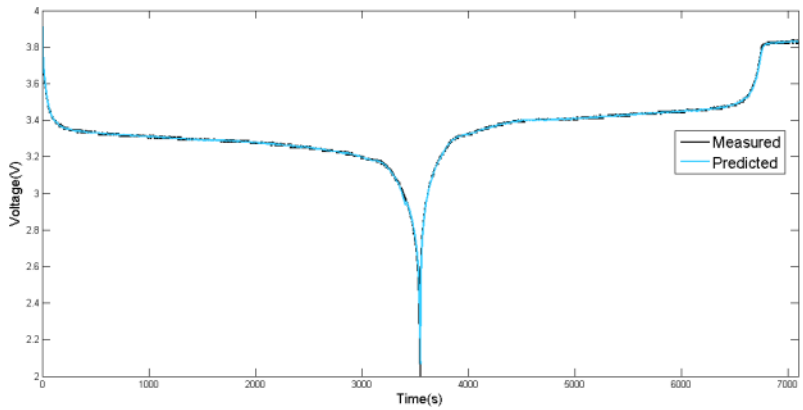

Figure 3-10: hysteresis-state model voltage prediction for a single cycle.

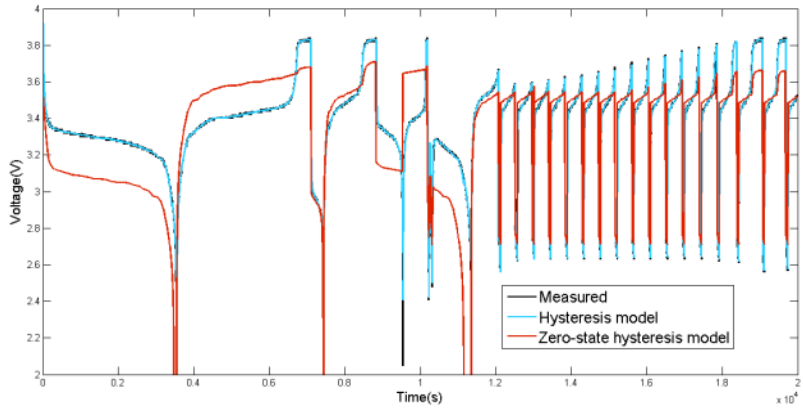

Figure 3-11: Comparing the hysteresis-state and zero-state hysteresis model in a dynamic environment.

3.4 SOC estimation

This section briefly describes the Kalman filtering method and its implementation to estimate the SOC of the battery. Two methods of Kalman filtering are considered: extended Kalman filter and dual extended Kalman filter. The results of these filters are also compared against the coulomb counting method. In the first part of this section the method is developed and applied to cylindrical cells, and then the developed methodology is applied to prismatic cell data.

In general, for a linear system, Kalman filtering provides an optimal estimate of the system states that are not directly measurable. However, in the case of nonlinear systems such as batteries, Kalman filtering is still an intelligent way to determine the states of the system. These states provide a

comprehensive representation of the internal condition of the system and summarize contributions of all past inputs of the system. A Kalman filter computes the states of the system by utilizing a process model, a measurement model and a set of noisy measurements of inputs and output of the system. While the process model contains all information about the system dynamics, the measurement model relates the outputs of the system to its inputs and states. The process and measurement models predict the present state and correct the raw state estimation obtained from the process model [59,78], respectively. A complete description of the Kalman filtering process is reported in reference [82].

In the design procedure of the Kalman filters applied to the estimations of the battery states, the current of the battery is the measured input, whereas the voltage measured on the battery terminals is the output. The required states to be estimated include state of charge, state of health, hysteresis, etc. In this work, the state considered is the SOC and the hysteresis will be incorporated in the state vector as well as the SOC when the hysteresis-state model is studied. The process model needs to relate the input current to the SOC, whereby the coulomb counting equation can be ideal for this purpose. Discretizing Equation (3-1) in terms of time results in

$$SOC_k = SOC_{k-1} + \frac{\eta_i i_{k-1} \Delta t}{C_n} \tag{3-6}$$

where η_i is the coulombic efficiency of the battery during charge and discharge. This factor is the ratio between consumed over available electrons in the charging or discharging processes. In other words, the energy provided by an external energy source cannot be totally stored in the battery due to mainly secondary reactions such as Li plating and electrolysis of water [78]. This ratio is assumed to be 0.992 during the charging period and 1.0 during discharging [45,78].

When the hysteresis-state model is considered for Kalman filtering, the hysteresis is also considered as a part of the state vector. Therefore, a different process model is incorporated in the Kalman filter design, connecting the hysteresis to the input current. The discrete version of the solution of Equation (3-4) provides this relation:

$$h_{k+1} = \exp\left(-\left|\frac{\eta_i i_k \gamma \Delta t}{Cn}\right|\right) h_k + \left(1 - \exp\left(-\left|\frac{\eta_i i_k \gamma \Delta t}{Cn}\right|\right)\right) M(SOC, \dot{SOC}) \tag{3-7}$$

The measurement models map the input current and states of the battery to the output voltage. Details of these models were discussed in Section 3.3. From this point, only the zero-state hysteresis and hysteresis-state models are considered. Table 3-1 summarizes these models.

Table 3-1: Summary of battery models.

Simple model:

$$SOC_{k+1} = SOC_k - \frac{\eta_i i_k \Delta t}{c_n}$$

$$V_k = OCV(SOC_k) - Ri_k$$

unable to follow the output voltage in constant voltage periods (not used)

Zero-state hysteresis model:

$$SOC_{k+1} = SOC_k - \frac{\eta_i i_k \Delta t}{c_n}$$

$$V_k = OCV(SOC_k) - Ri_k - s_k M$$

follow the output voltage in constant voltage periods, but, unable to follow the output voltage in dynamic environments (used)

Hysteresis model:

$$F(i_k) = \exp\left(-\left|\frac{\eta_i i_k \Delta t}{c_n}\right|\right)$$

$$\begin{bmatrix} h_{k+1} \\ SOC_{k+1} \end{bmatrix} = \begin{bmatrix} F(i_k) & 0 \\ 0 & 1 \end{bmatrix} \begin{bmatrix} h_k \\ SOC_k \end{bmatrix} + \begin{bmatrix} 0 & (1 - F(i_k)) \\ -\frac{\eta_i \Delta t}{c_n} & 0 \end{bmatrix} \begin{bmatrix} i_k \\ M_k \end{bmatrix}$$

$$V_k = OCV(SOC_k) - Ri_k + h_k$$

follows the output voltage in both constant voltage periods and dynamic environments (used)

First, we apply the Kalman filter process on the zero-state hysteresis model. The process model has a linear structure whereas the measurement relation is not linear with respect to the SOC, whence a nonlinear version of Kalman filter should be utilized. For this model, the extended Kalman filter was chosen and implemented since the constant parameters of the system have been already estimated. Note that the focus of this chapter is on the application and implementation of the Kalman filter to the battery SOC, whereby detailed algorithms of the Kalman filter itself should be consulted in reference [82]. The implementation of the extended Kalman filter using the zero-state battery model is summarized in Table 3-2.

Table 3-2: Extended Kalman filtering for zero-state hysteresis model [45].

Nonlinear state-space model:

$SOC_{k+1} = SOC_k - \frac{\eta_i i_k \Delta t}{C_n} + w_k$

$V_k = OCV(SOC_k) - Ri_k - s_k M + v_k$

where w_k and v_k are independent, zero-mean, Gaussian noises with covariance matrices P_v and P_w respectively.

Definitions: $\hat{C}_k = \frac{\partial OCV(SOC_k)}{\partial SOC_k}|_{SOC_k = S\hat{O}C_k^-}$

Initialization ($k = 0$):

$S\hat{O}C_0^+ = \mathbb{E}[SOC_0]$

$P_{S\hat{O}C,0}^+ = \mathbb{E}\left[\left(SOC_0 - S\hat{O}C_0^+\right)\left(SOC_0 - S\hat{O}C_0^+\right)^T\right]$

Computation ($k = 1,2, \ldots$):

Time updates

$S\hat{O}C_k^- = S\hat{O}C_{k-1}^+ - \frac{\eta_i i_{k-1} \Delta t}{C_n}$

$P_{S\hat{O}C,k}^- = P_{S\hat{O}C,k-1}^+ + P_w$

Measurement updates

$L_k = P_{S\hat{O}C,k}^- \hat{C}_k^T \left[\hat{C}_k P_{S\hat{O}C,k}^- \hat{C}_k^T + P_v\right]^{-1}$

$S\hat{O}C_k^+ = S\hat{O}C_k^- + L_k[V_k - OCV(SOC_k) + Ri_k + s_k M]$

$P_{S\hat{O}C,k}^+ = \left(I - L_k \hat{C}_k\right) P_{S\hat{O}C,k}^-$

In order to calculate the $\hat{C}_k$, the OCV lookup table and a central difference method around the SOC_k^- is used.

$$\hat{C}_k = \frac{OCV(SOC_k^- + \delta) - OCV(SOC_k^- - \delta)}{2\delta} \tag{3-8}$$

The value of δ is a small arbitrarily number perturbation, which represent the change in SOC within the model and selected to be 0.001 in this study. The next step to implement the extended Kalman filter is to determine the variances introduced in the model. The process noise parameter practically covers the uncertainties that are ignored in the modeling procedure and the input measurement noise. In this study, it is assumed that the process noise is entirely derived from the inaccuracy in the current measurement. A simple calculation of the accuracy of the sensors leads to the current variance of $P_w = 1.3 \times 10^{-10}$ [78]. However, this value may be small compared to the capacity of the battery, causing a very small error. Similarly, the measurement error is determined from the variance of the voltage measurement for the sensors. This value is around $P_v = 1.8 \times 10^{-4}$ [78].

Figure 3-12 depicts the results of coulomb counting method applied to the experimental data during the 45,000 s of cycling. In this figure, the experimental discharge line was obtained from the experimental data using a coulomb counting method starting from 19,000 s where the battery cell was fully charged at the end of each charging period. This observation was based on the current profiles obtained in Figure 3-4 starting from this time. As it is detectable, this method poorly predicts the SOC of the battery. This is due to accumulative error problem in the coulomb counting method and the fact that coulomb counting does not have a correcting mechanism.

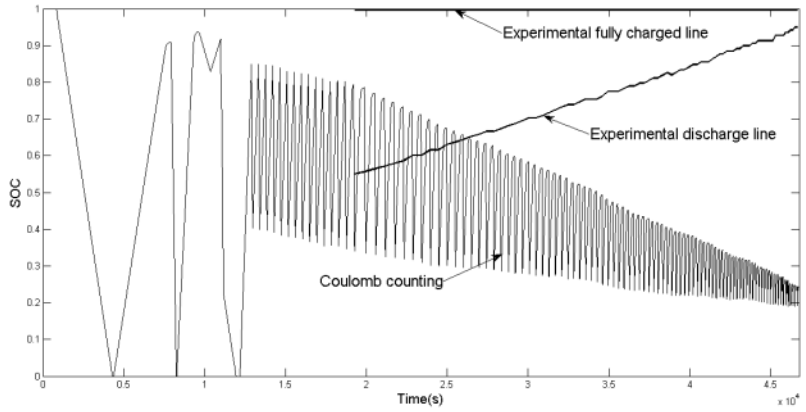

Figure 3-12: SOC estimation using coulomb counting method.

The result of SOC estimation utilizing the extended Kalman filter is shown in Figure 3-13. This figure is divided into three regions. In the first region the battery goes through a series of slow rate charge and discharge cycles whereas in the second region it goes through a series of fast rate charge and discharge cycles. The measured voltages reported in Figure 3-11 reveal that in the second time period, the battery does not get fully charged. In the third region, the rate of cycling is the same as it was in the second region while at the end of each charging period in the third region the battery gets fully charged.

Figure 3-14 compares the SOC predictions obtained from the coulomb counting and extended Kalman filtering methods to the experimental discharge line in the third region. Good agreement between the SOC estimation obtained from the extended Kalman filter method and the experimental discharge line (less than 1% error) is observed in this figure. Although the prediction obtained from the extended Kalman filtering is accurate in the third region, the results show inaccuracy in the

second region. As discussed, the battery does not get fully charged in second region while the extended Kalman filter predictions reported in Figure 3-13 show an opposite behavior. This deviation suggests poor voltage prediction of the zero-state model. Even with some weaknesses observed in the results of the proposed extended Kalman filter, it is superior to the common methods of the SOC estimation.

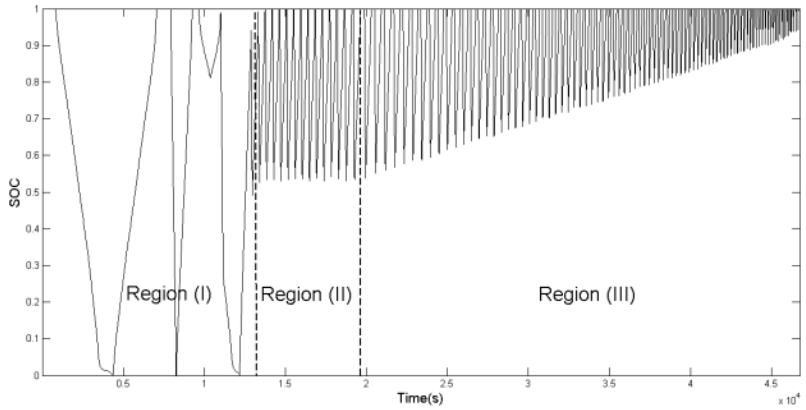

Figure 3-13: SOC estimation using extended Kalman filter in three regions of experiment. Three regions include: (I) slow rate cycling region (II) fast rate cycling region (III) fast rate cycling region with fully charging periods.

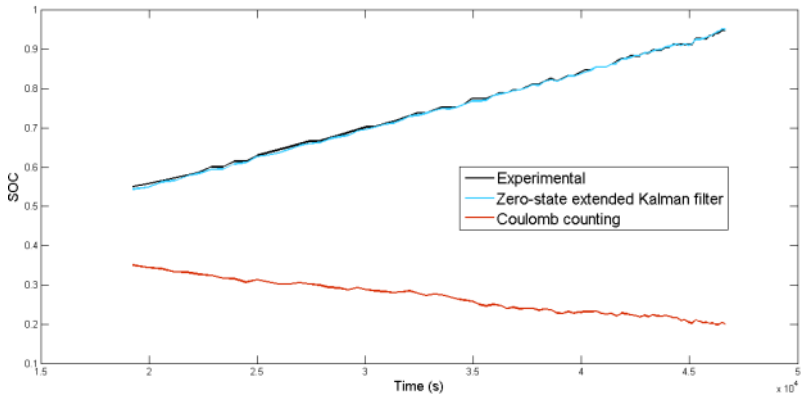

Figure 3-14: Comparing the results obtained from the experimental data, coulomb counting method and extended Kalman filtering.

In order to apply the Kalman filtering method to the hysteresis-state model, the extended Kalman filter cannot be used since the parameters of the model are not constant. For the hysteresis-state model the Kalman filter has to identify the system parameters and also estimate the states of the system. The researchers in dealing with this type of problems have taken two main approaches. First,

the joint Kalman filtering which estimates both parameters and states of the system using a single Kalman filter. In this method, the parameters and states form a larger state vector which is estimated by a Kalman filter [83]. Second, the dual Kalman filtering whose algorithm is described in Figure 3-15. In Figure 3-15 the x represents the states of the system, θ is parameters of the system and P is the error covariance. In fact, this method starts with the time update of the parameters; then, the updated parameters are used to update the states in time. Finally, both states and parameters are updated employing the output measurement. Since the dual Kalman filtering uses the most updated estimate in each iteration, it is expected to achieve the better estimations; it is used in this study.

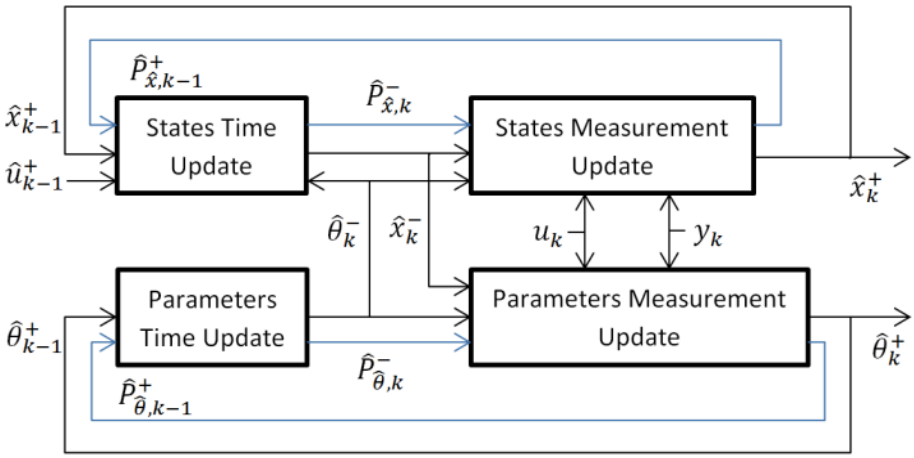

Figure 3-15: Dual Kalman filter [64].

More importantly, the dual extended Kalman filtering is used due the existence of the system nonlinearity. The details of the filtering method is not described here, and more studies on dual extended Kalman filter can be find in [64,84,85]. The implementation of the dual extended Kalman filter using the hysteresis-state battery model is summarized in Table 3-3 where functions $f(.)$ can be obtained from Table 3-1. In this filter, it is assumed that the parameters of the battery change very slowly during the time and the driving process may be captured by just a small noise r_k. Therefore, the process model for the parameter identification has the form of $\theta_{k+1} = \theta_k + r_k$. In the Table 3-3 the vector of the parameters, states, and inputs are

$$\theta_k = \begin{bmatrix} R_k^+ \\ R_k^- \\ M_k \\ \gamma_k \end{bmatrix}, x_k = \begin{bmatrix} h_k \\ SOC_k \end{bmatrix}, u_k = \begin{bmatrix} i_k \\ M_k \end{bmatrix}$$

The matrix A_{k-1} is also as follows:

$$A_{k-1} = \begin{bmatrix} F(i_{k-1}) & 0 \\ 0 & 1 \end{bmatrix}$$

The dual extended Kalman filter mentioned in Table 3-3 estimates the states and parameters of the system in such a way that the model follows the measured input and outputs as close as possible. As a result, this filter may yield estimations that have no direct physical representation. To ensure the filter converges to the voltage estimation that has physical meaning Plett [64] suggested adding an additional equation to the measurement model within the Kalman filter method. This extra equation is a rough estimation of the battery terminal voltage.

$$\begin{aligned} V_k &\approx OCV(SOC_k) - Ri_k \\ OCV(SOC_k) &\approx V_k - Ri_k \\ S\hat{O}C_k &= OCV^{-1}(V_k + Ri_k) \end{aligned}$$

By using the measures V_k, i_k and R from the previous step of dual extended Kalman filter, a rough estimation of the SOC is obtained which is enough to make the model converge to the true states. Consequently, adding this model to the hysteresis state model defines the function $g(.)$ used in Table 3-3.

$$g(x_k, u_k, \theta) = \begin{bmatrix} OCV(SOC_k) - Ri_k + h_k \\ SOC_k \end{bmatrix}$$

The measured output vector is also modified as

$$y_k = \begin{bmatrix} V_k \\ S\hat{O}C_k \end{bmatrix}$$

Then, the known function $g(.)$ is differentiated to obtain the C_k^x and C_k^θ

$$C_k^x = \begin{bmatrix} 1 & \dfrac{\partial OCV(SOC)}{\partial SOC} \\ 0 & 1 \end{bmatrix}_{SOC=S\hat{O}C_k^-}$$

where $\frac{\partial OCV(SOC)}{\partial SOC}$ is calculated using the right hand side of the Equation (3-8). Finally, the C_K^θ in Table 3-3 is calculated by utilizing the chain rule as follows:

$$C_k^\theta = \left.\frac{dg(\hat{x}_k^-, u_k, \theta)}{d\theta}\right|_{\theta=\hat{\theta}_k^-}$$

$$\frac{dg(\hat{x}_k^-, u_k, \theta)}{d\theta} = \frac{\partial g(\hat{x}_k^-, u_k, \theta)}{\partial \theta} + \frac{\partial g(\hat{x}_k^-, u_k, \theta)}{\partial \hat{x}_k^-}\frac{d\hat{x}_k^-}{d\theta}$$

$$\frac{d\hat{x}_k^-}{d\theta} = \frac{\partial f(\hat{x}_{k-1}^+, u_{k-1}, \theta)}{\partial \theta} + \frac{\partial f(\hat{x}_{k-1}^+, u_{k-1}, \theta)}{\partial \hat{x}_{k-1}^+}\frac{d\hat{x}_{k-1}^+}{d\theta}$$

$$\frac{d\hat{x}_{k-1}^+}{d\theta} = \frac{d\hat{x}_{k-1}^-}{d\theta} - L_{k-1}^x C_{k-1}^\theta$$

Here, it is assumed that the L_{k-1}^x is not function of θ, and adding more derivatives will not improve the accuracy of the filter. For the hysteresis-state model, the above differentiations are obtained as

$$\frac{\partial g(\hat{x}_k^-, u_k, \theta)}{\partial \theta} = \begin{bmatrix} -i_k^+ & -i_k^- & 0 & 0 \\ 0 & 0 & 0 & 0 \end{bmatrix}$$

$$\frac{\partial g(\hat{x}_k^-, u_k, \theta)}{\partial \hat{x}_k^-} = \left.\begin{bmatrix} 1 & \frac{\partial OCV(SOC)}{\partial SOC} \\ 0 & 0 \end{bmatrix}\right|_{SOC=S\hat{O}C_k^-}$$

$$\frac{\partial f(\hat{x}_{k-1}^+, u_{k-1}, \theta)}{\partial \theta} = \begin{bmatrix} 0 & 0 & (1-F_{k-1})sgn(i_{k-1}) & \left(M - \hat{h}_{k-1}^+\right)\left|\frac{\eta_i i_{k-1}\Delta t}{C_n}\right| F_{k-1} \\ 0 & 0 & 0 & 0 \end{bmatrix}$$

$$\frac{\partial f(\hat{x}_{k-1}^+, u_{k-1}, \theta)}{\partial \hat{x}_{k-1}^+} = \begin{bmatrix} F_{k-1} & 0 \\ 0 & 1 \end{bmatrix}$$

Now, the dual extended Kalman filter is implemented to estimate the SOC of the battery. Figure 3-16 shows the result of applying the dual extended Kalman filter to the SOC estimation. The variation of the SOC depicted in Figure 3-16 for the period of 12,000 s to 19,000 s, second region, does not show the problem reported in Figure 3-13 for the same period of time. On the other hand, the close examination of the measured voltage, measured current, and the OCV curve of the battery suggests that the dual extended Kalman filtering method correctly captures the actual SOC of the battery in this period. Figure 3-17 compares the experimental discharge line and the results obtained from the dual extended Kalman filter method. Good agreement between the discharge line and estimated SOC (less than 4%) is observed. Therefore, the dual extended Kalman filtering process is

able to accurately track the behavior of the battery and can consequently be employed as a reliable SOC estimator in the dynamic environment of a HEV or PHEV.

Table 3-3: Dual extended Kalman filtering [84].

Nonlinear state-space models

$x_{k+1} = f(x_k, u_k, \theta_k) + w_k \ , \ \theta_{k+1} = \theta_k + r_k$

$y_k = g(x_k, u_k, \theta_k) + v_k \ , \ d_k = g(x_k, u_k, \theta_k) + e_k$

where w_k, v_k, r_k, and e_k are independent, zero-mean, Gaussian noises with covariance matrices P_v, P_w, P_r, and P_e respectively

Definitions

$A_{k-1} = \frac{\partial f(x_{k-1}, u_{k-1}, \hat{\theta}_k^-)}{\partial x_{k-1}}|_{x_{k-1}=\hat{x}_{k-1}^+}$

$\hat{C}_k^x = \frac{\partial g(x_k, u_k, \hat{\theta}_k^-)}{\partial x_k}|_{x_k=\hat{x}_k^-}$

$\hat{C}_k^\theta = \frac{dg(x_k, u_k, \theta)}{\partial \theta}|_{\theta_k=\hat{\theta}_k^-}$

Initialization ($k = 0$)

$\hat{\theta}_0^+ = \mathbb{E}[\theta_0] \ , \ P_{\hat{\theta},0}^+ = \mathbb{E}\left[(\theta_0 - \hat{\theta}_0^+)(\theta_0 - \hat{\theta}_0^+)^T\right]$

$\hat{x}_0^+ = \mathbb{E}[x_0] \ , \ P_{\hat{x},0}^+ = \mathbb{E}[(x_0 - \hat{x}_0^+)(x_0 - \hat{x}_0^+)^T]$

Computation ($k = 1,2, \ldots$)

Time updates for parameters

$\hat{\theta}_k^- = \hat{\theta}_{k-1}^+$

$P_{\hat{\theta},k}^- = P_{\hat{\theta},k-1}^+ + P_r$

Time updates for states

$\hat{x}_k^- = f(\hat{x}_{k-1}^+, u_{k-1}, \hat{\theta}_k^-)$

$P_{\hat{x},k}^- = A_{k-1} P_{\hat{\theta},k-1}^+ A_{k-1}^T + P_w$

Measurement updates for states

$L_k^x = P_{\hat{x},k}^- (C_k^x)^T \left[C_k^x P_{\hat{x},k}^- (C_k^x)^T + P_v\right]^{-1}$

$\hat{x}_k^+ = \hat{x}_k^- + L_k^x \left[y_k - g(\hat{x}_k^-, u_k, \hat{\theta}_k^-)\right]$

$P_{\hat{x},k}^+ = (I - L_k^x C_k^x) P_{\hat{x},k}^-$

Measurement updates for parameters

$L_k^\theta = P_{\hat{\theta},k}^- (C_k^\theta)^T \left[C_k^\theta P_{\hat{\theta},k}^- (C_k^\theta)^T + P_e\right]^{-1}$

$\hat{\theta}_k^+ = \hat{\theta}_k^- + L_k^\theta \left[y_k - g(\hat{x}_k^-, u_k, \hat{\theta}_k^-)\right]$

$P_{\hat{\theta},k}^+ = (I - L_k^\theta C_k^\theta) P_{\hat{\theta},k}^-$

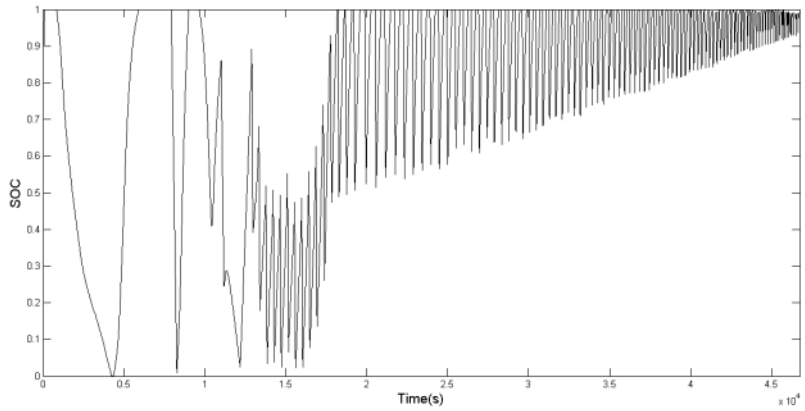

Figure 3-16: SOC estimation using Dual extended Kalman filter.

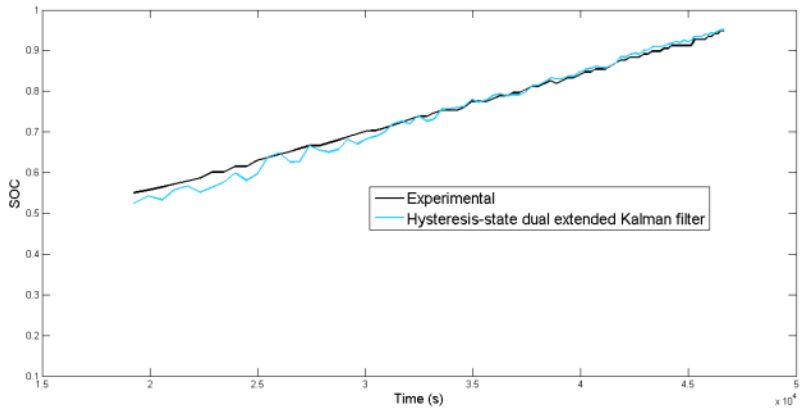

Figure 3-17: Comparing the results obtained from the experimental data and dual extended Kalman filtering.

3.5 Application of the model to A123 prismatic cells

In the next step, the proposed method is employed for the A123 prismatic batteries during different charge and discharge cycles to show the performance of the developed dual extended Kalman filter in observing the SOC of different types of batteries. These batteries contain similar cathode chemistry of $LiFePO_4$ and their nominal voltage and capacity are 3.3 V and 20 Ah, respectively. The experimental data contain a US06 drive cycle typically used to test vehicles at high speed and aggressive driving conditions. Figure 3-18 to Figure 3-20 show experimental measurements for current and voltage together with the simulation results for this drive cycle. The filter shows a good performance through cycling and can successfully simulates the measured SOC obtained by

coulomb counting method using an accurate current sensor. These results show the effectiveness of applying the developed method on both types of $LiFePO_4$ batteries. In fact, the designed observers are only different in some parameters. These parameters are OCV of the battery as function of SOC, capacity of the cell, and must-be-tuned covariance matrices. The first two parameters are properties of the battery while the covariance matrices are utilized as the part of the process and measurement model explained in Table 3-3. These matrices are diagonal whose elements are presented in Table 3-4, P^i represents the i^{th} element on the diagonal of the matrix. It should be noted that the covariance of the current and voltage vector measurements, P_w^2, P_v^1 and P_e^1, are set to the same values as in the previous test.

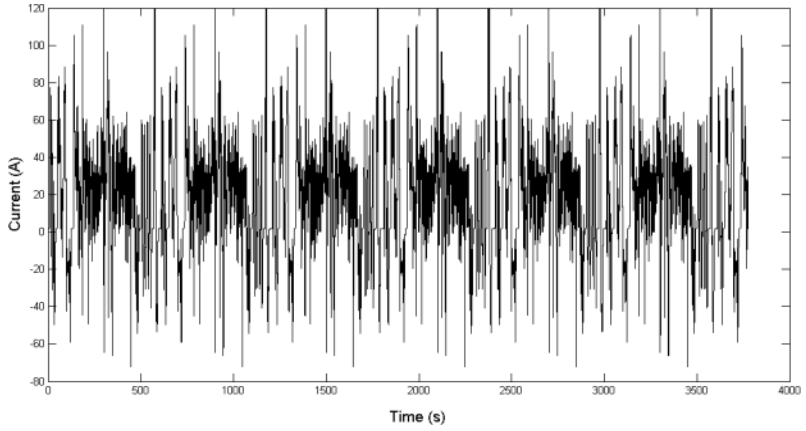

Figure 3-18: Measured current profile for the prismatic Li-ion batteries with $LiFePO_4$ cathode over the US-06 drive cycle.

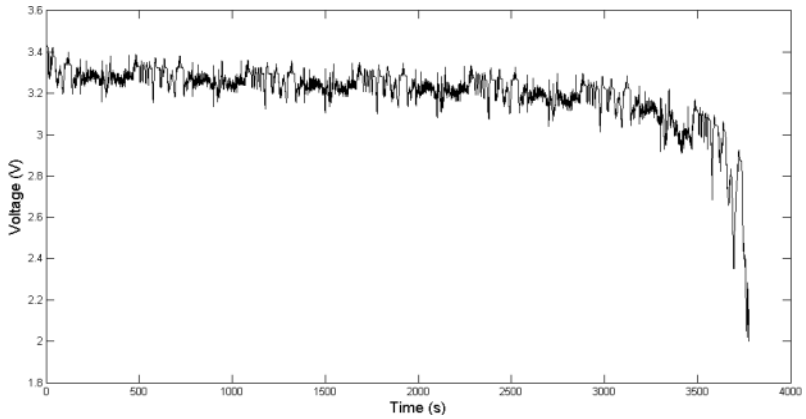

Figure 3-19: Measured voltage profile for the prismatic Li-ion batteries with $LiFePO_4$ cathode over the US-06 drive cycle.

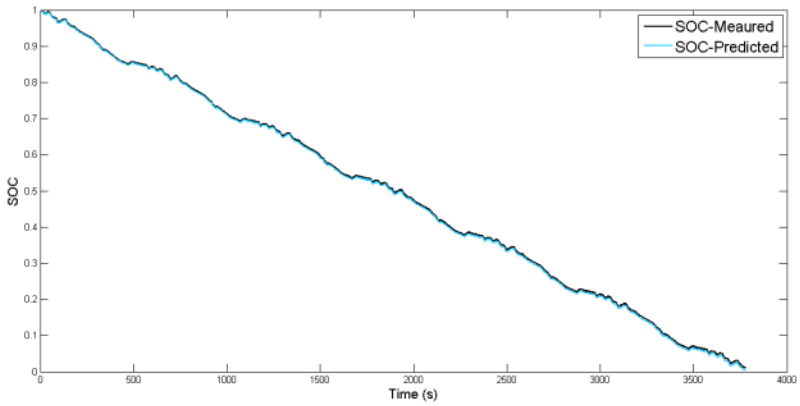

Figure 3-20: SOC prediction using the Dual extended Kalman filtering for the prismatic Li-ion batteries with $LiFePO_4$ cathode over US-06 drive cycle.

Table 3-4: Parameters of the dual extended Kalman filters for cylindrical and prismatic Li-ion batteries.

Parameters	Cylindrical battery	Prismatic battery
P_w^1	1.3×10^{-4}	1.3×10^{-8}
P_r^1	1.3×10^{-10}	1.3×10^{-13}
P_r^2	1.3×10^{-10}	1.3×10^{-13}
P_r^3	1.3×10^{-6}	1.3×10^{-8}
P_r^4	1.3×10^{-6}	1.3×10^{-8}
P_v^2	1.8×10^{-4}	1.8×10^{-4}
P_e^2	1.8×10^{-4}	1.8×10^{-4}

Moreover, the parameters P_r^1 and P_r^2 shown in Table 3-4 are the driving terms to update the internal resistances as a function of time. When these values decrease to 1.3×10^{-15} for the cylindrical cells, similar results are obtained in the extended Kalman filter with fixed-parameters. Table 3-4 shows that these two parameters can be up to three orders of magnitude larger for cylindrical cells than prismatic. These differences clearly suggest different magnitudes for the internal resistances operating within each battery during cycling.

Since both batteries (cylindrical and prismatic batteries of A123^{TM}) contain $LiFePO_4$ cathodes, the variation of these parameters is the result of distinct properties varying with geometry and electrode thickness, and whose impacts affect significantly the impedance of the batteries. It is known that cylindrical cells present a higher volume to outer surface ratio compared to the prismatic cells. Consequently, the heat generated during the operation of the cylindrical batteries would not be transferred to the outside as fast as in prismatic cells, and thus the temperature of cylindrical batteries

increases more than the prismatic ones during the cycling process. The temperature raise in these batteries both depends on, and influences their internal resistance, and this property can be utilized as an indicator of the impedance presents within each battery. Note that the cathode material for both batteries is the $LiFePO_4$ phase (0.005 S m^{-1}) that is generally a poor electronic conductor. Thus, several methods are needed to be implemented in order to increase its conductivity (e.g. carbon mixing, doping, particle size reduction) [86,87]. Undoubtedly, the application of these treatments at different scales or geometries (e.g. between cylindrical and prismatic batteries) modifies significantly the conductivity and other phenomena (e.g. diffusion, volume expansion of the cathode material) inside the batteries, and accordingly the extent of the impedance. Experimental evidence combined with model simulations has revealed that this type of transport limitations of the cathode material can also restrict the power of the batteries [88]. A similar situation might arise from variations in the electrolyte conductivity among the batteries. Therefore, it is not surprising to observe a variation between the parameters describing the behavior of these batteries, as a result of their reliance upon geometry-dependent impedances (and other factors affecting them).

The analysis of the filter parameters constitutes the first step to apply the method developed in this work for SOC estimation. This can be achieved via some trial-and-error initial studies. Once these parameters are established for the specific cell geometry and materials, the filter can be used to predict the SOC of the battery at different working situations. In addition, since the Li-ion batteries present in general the same controlling phenomena with different magnitudes due to modifications of the electrode materials, most likely, the method presented in this study could also be used for other type of batteries containing different cathode materials (e.g. Li_2MnO_4, $LiCoO_2$, NMC).

Chapter 4 Simplified one-dimensional Battery Model

The following section is based on previously published work by Mastali, M., Farhad, S., Farkhondeh, M., Fraser, R., and Fowler, M.

Journal of Power Sources 2015, 275: 633-643 [89].

"**Simplified Electrochemical Multi-particle Model for $LiFePO_4$ Cathodes in Lithium-ion Batteries**"

This thesis author specific contribution to this paper was to develop the model, conduct the simulations, prepare all the graphics and results, prepare the final manuscript and reviewer edits with direction from the project supervisors who were co-authors. All authors reviewed the manuscript.

4.1 Introduction

Many different materials are incorporated as the positive electrode of Li-ion batteries. Among all, $LiFePO_4$ (LFP), first introduced by Padhi et al. [90–92], has received lots of attention due to its durability, stability, low cost, and low environmental impact. The main concerns regarding this material are poor electronic conductivity [93–95] and low apparent diffusivity [96,97], that are improved by coating the particle surfaces with highly conductive (both electronically and ionically) materials, as well as reducing the LFP particle sizes to nano scales. The engineered $LiFePO_4$ is now commercialized and widely used in today's automotive-patterned Li-ion batteries necessitating the employment of reliable predictive models for design and control purposes.

The lithium insertion/deinsertion mechanism in LFP occurs through a two-phase process between Li-poor $Li_{\varepsilon}FePO_4$ and Li-rich $Li_{1-\varepsilon'}FePO_4$ phases (ε and $\varepsilon' \ll 1$). A proper model should ideally take this two-phase process into account while adequately capturing experimental charge/discharge data.

However, the actual mechanism of LFP lithiation/delithiation dynamics has not accurately been decoded yet, thus no such an ideal model exists in the literature. A few mathematical models are proposed that simulate the complicated behavior of LFP each tackling a specific aspect of this material [98–109]. These models include the core-shell [98–100], phase field [101–103], resistive-reactant (RR) [104–106], and variable solid-state diffusivity (VSSD) [107–109] models. While the core-shell and phase-field models consider the two-phase process, the RR model does not consider any specific description for phase transformation. The VSSD model, on the other hand, is a simple yet physically descriptive model based on the concentration-dependent chemical diffusivity of the inserted lithium that mimics the coexistence of the two phases within particles. Although helpful in improving fundamental understanding of LFP lithiation/delithiation dynamics, these models have not been used for large-scale applications where fast and accurate computation is required.

Such large-scale applications of fast physics-based battery models include: i) battery management systems that require real-time estimation of the state-of-charge (SOC) and other battery states [45,46,110,111], and ii) thermal analysis of battery packs which involves simultaneous electrochemical-thermal simulation of a large number of inter-connected cells [23,42,112,113]. In both cases having accurate and computationally economic models that demand minimal computing resources is crucial. Therefore, simplified models describing the characteristics of the smallest building block (i.e., cathode/separator/anode sandwich) of the battery during operation are being developed. The simplest model for the fast simulation of the cell performance is the single particle (SP) model wherein electrode-level losses (i.e., ionic and electronic transport across the cell) are ignored [114,115]. This assumption is reasonable for relatively low charge/discharge rates, thin, and highly conductive electrodes. If one of these conditions is violated, the model accuracy is noticeably degraded [115]. The SP model has been extended to a so-called “multi-particle (MP)” model to include an arbitrary number of particles. However, in the case of high rate/low temperature operating conditions where electrode-level losses are increased, implementation of porous-electrode theory becomes inevitable. Many mathematical methods have been proposed in the literature to speed up full-order porous-electrode models. These methods include but not limited to the perturbation techniques [116,117], residue grouping [61,118], proper orthogonal decomposition (POD) [119,120],

and Galerkin's method [121]. The general strategy is to reduce the system of partial differential algebraic equations (PDAE) to a simpler model such as a system of differential algebraic equations (DAE) that are less computationally demanding. However, none of these methods have been used to simulate the electrochemical performance of cells containing electrodes with active-material particles of different sizes or non-uniform properties.

The objective of this chapter is to develop an accurate yet computationally efficient model for Li-ion batteries that is able to handle an arbitrary number of active material particles. A simplified electrochemical multi-particle (SEMP) model is, therefore, developed and validated for the performance of a commercial LFP cathode. To this end, an MP model featuring VSSD formulation at the particle level is coupled with a simple polynomial approximation for the electrolyte variables at the electrode level making possible the prediction of the operating voltage of the cell at high charge/discharge rates.

4.2 Model development

The schematic of the half-cell modeled in this study is depicted in Figure 4-1. The half-cell assembly is made of a $LiFePO_4$ porous-electrode, a Li foil counter/reference electrode, a porous separator, and the electrolyte that fills the pores of the electrode and separator. The LFP electrode contains N particles that may vary in radius, $R_{p,k}$, surface contact resistance, $R_{s,k}$, and/or potential U_k. Such a multi-particle description may be applied to any porous electrode with significant non-uniformity of active material properties among particles.

During discharge, the electrochemical reaction occurs at the surface of LFP particles leading to an inward flux of Li to the particles and during charge, the process proceeds in the reverse direction from the fully lithiated toward the fully delithiated form. This reaction is represented by Equation (4-1) as follows:

$$Li_y^+ + e^- + FePO_4 \underset{\text{charge}}{\overset{\text{discharge}}{\rightleftharpoons}} Li_yFePO_4 \tag{4-1}$$

This section is started by describing the MP model and will be concluded with a modified porous-electrode model embedding multi-particle feature (SEMP model).

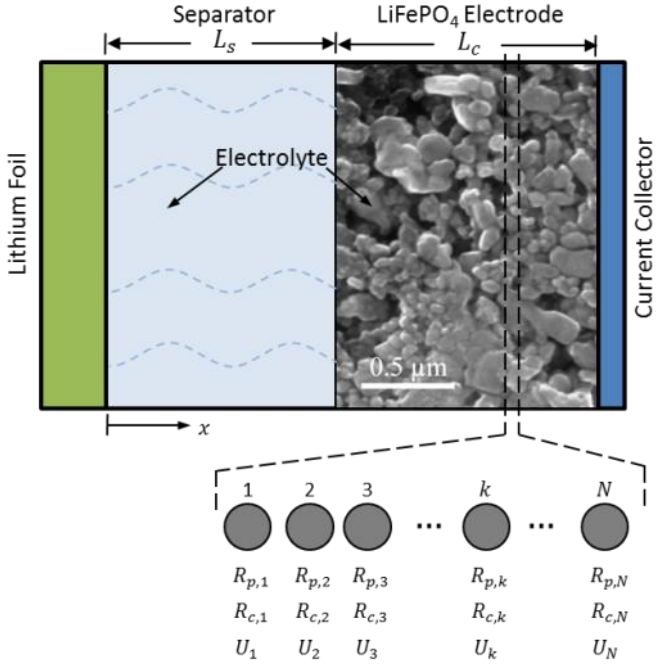

Figure 4-1: Schematic of a half-cell containing Li foil, $LiFePO_4$ porous electrode, porous separator, and the electrolyte in the pores. The LFP cathode is assumed to contain multiple particle sizes that are assumed to be spherical.

4.2.1 Multi-Particle (MP) model

To assist with the implementation and realization, the MP model of [108] is described here providing additional explanations. In general, there exist non-uniform distributions of physical and/or chemical properties of active material (such as particle size, surface resistance, or equilibrium potential) in a porous electrode that may significantly affect its electrochemical performance. The MP model can be regarded as an extension of the SP model and emerges where more than one particle is required to give a proper account of the particle-level phenomena. Similar to the SP model [114,115], the MP model assumes that all of the electrode active material is exposed to the same electronic and ionic environment. In other words, the variations of the solid-phase and liquid-phase electric potentials as well as the species concentration in the electrolyte across the cell are neglected [114,115]. Instead, a

simplistic representation of electrode-level losses is devised as an "equivalent Ohmic resistance" into which all of these limitations are lumped. The operating voltage of the cell will then be

$$V_{cell} = \phi_{s,c} - \phi_f - R_{eq} j_n \tag{4-2}$$

where, $\phi_{s,c}$ is the cathode solid-phase potential, ϕ_f is the Li foil potential, R_{eq} is the equivalent Ohmic resistance, and j_n is the current passes through the cell.

The VSSD concept is incorporated to account for Li transport losses inside each particle. This model, in fact, aggregates the bulk effects into a concentration-dependent diffusion coefficient and avoids explicit account of phase transformation and Li transport within the particles, which have not been precisely depicted to date. The theory and complete derivation of the VSSD model can be found in Refs. [108,109]. This model gives the mass balance of Li inside the spherical particles as [108,109]

$$\frac{\partial c_{s,k}}{\partial t} = \frac{1}{r_k^2} \frac{\partial}{\partial r_k} \left(r_k^2 \alpha_k \mathcal{D} \frac{\partial c_{s,k}}{\partial r_k} \right) \tag{4-3}$$

where, the subscript k denotes the properties for the k^{th} particle bin, $c_{s,k}$ is Li concentration inside the particles, r_k is the radial distance from the center of the particles, $\mathcal{D}$ is the solid-phase binary diffusion coefficient, and α_k is the thermodynamic factor defined as [108,109]:

$$\alpha_k = -\frac{F}{RT} y_k (1 - y_k) \frac{\partial U_k}{\partial y_k} \tag{4-4}$$

In Equation (4-4), F is the Faraday's constant, R is the universal gas constant, T is the temperature of the cell, $y_k = \frac{c_{s,k}}{c_s^{max}}$ is the mole fraction of Li concentration inside the particles, and U_k is the equilibrium potential of the LFP particles. The boundary and initial conditions of Equation (4-3) are as follows [108,109]:

$$\frac{\partial c_{s,k}}{\partial r_k}(r_k = 0, t) = 0 \tag{4-5}$$

$$\alpha_k \mathcal{D} \frac{\partial c_{s,k}}{\partial r_k}\left(r_k = R_{p,k}, t\right) = \frac{i_{n,k}}{F} \tag{4-6}$$

$$c_{s,k}(r_k, t = 0) = c_{s,k}^0 \tag{4-7}$$

where, $R_{p,k}$ is the radius of particles, $c_{s,k}^0$ is the initial Li concentration inside the particles, and $i_{n,k}$ is the reaction current density at the surface of the k^{th} particle bin.

The reaction current density is calculated using Butler-Volmer equation:

$$i_{n,k} = i_k^0 \left[exp\left(\frac{(1-\beta)F}{RT}\eta_k\right) - exp\left(\frac{-\beta F}{RT}\eta_k\right)\right] \quad (4\text{-}8)$$

In Equation (4-8), β is the charge-transfer coefficient for LFP lithiation/delithiation and η_k is the surface overpotential of the LFP particle bins defined as $\eta_k = \phi_{s,c} - R_{s,k} i_{n,k} - \phi_e - U_k$, where$R_{s,k}$ is the contact resistance between the LFP particles and conductive filler, and $\phi_{s,c}$ and ϕ_e are the cathode and electrolyte potentials, respectively. In this study, the value of the contact resistance is set to zero and no resistive-reactant feature is included. Furthermore, i_k^0 is the exchange current density corresponding to the k^{th} particle bin and is expressed as [109]:

$$i_k^0 = F k_c^0 c_s^{max} {c_e}^{1-\beta} \quad (4\text{-}9)$$

where, k_c^0 is the reaction rate constant and c_e is the electrolyte concentration. The exchange current density is assumed to be independent of Li concentration at the surface of the LFP particles. This assumption is justified by noticing that during the discharge (charge), the surface concentrations rise (drop) to a large (small) values and remain almost constant during the whole process. Since the MP model does not include electrolyte losses, the ϕ_e and c_e are independent of time and space and their values are zero and c_e^0 (the initial electrolyte concentration), respectively.

The cell applied current is related to the reaction current densities at the surface of the particles through a charge balance as [108]:

$$\sum a_k i_{n,k} = -\frac{j_n}{L_c} \quad (4\text{-}10)$$

where, L_c is the thickness of the cathode and a_k is the specific surface area of the k^{th} particle bin. The value of a_k is calculated by $3\varepsilon_k / R_{p,k}$ where ε_k is the volume fraction of the k^{th} particle bin referred to the electrode volume. Equations (4-3)-(4-10) are then solved together to calculate the

value of $\phi_{s,c}$. Finally, the reaction overpotential at the Li foil is obtained using the Butler-Volmer equation as follows:

$$j_n = i_f^0 \left(\frac{c_e}{c_e^0}\right)^{1-\beta_f} \left[exp\left(\frac{\beta_f F}{RT}\eta_f\right) - exp\left(\frac{-\beta_f F}{RT}\eta_f\right)\right] \tag{4-11}$$

where, i_f^0 is the Li foil exchange current density based on a 1 M reference concentration, referred to the counter electrode area. β_f is the Li foil charge-transfer coefficient, and η_f is the overpotential of the Li foil defined as $\eta_f = \phi_f - \phi_e$. Having the values of $\phi_{s,c}$ and ϕ_f computed and the apparent Ohmic resistance of the cell, R_{eq}, fitted, the operating voltage of the Li/LFP half-cell is determined from Equation (4-2).

4.2.2 Simplified Electrochemical Multi-Particle (SEMP) Model

The described MP model is only valid for low to medium charge/discharge rates (i.e., up to 1C) where the overall electrode potential loss is primarily affected by the charge-transfer kinetics at the surface and diffusion through the bulk of active material particles. At higher rates, the potential loss originates not only from particle-level phenomena, but also from electrode-level electronic and ionic transport limitations. As a result, the gradients of the electrolyte concentration and potential as well as the potential gradient in the solid phase must be taken into account [113,122,123]. The MP model may be incorporated into Newman's porous-electrode theory [19,21] with the concentrated-solution theory describing the transport of species in the electrolyte [124] and the Ohm's law describing the percolation resistance across the solid phase. Such a full-order model becomes computationally expensive when two or more particle bins are involved. It is also the case when multidimensional simulation of the cell (e.g., thermal analysis), repetitive simulations (e.g., high-rate aging simulation), or real-time state estimation (e.g., battery management system) are required.

For such applications, the model must be capable of accurately accounting for electrolyte limitations (as compared to the simplistic equivalent resistance, R_{eq}) yet avoiding the heavy computation duty associated with solving the particle-level equations at every mesh point across the cell thickness. To this end, the solutions of the governing PDEs at the electrode level are

approximated in the simplified electrochemical multi-particle model using a method originally formulated in Ref. [116]. In this method, the spatial distribution of potential and concentration in the electrolyte are approximated by polynomials in the space variable x, i.e., along the cell thickness, while the transient effects are captured by incorporating time-dependent polynomial coefficients. Different polynomial orders were examined and, as shown in Figure 4-2, a cubic polynomial is chosen for the electrolyte potential and concentration distributions of the cathode. The electrolyte concentration distribution across the separator is approximated by a quadratic polynomial while the distribution of the electrolyte potential in the separator is obtained by analytically solving the charge balance equation. These orders of the polynomials make the method as simple as possible while keeping the accuracy in an acceptable range.

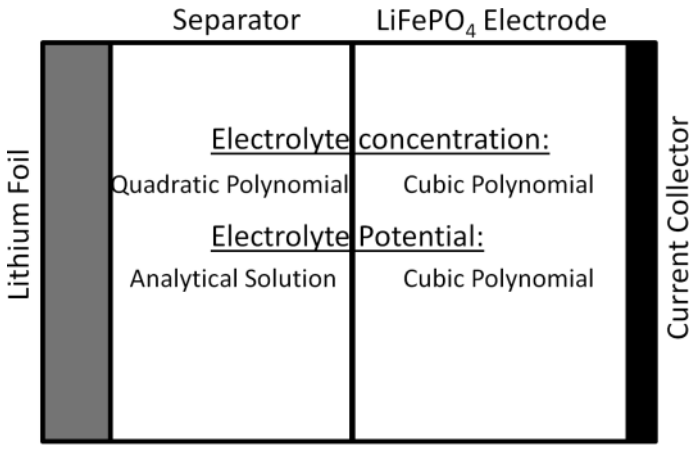

Figure 4-2: The degree of approximated polynomials for the concentration and potential of the electrolyte in the separator and cathode.

The following equations describe the electrolyte concentration distributions in the separator and cathode [122]:

$$c_{e,s}(x_s,t) = p_1(t)x_s^2 + p_2(t)x_s + p_3(t), 0 \le x_s \le 1 \quad (4\text{-}12)$$

$$c_{e,c}(x_c,t) = q_1(t)x_c^3 + q_2(t)x_c^2 + q_3(t)x_c + q_4(t), 0 \le x_c \le 1 \quad (4\text{-}13)$$

where, x_s and x_c are dimensionless length along the separator and cathode, respectively, and are defined as

$$x_s = \frac{x}{L_s}, 0 \le x \le L_s \quad (4\text{-}14)$$

$$x_c = \frac{(x - L_s)}{L_c}, L_s \le x \le L_s + L_c \tag{4-15}$$

L_s is the separator thickness and x is measured from the Li foil/separator interface across the cell. By incorporating the dimensionless lengths, the electrolyte mass balance equations [19,21] take the following form:

$$\varepsilon_s \frac{\partial c_{e,s}}{\partial t} = \frac{1}{L_s^2} \frac{\partial}{\partial x_s} \left(D_s^{eff} \frac{\partial c_{e,s}}{\partial x_s} \right) \tag{4-16}$$

$$\varepsilon_c \frac{\partial c_{e,c}}{\partial t} = \frac{1}{L_c^2} \frac{\partial}{\partial x_c} \left(D_c^{eff} \frac{\partial c_{e,c}}{\partial x_c} \right) + \frac{(1 - t_+^0)}{F} \sum a_k i_{n,k} \tag{4-17}$$

and the corresponding boundary conditions are:

$$\frac{\partial c_{e,s}}{\partial x_s}(x_s = 0, t) = -\frac{j_n (1 - t_+^0) L_s}{F D_s^{eff}} \tag{4-18}$$

$$\frac{\partial c_{e,c}}{\partial x_c}(x_c = 1, t) = 0 \tag{4-19}$$

$$c_{e,s}(x_s = 1, t) = c_{e,c}(x_c = 0, t) \tag{4-20}$$

$$-\frac{D_s^{eff}}{L_s} \frac{\partial c_{e,s}}{\partial x_s}(x_s = 1, t) = -\frac{D_c^{eff}}{L_c} \frac{\partial c_{e,c}}{\partial x_c}(x_c = 0, t) \tag{4-21}$$

where, ε_s is the separator porosity, ε_c is the cathode porosity, and t_+^0 is the Li^+ ion transference number. D_c^{eff} and D_s^{eff} are the effective diffusion coefficients of the electrolyte in the cathode and separator, respectively. They are obtained according to $D_i^{eff} = D_e \varepsilon_i^{\gamma}$ where the subscript i is c or s, D_e is the bulk electrolyte diffusivity, and γ is the Bruggeman exponent. Volume averaging of Equations (4-16) and (4-17) and using Equation (4-19) (i.e., the boundary condition at $x_c = 1$) yields:

$$\varepsilon_s \frac{dc_{e,s}^{avg}}{dt} = \frac{1}{L_s^2} \left(D_s^{eff} \frac{\partial c_{e,s}}{\partial x_s}(x_s = 1, t) - D_s^{eff} \frac{\partial c_{e,s}}{\partial x_s}(x_s = 0, t) \right) \tag{4-22}$$

$$\varepsilon_c \frac{dc_{e,c}^{avg}}{dt} = \frac{1}{L_c^2} \left(-D_c^{eff} \frac{\partial c_{e,c}}{\partial x_c}(x_c = 0, t) \right) - \frac{(1 - t_+^0)}{F} \frac{j_n}{L_c} \tag{4-23}$$

The average concentrations are calculated by volume averaging Equations (4-12) and (4-13) over the separator and cathode, respectively, as:

$$c_{e,s}^{avg}(t) = \frac{1}{3}p_1 + \frac{1}{3}p_2 + p_3 \tag{4-24}$$

$$c_{e,c}^{avg}(t) = \frac{1}{4}q_1 + \frac{1}{3}q_2 + \frac{1}{2}q_3 + q_4 \tag{4-25}$$

In order to solve for the coefficients of concentration polynomials, seven independent equations are required. Substitution of the polynomial approximations (Equations (4-12) and (4-13)) and the average concentrations (Equations (4-24) and (4-25)) into Equations (4-18)-(4-23), gives the following set of six DAEs:

$$p_2 = -\frac{j_n(1-t_+^0)L_s}{FD_s^{eff}} \tag{4-26}$$

$$3q_1 + 2q_2 + q_3 = 0 \tag{4-27}$$

$$p_1 + p_2 + p_3 = q_4 \tag{4-28}$$

$$\frac{D_s^{eff}}{L_s}(2p_1 + q_1) = \frac{D_c^{eff}}{L_c}q_3 \tag{4-29}$$

$$\frac{1}{3}\frac{dp_1}{dt} + \frac{1}{2}\frac{dp_2}{dt} + \frac{dp_3}{dt} = \frac{2D_s^{eff}}{\varepsilon_s L_s^2}p_1 \tag{4-30}$$

$$\frac{1}{4}\frac{dq_1}{dt} + \frac{1}{3}\frac{dq_2}{dt} + \frac{1}{2}\frac{dq_3}{dt} + \frac{dq_4}{dt} = -\frac{D_c^{eff}}{\varepsilon_c L_c^2}q_3 - \frac{1-t_+^0}{\varepsilon_c F}\frac{j_n}{L_c} \tag{4-31}$$

The last equations is obtained by solving the mass balance equation (Equations (4-17)) at one arbitrary point inside the cathode, $x_{c,a}$, leading to [122]:

$$\begin{aligned} &x_{c,a}^3\frac{dq_2}{dt} + x_{c,a}^2\frac{dq_2}{dt} + x_{c,a}\frac{dq_3}{dt} + \frac{dq_4}{dt} \\ &= \frac{D_c^{eff}}{\varepsilon_c L_c^2}\left(6q_1x_{c,a} + 2q_2\right) + \frac{(1-t_+^0)}{\varepsilon_c F}\sum a_k i_{n,k}\left(x_{c,a}, t\right) \end{aligned} \tag{4-32}$$

This equation requires the reaction current densities, $i_{n,k}$, to be calculated at $x_{c,a}$ by solving particle-level equations (Equations (4-3)-(4-9)) at that location (i.e., plugging $\phi_e\left(x_{c,a}, t\right)$ and $c_e\left(x_{c,a}, t\right)$ into Equations (4-8) and (4-9)).

Furthermore, it is assumed that the cell is at rest prior to discharge and the initial concentration of the electrolyte is uniform, c_e^0. This leads to zero value for all polynomial coefficients at $t = 0$ except for a_3 and b_4 whose initial values are equal to c_e^0. However, having zero initial value does not satisfy Equation (4-26) at $t = 0$. To overcome this numerical issue, a dynamic behavior for the coefficient

p_2 is artificially devised, that is, the value of p_2 is zero initially, but rapidly evolves to its value dictated by Equation (4-26). Such an arbitrary dynamics can be described as:

$$\frac{dp_2}{dt} = -Mp_2 - M\frac{j_n(1-t_+^0)L_s}{FD_s^{eff}} \tag{4-33}$$

where, M is a large number to guarantee rapid convergence of p_2 to its actual value. Solution of Equation (4-33) yields:

$$p_2 = -\frac{j_n(1-t_+^0)L_s}{FD_s^{eff}}(1 - exp(-Mt)) \tag{4-34}$$

which replaces Equation (4-26) in the model. It should be noted that despite the absence of a rigorous local mass balance and, thus, unavoidable inaccuracies in approximating the electrolyte concentration and potential distributions, the polynomial profiles were chosen according to two criteria: i) minimum polynomial orders are considered in the model to minimize computational costs, and ii) the final operating voltage predictions of the model are accurate enough. In other words, similar to the non-conservative numerical algorithms such as finite-element and finite-difference methods, where the local mass balance is not rigorous (compared to the finite-volume method), the objective here is to obtain a sufficiently close approximation to the solution of the mass balance that meets the above criteria while maintaining computational efficiency. This approach resulted in a second order polynomial inside the separator and a third order polynomial inside the cathode as described in detail above. Therefore, the operating voltage of the cell is well captured with minimal computational cost.

After approximating the electrolyte concentration distribution, the potential distribution of the electrolyte is to be addressed. The charge balance inside the separator and the corresponding boundary conditions are formulated as [19,21]:

$$-\frac{\partial^2\phi_{e,s}}{\partial x_s^2} + \frac{2RT(1-t_+^0)}{F}\frac{\partial}{\partial x_s}\left(\frac{1}{c_{e,s}}\frac{\partial c_{e,s}}{\partial x_s}\right) = 0 \tag{4-35}$$

$$\phi_{e,s}(x_s = 0, t) = 0 \tag{4-36}$$

$$-\frac{\kappa_s^{eff}}{L_s}\frac{\partial\phi_{e,s}}{\partial x_s}(x_s = 1, t) = -\frac{\kappa_c^{eff}}{L_c}\frac{\partial\phi_{2,c}}{\partial x_c}(x_c = 0, t) \tag{4-37}$$

κ_s^{eff} is the effective electrolyte conductivity in the separator and is defined as $\kappa_s^{eff} = \kappa\varepsilon_s^{\gamma}$ where κ is the bulk ionic conductivity of the electrolyte, assumed to be constant. The electrolyte potential at the Li foil/separator interface is arbitrary set to zero as the reference electric potential of the electrolyte. Equations (4-35)-(4-37) are then solved analytically and the electrolyte potential distribution inside the separator is as follows:

$$\phi_{e,s}(x_s,t) = \frac{2RT(1-t_+^0)}{F} ln\frac{p_1x_s^2 + p_2x_s + p_3}{p_3} + \left(\frac{\kappa_c^{eff}L_s}{\kappa_s^{eff}L_c}s_3 - \frac{2RT(1-t_+^0)}{F}\frac{2p_1+p_2}{p_1+p_2+p_3}\right)x_s \tag{4-38}$$

where, s_3 is the third coefficient in the cubic polynomial approximation of the electrolyte potential across the cathode.

The cathode electrolyte potential is then approximated using the following cubic polynomial:

$$\phi_{e,c}(x_c,t) = s_1(t)x_c^3 + s_2(t)x_c^2 + s_3(t)x_c + s_4(t) \tag{4-39}$$

The charge balance in the cathode and the corresponding boundary conditions are:

$$-\frac{\partial^2\phi_{e,c}}{\partial x_c^2} + \frac{2RT(1-t_+^0)}{F}\frac{\partial}{\partial x_c}\left(\frac{1}{c_{e,c}}\frac{\partial c_{e,c}}{\partial x_c}\right) = \frac{L_c^2}{\kappa_c^{eff}}\sum a_k i_{n,k} \tag{4-40}$$

$$\frac{\partial\phi_{e,c}}{\partial x_c}(x_c = 1,t) = 0 \tag{4-41}$$

$$\phi_{e,c}(x_c = 0,t) = \phi_{e,s}(x_s = 1,t) \tag{4-42}$$

where, κ_c^{eff} is the effective electrolyte conductivity in the cathode and is defined as $\kappa_c^{eff} = \kappa\varepsilon_c^{\gamma}$. By employing the boundary conditions for the electrolyte potential and concentration, volume-averaged charge balance equation reads:

$$\frac{\partial\phi_{e,c}}{\partial x_c}(x_c = 0,t) - \frac{2RT(1-t_+^0)}{F}\left(\frac{1}{c_{e,c}}\frac{\partial c_{e,c}}{\partial x_c}\right)|_{x_c=0} = -\frac{j_nL_c}{\kappa_c^{eff}} \tag{4-43}$$

The approximate solution for $\phi_{e,c}$ (Equation (4-39)) is then substituted into Equations (4-41)-(4-43) to give the following three equations for the polynomial coefficients of the electrolyte potential:

$$3s_1 + 2s_2 + s_3 = 0 \tag{4-44}$$

$$s_4 = \frac{2RT(1-t_+^0)}{F} ln \frac{p_1(t)+p_2(t)+p_3(t)}{p_3(t)} + \frac{\kappa_c^{eff} L_s}{\kappa_s^{eff} L_c} s_3 - \frac{2RT(1-t_+^0)}{F} \frac{2p_1+p_2}{p_1+p_2+p_3} \tag{4-45}$$

$$s_3 - \frac{2RT(1-t_+^0)}{F} \frac{q_3}{q_4} = -\frac{j_n L_c}{\kappa_c^{eff}} \tag{4-46}$$

The estimation of Equation (4-40) on the arbitrary point in the cathode, $x_{c,a}$, gives the last required equation:

$$-\left(6s_1 x_{c,a} + 2s_2\right) + \frac{2RT(1-t_+^0)}{F}\left(\frac{1}{c_{e,c}}\frac{\partial c_{e,c}}{\partial x_c}\right)|_{x_c=0} = \frac{L_c^2}{\kappa_c^{eff}} \sum a_k i_{n,k}\left(x_{c,a}, t\right) \tag{4-47}$$

where, the second term on the left-hand-side is calculated using the estimated cathode concentration polynomial. The reaction current densities appeared on the right-hand-side of Equation (4-47) are obtained at $x_{c,a}$ in the same way as described earlier for Equation (4-32).

In summary, one quadratic polynomial (Equation (4-12)) approximates the electrolyte concentration distribution in the separator while an analytic solution (Equation (4-38)) gives the potential distribution of the electrolyte in this region. Moreover, two cubic polynomials (Equations (4-13) and (4-39)) describe the concentration and potential distributions of the electrolyte across the cathode. The polynomial coefficients of Equations (4-12), (4-13), and (4-39) are calculated using Equations (4-26)-(4-32), (4-34), and (4-44)-(4-47). Finally, the estimated electric potential and concentration distributions of the electrolyte across the cathode are spatially averaged and fed back to the charge-transfer equations at the particle level (i.e., ϕ_e in Equation (4-8) and c_e in Equation (4-9)). Having incorporated these average values, the particle-level equations are solved simultaneously with the simplified electrode-level equations to give the electrode potential, $\phi_{s,c}$.

In addition to the electrolyte simplifications, according to the recent multi-probe conductometric experiments, even though LFP is intrinsically insulating, applying carbon coating on its surface and addition of conductive filler significantly decrease the percolation resistivity of the composite electrode. As a result, it is not a limiting factor even at rates as high as 5C [109,125]. Hence, the

electronic losses across the solid phase are ignored in this model (i.e., $\phi_{s,c}$ is uniform across the electrode). The Cell voltage will eventually be the difference between the time-varying solid-phase potential $\phi_{s,c}$ and the electric potential of the Li foil ϕ_f.

4.2.3 Solution Procedure

In order to obtain operating voltage of the cell, the governing equations of the SEMP model are solved numerically using the finite element method in COMSOL Multiphysics software [126]. This model solves for the Li concentration inside the particles twice, one time to calculate the cathode potential based on the average values of the electrolyte potential and concentration and one time to estimate the polynomial coefficients based on the electrolyte variables at an arbitrary point inside the cathode, $x_{ct,a}$.The particles are discretized into 20 elements whose sizes gradually decrease while approaching the particle surfaces with the minimum to maximum element-size ratio of 0.2. As a result, the SEMP model requires solution of:

- $2\times20\times N$ equations accounting for Li concentration inside the N particle bins,
- $2\times N$ Butler-Volmer equations accounting for electrochemical reaction at the surface of the N particle bins,
- 1 equation for the Li foil potential, and,
- 11 equations to calculate the polynomial coefficients,

which form a system of $12+42\times N$ partial differential algebraic equations that must be solved simultaneously. The full-order model, on the other hand, requires not only solving for Li concentration inside the particles but also for the dependent variables, $\phi_{s,c}$, ϕ_e, and c_e, across the thickness of the cell. If the cathode and separator are each discretized into 10 equal elements while the number of elements inside the particles remains the same as that in the SEMP model, the system of PDAEs for this model consists of $51+210\times N$ equations, that is, $2\times2\times10$ equations for the electrolyte concentration and potential in the separator and cathode, 10 equations for the solid-phase potential in the cathode, 1 equation for the Li foil potential, $10\times N$ equations for the electrochemical

reactions at the surface of the N particle bins, and $10\times20\times N$ equations for the Li concentration inside the N particle bins. The approximation becomes more computationally beneficial when a larger number of particle bins is required in the model.

4.3 Results and Discussion

In this section, all the described models (full-order, SP, MP, and SEMP models) are separately implemented to predict a set of experimental galvanostatic discharge data obtained from the literature [109]. The experimental data consists of various operating rates from C/25 to 5C; thus, it can effectively examine the performance of the models over a wide operating range typical of that seen in electrified vehicles. The Newman's full-order model is used as an accurate benchmark to compare the SEMP model with whereas the SP an MP models are used to establish the limit of implementation simplicity and numerical facility. The required parameters are imported directly from Ref. [109] and are listed in Appendix A. Four particle bins are considered to cover the wide PSD observed in SEM images. Among all, one particle bin (i.e., the 2^{nd} bin) constitutes most of the active material volume fraction and is obtained from the actual PSD of the electrode (i.e., d_{50}). The rest of the particle sizes and volume fractions are fitted to capture the end capacities of the electrode. Details on the justification for, and empirical curve fitting approach to, determining the particle sizes and number of particles in the 4-particle PSD is not covered in this chapter, but can be found in [108] and [109].

The electrode open-circuit potential (OCP) is approximated experimentally from low-rate galvanostatic discharge of the cell and is shown in Appendix A. Using this experimental pseudo OCP, the thermodynamic factor can then be calculated according to Equation (4-4) and is shown in Appendix A.

The simulation results of the full-order model for the galvanostatic discharge rates from C/25 to 5C at 25 ºC show good agreement with the experimental data and are presented in Figure 4-3. These simulation results are used to assess the accuracy of the alternative models including the SP, MP, and SEMP models throughout this section. As the simplest approach, the SP model is used to

simulate the full-range galvanostatic discharges and to see how the inclusion of an artificial Ohmic resistance at the electrode level improves the high-rate simulation results. The SP model is a special case of the MP model wherein only one particle bin is incorporated ($N = 1$). Therefore, the same equations used for the MP model (Equations (4-2)-(4-11)) are employed in the SP model with only one particle size. This particle size is chosen to be the d_{50} particle size (72 nm). The required model parameters are taken from Appendix A and the value of R_{eq} is set to 2.15×10^{-3} Ω (best fitted). As shown in Figure 4-4, the SP model fails to predict the end-of-discharge capacities even at low discharge rates. Based on the transmission electron microscope (TEM) imaging of LFP electrodes, Srinivasan and Newman [98] attributed this effect to the inevitable presence of particle size distribution (PSD) in composite electrodes and unusually low apparent solid-phase diffusion coefficient of LFP. In addition, the error in the voltage predictions significantly increase as the applied current increases which is mainly caused by simplistically estimating the electrode-level losses using an equivalent Ohmic resistance, R_{eq} [122,123].

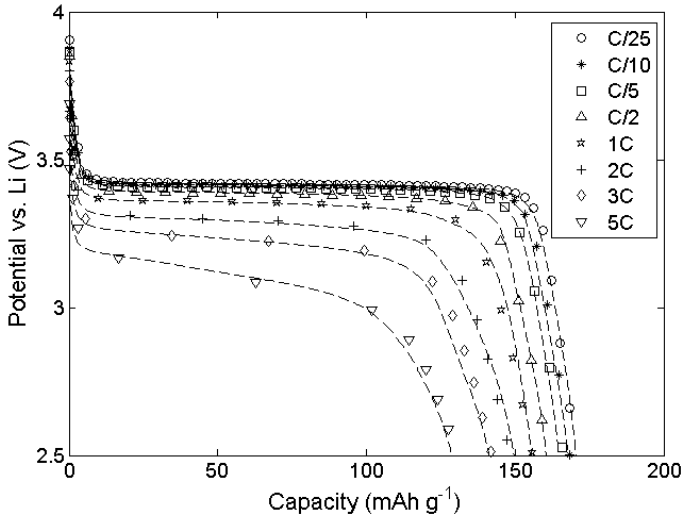

Figure 4-3: Comparison between the experimental data (symbols) and simulation results of the Newman's full-order model (dashed lines) for the galvanostatic discharge rates from C/25 to 5C at 25 ºC.

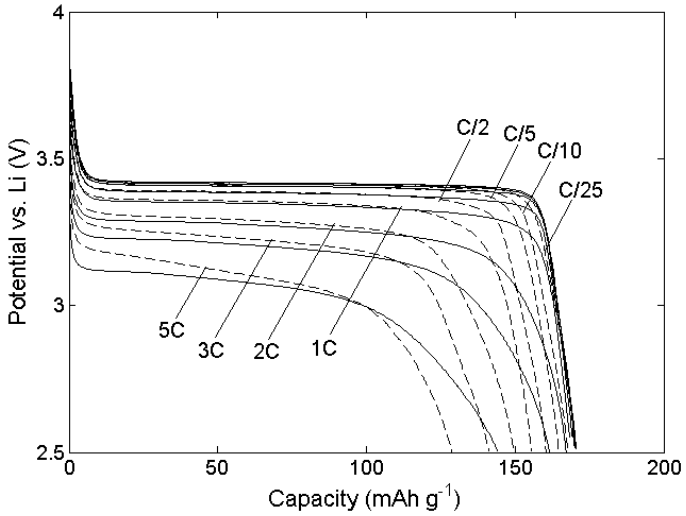

Figure 4-4: Comparison between the Newman's full-order model (dashed lines) and simulation results of the SP model (solid lines) for the galvanostatic discharge rates from C/25 to 5C at 25 ºC.

In order to predict the end-of-discharge capacities at different operating ranges, the particle size distribution should be considered in the model yielding the MP model [98]. In this model, the same particle bins as those in the full-order model (Appendix A) are considered. Other parameters are set to be the same as the SP model. The simulation results are compared with the full-order model in Figure 4-5. It is observed that, similar to the full-order model, the MP model can predict the end-of-discharge capacities at all discharge rates. This is due to the fact that both of these models ascribe the final capacities to the limitations of the sluggish diffusion (extremely low diffusion coefficient of 5×10^{-19} m^2 s^{-1}) inside the LFP particles for which the effect of size non-uniformities become significant. The attribution of end-capacities to the diffusion of host species within the insertion materials is intuitively acceptable for solid-solution materials and regularly yields successful results having only one particle bin incorporated. However, the need for introducing more than one LFP particle with different sizes to the model and the dependence of apparent (fitted) PSD on the applied current [109,127] disclose a more complicated mechanism than a simple diffusion or a core-shell phase-change mechanism [128].

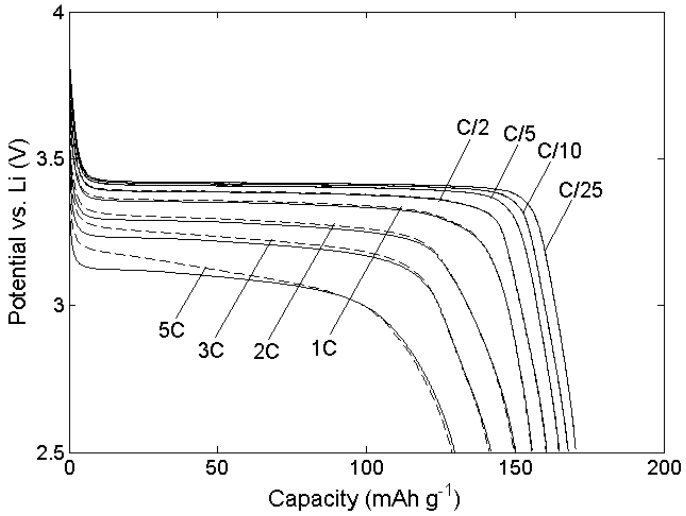

Figure 4-5: Comparison between the Newman's full-order model (dashed lines) and simulation results of the MP model (solid lines) for the galvanostatic discharge rates from C/25 to 5C at 25 ºC.

It is depicted in Figure 4-5 that the MP simulation results successfully match the voltage-capacity curves obtained by the full-order model at the discharge rates up to the 1C. However, similar to the case of the SP model, the discrepancy between the two model predictions increases as the discharge rate increases. To maintain the simplicity and, at the same time, to improve the model accuracy especially at lower capacity, the MP model is extended to the SEMP model. Model parameters are taken to be the same as those used in the full-order model. In addition to these parameters, the location of the arbitrary point inside the LFP electrode, $x_{c,a}$, introduces a new fitting parameter to the SEMP model. Since the mass and charge balance equations in the electrolyte must be satisfied at this point, its location can highly affect the obtained electrolyte concentration and potential distributions across the cell and hence the cell operating voltage. This parameter is estimated by manually fitting the voltage predictions of the SEMP model to the full-order model yielding the value of 0.22 for $x_{c,a}$ that is kept constant during all the simulations. In fact, there is some flexibility in the choice of this arbitrary location; it was varied to optimize the matching of results between the SEMP and those obtained using the Newman's full-order model.

The simulation results generated by the SEMP model is compared against those of the full-order model at the discharge rates from C/25 to 5C and are presented in Figure 4-6(a). The results show

that the SEMP model can simulate not only the end-of-discharge capacities, but also the onset and slope of the voltage-capacity curves with high accuracy. The relative error of the model defined as $\frac{abs(V_{SEMP}-V_{full})}{V_{full}} \times 100$ is depicted in Figure 4-6(b) where V_{SEMP} and V_{full} are the operating voltages of the cell predicted by SEMP and full-order models, respectively. It shows that even in the worst condition, which occurs at the end of 5C discharge, the relative error of the SEMP model does not exceed 1.7% highlighting the adequacy of the SEMP model relative to the full-order formulation.

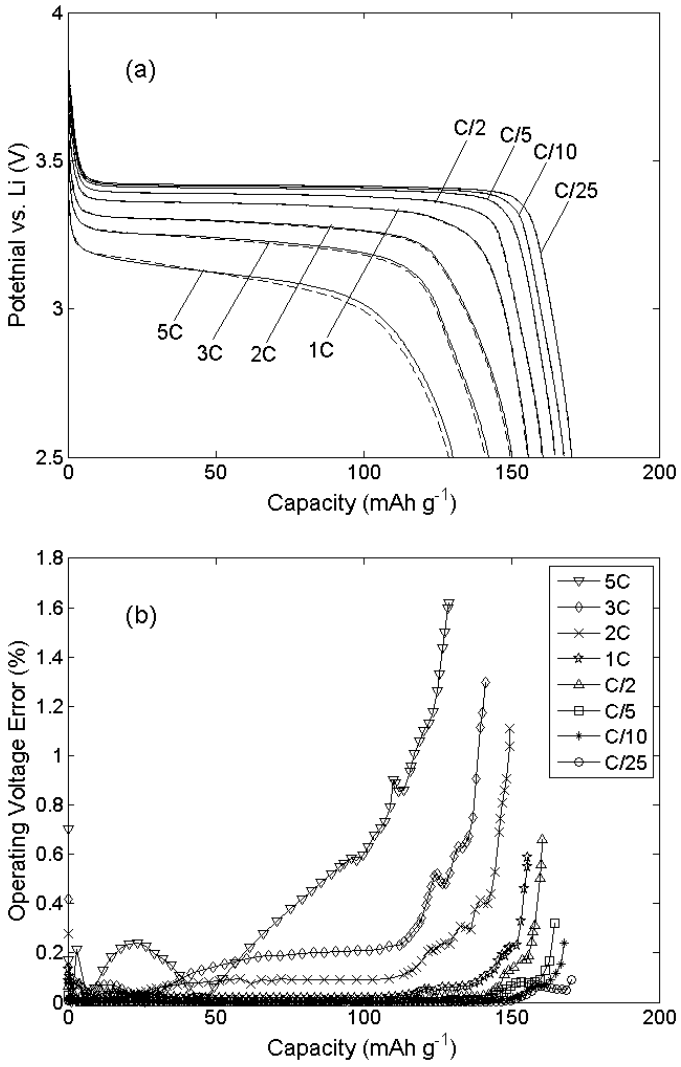

Figure 4-6: (a) Comparison between the Newman's full-order model (dashed lines) and simulation results of the SEMP model (solid lines), and (b) the relative error of the SEMP model with respect to Newman's full-order model for the galvanostatic discharge rates from C/25 to 5C at 25 ºC.

The full-order model predictions of the solid-phase potential across the cathode are presented in Figure 4-7. As it is observed, the solid-phase potential is almost constant across the electrode even at a rate as high as 5C, in line with our assumption in the SEMP model that the solid-phase potential depends only on time and not space. Very large discharge rates can, however, cause some solid-phase potential variations across the cathode, but they are not covered in this paper since the main focus here is on batteries for electric vehicles and plug-in vehicles applications for which a 5C discharge condition is aggressive. Some further analysis and descriptions on this subject may also be found in Appendix B.

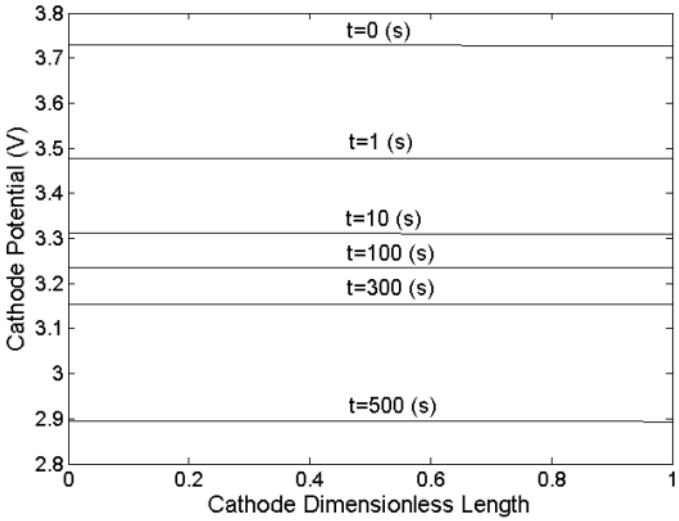

Figure 4-7: Solid-phase potential distribution inside the cathode at various times and at 5C discharge rate obtained from the Newman's full-order model.

In order to further investigate the accuracy of the SEMP model, a sensitivity analysis is attempted for design parameters such as the thickness and active material loading of the electrode. Three values for each parameter (30, 60, and 90 μm for the cathode thickness and 0.22, 0.3, 0.38 for the cathode active material volume fraction) are considered of which different combinations are examined while other model parameters are kept unchanged. It should be noted that enough attention has been paid to keep the ratio of the active material and conductive filler plus the binder constant when the active material volume fraction is changed; the higher active material loading, the higher binder/filler content and the lower porosity of the electrode. Figure 4-8(a-i) show the results of the full-order and SEMP models in all cases. In addition, the relative and average errors of the SEMP model at 5C

discharge rate for all cases are depicted in Figure 4-8(j) and Figure 4-8(k), respectively. The relative error is calculated from the same relation as used for Figure 4-6(b) while the average error is defined as $\frac{\sum abs(V_{SEMP}-V_{full})}{\sum V_{full}} \times 100$ that is the area between the operating voltage curves predicted by the SEMP and full-order models divided by the area under the operating voltage curve of the full-order model. Figure 4-8(j) shows that the maximum relative error of the SEMP model is about 2% in all cases except the case (i) where the electrolyte is almost depleted at the end of discharge and the error reaches to a maximum of 5%. Figure 4-8(k), however, demonstrates that in average incorporating the SEMP model yields the prediction error of less than 1%. As a result, good agreement between the results of the SEMP and the full-order models in all cases is observed and the developed SEMP model proved valid for a wide range of electrode designs.

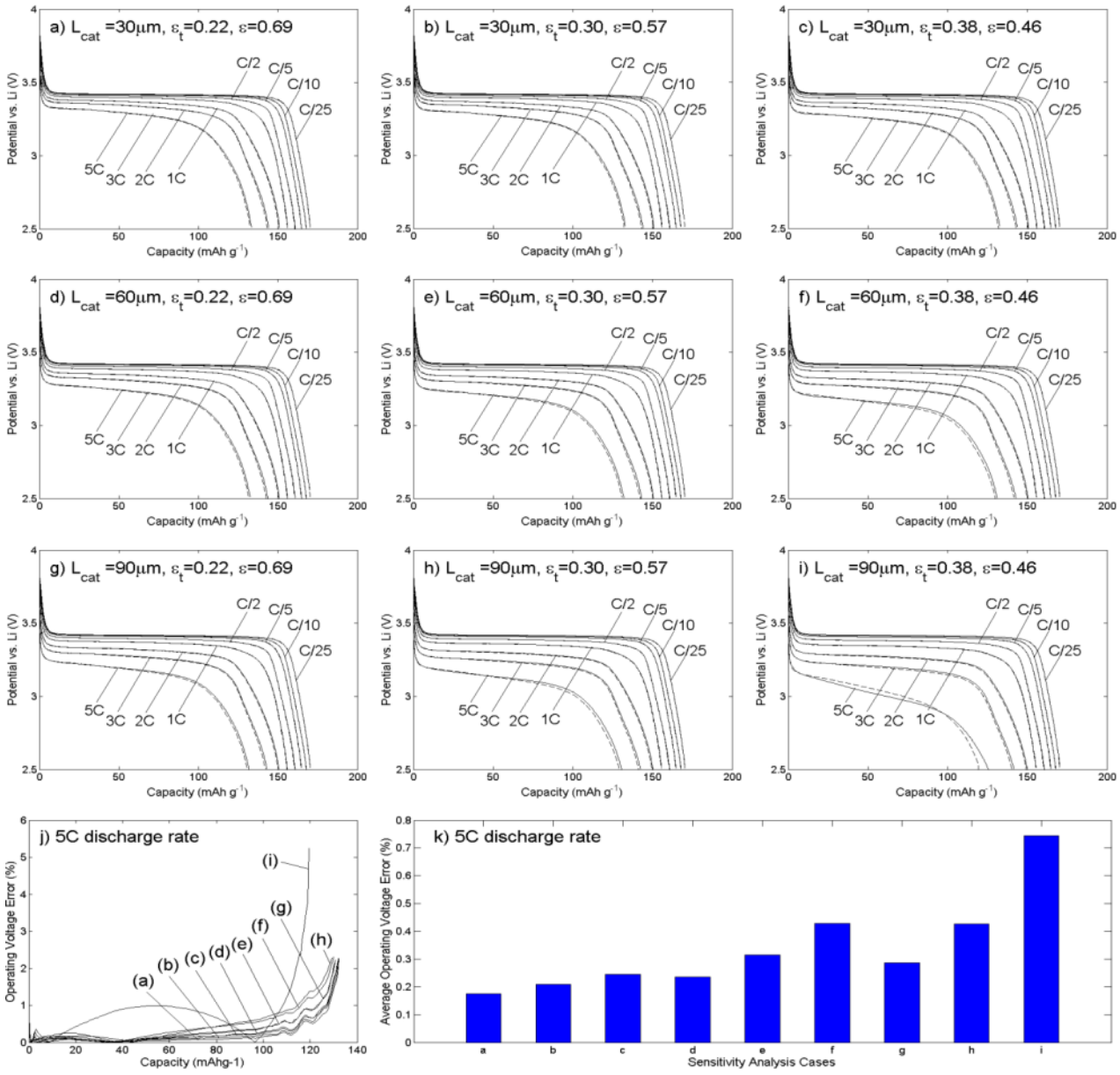

Figure 4-8: (a-i) Comparison between the Newman's full-order (dashed lines) and SEMP models (solid lines) for discharge rates from C/25 to 5C at 25 ºC in different cathode thicknesses (L_{cat}) from 30 nm to 90 μm, and cathode active material volume fractions (ε_t) from 0.22 to 0.38, (j) the relative, and (k) the average error of the SEMP model with respect to the Newman's full-order model at 5C discharge rates for different sensitivity analysis cases.

Chapter 5 Three-Dimensional Battery Model

The following section is based on previously published work by Mastali, M., Samadani, E., Farhad, S., Fraser, R., and Fowler, M.

Electrochimica Acta 2016, 190: 574–587 [129].

"**Three-dimensional Multi-Particle Electrochemical Model of $LiFePO_4$ Cells based on a Resistor Network Methodology**"

This thesis author specific contribution to this paper was to develop the models, conduct the simulations, prepare all the graphics and results, prepare the final manuscript and reviewer edits with direction from the project supervisors who were co-authors. All authors reviewed the manuscript.

Reproduced with the permission from Elsevier.

5.1 Introduction

The battery models should be applicable not only to small coin-sized, but also to the pouch-sized batteries that are utilized in electric vehicles, and as such computational efficiency is needed. Incorporating VSSD approach in Newman pseudo two-dimensional (P2D) model results in relatively slow simulations and therefore is not suitable to be integrated in the full-sized pouch configuration battery models or control simulations. To solve this issue, Chapter 4 presented a simplified method that is fast and yet accurate in predicting the operating voltage of these batteries. In addition to reviewing this method, another approach is also described in this chapter that is faster and at the same time more accurate than the model presented in Chapter 4.

In order to design larger pouch configuration batteries for electric vehicle applications, which include multilayered cell, the study of small coin cells is not adequate, as the interaction between the layers cannot suitably predicted. Distributions of the electrochemical reaction and temperature over full-sized pouch configuration batteries should also be considered [44,130–134]. These distributions may result in locally higher degradation rates and thus shorten battery life [135–137]. For such

studies, three-dimensional models that are able to capture the above-mentioned distributions play an important role. The major proposed approach in the literature is to expand the one-dimensional models into the three dimensions by simply combining them [22,23,112,138,139]. This approach is very straightforward, but it may not be physically accurate because of the large number of assumptions involved. In contrast, including all three-dimensional effects can tremendously increase the complexity of the model as well as the simulation time. Therefore, an alternative approach for three-dimensional simulations is presented in this paper that utilizes fewer simplifying assumptions yet improves accuracy while maintaining or improving on computational time.

In the following sections, as summarized in Figure 5-1, three one-dimensional and two three-dimensional models for LFP batteries are presented. The first one-dimensional model is the P2D model incorporating the VSSD model for capturing two-phase behaviour of LFP particles. To increase the simulation speed, however, two simplified one-dimensional models are presented. The first model (simplified electrochemical multi-particle (SEMP) model) is an extension to the single particle (SP) model which includes electrolyte effects [114,115,140]. The second model (homogenous pseudo-two-dimensional (HP2D) model) is the same as the P2D model but with the additional assumption of homogenous electrochemical reaction across the electrode. Next, the simplified one-dimensional models are expanded to three dimensions using two different approaches. The first one is the general approach reported in the literature [22,23,112,138,139] in combination with SEMP model. To prevent unnecessary assumptions associated with the first approach, the HP2D model is expanded to three dimensions as a second three-dimensional approach. The main assumptions of the models and their connections are summarized in Figure 5-1.

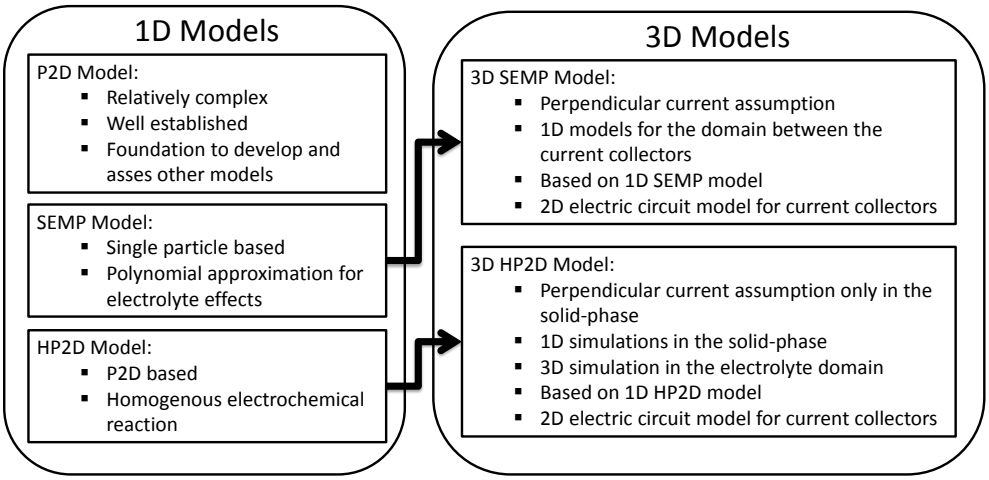

Figure 5-1: Schematic of the presented models in this paper (one-dimensional and three-dimensional), their main assumption, and their relation with each other.

5.2 One-Dimensional Modeling

In this section, the Newman pseudo two-dimensional (P2D) model for a small coin cell, which is presented in Figure 4-1, is first summarized. Then, two simplified versions of this model are presented. Although the models are reported for a half-cell battery, they can be easily expanded to full-cell batteries by replacing the lithium foil with a negative electrode. In addition, the cathode material may contain different particle sizes and even different particle materials as shown in Figure 4-1.

5.2.1 The Newman Pseudo Two-Dimensional Model

The Newman pseudo-two-dimensional (P2D) model, which is originally introduced by Doyle et al. [19,20] and used by other researchers [109,141], divides the battery into the particle and electrode domains. In the particle domain, the conservation of lithium is solved. The particles are usually considered to be spherical and Fick's law governs the particle lithium diffusion. In the electrode domain, the conservation of charge in the solid-phase and electrolyte as well as the conservation of mass in the electrolyte is solved. The particle and electrode domains are then connected by the electrochemical reaction at the particle/electrolyte interphase that is governed by Butler-Volmer equation. The P2D model governing equations and the corresponding boundary conditions are

adopted from [109,142] for the system shown in Figure 4-1 and are presented in Table 5-1. Finally, the operating voltage of the LFP half-cell is calculated according to the Equation (5-1).

$$V_{cell} = \phi_s|_{x=L} - \phi_f \tag{5-1}$$

Table 5-1: The governing equations and corresponding boundary conditions of the pseudo-two-dimensional model [109,142].

Particle-level governing equations	
Cathode active materials	Boundary conditions
$\frac{\partial c_{s,k}}{\partial t} = \frac{1}{r_k^2}\frac{\partial}{\partial r_k}\left(r_k^2 \alpha_k \mathcal{D}\frac{\partial c_{s,k}}{\partial r_k}\right)$ $\alpha_k = -\frac{F}{RT} y_k(1-y_k)\frac{\partial U_k}{\partial y_k}$, $y_k = c_{s,k}/c_s^{max}$ $i_{n,k} = i_k^0\left[\exp\left(\frac{(1-\beta)F}{RT}\eta_k\right) - \exp\left(\frac{-\beta F}{RT}\eta_k\right)\right]$ $\eta_k = \phi_s - \phi_e - U_k$, $i_k^0 = F k_c^0 {c_e}^{1-\beta} c_s^{max}(1-y_k)^{1-\beta} y_k^{\beta}$	$\frac{\partial c_{s,k}}{\partial r_k}|_{r_k=0} = 0$ $\alpha_k \mathcal{D}\frac{\partial c_{s,k}}{\partial r_k}|_{r_k=R_{p,k}} = \frac{i_{n,k}}{F}$ $c_{s,k}|_{t=0} = c_{s,k}^0$
Electrode-level governing equations	
Cathode	Boundary conditions
$\nabla.\left(\sigma_c^{eff}\nabla\phi_s\right) = \sum a_k i_{n,k}$ $\sigma_c^{eff} = \sigma_c(1-\varepsilon_c)^{\gamma}$ $\nabla.\left(-\kappa_c^{eff}\nabla\phi_e\right) + \nabla.\left(\kappa_{D,c}^{eff}\nabla\ln c_e\right) = \sum a_k i_{n,k}$ $\kappa_c^{eff} = \kappa_c\varepsilon_c^{\gamma}$, $\kappa_{D,c}^{eff} = \frac{2RT\kappa_c^{eff}}{F}(1-t_+^0)\left(1+\frac{d\ln f_{\pm}}{d\ln c_e}\right)$ $\frac{\partial(\varepsilon_c c_e)}{\partial t} = \nabla.\left(D_{e,c}^{eff}\nabla c_e\right) + \frac{1-t_+^0}{F}\sum a_k i_{n,k}$ $D_{e,c}^{eff} = D_e\varepsilon_c^{\gamma}$	$\sigma_c^{eff}\nabla\phi_s|_{x=L_s} = 0$ $\sigma_c^{eff}\nabla\phi_s|_{x=L} = j_n$ $\kappa_c^{eff}\nabla\phi_e|_{x=L} = 0$ continuity at $x = L_s$ $D_{e,c}^{eff}\nabla c_e|_{x=L} = 0$ continuity at $x = L_s$ $c_e|_{t=0} = c_e^0$
Separator	Boundary conditions
$\nabla.\left(-\kappa_s^{eff}\nabla\phi_e\right) + \nabla.\left(\kappa_{D,s}^{eff}\nabla\ln c_e\right) = 0$ $\kappa_s^{eff} = \kappa_s\varepsilon_s^{\gamma}$, $\kappa_{D,s}^{eff} = \frac{2RT\kappa_s^{eff}}{F}(1-t_+^0)\left(1+\frac{d\ln f_{\pm}}{d\ln c_e}\right)$ $\frac{\partial(\varepsilon_s c_e)}{\partial t} = \nabla.\left(D_{e,s}^{eff}\nabla c_e\right)$ $D_{e,s}^{eff} = D_e\varepsilon_s^{\gamma}$	$\phi_e|_{x=0} = 0$ continuity at $x = L_s$ $D_{e,s}^{eff}\frac{\partial c_e}{\partial x}|_{x=0} = -\frac{j_n(1-t_+^0)}{F}$ continuity at $x = L_s$ $c_e|_{t=0} = c_e^0$
Lithium foil electrode	
$j_n = i_f^0 {c_e}^{1-\beta_{Li}}\left[\exp\left(\frac{(1-\beta_{Li})F}{RT}(\phi_f-\phi_e)\right) - \exp\left(\frac{\beta_{Li}F}{RT}(\phi_f-\phi_e)\right)\right]$, $i_f^0 = F\varepsilon_s k_{Li}^0$	

5.2.2 Simplified Electrochemical Multi-Particle Model

The simplified electrochemical multi-particle (SEMP) model is developed in Chapter 4. However, the main equations and the solution procedure are reviewed here. In the SEMP model, the solid-phase potential gradient across the cathode is not considered as a result of the high electrical conductivity of the solid-phase. In SEMP model the potential drop inside the electrolyte is taken into

the account calculated by approximating the electrolyte concentration and potential distributions using the polynomial equations. The time-dependent polynomial coefficients are calculated using a number of ordinary differential equations (ODE) shown in Table 5-2. The particle-level equations shown in Table 5-1 are solved using the calculated potential drop in the electrolyte. Finally, the cell potential is determined by

$$V_{cell} = \phi_{s,c} - \phi_f \tag{5-2}$$

where $\phi_{s,c}$ is the averaged solid-phase potential across the cathode and ϕ_f is the lithium foil potential.

Table 5-2: Summary of the polynomial approximation of the electrolyte concentration and potential [89].

Electrolyte polynomial distributions	
Electrolyte concentration	Polynomial coefficient equations
$c_e(x_s,t) = p_1(t)x_s^2 + p_2(t)x_s + p_3(t)$ $0 \le x_s = \frac{x}{L_s} \le 1$	$p_2 = -\frac{j_n(1-t_+^0)L_s}{FD_{e,s}^{eff}}(1-\exp(-Mt))$ $3q_1 + 2q_2 + q_3 = 0$ $p_1 + p_2 + p_3 = q_4$ $\frac{D_{e,s}^{eff}}{L_s}(2p_1 + q_1) = \frac{D_{e,c}^{eff}}{L_c}q_3$ $\frac{1}{3}\frac{dp_1}{dt} + \frac{1}{2}\frac{dp_2}{dt} + \frac{dp_3}{dt} = \frac{2D_{e,s}^{eff}}{\varepsilon_s L_s^2}p_1$
$c_e(x_c,t) = q_1(t)x_c^3 + q_2(t)x_c^2 + q_3(t)x_c + q_4(t)$ $0 \le x_c = \frac{(x-L_s)}{L_c} \le 1$	$\frac{1}{4}\frac{dq_1}{dt} + \frac{1}{3}\frac{dq_2}{dt} + \frac{1}{2}\frac{dq_3}{dt} + \frac{dq_4}{dt} = -\frac{D_{e,c}^{eff}}{\varepsilon_c L_c^2}q_3 - \frac{1-t_+^0}{\varepsilon_c F}\frac{j_n}{L_c}$ $x_{c,a}^3\frac{dq_2}{dt} + x_{c,a}^2\frac{dq_2}{dt} + x_{c,a}\frac{dq_3}{dt} + \frac{dq_4}{dt} = \frac{D_{e,c}^{eff}}{\varepsilon_c L_c^2}(6q_1x_{c,a} + 2q_2) + \frac{(1-t_+^0)}{\varepsilon_c F}\sum a_k i_{n,k}\,|_{x_c=x_{c,a}}$ $p_1(0) = p_2(0) = q_1(0) = q_2(0) = q_3(0) = 0$ $p_3(0) = q_4(0) = c_e^0$
Electrolyte potential	**Polynomial coefficient equations**
$\phi_e(x_s,t) = \frac{2RT(1-t_+^0)}{F}\ln\frac{p_1x_s^2 + p_2x_s + p_3}{p_3}\left(\frac{\kappa_c^{eff}L_s}{\kappa_s^{eff}L_c}s_3 - \frac{2RT(1-t_+^0)}{F}\frac{2p_1+p_2}{p_1+p_2+p_3}\right)$ $0 \le x_s = \frac{x}{L_s} \le 1$	$3s_1 + 2s_2 + s_3 = 0$ $s_4 = \frac{2RT(1-t_+^0)}{F}\ln\frac{p_1+p_2+p_3}{p_3} + \frac{\kappa_c^{eff}L_s}{\kappa_s^{eff}L_c}s_3 - \frac{2RT(1-t_+^0)}{F}\frac{2p_1+p_2}{p_1+p_2+p_3}$ $s_3 - \frac{2RT(1-t_+^0)}{F}\frac{q_3}{q_4} = -\frac{j_n\square_c}{\kappa_c^{eff}}$
$\phi_e(x_c,t) = s_1(t)x_c^3 + s_2(t)x_c^2 + s_3(t)x_c + s_4(t)$ $0 \le x_c = \frac{(x-L_s)}{L_c} \le 1$	$-(6s_1x_{c,a} + 2s_2) + \frac{2RT(1-t_+^0)}{F}(\nabla\ln c_e)|_{x_c=0} = \frac{L_c^2}{\kappa_c^{eff}}\sum a_k i_{n,k}\,|_{x_c=x_{c,a}}$

5.2.3 Homogeneous Pseudo Two-Dimensional Model

The last model presented in this thesis is similar to the main Newman P2D model, but it includes the additional assumption of the homogenous electrochemical reaction across the cathode; thus, this model is named homogeneous pseudo-two-dimensional (HP2D) model. The idea behind developing this model is to somehow disconnect the electrode- and particle-level equations across the electrode since the main computational effort of the P2D model arises from this connection. When the electrochemical reaction rate is constant across the electrode, the particle-level equations are not solved at each mesh point across the electrode. Therefore, they are solved only once, which significantly reduces the computational costs. This simplification (with four particle groups for the cathode) is depicted in Figure 5-2. The governing equations of the HP2D model are the same as the P2D model (Table 5-1), but the electrode-level equations are modified according to Table 5-3. As it is observed in Table 5-3, the electrochemical reaction is appeared as a known constant source term on the right-hand-side of all the equations. The operating voltage of the half-cell is also calculated based on Equation (5-1). This model can again be thought as an extension to the SP model that considers the effect of electrolyte. However, the electrode domain governing equations are solved completely here that enables the model to predict the operating voltage of the half-cell even at high-discharge rates.

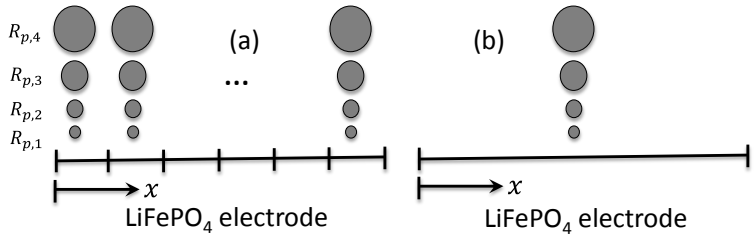

Figure 5-2: Comparison of the particle groups needed for (a) the P2D and (b) the HP2D models.

To show the computational efficiency of the HP2D model compared to the P2D model, the number of involved equations for each model is counted here. If the cathode thickness is divided into 10 elements and *N* particle sizes considered for the LFP each discretized into 20 elements [89,109], the total number of $51 + 210 \times \mathrm{N}$ equations would be required for the P2D model. Among these equations, $2 \times 2 \times 10 + 10$ equations calculate the electrode-level variable distributions across the

separator and cathode, 1 equation governs the lithium foil reaction while $10 \times \mathrm{N}$ equations accounts for the electrochemical reactions at the surface of cathode particles, and $10 \times \mathrm{N} \times 20$ equations solve the conservation of mass inside the particles at each element across the cathode. The HP2D model, however, requires only the total number of $51 + 21 \times \mathrm{N}$ equations since it needs to solve particle-level equations only once for each particle group. As a result, if four particle groups are considered for the cathode, the P2D model solves 891 equations while the HP2D model has 135 equations. It is seen that the number of required equations are reduced by a factor of 6.6 for each time step in the HP2D model. This factor can even be increased if more particles or elements are employed for the battery simulations. In addition, the required number of equations for the SEMP model is reported $12 + 42 \times \mathrm{N}$ in Ref. [89]. By using the same four particle groups, 180 equations are incorporated for the SEMP model. It is seen that the HP2D is computationally the most efficient model among these three models.

Table 5-3: Electrode-level governing equations across the cathode for the HP2D model.

Cathode governing equations	Boundary conditions
$\nabla.\left(\sigma_c^{eff}\nabla\phi_s\right) = \frac{I_{app}}{L_c}$	$\sigma_c^{eff}\nabla\phi_s\vert_{x=L_s} = 0$
$\sigma_c^{eff} = \sigma_c(1-\varepsilon_c)^{\gamma}$	$\sigma_c^{eff}\nabla\phi_s\vert_{x=L} = I_{app}$
$\nabla.\left(-\kappa_c^{eff}\nabla\phi_e\right) + \nabla.\left(\kappa_{D,c}^{eff}\nabla\ln c_e\right) = \frac{I_{app}}{L_c}$	$k_c^{eff}\nabla\phi_e\vert_{x=L} = 0$
$\kappa_c^{eff} = \kappa_c\varepsilon_c^{\gamma},\ \kappa_{D,c}^{eff} = \frac{2RT\kappa_c^{eff}}{F}(1-t_+^0)\left(1+\frac{\partial\ln f_{\pm}}{\partial\ln c_e}\right)$	continuity at $x = L_s$
$\frac{\partial(\varepsilon_c c_e)}{\partial t} = \nabla.\left(D_{e,c}^{eff}\nabla c_e\right) + \frac{1-t_+^0}{F}\frac{I_{app}}{L_c}$	$D_{e,c}^{eff}\nabla c_e\vert_{x=L} = 0$
	continuity at $x = L_s$
$D_{e,c}^{eff} = D_e\varepsilon_c^{\gamma}$	$c_e\vert_{t=0} = c_e^0$

5.3 Three-Dimensional Modeling

In this section, the SEMP and HP2D models developed for coin-cell-sized LFP half-cells are expanded to larger-sized LFP half-cells. Since three-dimensional simulations have to cover all the involved phenomena occurring in a wide range of length scales (from diffusion in nano particles to the electric current transfer in the current collector plates), their computation might become tremendously complicated and computationally intensive. Therefore, almost all simulations for larger batteries assume perpendicular current flow between current collectors [22,23,40–42,112,138,143–146]. They actually consider the electric current is distributed two-dimensionally on

the current collectors and crosses the inside layers of the battery perpendicular to the current collectors' plane. This assumption seems to be reasonable by noticing the following: the current collectors of LIBs are orders of magnitude more conductive than other battery layers (anode, separator, and cathode), and the length and height of a typical full-sized pouch configuration battery is also orders of magnitude larger than its thickness. According to the above assumption, Figure 5-3 illustrates the described current distribution in a battery cell. It should be noted that the lithium foil acts simultaneously as the source of lithium and the negative current collector in the half-cell, as illustrated in Figure 5-3.

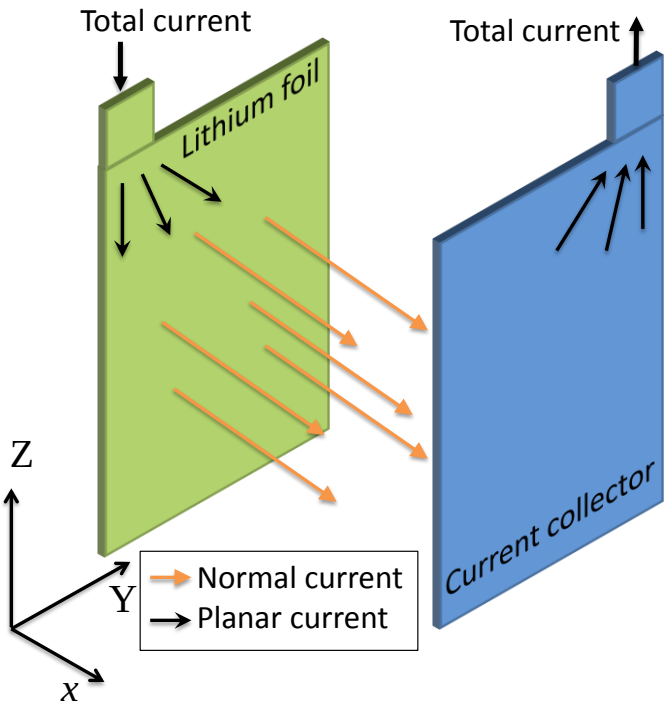

Figure 5-3: Schematic of the current flow between the lithium foil and the current collector in a large-sized LFP half-cell, the orange arrows show the normal current to the collectors and the black arrows show the current in the collectors' plane.

5.3.1 Three-Dimensional SEMP Model

The electrical current distribution shown in Figure 5-3 suggests that the large-sized LFP half-cell might be treated as a combination of one-dimensional half-cells placed between two current

collectors. In this approach, there is no direct interaction between one-dimensional half-cells. Instead, they interact through their effect on the normal current distribution in the large-sized LFP half-cell. Therefore, the large-sized battery is divided into two domains: one-dimensional electrode domain and two-dimensional current collector domain, whose relation is shown in Figure 5-4. In this figure, for the sake of the illustration, the region between the current collectors is divided into six one-dimensional electrode domains. However, in the actual model many more domains are incorporated. The governing equations for one-dimensional half-cells apply to the electrode domains, while the charge conservation equation applies to the current collector domain. These domains are then coupled by interchanging the necessary variables. The detail of the equations and their coupling approach are explained in the following.

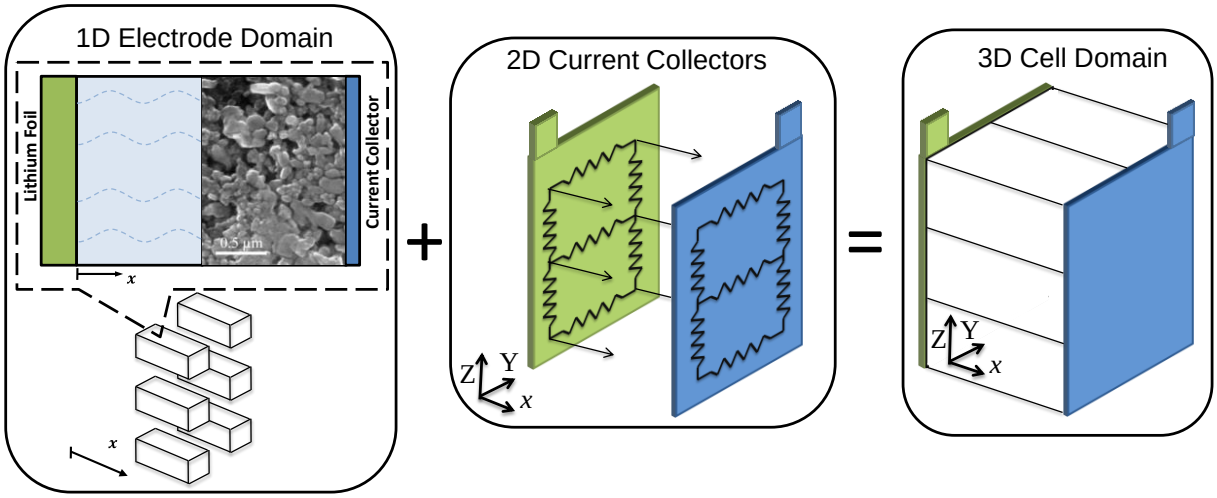

Figure 5-4: Schematic of the electrode and cell domains of a $LiFePO_4$ half-cell battery and their relation.

For the electrode domain, any one-dimensional LIB model can be incorporated; that is, all the described models in Section 5.2 or even simple equivalent-electric-circuit models [45,46,147] are acceptable. However, to keep the model simple and at the same time including required battery information, the one-dimensional SEMP model is chosen. This model, which has already been discussed, accurately predicts the operating voltage of the cell even at high discharge rates. It should be noted that both the P2D and HP2D models, apart from their required computational time, lead to the same results as the SEMP model since all these models predict the output voltage of the LFP half-cell almost with the same accuracy. The inputs of the SEMP model are the applied current, the

physical properties of the half-cell, and the initial condition for the required electrochemical variables. The physical properties of the half-cell are obtained from the literature and are given in Appendix A. The applied current is entered from the current collector domain calculations and the electrochemical variables are obtained from the last time step values or initial conditions. In addition, the output of SEMP models is either the voltage-current relationship of the half-cell or the new state for all electrochemical variables.

The applied model to the current collector domain is simply a charge conservation equation formulated as follows:

$$\sigma_i \frac{\partial^2 \Phi_i}{\partial Y^2} + \sigma_i \frac{\partial^2 \Phi_i}{\partial Z^2} = \frac{j_n}{L_i}, \qquad i = foil, PCC \tag{5-3}$$

where σ is the conductivity of the current collectors, Φ is the potential of the current collectors, L is the thickness of the current collectors, Y and Z are the coordinate system axes and j_n is the normal current density flows between the current collectors shown in Figure 5-3. The subscript i is also stands for the lithium foil (negative current collector) or positive current collector. It should be noted that other researchers have also been incorporate similar models [22,23,138]. However, each model shows some variations on how it interacts with the electrode domain model. The strength of the algorithm presented here, compared to the other approaches, lies in coupling the electrode and current collector models implicitly, but with the minimum computational cost.

Equation (5-3) is discretized and applied to both current collectors. By knowing the conductivity and geometry of the current collectors, the only unknown in this equation, except the potential distribution on both current collectors that the equation is solved for, is the normal current density distribution between current collectors. The model presented here is not explicit; thus, one does not substitute this value from the previous time step. Instead, a linear relation replaces the normal current density between the current collectors as follows:

$$\sigma_i \frac{\partial^2 \Phi_i}{\partial Y^2} + \sigma_i \frac{\partial^2 \Phi_i}{\partial Z^2} = \frac{a\,\nabla\Phi_{hf} + b}{L_i}, \qquad i = foil, pcc \tag{5-4}$$

where $\nabla\Phi_{hf}$ is the operating voltage of the half-cell defined as $\nabla\Phi_{hf} = \Phi_{pcc} - \Phi_f$, and a and b are the constants of the linear relation. These constants are functions of time and space (Y and Z); thus, have to be calculated at each time step and for each one-dimensional model between the current collectors. To obtain these constants, in each time step, the one-dimensional model is solved twice for each one-dimensional electrode domain. The inputs for this twice solution of one-dimensional models are normal current densities obtained in the last time step and a current density close to that value. The outputs are then two potential variations across one-dimensional electrodes corresponding to two input current densities. A linear relation between the normal current density and the potential variation is then obtained for each one-dimensional electrode between the current collectors. These relations, actually, show the behaviour of the LFP half-cell and are applied to all nodes of the current collectors. Figure 5-5, for instance, shows the linear current-voltage relation for one of the one-dimensional models as a function of time. As it is observed in this figure, both the slope and y-intercept vary during the time. It must also be noted that the normal current flow of one node on the lithium foil equals the negative of that value for the corresponding node on the positive current collector.

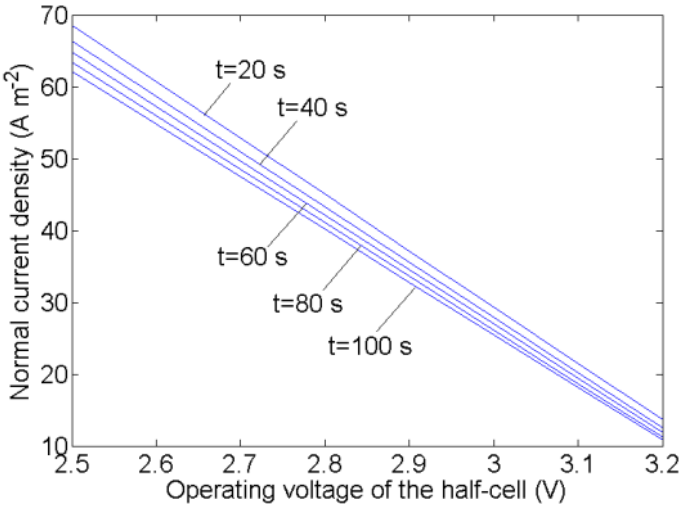

Figure 5-5: Current-voltage relations for a node on the current collectors obtained from the SEMP one-dimensional model during the initial period of 5C discharge rate at 25˚C.

The boundary conditions of Equation (5-4) are zero reference potential at the lithium foil tab and Equation (5-5) at the positive current collector tab:

$$n \cdot (-\sigma_{PCC} \nabla \Phi_{PCC}) = I_{app,PT} \quad (5\text{-}5)$$

where n is the unit vector pointing outward, σ_{PCC} is the conductivity of the positive current collector, $\nabla \Phi_{pcc}$ is the potential gradient on the tab, and $I_{app,PT}$ is the applied outward current density based on the cross section at the top of the positive tab. It is assumed that the applied current density is uniform on the cross section of the positive tab. Note that the no flux condition is applied to the rest of current collector boundaries. Once the conservation of the charge is solved for all the nodes on the lithium foil and the positive current collector, the obtained potential distributions are utilized to calculate the planar and normal current density distributions in the large-sized half-cell (Figure 5-3). The normal current densities are, then, used as the input for one-dimensional SEMP models to calculate the new values for the electrochemical variables. This process is repeated until the output voltage of the half-cell falls below a lower cut-off voltage (2.5 V here). To make the three-dimensional solution procedure more clear, the incorporated algorithm is summarized in Figure 5-6.

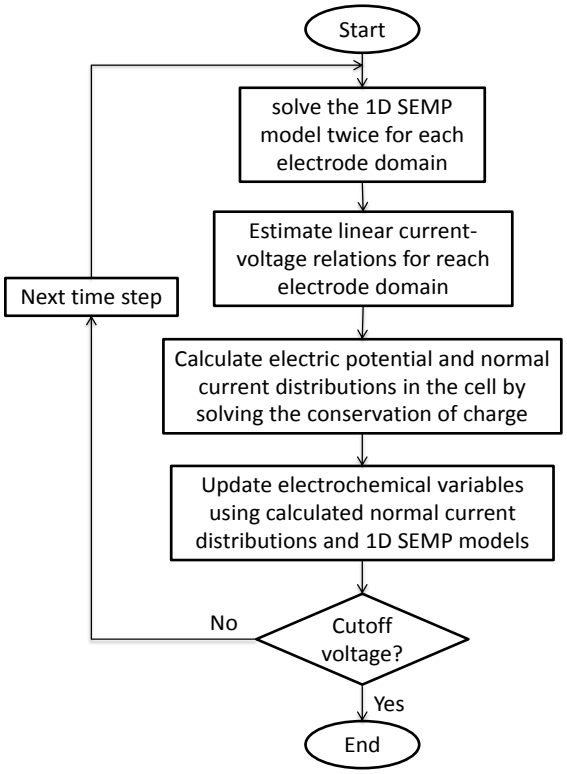

Figure 5-6: Schematic diagram showing the overall solution procedure for the three-dimensional SEMP model.

5.3.2 Three-Dimensional HP2D Model

In Section 5.3.1, based on the one-dimensional SEMP model, a three-dimensional model was developed for large-sized LFP half-cells (i.e. a size consistent with automotive pattern pouch cells). The incorporation of one-dimensional models, however, results in ignoring the diffusion in directions parallel to the current collector plane. This simplification seems to be reasonable for the solid-phase wherein the connection between the particles is weak. However, ignoring the diffusion might not be suitable for the continuous electrolyte phase. Therefore, another three-dimensional method that considers the electrolyte as a continuous phase is developed. It is, therefore, an expansion to the three-dimensional SEMP model and it provides the required tool to assess the validity of ignoring electrolyte diffusion in directions parallel to the current collector planes.

As explained in Section 5.2.3, the homogenous-electrochemical-reaction assumption of the HP2D model allows electrolyte and solid-phase equations to be solved separately. When the HP2D model is expanded to the three dimensions, this feature empowers the model to easily solve the governing equations in the electrolyte region three-dimensionally. Furthermore, since the electrolyte potential is solved three-dimensionally, the assumption of the fully perpendicular current between the current collectors is not valid anymore. Instead, the three-dimensional HP2D model allows the current flows in any pattern in the electrolyte region. However, it still has to flow one-dimensionally in the solid-phase, which is a reasonable assumption noticing the fact that the conductivity of solid-phase is orders of magnitude lower than the positive current collector (aluminum). In addition, the amount of the electrical current entering the electrolyte from one point on the lithium foil leaves the cell cathode material from the corresponding point on the positive current collector. In other words, the same normal current density is applied on the same locations of the current collectors.

Perceiving the above discussions, the electrochemical simulation in the region between two current collectors can be explained as follows. First, conservation of mass and charge equations in the electrolyte (Table 5-1 and Table 5-3) are solved three-dimensionally. The no-flux condition is applied to all the boundaries normal to the Y and Z axes (Figure 5-3). The appropriate conditions on boundaries normal to x axis are also mentioned in Table 5-1 and Table 5-3. The upper-right-hand-

side of the electrolyte domain (in connection with the lithium foil tab) is considered as the reference potential. Then, the three-dimensional solutions of potential and lithium ion concentration in the electrolyte are fed to the rest of one-dimensional HP2D equations to calculate the other electrochemical variables as well as the potential variations between the current collectors. Therefore, in three-dimensional HP2D model, a combination of one-dimensional and three-dimensional solutions is incorporated, instead of purely one-dimensional approach of the method in Section 5.3.1.

Since the same normal current densities are assumed on the current collectors, the linear current-voltage relations can still connect the corresponding nodes on the current collectors. To obtain these linear relations, similar to the three-dimensional simplified electrochemical multi-particle (SEMP) model, the electrochemical equations are solved twice utilizing appropriate normal current density distributions on the current collectors. Again, a linear relation is fit to the input normal current densities and output voltage gradients to describe the behaviour of the LFP half-cell. The conservation of the charge equation is then applied to the both current collectors. Similar to the three-dimensional SEMP model, the obtained potential distribution on both current collectors is used to calculate their planar and normal current densities. Finally, the current collectors' normal current densities are incorporated to update the electrochemical variables. In this step, again, a combination of three-dimensional and one-dimensional calculations is followed. To better understand the three-dimensional HP2D model, the different steps of this model are summarized in Figure 5-7.

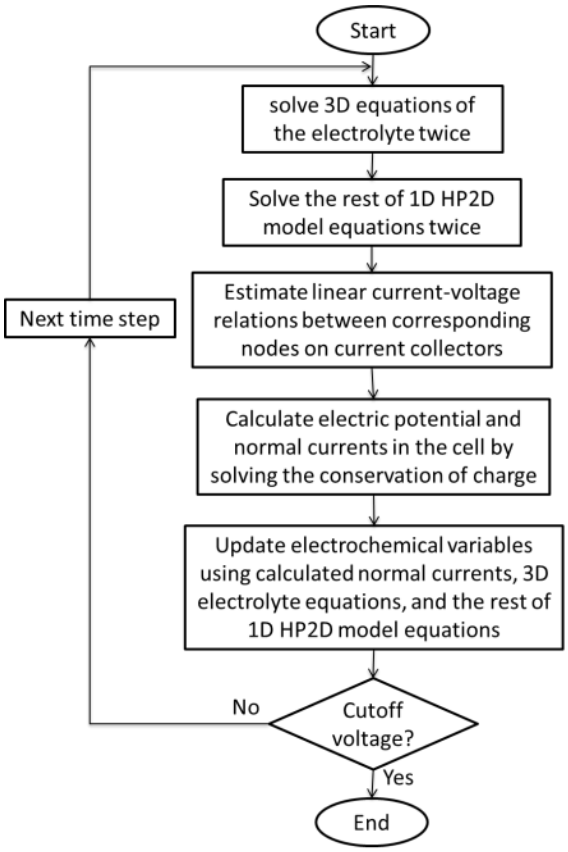

Figure 5-7: Schematic diagram showing the overall solution procedure for the three-dimensional HP2D model.

5.4 Results

In this section, the results of all previously explained models are presented. Since the results of P2D (full-order) and SEMP models are given in Chapter 4, the results of only HP2D model is validated against the experimental data in Section 5.4.1. Moreover, in Section 5.4.2 the results of the three-dimensional models are shown.

5.4.1 One-Dimensional Model Results

As explained in Chapter 4, the required physical parameters for the models are obtained from [89,109] and are listed in Appendix A. Again, one-dimensional simulations are performed using COSMOL Multiphysics software [126]. The particles are discretized according to the method

explained in Section 4.2.3. For the case of P2D and HP2D models, which needs discretization of the separator and cathode, 10 elements in each region is considered. Figure 5-8(a) shows the results of the HP2D model together with the results of the P2D model. It is seen that the HP2D model fits well with the P2D model simulations. The relative error defined as $abs(V_{HP2D} - V_{P2D})/V_{P2D} \times 100$ is also used to quantify the introduced error by using the simplified HP2D model. As it is shown in Figure 5-8(b), the maximum error of this model is less than 1.5% for all discharge rates, lower than relative error of the SEMP model. Furthermore, the regions with higher relative error are limited to the end-of-discharge regions with maximum relative error happening at the end of the discharge cycle (except for the C/25 rate). Therefore, for most of the discharge period, the prediction error is negligible; hence, the HP2D model that is both accurate and computationally efficient is considered as the best model here.

In order to confirm the computationally efficiency of the HP2D and SEMP models compared to P2D model, Table 5-4 indicates the computational time of each model for C/2 and 5C discharge rates. The same grid and the same numerical methods are used for the all simulations. As it is seen, the computational time of the HP2D model is almost one order of magnitude less than the computational time of the P2D model and is the least between all the one-dimensional models. In addition, the SEMP model is more efficient than the P2D model, but a little less efficient than the HP2D model. This observation is in agreement with our discussion about the number of involved equations for each model in section 5.2.3. According to these results, it is also concluded when SEMP and HP2D models are expanded to three dimensions, they can keep their advantage regarding the computational efficiency. In addition, since many numbers of one-dimensional models are used for three-dimensional simulations, the improvement compared to the P2D model is very significant.

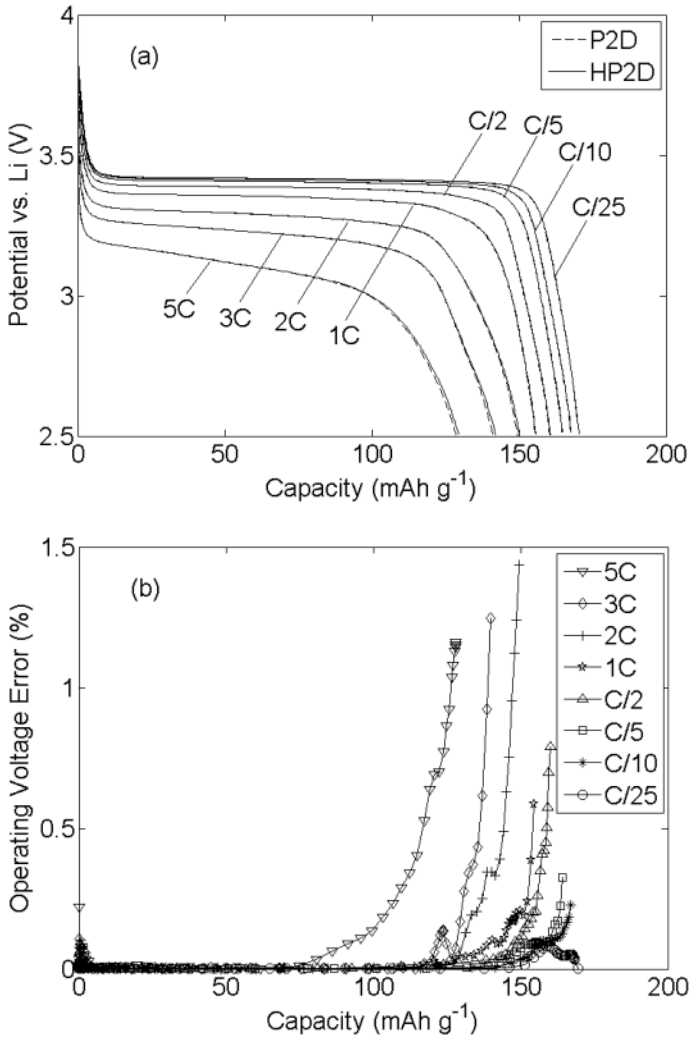

Figure 5-8: (a) Comparison between the HP2D model (solid lines) and the P2D model (dashed lines) simulations, and (b) the relative error of the HP2D model with respect to the P2D model, in various discharge rates (from C/25 to 5C) and at room temperature (25 ºC).

Table 5-4: Comparison between the computational time of different one-dimensional models of the LFP half-cell at room temperature (25 ºC).

Discharge rate	Computational time (s)		
	P2D Model	SEMP Model	HP2D Model
C/2	43	6	4
5C	44	8	5

5.4.2 Three-Dimensional Model Results

In this section, the simulation results of a full-sized LFP half-cell are presented. Two three-dimensional models are incorporated for these simulations: three-dimensional SEMP model and three-dimensional HP2D model. The additional parameters for three-dimensional modeling are also given in Appendix A including the geometrical parameters and current collectors' electrical conductivities. It should be mentioned that the thicknesses of the current collectors are chosen to have the same electrical resistance in both current collectors. The tab locations are also depicted in Figure 5-3.

From the implementation point of view, both models are implemented using Fortran. The main reason for choosing Fortran is its speed and flexibility. In fact, the methods incorporated in this paper could not effectively be implemented in commercial software such as COMSOL Multiphysics. COMSOL would have the necessity of calling the one-dimensional model many times during each time-step leading to a very slow simulation for commercial software. In contrast, Fortran is very flexible and can economically manage such complexities. In addition, the developed Fortran code converges even faster than COMSOL model. For example, the developed Fortran code for the one-dimensional HP2D model converges in less than a second that is much better than the COMSOL model according to the results reported in Table 5-4. For all presented simulations, a grid containing 600 nodes on each current collector, 20 along the Y axis and 30 along the Z axis is utilized. It should be noted that this grid is finer than required and even coarser grids showed almost the same accuracy. The grid used for the one-dimensional models are also the same as the grid explained in Section 5.4.1.

The results of the three-dimensional SEMP model are shown in Figure 5-9. In this figure, the normal current density between the current collectors is presented for the beginning, middle, and end of discharge. The discharge rate is 5C and the battery temperature is 25 ºC. As can be observed, the selection of the same electrical resistance for the current collectors results in all three figures showing symmetric current distribution around the line passing through the middle points of the cell widths ($Y = 10$). In addition, at the beginning of the discharge, Figure 5-9(a), the normal current

density is much larger at locations close the tabs, which is in agreement with previous studies [22,23,40–42,112,138,144–146,148]. In this figure, the deviation between the maximum and minimum current densities defined as $(max(j_n) - min(j_n))/\, min(j_n) \times 100$ reaches to more than 13%. When all the points between the current collectors are at the same electrochemical state, the pathways with lower electrical resistance generate more current due to the negative slope of the current-voltage relation (Figure 5-5). After a period of discharge, since the materials closer to the tabs are more discharged, the current generation distribution becomes gradually more uniform which is clearly seen in Figure 5-9(b). In this figure, the deviation between maximum and minimum current densities is only 2.3%. At the end of discharge, the materials closer to the tabs are almost depleted; thus, most of the required current is generated in locations far from the tabs as shown in Figure 5-9(c). Finally, the deviation between the maximum and minimum normal current densities in Figure 5-9(c) is 10.3% with the minimum current densities at locations close to the tabs.

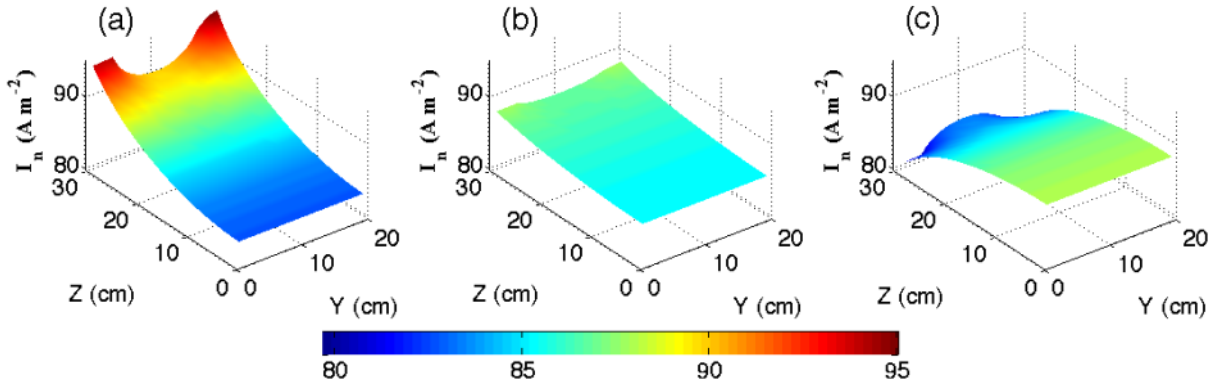

Figure 5-9: The distribution of the normal current density between the current collectors during the 5C discharge rate and at room temperature (25 ºC) for (a) start, (b) middle, and (c) end of the discharge using the three-dimensional SEMP model.

In Figure 5-10, the result of the three-dimensional HP2D model is presented for different stages of the discharge. In this figure, the normal current density distributions at the beginning, middle, and end of 5C discharge rate are shown respectively. The prediction of the three-dimensional HP2D model for the normal current density distribution is the same as three-dimensional SEMP model with the maximum deviation of almost 1% between two models. The similarity of the obtained results, first, confirms the accuracy of the two different three-dimensional models. Secondly, it suggests that

the perpendicular assumption employed in the three-dimensional SEMP model is a reasonable assumption. It can be concluded that the current flow between the current collectors, no matter of the effects of the continuous electrolyte phase, always follow a perpendicular direction. Therefore, if the three-dimensional simulation is only aimed at predicting the current distribution in the full-sized pouch configuration battery, those models that simplify the simulations with the perpendicular current assumption are still applicable.

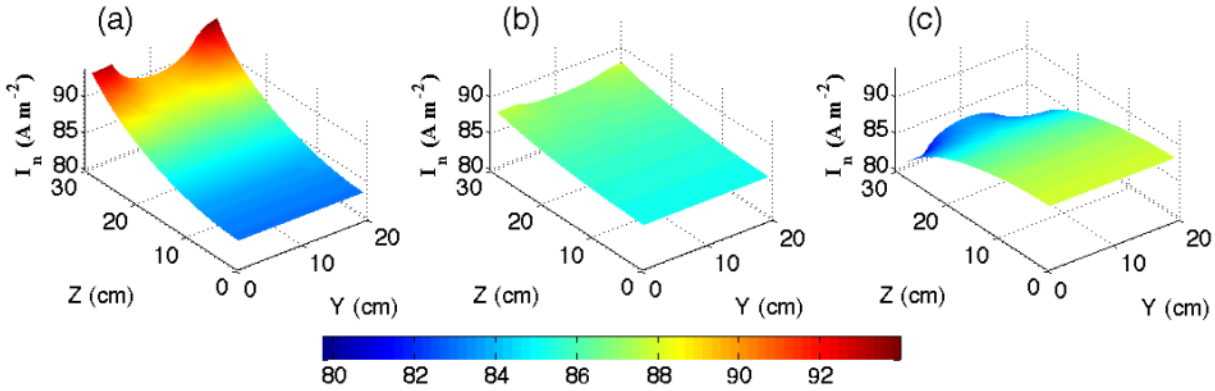

Figure 5-10: The distribution of the normal current density between the current collectors during the 5C discharge rate and at room temperature (25 ºC) for (a) start, (b) middle, and (c) end of the discharge using the three-dimensional HP2D model.

5.4.3 Thermal Modeling

The described three-dimensional models in Sections 5.4.1 and 5.4.2 can be utilized to study the temperature distribution in full-sized pouch configuration batteries. As explained in [52,54], one heat generation source is Joule heating that results from concentration and potential gradients inside the electrolyte. In the case of the three-dimensional SEMP model, since the electrolyte is treated as a combination of one-dimensional SEMP models, it cannot calculate the mentioned gradients along the *Y* and *Z* axes (Figure 5-3). In contrast, since the three-dimensional HP2D model simulates the electrolyte domain three-dimensionally, it can more effectively be used for thermal studies. Figure 5-11, for instance, shows the electrolyte potential obtained from the three-dimensional HP2D model at the separator/cathode interface during the 5C discharge rate at the beginning, middle, and end of the discharge. As it is seen, the electrolyte potential variation is noticeable, especially closer to the tabs, and taking this potential into account results in a better thermal model.

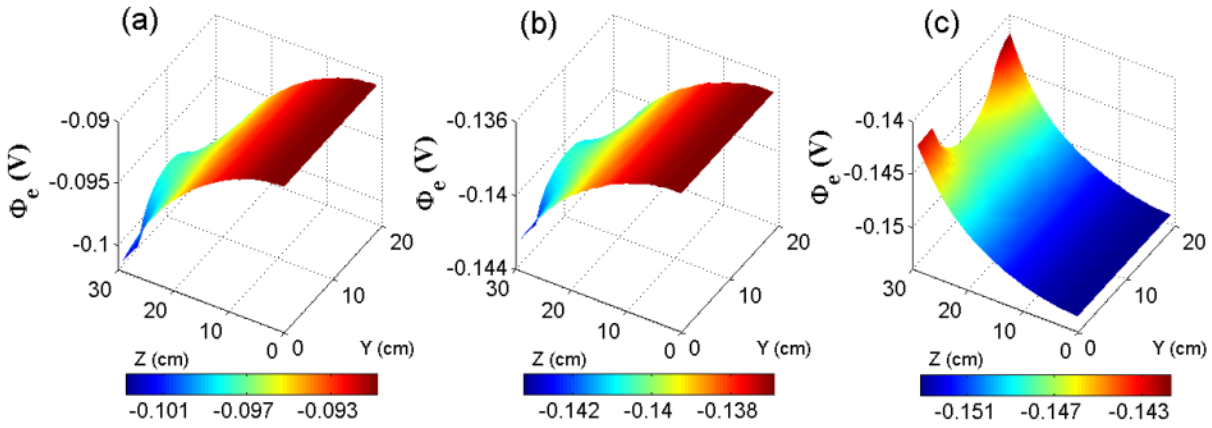

Figure 5-11: The distribution of the electrolyte potential at the separator/cathode interface during the 5C discharge rate and at room temperature (25 ºC) for (a) start, (b) middle, and (c) end of the discharge using the three-dimensional HP2D model.

In conclusion, since the simulation times of both three-dimensional approaches are almost the same, the HP2D model should be used for thermal modelling over the SEMP model given its ability to capture three-dimensional electrolyte effects. In addition, as explained, all the models presented in this chapter are for a LFP half-cell. However, they can easily be expanded to a full-cell battery by replacing the lithium foil with a current collector and an anode electrode (usually graphite). Expanding this work to full-cell batteries is in the next chapters.

Chapter 6 Improve the Battery Durability

The following section is based on previously submitted work by Mastali, M., Samadani, E., Farhad, S., Fraser, R., and Fowler, M.

SAE Technical Paper 2015-01-1182, 2015, doi: 10.4271/2015-01-1182 [130].

"**Three-Dimensional Electrochemical Analysis of a Graphite/$LiFePO_4$ Li-Ion Cell to Improve Its Durability**"

This thesis author specific contribution to this paper was to assist in experiment, develop the model, conduct the simulations, prepare all the graphics and results, prepare the final manuscript and reviewer edits with direction from the project supervisors who were co-authors. All authors reviewed the manuscript.

Reproduced with the permission from SAE.

6.1 Introduction

It is predicted that electric vehicles will form almost 60% of the passenger-car market by 2050 [149]. Increasing the life of LIBs to the average life of cars can significantly help this prediction come true. Thus, in addition to the research on new durable materials, research is needed on avoiding ageing of current commercial LIBs [150,151]. The objective of this chapter is to study the effect of certain geometric parameters such as tab location and current collector thickness on the durability of LIBs using the developed full-size battery model.

6.2 Results and Discussions

For the simulations presented in this chapter the required parameters are obtained from the literature. However, some parameters like geometrical parameters are estimated. The thickness of the anode is calculated by the cathode thickness and the reported ratio between the cathode and anode thicknesses in [106]. The initial stoichiometry and active material volume fraction of graphite are chosen for a

fresh battery [152]. The porosity of graphite is also estimated using this active material volume fraction and the volume of added filler reported in [153]. All these parameters are listed in Appendix A. Furthermore, the required thermodynamic factor of the cathode particles is also shown in Appendix A.

Wang et al. [135] argue that for a commercial graphite/$LiFePO_4$ cell, the cumulative charge delivered by the battery is the key parameter in its ageing. It is depicted in Figure 6-1 that the highest cell current is generated close to the tabs (Nodes 1 and 2) while the lowest electrochemical current is generated at the bottom of cell (Nodes 3 and 4). Therefore, the close-to-the-tab parts of the battery are more probable to be aged. This can also be reflected in the spatial distribution of ΔSOC (change in the state of charge during operation) in the cell. Locations closer to tabs have higher ΔSOC, and the farther locations show lower values for ΔSOC. It is reported in the literature that higher ΔSOC causes cathode degradation as well as SEI layer development resulting in higher degradation of the close-to-the-tab locations [136,137].

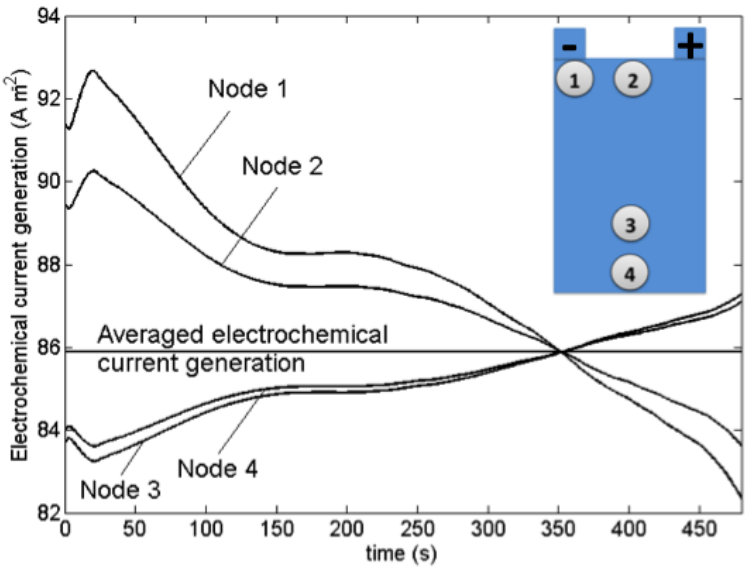

Figure 6-1: The electrochemical current generations at different locations of a cell during 5C discharge as a function of time.

It is also argued that higher C-rates result in a higher diffusion induced stress field in the active material [135,154]. The higher diffusion stress field also increases the rate of chemical reactions that

consume active lithium. Therefore, a non-uniform electrochemical process distribution results in the non-uniform ageing of the battery. According to Figure 6-1, again, the parts of the battery closer to the tabs are ageing more. In addition, the places with higher electrochemical reaction are prone to higher temperatures. It is reported that elevated temperatures accelerate the undesired side reactions such as SEI formation which permanently consume the cyclable lithium content of the battery [135,152,155]. The non-uniform electrochemical reactions in the cell lead to locally higher temperature in regions close to the tab that in turn yields higher degradation at those locations. In conclusion, having a more uniform distribution for electrochemical current generation not only improves performance, but also increases the durability of the cell.

To evaluate the effect of the current collectors' thickness on distribution of the electrochemical reaction, three other thicknesses for the negative and positive current collectors are considered. The results of the simulations at 5C discharge rate and 25 ºC are shown in Figure 6-2 and Figure 6-3 for the beginning and end of discharge, respectively. These figures illustrate as the current collector thickness decreases the non-uniformity in distribution of the electrochemical reaction increases. On the other hand, thickening the current collectors can easily suppress the non-uniformity in the electrochemical current generation. The maximum variation in this current generation is 14% observed in Figure 6-2(b) while the minimum is 3% in Figure 6-2(d). It should be noted that although making the current collectors thicker effectively levels off the distribution of the electrochemical current generation, it comes at the expense of increasing the battery weight and should be attempted cautiously.

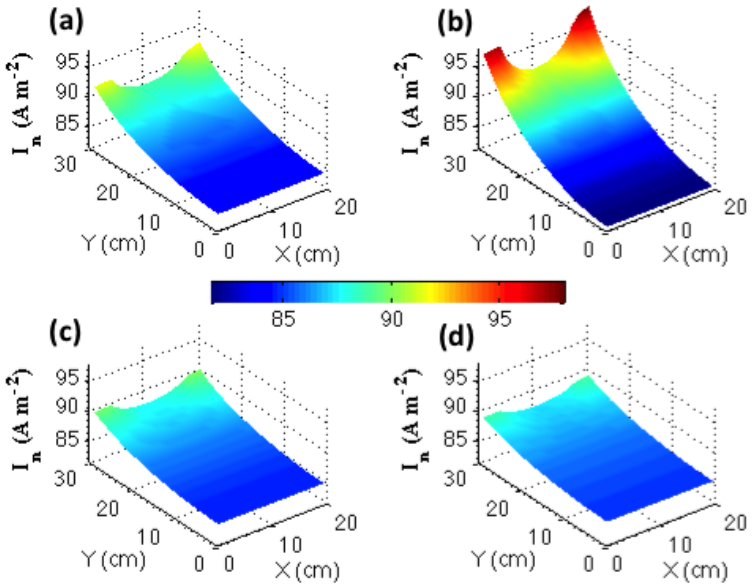

Figure 6-2: Distribution of the electrochemical current generation at the beginning of 5C discharge rate and 25 ºC for the negative and positive current collector's thicknesses of (a) 6.2 and 10 µm, (b) 3.1 and 5 µm, (c) 9.3 and 15 µm, and (d) 12.4 and 20 µm, respectively.

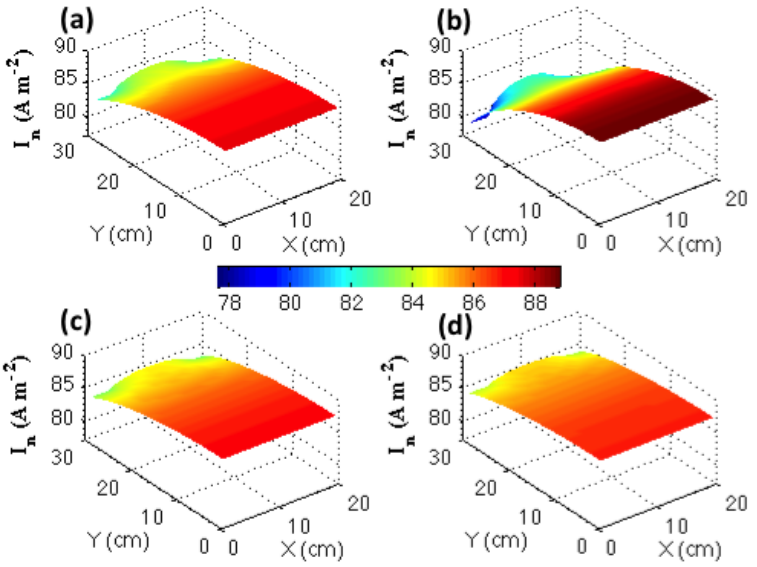

Figure 6-3: Distribution of the electrochemical current generation at the end of 5C discharge rate and 25 ºC for the negative and positive current collector's thicknesses of (a) 6.2 and 10 µm, (b) 3.1 and 5 µm, (c) 9.3 and 15 µm, and (d) 12.4 and 20 µm, respectively.

To study the effect of the battery tab location on distribution of the electrochemical current generation, four different configurations are considered. In the design (a), the original configuration

is considered while in the design (b) the width of battery tabs are doubled. One of the tabs is then moved to the other side of the cell to obtain the design (c) and finally in design (d) the tabs are moved to the middle and opposite side of the cell. Figure 6-4 illustrates the described configurations.

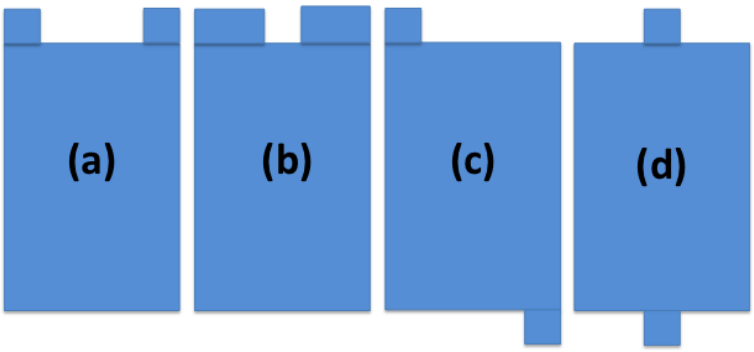

Figure 6-4: Different designs for the battery tab configurations: (a) original tab design, (b) extended tab design, (c) counter-side tab design, and (d) counter-middle tab design.

In Figure 6-5 and Figure 6-6, distribution of the electrochemical current generation in the Graphite/$LiFePO_4$ cell at 5C discharge rate and 25 ^oC for the beginning and end of discharge process is represented. As it is observed in these figures, extending the battery tabs can reduce the non-uniformity in distribution of the electrochemical reaction. However, since the maximum variation in current density is reduced from almost 10% for the original configuration to 8% for the extended tab design at beginning of discharge and from 7% to 6% at the end of discharge, this factor might not be understood as a very significant factor. Moving the positive current collector's tab to the other side of the cell, on the other hand, shows more impact on distribution of the electrochemical current generation. It reduces the maximum variation of the current generation to 6% at the beginning and to less than 5% at the end of discharge. Finally, it is observed that the configuration (d) in Figure 6-4 can significantly improve the uniformity of electrochemical reaction. This design decreases the maximum electrochemical current generation variation to 3% and 2% at the beginning and end of discharge, respectively. Therefore, one successful scenario to reduce the non-uniformities and increase the durability of the battery could be moving the tabs to the middle and opposite side of the cell and then extending them in the width of the cell as much as possible.

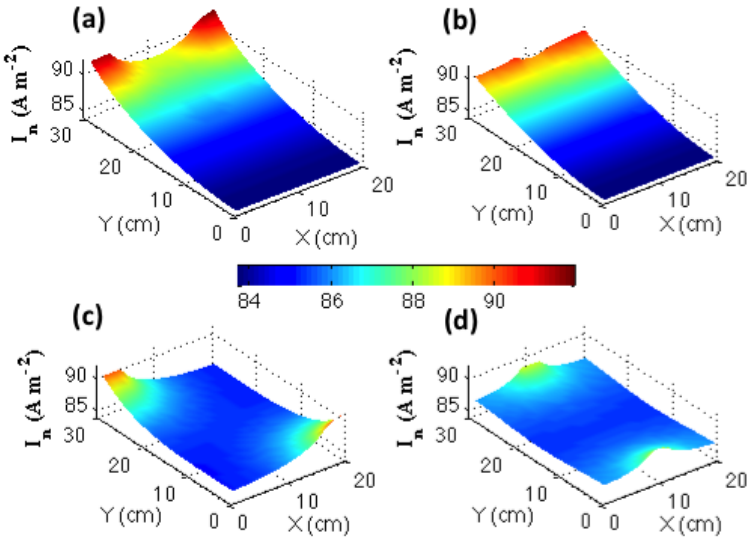

Figure 6-5: Distribution of the electrochemical current generation at the beginning of 5C discharge rate and 25 ºC for (a) original tab design, (b) extended tab design, (c) counter-side tab design, and (d) counter-middle tab design.

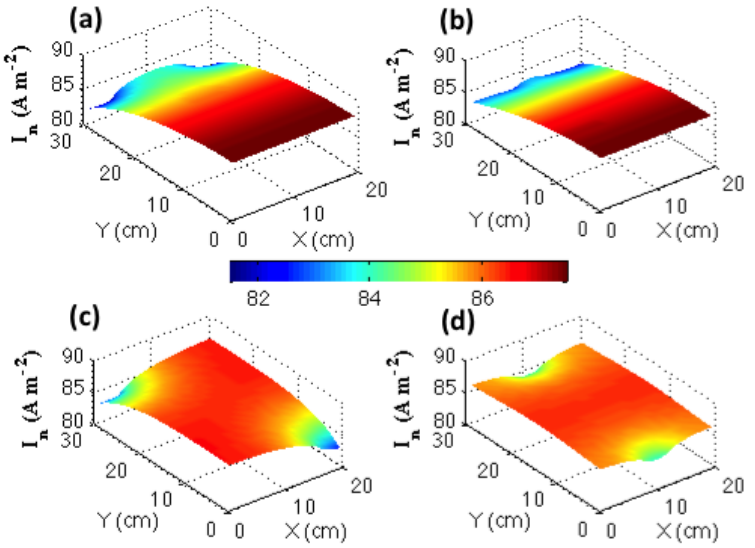

Figure 6-6: Distribution of the electrochemical current generation at the end of 5C discharge rate and 25 ºC for (a) original tab design, (b) extended tab design, (c) counter-side tab design, and (d) counter-middle tab design.

The results presented in this chapter are qualitatively in agreement with the results in [23], but much sever variations is observed here. This dissimilarity is mainly attributed to the difference between the current collector's thicknesses and also between the width and height of the employed

batteries in Ref. [23] and here. As describe in this section, the variation in the current collector's thickness can lead to even more than 10% variation in the electrochemical current generation. In addition, Figure 6 of Ref. [23] shows that increasing the size of the battery also worsen the current generation non-uniformities. Therefore, the more non-uniform electrochemical current generation of the battery studied in this paper may be explained by its narrower current collectors and also its larger width and height. In addition, it is explained in [23] that the steep changes in the open circuit potential helps to mitigate the non-uniformities. However, the cathode material of the battery in this paper ($LiFePO_4$) has a much smaller slope compared to $Li(NCA)O_2$, the cathode material in [23]. As a result, the battery studied here experiences more non-uniform profiles for electrochemical current generation. By comparing the results of this paper with the other papers, it is concluded that although the studied parameters improve the performance and durability of batteries, the exact amount of this improvement depends on many battery geometric and material properties and can be estimated in each case using careful examination/modeling.

Chapter 7 Parameter Characterization

The following section is based on previously submitted work by Mastali, M., Farkhondeh, M., Farhad, S., Fraser, R., and Fowler, M.

Journal of the Electrochemical Society (JESP-16-0494).

"**Electrochemical Modeling of Commercial $LiFePO_4$ and Graphite Electrodes: Kinetic and Transport Properties and Their Temperature Dependence**"

This thesis author specific contribution to this paper was to cooperate in material preparation, design and conduct the experiments, develop the models and conduct the simulations, prepare all the graphics and results, prepare the final manuscript and reviewer edits with direction from the project supervisors who were co-authors. All authors reviewed the manuscript.

7.1 Introduction

In addition to the $LiFePO_4$ (LFP) used as the positive electrode material (discussed in the previous chapters), graphite is the most commonly used negative electrode material in today's commercial Li-ion batteries due to its relatively high theoretical capacity (372 mAh g^{-1}), low equilibrium potential with respect to Li/Li^+, its higher safety compared to metallic lithium electrode, eco-friendliness, and low cost [156,157].

In the graphite particles, the lithiation/delithiation proceeds through multiple stages, each of which can be regarded as a distinct phase [158–162]. Various models have been reported for graphite electrodes. Most of these models ignore the phase transition process [53,163–165] while a few others account for these phase transitions via a modified form of Avrami equation [166], or the VSSD model [167–169]. It is shown in Ref. [167,168] that, similar to the case of a LFP electrode [108], the VSSD model can capture the moving phase boundary by considering the species chemical potential as the diffusion driving force within the graphite particles. However, the model for graphite has not been validated against experimental data in the referenced works. This paper addresses this

deficiency in the literature, and validates the VSSD model for graphite electrode by comparing simulations to galvanostatic charge/discharge voltage data at various charge/discharge rates and electrode temperatures.

A major concern for Li-ion battery models is the accuracy of physico-chemical model parameter estimates and their temperature dependency. In the case of LFP electrodes, few papers report the temperature dependency of the solid-state transport and kinetic properties [106,170–172]. In these papers, however, the estimation methods (e.g., electrochemical impedance spectroscopy and resistive-reactant model) rely on simplifying assumptions that may not be consistent with the end-use electrochemical models [106,170,171]. Furthermore, Ref. [50] does not provide any information regarding the parameter estimation approach used. Similar inconsistent assumptions, or lack of explanation issues also exists for the temperature dependency of graphite electrode transport and kinetic parameters [52,53,106,172–174]. In addition, in many cases, due to the lack of reliable data, parameters reported for similar but not identical negative electrode materials, such as petroleum coke [175] and graphitized carbonized cloth [176], are used in place of unknown graphite electrode parameters. In some works parameters are assumed for the temperature dependency for transport and kinetic parameters but in no way validated [177]. Lastly, in Ref. [178] the temperature dependency of graphite kinetic and transport properties is adjusted within a three-dimensional thermal model to fit experimental electrochemical/thermal data. However, the process used in Ref. [178] introduces uncertainties in parameter determination since it determines graphite parameters through fitting with a three-dimensional model, which has more degrees of freedom than a half-cell model.

The objective of this chapter is to expand determination of the transport and kinetic properties for graphite and LFP electrodes at different temperatures. A series of galvanostatic charge/discharge experiments are conducted on electrodes obtained from a commercial graphite/LFP pouch cell for a wide range of C-rates (C/5 to 5C) and temperatures (10 ºC, 23 ºC, 35 ºC, and 45 ºC). The performance of both electrodes is simulated using the VSSD model that enables the determination of transport and kinetic parameters through experimental data fitting. Having accurate temperature dependency for model parameters is crucial, especially for thermal and aging modeling of large Li-ion batteries and for the design of reliable battery management systems. The reported parameters

may be used for temperature conditions relevant to battery operation in applications such as electric or hybrid electric vehicles.

7.2 Experimental

The electrode materials used for making graphite and LFP half-cells are from a 20 Ah prismatic lithium-ion battery designed for electric vehicle applications. The prismatic cell is first discharged to 2.0 V at C/10 (constant current) and then held at 2.0 V (constant voltage) until the current response reaches the cut-off value of C/50. Afterwards, the cell is disassembled and cleansed several times using anhydrous dimethyl carbonate (DMC) in an argon-filled glove box (<1 ppm H_2O, <1 ppm O_2). Scanning electron microscopy (SEM) is performed utilizing a Zeiss ULTRA Plus electron microscope on both electrodes to extract the electrode thickness and particle sizes. A P-6 Stylus Profiler (KLA-Tencor, USA) is also used to confirm the electrode thickness. For the electrodes used for electrochemical tests, the coating on one side of the double-sided electrode laminate is carefully removed inside the glove box by means of a cotton-based wipe soaked in N-methyl-2-pyrrolidone (NMP). The graphite and LFP electrodes are then punched using 9.7 and 11.7 mm punchers, respectively. Two half-cells per electrode type (i.e., 2 replicates) are assembled in a CR2032-type coin cell with a 12.7 mm lithium metal disk as the reference/counter electrode and Celgard 2500 polypropylene membrane sheet as the separator between the working and reference/counter electrodes. A 1 mol L^{-1} solution of $LiPF_6$ in 1:1 volumetric mixture of ethylene carbonate (EC) and dimethyl carbonate is used as the electrolyte. In addition to the graphite and LFP half-cells, three Li/Li symmetric cells (i.e., 3 replicates) are also assembled inside the glove box to characterize the charge-transfer reaction at the surface lithium metal foil. For the sake of consistency, the same electrolyte, separator, and coin-cell setup are utilized for the symmetric Li/Li cell assembly.

The assembled coin cells are then tested in a Cincinnati Sub-Zero MCB-1.2 (USA) temperature chamber using a Neware CT-3008-5V10 mA-164-U (China) battery cycler. The Li/Li symmetric cells are cycled at 0.16 mA (10 hours in each direction), 0.32 mA (5 hours in each direction), and 0.8 mA (2 hours in each direction) at 23 °C, and 35 °C after being cycled five times at 0.8 mA (2 hours in each direction) at 23 °C (formation cycles). At 10 °C, the symmetric cells are cycled at

smaller rates of 0.054 mA (30 hours in each direction), 0.08 mA (20 hours in each direction), and 0.16 mA (10 hours in each direction) to assure the electrolyte losses remain negligible. The applied currents are chosen to be close to the values used to cycle the LFP and graphite electrodes assuring similar operating conditions. Before conducting the rate capability experiments, the Li/LFP and Li/graphite cells are cycled five times (formation cycles) at C/2 rate (1C rate is equivalent to 1.696 mA of applied current for the LFP and 1.242 mA for the graphite electrode) between the lower (2.5 V for LFP and 0.005 V for graphite) and upper (4.2 V for LFP and 1.5 V for graphite) cut-off potentials at 23 °C. In these cycles, the charge steps are followed by a constant voltage step until the current reaches C/50, while the discharge steps are followed by another constant current step at C/50 until the lower cut-off potential is reached. The rest periods between charge and discharge steps are set to 15 minutes. The rate capability tests are carried out at 4 different temperatures in the following order: 23 °C, 10 °C, 35 °C and 45 °C. The higher temperature tests are conducted last to minimize the influence of side reactions accelerated at high temperatures, which may impact measurements at other temperatures. At 23 °C, a series of galvanostatic charge/discharge cycles are conducted at rates C/5, C/2, 1C, 2C, 3C, and 5C, each of which consisting of the following steps: i) charging at a particular rate until the upper cut-off potential is reached, ii) 10-minute rest period, iii) charging at C/50 until the upper cut-off potential is reached again, iv) 1-hour rest period, v) discharging at the same rate as that in step i) until the lower cut-off potential is reached, vi) 10-min rest period, vii) discharging at C/50 until the lower cut-off potential is reached again, and viii) 1-hour rest period. Similar galvanostatic cycling but at one or two rates are conducted at other temperatures in the following sequence: i) C/5 (C/2 and 1C & 2C) charge at 10 °C (35 °C and 45 °C) until the upper cut-off potential is reached, ii) 1-hour rest period, iii) C/5 (C/2 and 1C & 2C) discharge at 10 °C (35 °C and 45 °C) until the lower cut-off potential is reached, iv) 1-hour rest period, v) soaking the cells thermally at 23 °C for 3 hours, vi) C/50 discharge at 23 °C until the lower cut-off potential is reached again. The latter step is to make sure the electrodes are reached the same fully discharged condition before the next cycle starts. It should also be noted that lower charge/discharge rates are applied at lower temperatures in order to: i) minimize lithium foil overpotential which is a source of error due to the complicated electroplating/stripping process at its surface not accounted for in the model, ii)

minimize electrolyte polarization for which accurate estimates of transport properties are not available, iii) minimize potential losses associated with the solid-electrolyte interphase (SEI) layer which is not accounted for in the model, and iv) assure the cell temperature is well controlled at the chamber temperature, i.e., sufficient heat dissipation from the cell. On the other hand, the applied current is increased for cycling at higher temperatures in order to guarantee discernible LFP (graphite) solid-state diffusion as well as charge-transfer reaction limitations. Altogether, these operating conditions assure an acceptable level of signal-to-noise ratio within the constraints posed by the model assumptions.

7.3 Results and Discussions

The experiment and simulation results are presented in this section. It should be mentioned that the simulations are performed using the one-dimensional model presented in Section 5.2.1. Three subsections dedicated to Li foil, LFP electrode, and graphite electrode are included here. The main purpose is to use mathematical models for the Li/LFP and Li/graphite half-cells to estimate the kinetic and transport properties of LFP and graphite and their temperature dependencies. To this end, the model is fitted to the experimental data, as is described later in this section. Active particle-size distributions (PSD) for the LFP and graphite electrodes are estimated by examining ~270 and ~330 particles counted across the SEM images, respectively. It is not required to incorporate the complete size distribution, rather, based on the operating voltage curves of the half-cells, a minimum number of particle bins representing the entire PSD is used without compensating for accuracy [108]. The minimum number of particle bins is determined by the overall error between simulation results and experimental data being 1% or less.

7.3.1 Li Foil Kinetics Temperature Dependency

Prior to the determination of the temperature dependency of the LFP and graphite lithiation/delithiation dynamics, it is required to determine the temperature dependency of charge-transfer kinetics at the surface of the metallic lithium reference/counter electrode in order to separate associated potential losses. As explained in Section 7.2, three different currents in each charge or

discharge direction (total of six) are applied to three Li/Li cell replicates maintained at three different temperatures and the voltage response of the cell to each applied current is recorded. The recorded potential differences are averaged to yield single values for each of the six measurements. It is assumed that both lithium electrodes in the symmetric cells contribute the same to the output potential difference; hence, to obtain the surface overpotential of each electrode, the averaged potential difference is divided by two. The Butler-Volmer relation is fitted to the experimental data using the Matlab's nonlinear least-square curve fitting routine 'lsqcurvefit' [179]. The charge-transfer coefficient is assumed to be 0.5 [26] and the gradient of electrolyte concentration and potential across the separator ($L_s = 25 \times 10^{-6}$ m) is neglected under the experimental conditions. Figure 7-1 shows both the averaged experimental data points and the fitted curves for all three temperatures. As seen, the fitted curves are almost linear in the current density range of consideration in this work. If the exponential function in the Butler-Volmer relation is estimated by the first term of its Taylor expansion about the zero lithium foil potential, the slope of fitted lines is $\frac{RT}{\beta_{Li}F^2\varepsilon_s k_{Li}^0 c_e^{1-\beta_{Li}}}$. The estimated rate constants of electrochemical reaction at lithium foil are given in Table 7-1, which are well in the range of reported values in the literatures [19,105,107].

Table 7-1: The electrochemical reaction rate constants at the lithium foil for different temperatures.

Temperature (°C)	Rate constant, k_{Li}^0, (mol/[m^{2}s(mol/m^3)$^{0.5}$])
10	2.62×10^{-6}
23	6.64×10^{-6}
35	1.21×10^{-5}

Since the rate constant of electrochemical reaction obeys Arrhenius behavior, the following relation explains its temperature dependency [140,173,175]:

$$\ln(k_{Li}^0) = \frac{-E_{k_{Li}^0}^a}{R}\left(\frac{1}{T}\right) + C_1 \tag{7-1}$$

where $E_{k_{Li}^0}^a$ is the activation energy of charge-transfer reaction at the lithium electrode , R is the universal gas constant, T is the temperature, and C_1 is a constant with regard to temperature. The activation energy and the constant are then determined by least square curve fitting to the rate

constants obtained for the three temperatures. Figure 7-2 depicts the logarithm of the rate constant of the charge-transfer reaction at the metallic lithium electrode fitted by the Arrhenius equation.

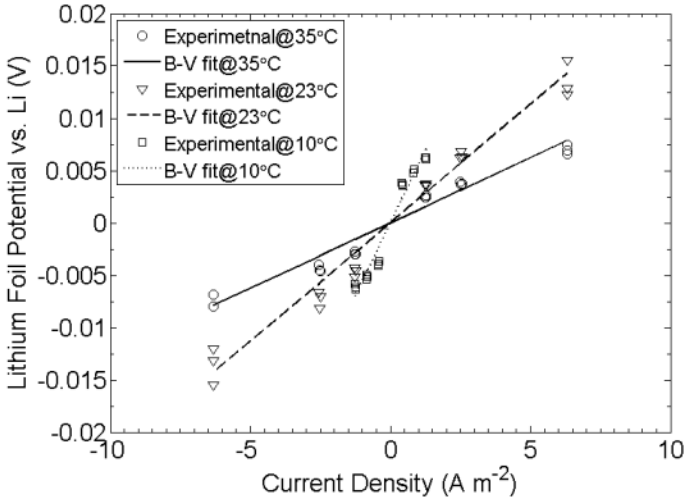

Figure 7-1: Surface overpotential of metallic Li electrode measured as a function of the applied current density at 10 °C, 23 °C, and 35 °C (symbols) and the curve fit using the Butler-Volmer relation (lines).

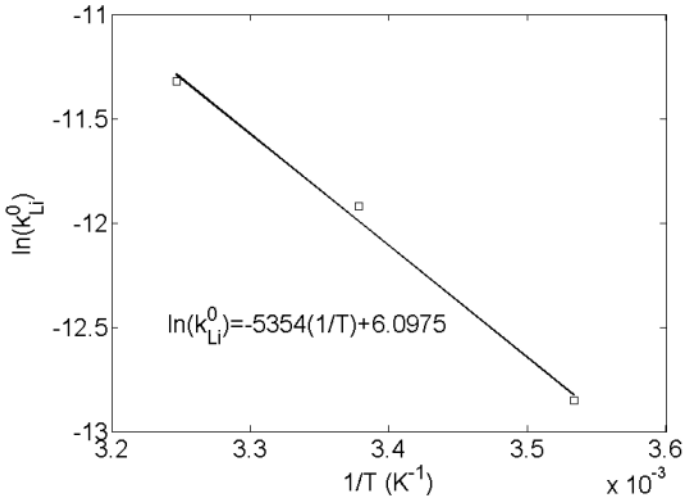

Figure 7-2: The logarithm of the electrochemical reaction rate constant at metallic lithium electrode, $\ln(k_{Li}^0)$, as a function of the inverse of temperature.

7.3.2 Li_yFePO_4 Electrode

In this section, a Li/LFP half-cell is modeled. First, the required parameters are obtained mostly from non-electrochemical measurements and then the rest of the parameters are estimated by fitting the

model to the experimental galvanostatic charge/discharge data. In the inset of Figure 7-3, an SEM image taken of the LFP electrode is given. Although the active particles are partially agglomerated and have various shapes, it is assumed that they are spherical and grouped into 13 different bins. The resulting PSD is shown in Figure 7-3. Particle sizes range from ~0.05 μm to ~1.4 μm with the median diameter (d_{50}) of ~320 nm.

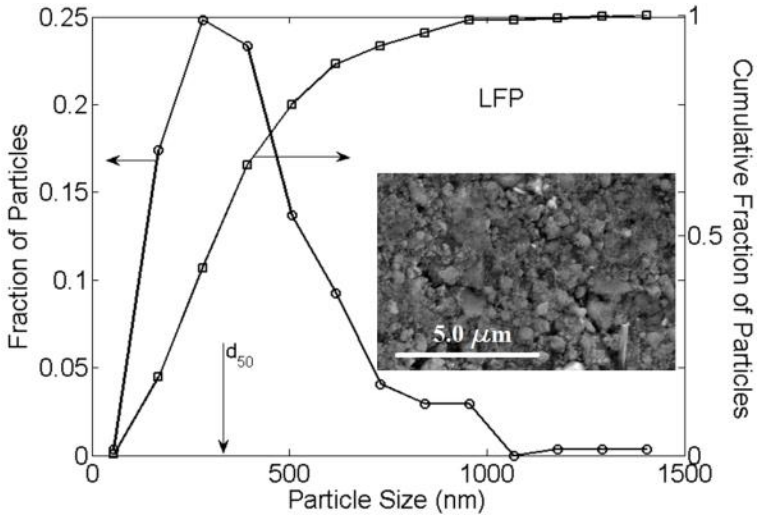

Figure 7-3: Particle size distribution of LFP electrode from an analysis of SEM image shown in the inset.

Separate LFP equilibrium potentials are considered for charge and discharge simulations of the Li/LFP half-cell [108]. The charge/discharge equilibrium potential of the LFP electrode is obtained by slowly charging/discharging the LFP electrode at a C/50 rate and at 23 °C. The lithium foil is taken to be the reference electrode; hence, given a slow enough applied current, the recorded cell voltage approximates the LFP electrode equilibrium potential. As seen in Figure 7-4(a), the equilibrium potential measured during C/50 charge is almost ~0.03 V higher than the equilibrium potential measured during C/50 discharge. This "quasi-static" potential hysteresis [180] is not explained by the VSSD model [108,181] and is, therefore, excluded from the analysis by taking two separate equilibrium potentials one on charge and one on discharge as mentioned above. The temperature dependency of the LFP equilibrium potential is directly proportional to the entropy change of the electrode due to changes in the extent of lithiation/delithiation ($\left(\frac{\partial U_{LFP}}{\partial T}\right)_{P,y} = \frac{\Delta S(y)}{nF}$). This correlation can be approximated by Taylor's expansion as follows:

$$U_{LFP}(y,T) = U_{LFP}(y,T_R) + \frac{\partial U_{LFP}}{\partial T}|_{y,T_R}(T - T_R) \tag{7-2}$$

where T_R is the reference temperature. Dodd et al. [182,183] reported entropy change, $\Delta S(y)$, as a function of lithium concentration. They charged or discharged the Li/LFP half-cell at C/20 rate in 5% SOC steps. At each step, the half-cell was cooled down using a Peltier plate to five temperatures between the room temperature and 12 ºC and the equilibrium potential was recorded for each temperature. The variation of LFP electrode equilibrium potential with respect to temperature was then used to determine the entropy change at the specified SOCs. The reported entropy change is, however, very small for all lithium concentrations and therefore ignored in this study. Although the LFP base material is the same, the electrode studied by Dodd may differ in active particle sizes, and impurities and defects, to that studied in this paper; it is nonetheless assumed that these possible differences are negligible. It should be noted that other papers also reported similar values for entropy change as a function of lithium content of LFP electrode [184,185].

The phase-change process within the electrode particles is approximated by considering a non-unity thermodynamic factor, $\alpha_{LFP,k}$, also known as the activity-correction factor [108], in the diffusion equation. Experimentally, the thermodynamic factor is found to differ for charging than for discharging (i.e., due to difference in equilibrium potentials considered), however physically it should be the same. Therefore, the best estimate used for the thermodynamic factor in this work is the average of the thermodynamic factors calculated from C/50 galvanostatic charge and discharge data (i.e., assumed equilibrium potentials). The thermodynamic factors are determined by the numerical differentiation of the equilibrium potentials following Equation (7-3) [108,186]:

$$\alpha_{LFP,k} = -\frac{F}{RT} y_{LFP,k}\left(1 - y_{LFP,k}\right)\frac{\partial U_{LFP,k}}{\partial y_{LFP,k}} \tag{7-3}$$

where F is the Faraday's constant, y_{LFP} is the lithium mole fraction in the LFP particles, U_{LFP} is the charge/discharge equilibrium potential for LFP, and the subscript k represents the k^{th} bin of particles. The result is shown in Figure 7-4(b) where the maximums at both ends of the diagram correspond to the single lithium poor and lithium rich phases, or high and low SOC regions, respectively. Very small thermodynamic factor values in the intermediate composition range, which

is between the lithium poor and rich regions, results in low Fickian diffusivities resembling a sluggish phase-boundary propagation rate [108]. It should be noted that, although a two-phase lithiation/delithiation mechanism theoretically requires the equilibrium potential as a function of composition to appear as a perfect plateau in the mid stoichiometry range, the actual electrode potential is never perfectly flat [128] regardless of the measurement conditions. This gives rise to a very small but non-zero thermodynamic factor as a means for approximating the presumed phase-boundary movement across LFP particles.

The electrolyte transport and thermodynamic properties for $LiPF_6$ in PC/EC/DMC solution as a function of temperature and concentration are adopted from [187]. Although the electrolyte of [187] differs from the one used in the coin cells studied in this paper, it is assumed that both electrolytes have similar properties as a function of temperature given the additional PC in [187] is a small fraction, 10 percent, of the total electrolyte. This assumption is required due to the lack of measurements of transport and thermodynamic properties in the literature for $LiPF_6$ in EC/DMC. All the properties from [187] are valid for temperatures between -10 °C and 60 °C and for $LiPF_6$ concentrations ranging from 0.4 mol L^{-1} to 3.3 mol L^{-1}. The ionic conductivity of the electrolyte, κ, in mS cm^{-1} is expressed as follows:

$$\kappa(c_e, T) = c_e(-10.5 + 0.0740T - 6.96 \times 10^{-5}T^2 + 0.668c_e - 0.0178c_eT + 2.80 \times 10^{-5}c_eT^2 + 0.494c_e^2 - 8.86 \times 10^{-4}c_e^2T)^2 \quad (7\text{-}4)$$

where c_e is the electrolyte concentration in mol L^{-1}, and T is the temperature in K. In addition, the diffusion coefficient of the electrolyte, D_e, in cm^2 s^{-1} is as follows:

$$\log_{10} D_e(c_e, T) = -4.43 - \frac{54}{T - (229 + 5.0c_e)} - 0.22c_e \quad (7\text{-}5)$$

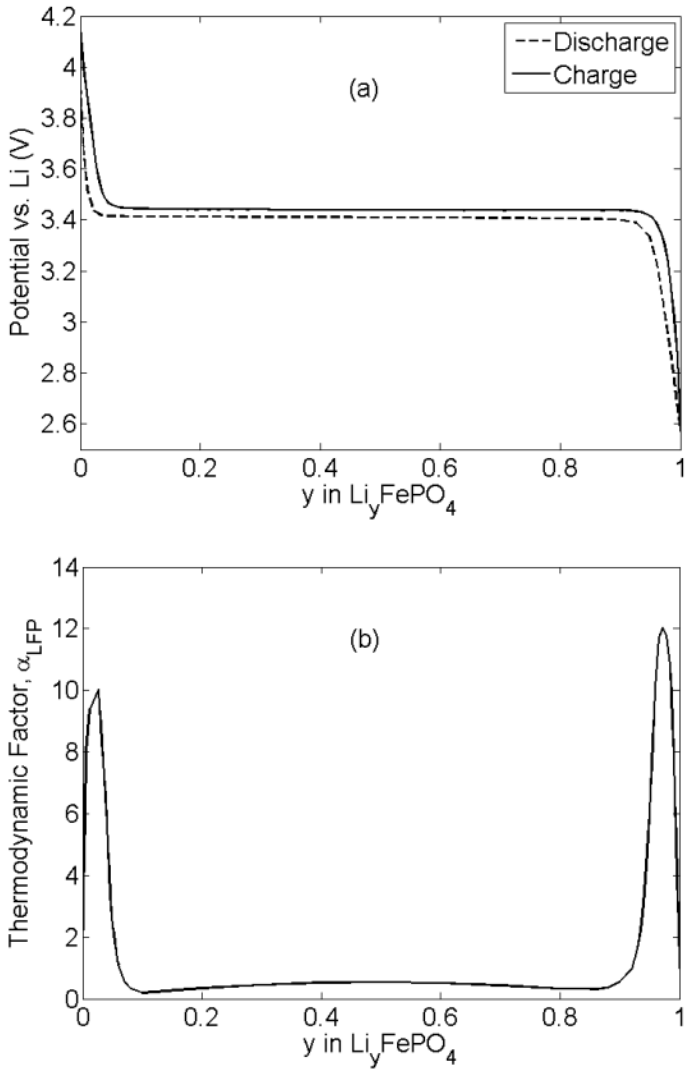

Figure 7-4: (a) The equilibrium potentials, $U_{LFP,k}$, and (b) the thermodynamic factor, $\alpha_{LFP,k}$, used for discharge and charge simulations of the LFP electrode.

Finally, the electrolyte thermodynamic factor is given as follows:

$$\left(1+\frac{d\ln f_{\pm}}{d\ln c_e}\right)=\frac{1}{1-t_+^0}\left[0.601-0.24c_e^{\frac{1}{2}}+0.982\left(1-0.0052(T-T_0)\right)c_e^{\frac{3}{2}}\right] \qquad (7\text{-}6)$$

where T_0 is the reference temperature with the value of 294 K, and the t_+^0 is the lithium ion transference number whose value is 0.38 [187]. It should be noted that there is a discrepancy between the assumptions adapted here and those considered in Ref. [187] for electrolyte parameter estimation. The above estimates of the transport and thermodynamic properties are measured

assuming non-zero convection in the electrolyte whereas convection is neglected in the model developed here. However, this inconsistency, in addition to the difference in the electrolyte composition, is expected not to introduce significant errors in the model predictions and is, therefore, ignored.

The thickness of the LFP electrode coating was measured to be 59 μm using the profilometer after carefully stripping away a portion of the electrode coating on one side of the double-sided LFP electrode (see Figure 7-5). The profilometer scanned the surface of the LFP electrode, and then moved into the region of only the aluminum current collector thus providing a measure of the thickness of the missing electrode coating. An SEM image as shown in Figure 7-5 did not yield an accurate measure for the thickness of the electrode coating as SEM sample cross-sections (factory-cut) were likely distorted due to the mechanical pressure applied locally by the cutter. This distortion can be seen in Figure 7-5 as the total thickness in the SEM is ~122 μm while that measured away from the electrode edge (using a micrometer) is ~137 μm. In contrast, the thickness of the aluminum can be measured on the SEM image at 19 μm as the cutter does not noticeably compress or distort the aluminum.

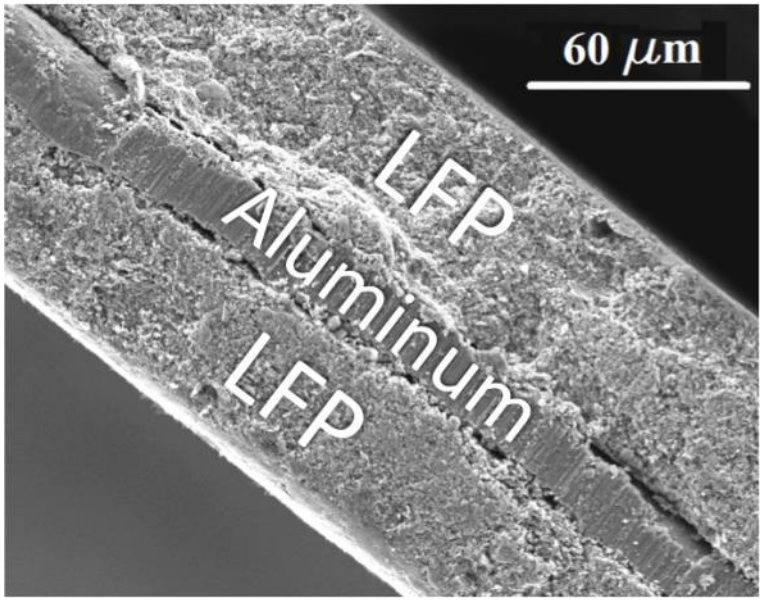

Figure 7-5: The SEM image of the cross-section of a double-sided LFP electrode.

The capacity of the LFP electrode is assumed to be equal to the total charge throughput measured at the end of C/50 galvanostatic discharge at the cut-off voltage of 2.5 V. From the experimental data, a capacity of 1.696 mAh is obtained for the LFP electrode. Given the puncher size (11.7 mm for LFP), the area of the LFP electrode is also known. Using the LFP thickness determined above, and the capacity and area, as well as the theoretical capacity and density of LFP, which are 170 mAh gr^{-1} and 3.6 gr cm^{-3} [92], respectively, the active material volume fraction of the LFP electrode is calculated to be ~0.437. If a typical 0.1 volume fraction is considered for the binder and conductive materials in the LFP electrode [188], the porosity of the LFP electrode is then estimated to be ~0.463. Based on the available data from the manufacturer [189], the thickness and porosity of the separator are 25 μm and 0.55, respectively.

Aside from the electrochemical reaction rate constant, k_{LFP}^{0}, and solid-state binary diffusion coefficient, $\mathcal{D}_{LFP}$, and the parameters determined in the previous two paragraphs, the other parameters are considered fix and depend on electrode morphology (the Bruggeman exponent, γ), electrolyte composition (initial electrolyte concentration, c_e^0), known material properties (maximum lithium concentration in LFP, c_{LFP}^{max}), and assumed kinetics of anodic/cathodic reactions (charge transfer coefficient, β). As mentioned in Section 7.2, the initial electrolyte concentration is 1 mol L^{-1}. The maximum lithium concentration is assumed to be constant at 22,806 mol m^{-3} since the LFP density is considered to be independent of lithium concentration [98]. The Bruggeman exponent and the charge transfer coefficient are set to 1.5 and 0.5, respectively [109,190,191].

The electrochemical reaction rate constant and solid-state binary diffusion coefficient are estimated by fitting the model to the experimental galvanostatic charge/discharge data. Given a single particle size obtained from the SEM image analysis (i.e., d_{50}), this provides two degrees of freedom for minimizing the difference between model and experiment. The rate constant primarily affects the match to the experiment in the onset and plateau regions of the operating voltage curves, and the diffusion coefficient primarily affects the match to experiment in the end-capacity region of the operating voltage curves. Through manual iteration the difference between the experiment and simulation results was minimized. The rate constant using the two degree-of-freedom model is

determined to be of 8.8×10^{-12} mol/[m^2s$(mol/m^3)^{1.5}$] at 23 °C which is in agreement with the reported values in the literature [108,109,128]. The rate constant is considered to be independent of applied current, consistent with [108,109,128], but contrary to [105]. The end-capacity region of the experimental data is used to determine the binary diffusion coefficient; however, it generates a poor fit to the experimental data as long as only one particle size is considered as similarly observed by Farkhondeh and Delacourt [108]. In other words, the effect of the non-uniform particle size distribution, rather than only the median particle size, should be taken into account [89,98,108] leading to an increase in the number of degrees of freedom.

It has been shown that inclusion of the actual PSD obtained from the SEM image analysis (Figure 7-3) in the model does not yield a good fit to the end-capacity region of the experimental galvanostatic charge/discharge data regardless of the number of bins [108]. Consequently, trial and error iteration was used to determine the number of particle bins, their sizes, and their volume fraction in order to obtain a reasonably good fit. As more particle bins are added to the model, the end-capacity fit to experiment continually improves as shown in [109], however, this accuracy comes in the cost of higher computational effort. Therefore, in order to keep the computational effort reasonable the number of particles added to improve the fit should be as small as possible while still yielding a good model-to-experiment fit. Eventually four particle bins were selected as providing a good compromise between accuracy and computational cost. This fitting process involved an increase in the corresponding degrees of freedom from one, for the binary diffusion coefficient, to seven when both the size and volume fractions of the three additional particle bins are added. Table 7-2 lists d_{50} and the adjusted bin sizes together with their volume fractions. The adjusted PSD is well within the range of the PSD obtained experimentally. Along with the adjusted PSD, the resulting fit of the model to the experimental voltage data, seen in Figure 7-6, yields the solid-sate binary diffusion coefficient of Li^+ inside LFP particles.

The asymmetry observed in Figure 7-6 between the charge and discharge end-capacities for different C-rates is consistent with the observations of Srinivasan and Newman [192]. This phenomenon is commonly attributed to the different transport properties in the lithium-poor and lithium-rich phases [105,192–194]. Safari and Delacourt [105,106] considered this effect in their

resistive-reactant model by assuming a larger diffusion coefficient for the lithium-poor phase, while Farkhondeh and Delacourt [108] adjusted the thermodynamic factor in their variable diffusivity model to capture this behavior. In this paper, however, in an effort to minimize the additional degrees of freedom needed to capture the asymmetry between charge and discharge end-capacities, the approach of Farkhondeh and Delacourt [108] is not used. If the approach of Farkhondeh and Delacourt [108] was to be used it would require adjusting the 'shape' of the thermodynamic factor at each temperature and making this parameter a function of temperature as well as lithium concentration. Instead, this paper utilizes two different temperature dependent binary diffusion coefficients for charge and discharge simulations as discussed in more detail in Section 7.3.2.1. The obtained value for the discharge- and charge-fitted binary diffusion coefficients at 23 °C, for instance, are 5.5×10^{-18} m^2 s^{-1} and 3.0×10^{-17} m^2 s^{-1}, respectively. These values are well within the range reported in the literature [105,108,171,195,196]. Discharge- and charge-fitted binary coefficients at other temperatures are provided in Table 7-6 in Section 7.3.2.1 as part of the $LiFePO_4$ temperature effects results and discussion.

Table 7-2: Particle size distribution of the LFP electrode obtained by fitting the simulation results to the experimental galvanostatic discharge data at all C-rates ranging from C/5 to 5C at 23 °C (f: fitted, m: measured (d_{50}), and c: calculated using $1-\sum_{k=1}^{3}\varepsilon_k/\varepsilon_{t,LFP}$).

Particle group	Particle size, $2R_{LFP,k}$ (nm)	Volume fraction, $\varepsilon_k/\varepsilon_{t,LFP}$
1	160[f]	0.4[f]
2	320[m]	0.41[f]
3	680[f]	0.12[f]
4	1500[f]	0.07[c]

All the measured, calculated, and adjusted model parameters for Li/LFP half-cell simulations are summarized in Table 7-2 and Table 7-3. The results of the Li/LFP half-cell simulations together with the experimental data for all galvanostatic discharge and charge rates ranging from C/5 to 5C at 23 °C are presented in Figure 7-6. Good agreement between the experimental data and simulation results is observed in all charge and discharge rates.

Table 7-3: List of the model parameters used for Li/LFP half-cell simulations at 23 ºC (a: assumed, s: set, f: fitted, c: calculated, m: measured, fa: Farkhondeh et al. [109], ce: Celgard [189], e: Ender et al. [125], v: Valoen and Rimeres [187]).

Parameter	Symbol	Value
LFP charge-transfer coefficient	β_{LFP}	0.5[a]
Li foil charge-transfer coefficient	β_{Li}	0.5[a]
Bruggeman exponent	γ	1.5[a]
Initial salt concentration in the electrolyte (mol m^{-3})	c_e^0	1000[s]
Maximum Li concentration in the LFP particles (mol m^{-3})	c_{LFP}^{max}	22,806[fa]
Discharge-fitted binary diffusion coefficient in LFP (m^2 s^{-1})	$\mathcal{D}_{LFP}^{d}$	5.5×10^{-18}[f]
Charge-fitted binary diffusion coefficient in LFP (m^2 s^{-1})	$\mathcal{D}_{LFP}^{c}$	3.0×10^{-17}[f]
Porosity of the separator	ε_s	0.55[ce]
Porosity of the LFP electrode	ε_{LFP}	0.463[c]
Total active material volume fraction of the LFP electrode	$\varepsilon_{t,LFP}$	0.437[c]
Electrochemical reaction rate constant of LFP (mol/[m^2s(mol/m^3)$^{1.5}$])	k_{LFP}^0	8.8×10^{-12}[f]
Separator thickness (m)	L_s	25×10^{-6}[ce]
LFP electrode thickness (m)	L_{LFP}	59×10^{-6}[m]
Effective electronic conductivity of the LFP electrode (S m^{-1})	σ_{LFP}^{eff}	6.75[e]
Li^+ transference number	t_+^0	0.38[v]
Geometric area of the LFP electrode (m^2)	A_{LFP}	1.057×10^{-4}[m]
Lower cut-off potential of the LFP electrode (V)	$V_{cut,LFP}^{min}$	2.5
Upper cut-off potential of the LFP electrode (V)	$V_{cut,LFP}^{max}$	4.2

It should be mentioned that although the LFP binary diffusion coefficient and electrochemical reaction rate constant are obtained by fitting the VSSD one-dimensional model to experimental data, it is expected that these values are good estimates for actual LFP binary diffusion coefficient and electrochemical reaction rate constant. This is due to the fact that the VSSD one-dimensional model can capture the required involved physical phenomena and accurately predicts the behavior of Li/LFP half-cells in temperatures and operating rates considered in this thesis [108,109]. Table 7-4 and Table 7-5 compare the obtained LFP binary diffusion coefficient and electrochemical reaction rate constant in this thesis with those reported in the literature, respectively. As shown in these tables, the obtained values are well within the range of the values reported in the literature showing the accuracy of the estimated parameters.

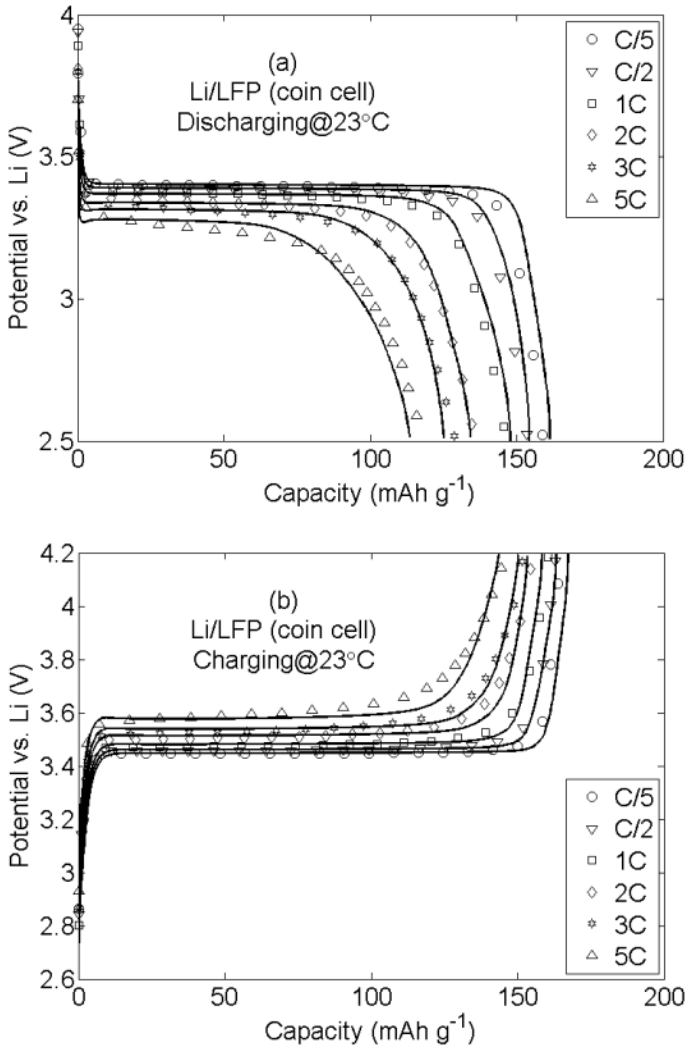

Figure 7-6: Comparison between the experimental data (symbols) and simulations (solid lines) of the Li/LFP half-cell for (a) galvanostatic discharge and (b) galvanostatic charge rates ranging from C/5 to 5C at 23 °C.

Table 7-4: Comparing the lithium diffusion coefficient of $LiFePO_4$ particles reported in literature with the obtained valued in this thesis.

Reference	Diffusion coefficient, $\mathcal{D}_{LFP}$, ($m^2\ s^{-1}$)	
Safari and Delacourt [105]	3.9×10^{-19}-1.18×10^{-18}	Depends on the lithium concentration
Farkhondeh and Delacourt [108]	5.0×10^{-19}-1.04×10^{-17}	Depends on the coin cell assembled
Yu et al. [171]	1.4×10^{-18}	
Churikov et al. [195]	6.0×10^{-19}-2.3×10^{-17}	Depends on the lithium concentration and direction of electrochemical reaction
Matsui et al. [196]	7.16×10^{-19}-1.17×10^{-18}	Depends on the current direction
This thesis	5.5×10^{-18}-3.0×10^{-17}	Depends on the current direction

Table 7-5: Comparing the electrochemical reaction rate constant of $LiFePO_4$ reported in literature with the obtained valued in this thesis.

Reference	Electrochemical reaction rate constant, k^0_{LFP}, (mol/[m^{2}s(mol/m^3)$^{1.5}$])	
Farkhondeh and Delacourt [108]	1.4×10^{-13}-2.4×10^{-12}	Depends on the lithium concentration and coin cell assembled
Farkhondeh et al. [109]	2.5×10^{-13}	
Safari et al. [128]	5.7×10^{-13}-2.8×10^{-12}	Depends on the lithium concentration
This thesis	8.8×10^{-12}	

7.3.2.1 $LiFePO_4$ Properties Temperature Dependency

Both transport and kinetic properties of LFP are functions of temperature. Generally, an Arrhenius relation is considered to describe temperature dependency of rate constants and solid-state diffusion coefficients [140,173,175]. Therefore, for LFP one can write,

$$\ln(k^0_{LFP}) = \frac{-E^a_{k^0_{LFP}}}{R}\left(\frac{1}{T}\right) + C_2 \tag{7-7}$$

$$\ln(\mathcal{D}_{LFP}) = \frac{-E^a_{\mathcal{D}_{LFP}}}{R}\left(\frac{1}{T}\right) + C_3 \tag{7-8}$$

where $E^a_{k^0_{LFP}}$ is the activation energy of the charge-transfer reaction at the surface of LFP particles, $E^a_{\mathcal{D}_{LFP}}$ is the activation energy of the solid-sate diffusion of Li^+ within LFP, and C_2 and C_3 are constants with regard to temperature. The activation energies, and C_2 and C_3, in Equations (7-7) and (7-8) are evaluated by fitting the mathematical model to the experimental galvanostatic charge and discharge data at the four temperatures of 10 °C, 23 °C, 35 °C, and 45 °C. Recall from Section 7.3.1, the model also includes temperature dependencies for the electrolyte parameters and for the kinetic parameters of the metallic lithium reference/counter electrode. The results for discharge and charge rates ranging from C/5 to 5C at 23 °C are illustrated in Figure 7-6. The results for 10 °C, 35 °C, and 45 °C are presented next.

As explained in Section 7.2, the experiments for 10 °C and 35 °C were conducted at C/5 and C/2 charge and discharge rates, respectively, and at 1C and 2C rates for 45 °C. Again, the electrochemical reaction rate constant for LFP is used to fit the onset and plateau regions of the experimental data while the binary diffusion coefficient is varied to capture the end-capacities. Other

model parameters including the adjusted PSD remained unchanged. It should be noted that at 10 °C, 35 °C, and 45 °C, the Li/LFP half-cell is charged first at a given rate and then discharged at the same C-rate. As a result, the electrode is not fully delithiated at the beginning of the discharge processes. For example, when the battery is discharged at 1C it would have been charged at 1C, however, to fully delithiate the electrode the C-rate would need to be reduced as full capacity is approached. Therefore, the initial lithium content of the LFP electrode is adjusted in the model to fit the operating voltage of the cell at the beginning of discharge. In contrast the Li/LFP half-cell is fully discharged at the beginning of the charge processes, according to the experimental protocol followed. The resulting best fits to the galvanostatic discharge and charge data at temperatures of 10 °C, 35 °C, and 45 °C are shown in Figure 7-7. Good agreement between the experimental data and simulation results is achieved in all charge and discharge rates and temperatures. The estimated electrochemical reaction rate constants and binary diffusion coefficients for LFP are given in Table 7-6.

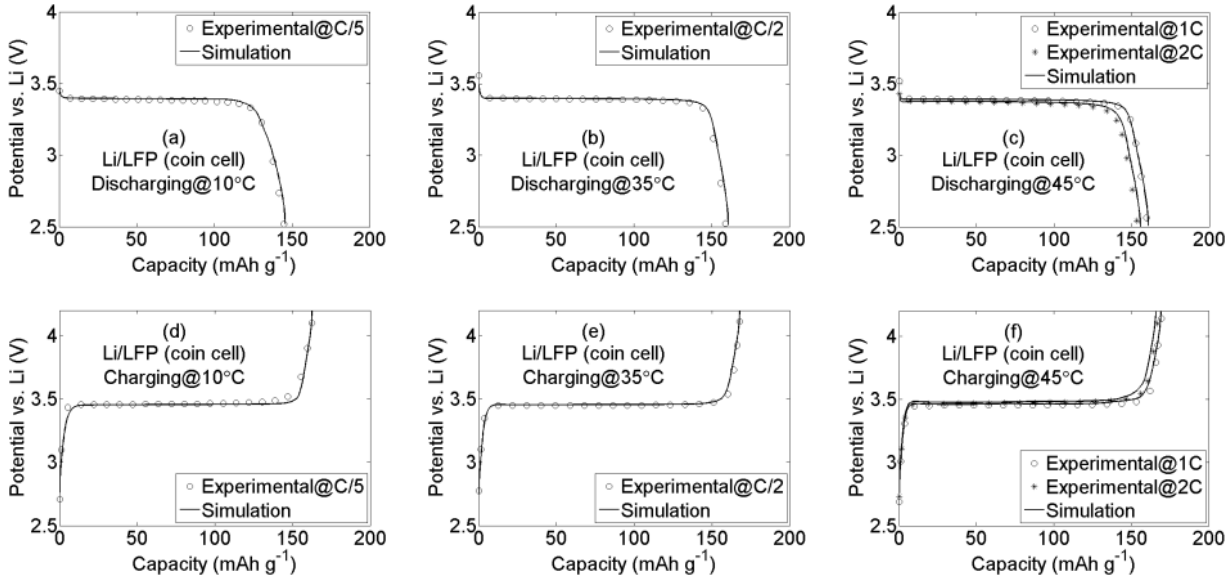

Figure 7-7: Fitting the experimental galvanostatic discharge and charge data with the mathematical model for (a) discharge at 10 °C, (b) discharge at 35 °C, (c) discharge at 45 °C, (d) charge at 10 °C, (e) charge at 35 °C, and (f) charge at 45 °C for a Li/LFP half-cell.

Table 7-6: The estimated kinetic and transport parameters for LFP at different temperatures.

Temperature (°C)	Operating rate	Electrochemical reaction rate constant, k^0_{LFP}, (mol/[m^{2}s(mol/m^3)$^{1.5}$])	Discharge-fitted binary diffusion coefficient, $\mathcal{D}^d_{LFP}$, (m^2 s^{-1})	Charge-fitted binary diffusion coefficient, $\mathcal{D}^c_{LFP}$, (m^2 s^{-1})
10	C/5	7.5×10^{-12}	9.0×10^{-19}	7.3×10^{-18}
23	C/5 to 5C	8.8×10^{-12}	5.5×10^{-18}	3.0×10^{-17}
35	C/2	1.0×10^{-11}	1.9×10^{-17}	1.3×10^{-16}
45	1C & 2C	1.15×10^{-11}	5.1×10^{-17}	4.0×10^{-16}

Linear least square fitting Equations (7-7) and (7-8) to the parameter values in Table 7-6 yields the corresponding activation energies and constants as given in Table 7-7.

Table 7-7: The activation energies and Equations (7-7) and (7-8) constants used to describe the temperature dependency of the kinetic and transport properties of LFP.

Parameter	Electrochemical reaction rate constant	Discharge-fitted binary diffusion coefficient	Charge-fitted binary diffusion coefficient
Activation energy (J mol^{-1})	9×10^3	8.6×10^4	8.6×10^4
Constants	C_2=-21.805	C_3=-4.9884	C_3=-2.9943

Figure 7-8 and Figure 7-9 show the curve fits used to arrive at the activation energies and constants in Table 7-7. Note the shift in $\ln \mathcal{D}_{LFP}$ as a function of $1/T$ in Figure 7-9 between the values estimated on charge and those on discharge. It turns out that, the temperature dependencies of charge- and discharge-fitted binary diffusion coefficients are the same and the estimated activation energies are identical. In general, temperature increase favors the kinetic and transport properties of the active material and improves electrochemical performance of the electrode. However, increasing the temperature has drawbacks such as an accelerated degradation or an increased risk of thermal runaway fires. Note that the activation energy for the electrochemical reaction is approximately an order of magnitude smaller than that for the solid-state diffusion. This means that solid-state diffusion within the LFP particles is thermally activated more pronouncedly as compared to the charge-transfer reaction at the surface of the LFP particles. This leads to a much stronger improvement in solid-state diffusion upon an increase in temperature compared to the charge-transfer reaction.

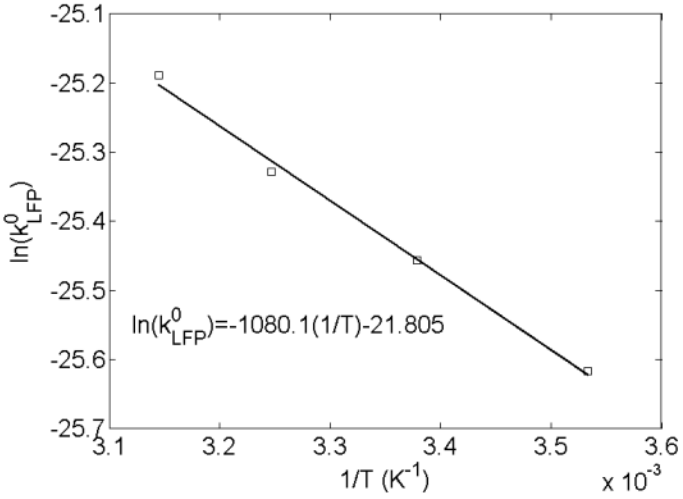

Figure 7-8: The logarithm of the rate constant of electrochemical reaction at the surface of LFP particles, $\ln(k^0_{LFP})$, as a function of the inverse of temperature.

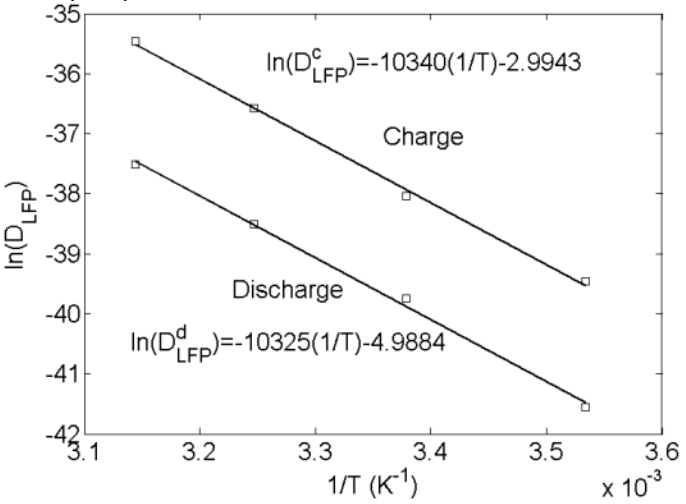

Figure 7-9: The logarithm of discharge-fitted, $\ln(\mathcal{D}^d_{LFP})$, and charge-fitted, $\ln(\mathcal{D}^c_{LFP})$, binary diffusion coefficient of Li^+ inside LFP particles as a function of the inverse of temperature.

Having demonstrated the ability of the presented electrochemical model to capture the temperature dependence of the operating voltage for a Li/LFP half-cell, it is useful to summarize how this model compares to other relevant models presented in the literature that also capture the operating voltage well.

Table 7-8: Comparison between the scope and approach taken in this paper to fit the Li/LFP half-cell operating voltage to the scope and approach taken by Safari and Delacourt [105,106] and Farkhondeh and Delacourt [108,109].

	Safari and Delacourt [105,106]	Farkhondeh et al. [108,109]	This paper
Model Differences			
Adjusted parameter to enable match of operating voltage onset and plateau	Electrochemical reaction rate constant, and four different surface resistances	Electrochemical reaction rate constant	Electrochemical reaction rate constant
Added parameters to enable match of end-of-discharge capacity variations	Different connectivity of active materials to the conductive matrix. Specifically, four different surface resistances	Expanded particle size distribution to four particle bins	Expanded particle size distribution to four particle bins
Added parameter flexibility to enable match of different charge and discharge end-capacities	Diffusion coefficient changed from constant to a function of lithium concentration	Changed the shape of the thermodynamic factor function, changing the concentration-dependence	Changed charge and discharge diffusion coefficients as per Table 7-6
To enable matching of operating voltages at different battery temperatures	Made electrochemical reaction rate constant, and diffusion coefficient, functions of temperature	NA (Did not consider different half-cell temperatures)	Made electrochemical reaction rate constant, and diffusion coefficient, functions of temperature
Model Scope			
Maximum operating C-rate	1C Charge and discharge	1C charge 5C discharge	5C Charge and discharge
Temperatures range (ºC)	25, 45	23	10, 23, 35, 45

7.3.3 Graphite Electrode

This section presents the simulation results of a Li/graphite half-cell. Similar to Section 7.3.2, the parameters of the model are primarily obtained from separate non-electrochemical measurements and the rest of parameters including the electrochemical reaction rate constant and binary diffusion coefficient are obtained by fitting the model to experimental galvanostatic discharge and charge data. The temperature dependency of kinetic and transport properties of graphite is also discussed. In the inset of Figure 7-10, an SEM image of the graphite electrode is shown. In contrast to the LFP electrode, which contains mostly spherical-shaped particles, the graphite has a distinctly flaky morphology. For the sake of modeling, however, the graphite flakes are modeled as spherical particles. Due to the broad range of particle sizes observed in the SEM image, the graphite particles are categorized into 25 bins to give a good representation of the shape of the particle size

distribution. Counting the particles/flakes in each bin gives the PSD of the graphite electrode as observed in Figure 7-10. The graphite particle diameters vary from ~0.25 μm to ~13.2 μm with the median diameter (d_{50}) of ~2.9 μm.

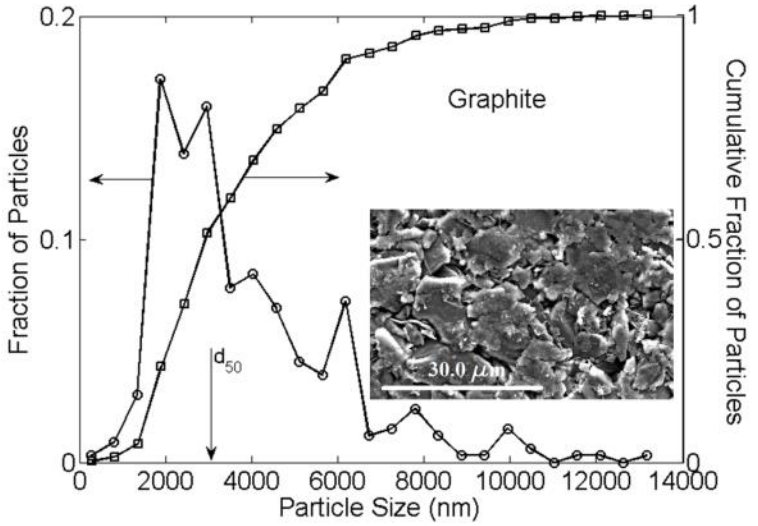

Figure 7-10: Particle size distribution of the graphite electrode from an analysis of the SEM image shown in the inset.

Separate graphite equilibrium potentials are considered for Li/graphite half-cell discharge and charge simulations. These equilibrium potentials are obtained by discharging/charging the Li/graphite half-cell at a very slow operating rate of C/50 and at 23 °C. The lithium electrode is taken as the reference electrode, and thus the output voltage approximates the equilibrium potential of the graphite as a function of lithium concentration in graphite. Due to the lithium intercalation/deintercalation in the discharge/charge process, the entropy of the graphite electrode changes giving rise to a temperature dependent equilibrium potential. Reynier et al. [197,198] estimated this entropy change by measuring the equilibrium potential of an electrically-insulated Li/graphite half-cell placed in a thermal water bath whose temperature varies in approximately 5 °C intervals from 0 °C to 23 °C. However, the reported entropy change as a function of the lithium concentration in the graphite (Li_yC_6) is very small and hence is ignored here. Similar results can also be found in [185,199,200]. Figure 7-11(a) shows the charge and discharge equilibrium potentials of the graphite where the expected multiple stages can be observed. For example, during lithium intercalation, the distinct plateau between y~0.62 and ~0.9 corresponds to the formation of stage-1

graphite intercalation compound (GIC) Li_yC_6, while the plateau between y~0.3 and ~0.5 corresponds to the stage-2 GIC Li_yC_{12} formation. Another plateau between y~0.07 and ~0.1 is also observed corresponding to the formation of satge-3 GIC Li_yC_{32}. Finally, at higher states of delithiation (y<0.07), stage-1L graphite exists with a steep slope in equilibrium potential [157,166]. In addition, as also seen in Figure 7-11(a), the measured equilibrium potential for the discharge is ~0.02 V lower than the equilibrium potential measured for the charge. Unlike the quasi-static hysteresis in LFP, this potential gap is expected to vanish as the applied current approaches zero. However, for the sake of consistency with the LFP analysis, two equilibrium potential curves are considered separately for charge and discharge simulations as mentioned before.

Staging processes in the graphite particles are captured by the variable solid-state diffusivity model, i.e., an extremely non-ideal solid-state binary solution giving rise to a concentration-dependent thermodynamic factor. As explained in Section 7.3.2, the thermodynamic factor, α_G, is calculated by averaging its values calculated from C/50 charge and C/50 discharge data using Equation (7-9).

$$\alpha_G = -\frac{F}{RT} y_G (1 - y_G) \frac{\partial U_G}{\partial y_G} \tag{7-9}$$

The result of this calculation is presented in Figure 7-11(b). Several peaks are observed in Figure 7-11(b) corresponding to the aforementioned graphite stages. The low thermodynamic factor values are explained by the formation of each stage during the charging/discharging process. According to the discussion in the above paragraph, these two-phase regions, that are the plateau regions, correspond to the formation of stage-3 (0.07<y<0.1), stage-2 (0.3<y<0.5), and stage-1 (0.62<y<0.9) graphite. In these two-phase regions the thermodynamic factor is at its lowest values. As explained in Section 7.3.2, these low thermodynamic factors then translate to low solid-state Fickian diffusion coefficients which tend to mimic the displacement of phase-boundaries involved in an active staging process within graphite particles. Again, it should be emphasized that although a perfectly flat voltage profile is expected during each staging step, the measured voltage values never contain perfect plateaus, thus the resulting Fickian diffusion coefficient according to the VSSD model is always greater than zero.

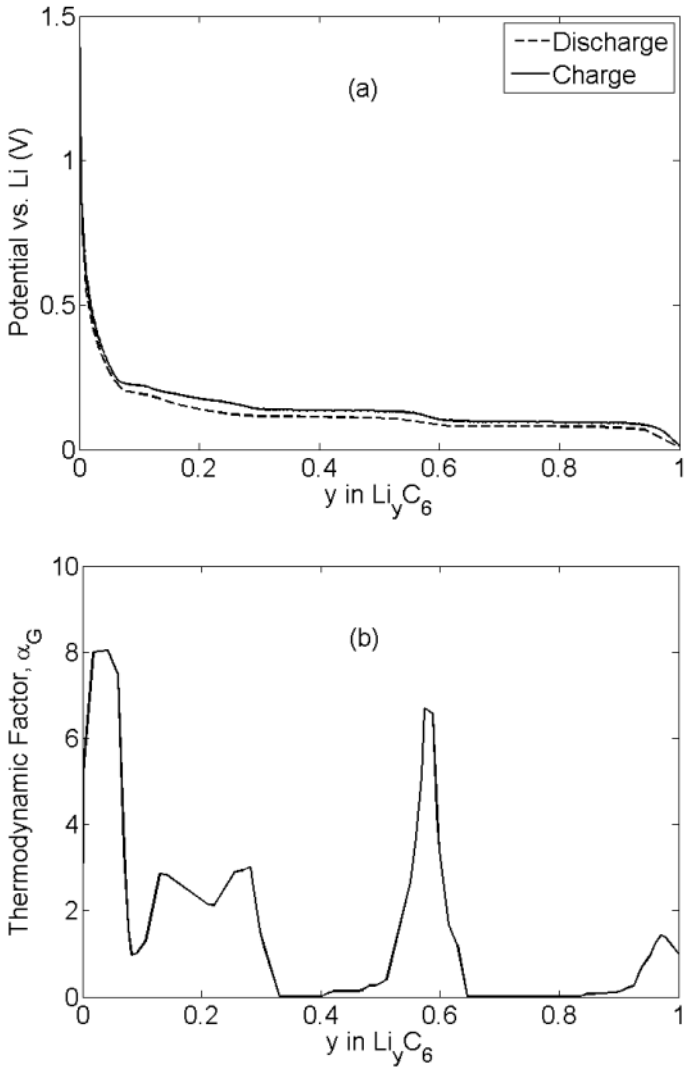

Figure 7-11: (a) The equilibrium potentials, and (b) the thermodynamic factor, α_G, used in discharge and charge simulations of the graphite electrode.

Since the electrolyte used in Li/graphite coin cell assembly is the same as that used in Li/LFP cell, the same electrolyte parameters from Section 7.3.2 are utilized. Profilometry is utilized to measure the thickness of graphite electrode. This thickness is found to be 46 μm. As explained in Section 7.3.1, an SEM image from the cross-section of the double-sided graphite electrode (shown in Figure 7-12) cannot be used reliably for this measurement. For comparison, the double-sided graphite electrode thickness in Figure 7-12 is ~96 μm while its thickness away from the electrode

edges is 102 μm. Again, since the compression does not change the copper thickness, it can be measured from Figure 7-12 at 10 μm.

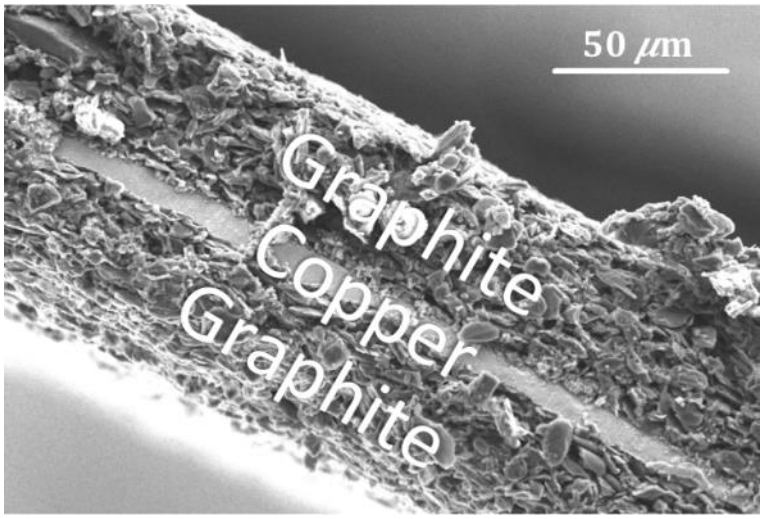

Figure 7-12: SEM image from cross-section of a double-sided graphite electrode.

The capacity of the graphite electrode is estimated by measuring the total charge throughput at the end of a discharge process (corresponding to the cut-off potential of 0.005 V) that proceeds at the slow rate of C/50. This results in 1.242 mAh as the capacity of the graphite electrode. A 9.7 mm diameter puncher was used to cut the graphite electrode; thus the area of the electrode is known. Using the electrode area, thickness, and capacity, and utilizing the graphite theoretical capacity and density, which are 372 mAh gr^{-1} and 2.26 gr cm^{-3} [201], respectively, the volume fraction of graphite in the electrode is determined to be ~0.432. If a typical 0.1 volume fraction is considered, [188], for the binder and other additives to the graphite electrode, the porosity of the electrode is found to be ~0.468. Since the separator used to assemble the Li/graphite coin cell is the same as the used in the Li/LFP cell assembly, all the parameters related to the separator are the same as in Section 7.3.2. And as in Section 7.3.2, the Bruggeman exponent is also 1.5 and charge transfer coefficient is set to 0.5. Finally, the maximum lithium concentration in the graphite electrodes is considered to be constant at 31,370 mol m^{-3} [106].

After finding the above graphite electrode parameters, the electrochemical reaction rate constant, k_G^0, and binary diffusion coefficient, $\mathcal{D}_G$, have to be estimated. To find these parameters the

simulation results of the mathematical model for the Li/graphite half-cell are fitted to the experimental galvanostatic discharge and charge data. The fitting process is first performed at 23 °C and for rates ranging from C/5 to 5C. The temperature dependency of the parameters are then studied by repeating the fitting process at three more temperatures of 10 °C, 35 °C, and 45 °C. Similar to Section 7.3.2, the electrochemical reaction rate constant of graphite lithiation/delithiation is evaluated by fitting the onset and plateaus of the experimental galvanostatic discharge and charge data. This value is found to be 1.5×10^{-11} mol/[m^2s(mol/m^3)$^{1.5}$] at 23 °C, and is in the range reported in the literature [53,106,117].

Binary diffusion coefficient of the intercalated species within graphite particles is adjusted to capture the end-capacities of the experimental data. Contrary to the Li/LFP half-cell simulations, it turns out that a constant binary diffusion coefficient and only one representative particle size (d_{50}) in the graphite electrode yields satisfactory fits to all of the experimental end-capacities both on charge and on discharge. The binary diffusion coefficient of Li^+ in graphite is obtained to be 1.0×10^{-15} m^2 s^{-1} at 23 °C in agreement with values reported in the literature [106,117,157,166].

The model parameters for the Li/graphite half-cell simulations are summarized in Table 7-9. Simulation results compared to experimental galvanostatic discharge and charge data at rates ranging from C/5 to 5C and at 23 °C are shown in Figure 7-13. Generally, good agreement between the model results and experimental data is observed in all charge and discharge rates. Figure 7-13(a), however, illustrates that the model prediction for the half-cell end-capacity at the C/2 discharge rate is noticeably higher than the corresponding experimental value. This difference is not attributed to the number of particles used in the model as simulations using four particles did not improve the C/2 end-of-discharge deviation. This difference may be attributed to the simplicity of the mathematical model compared to the actual physics of graphite lithiation dynamics. While lithium transport inside the graphite particles includes complex mechanisms such as movement of multiple phase boundaries, grain-boundary diffusion, and diffusion in each phase, the proposed model is based on a lumped parameter, i.e., the thermodynamic factor, which may not be completely satisfactory.

Table 7-9: List of the model parameters used for Li/graphite half-cell simulations at 23 ºC (a: assumed, s: set, f: fitted, c: calculated, m: measured, sa: Safari and Delacourt [106], ce: Celgard [189], e: Ender et al. [125], v: Valoen and Rimeres [187]).

Parameter	Symbol	Value
Graphite charge-transfer coefficient	β_G	0.5[a]
Li foil charge-transfer coefficient	β_{Li}	0.5[a]
Bruggeman exponent	γ	1.5[a]
Initial salt concentration in the electrolyte (mol m^{-3})	c_e^0	1000[s]
Maximum Li concentration in the graphite particles (mol m^{-3})	c_G^{max}	31,370[sa]
Graphite particle binary diffusion coefficient (m^2 s^{-1})	$\mathcal{D}_G$	1.5×10^{-15}[f]
Porosity of the separator	ε_s	0.55[ce]
Porosity of the graphite electrode	ε_G	0.468[c]
Total active material volume fraction of the graphite electrode	$\varepsilon_{t,G}$	0.432[c]
Electrochemical reaction rate constant of graphite (mol/[m^2s(mol/m^3)$^{1.5}$])	k_G^0	1.5×10^{-11}[f]
Separator thickness (m)	L_s	25×10^{-6}[ce]
Graphite electrode thickness (m)	L_G	46×10^{-6}[m]
Effective electronic conductivity of the graphite electrode (S m^{-1})	σ_G^{eff}	2203.8[e]
Li^+ transference number	t_+^0	0.38[v]
Geometric area of the electrode (m^2)	A_G	0.739×10^{-4}[m]
Lower cut-off potential of the graphite electrode (V)	$V_{cut,G}^{min}$	0.005
Upper cut-off potential of the graphite electrode (V)	$V_{cut,G}^{max}$	1.5

Similar to the explanation given in Section 7.3.2, it is expected that the obtained parameters for graphite are good estimates of their actual values since the VSSD one-dimensional model used for Li/graphite simulations captures the required physical phenomena (such as staging process inside the active particles) and accurately predicts the behavior of the half-cell in temperatures and operating rates studies in this thesis [157]. [108,109]. Table 7-10 and Table 7-11 compare the obtained graphite binary diffusion coefficient and electrochemical reaction rate constant in this thesis with those reported in the literature, respectively. As shown in these tables, the obtained values are well within the range of the values reported in the literature showing the accuracy of the estimated parameters.

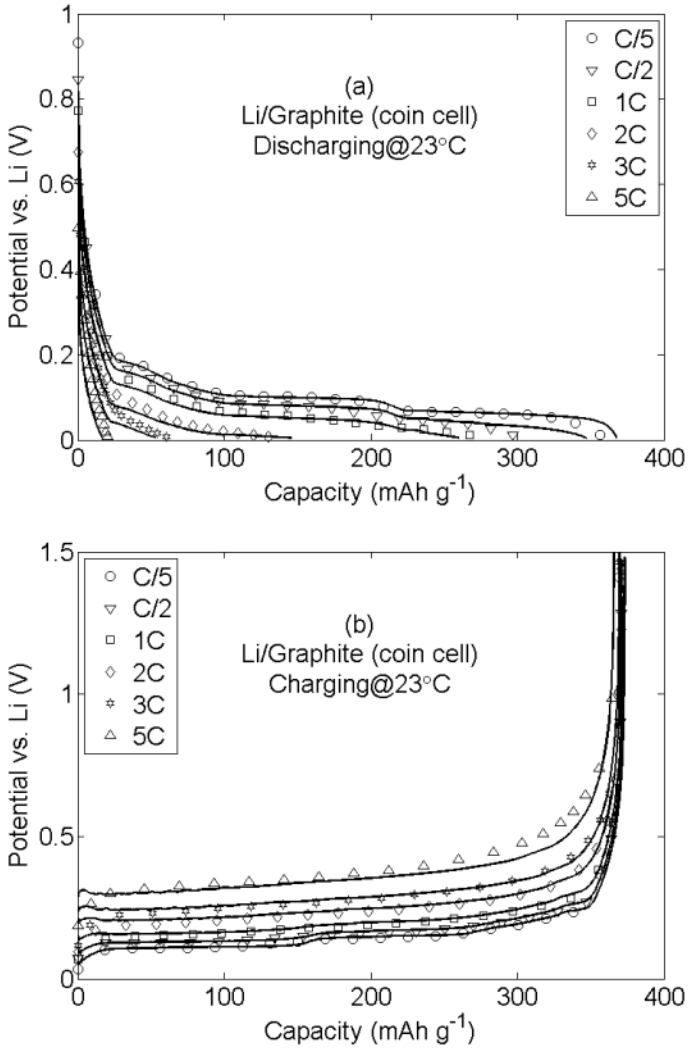

Figure 7-13: Comparison between the experimental data (symbols) and simulations (solid lines) of a Li/graphite half-cell for (a) galvanostatic discharge and (b) galvanostatic charge rates ranging from C/5 to 5C at 23 °C.

Table 7-10: Comparing the lithium diffusion coefficient of LiC_6 particles reported in literature with the obtained valued in this thesis.

Reference	Diffusion coefficient, $\mathcal{D}_G$, ($m^2\ s^{-1}$)
Safari and Delacourt [106]	2.0×10^{-14}
Subramanian et al. [117]	3.9×10^{-14}
Heß and Novák [157]	1.0×10^{-13}
Gallagher et al. [166]	3.5×10^{-17}-8.0×10^{-17}†
This thesis	1.0×10^{-15}

†Depends on the lithium concentration

Table 7-11: Comparing the electrochemical reaction rate constant of LiC_6 reported in literature with the obtained valued in this thesis.

Reference	Electrochemical reaction rate constant, k_G^0, (mol/[m^2s(mol/m^3)$^{1.5}$])
Kumaresan et al. [53]	1.764×10^{-11}
Safari and Delacourt [106]	8.19×10^{-12}
Subramanian et al. [117]	5.0307×10^{-11}
This thesis	1.5×10^{-11}

7.3.3.1 Graphite Properties Temperature Dependency

In this section, the temperature dependency of the electrochemical reaction rate constant at the surface and the solid-state binary diffusion coefficient of Li^+ within the graphite particles is studied. An Arrhenius relation is considered to describe these parameters as functions of temperature as follows,

$$\ln(k_G^0) = \frac{-E_{k_G^0}^a}{R}\left(\frac{1}{T}\right) + C_4 \tag{7-10}$$

$$\ln(\mathcal{D}_G) = \frac{-E_{\mathcal{D}_G}^a}{R}\left(\frac{1}{T}\right) + C_5 \tag{7-11}$$

In Equations (7-10) and (7-11), $E_{k_G^0}^a$ is the activation energy of charge-transfer reaction at the surface and $E_{\mathcal{D}_G}^a$ is the activation energy of Li^+ diffusion within the graphite particles. C_4 and C_5 are constants with regard to the temperature. To estimate these values, a procedure similar to that explained in Section 7.3.2.1 is repeated here. The graphite electrochemical reaction rate constants and binary diffusion coefficients are first obtained by fitting the model to the experimental data at different temperatures of 10 °C, 23 °C, 35 °C, and 45 °C. Note that the temperature dependency of the electrolyte and lithium foil electrochemical reaction rate constants is already included in the model.

As explained in Section 7.2, experiments at 10 ºC and 35 ºC were conducted at C/5 and C/2 rates, respectively whereas at 45 ºC the galvanostatic cycling was performed at two rates of 1C and 2C rates to assure maximum accuracy. It is worth restating that according to the experimental procedure at 10 °C, 35 °C, and 45 °C, the graphite electrode was not fully charged prior to being discharged. Therefore, the initial graphite stoichiometry is adjusted to fit the initial Li/graphite half-cell

operating voltage. In contrast, the graphite electrode was fully lithiated prior to being charged. The results of the fitting process at 23 °C are given in Figure 7-13 and Table 7-9. The simulation results at the other temperatures are shown in Figure 7-14, and the estimated electrochemical reaction rate constants and binary diffusion coefficients are listed in Table 7-12. The simulation results are in a good agreement with the experimental in all charge and discharge rates and temperatures.

The activation energies and constants of Equations (7-10) and (7-11) are determined by linear least square fitting Equations (7-10) and (7-11) to the estimated graphite electrochemical reaction rate constants and binary diffusion coefficients in Table 7-12. The resulting values are reported in Table 7-13.

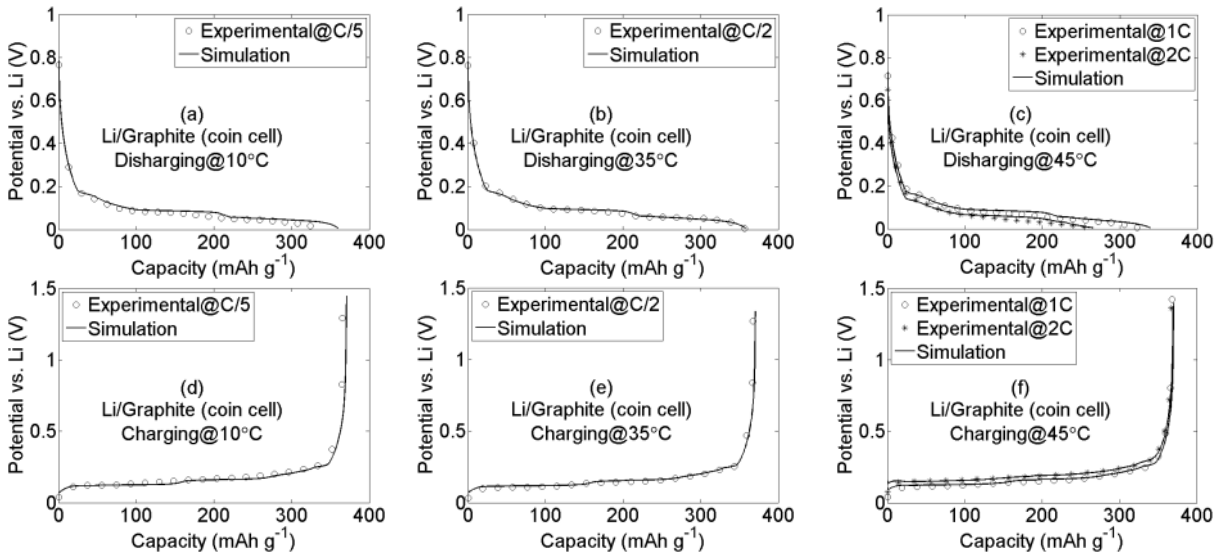

Figure 7-14: Fitting the experimental galvanostatic discharge and charge data with the mathematical model for (a) discharge at 10 °C, (b) discharge at 35 °C, (c) discharge at 45 °C, (d) charge at 10 °C, (e) charge at 35 °C, and (f) charge at 45 °C for a Li/graphite half-cell.

Table 7-12: The estimated kinetic and transport properties of graphite at different temperatures.

Temperature (°C)	Operating rate	Electrochemical reaction rate constant, k_{Li}^{0}, (mol/[m^{2}s(mol/m^3)$^{1.5}$])	Discharge binary diffusion coefficient, $\mathcal{D}_G$, (m^2 s^{-1})
10	C/5	1.0×10^{-11}	1.0×10^{-15}
23	C/5 to 5C	1.5×10^{-11}	1.5×10^{-15}
35	C/2	2.0×10^{-11}	2.0×10^{-15}
45	1C & 2C	2.5×10^{-11}	2.5×10^{-15}

Table 7-13: The activation energies and Equations (7-10) and (7-11) constants used to describe the temperature dependency of the kinetic and transport properties of graphite.

Parameter	Electrochemical reaction rate constant	Binary diffusion coefficient
Activation energy (J mol^{-1})	2×10^4	2×10^4
Constants	C_4=-17.017	C_5=-26.227

Figure 7-15 and Figure 7-16 show the curve fits used to derive the reported activation energies in Table 7-13. It is observed that the slope of the fitted curve in Figure 7-16 for graphite is much smaller compared to that in Figure 7-9 for LFP showing diffusion in graphite is less temperature dependent compared to LFP. In addition, it is observed that the slope of the fitted curve in Figure 7-15 for graphite is higher than that in Figure 7-8 for LFP showing higher temperature dependency of charge-transfer kinetics at the surface of graphite particles compared to LFP particles. Note that the reported transport and kinetic parameters are valid for the discussed operating conditions and are applicable to models with similar assumptions to those adapted in this paper. However, the high quality of the fit to the data shown in this paper suggests the possibility of using the reported values at other operating conditions than those considered here.

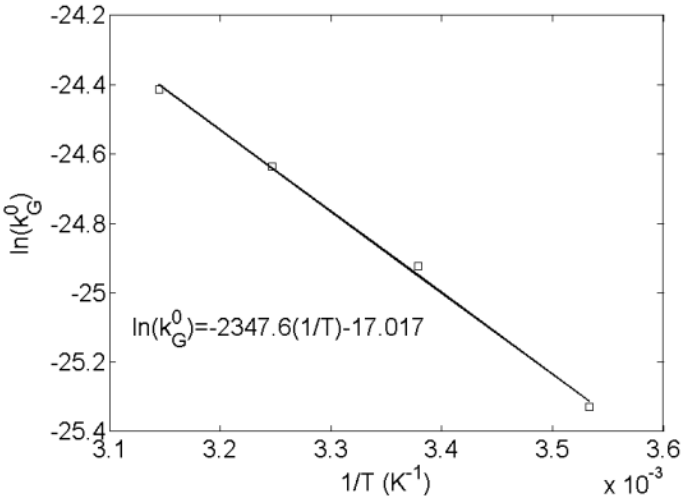

Figure 7-15: The logarithm of the rate constant of electrochemical reaction at the surface of graphite particles, $\ln(k_G^0)$, as a function of the inverse of temperature.

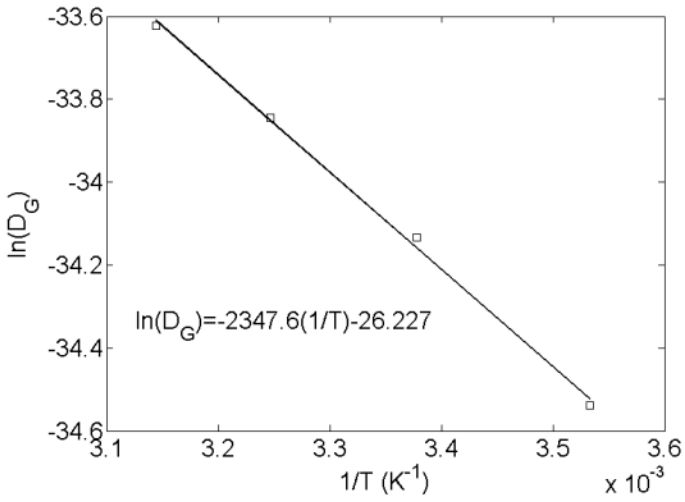

Figure 7-16: The logarithm of graphite binary diffusion coefficient, $ln(\mathcal{D}_G)$, as a function of the inverse of temperature.

Chapter 8 Prismatic Cell Model

The following section is based on previously submitted work by Mastali, M., Foreman, E., Modjtahedi, A., Farhad, S., Fraser, R., and Fowler, M.

Journal of the Power Sources.

"**Electrochemical-Thermal Modeling of a Commercial Graphite/$LiFePO_4$ Prismatic Cell**"

This thesis author specific contribution to this paper was to cooperate in designing and conducting the experiments, develop the model and conduct the simulations, prepare all the graphics and results, prepare the final manuscript and reviewer edits with direction from the project supervisors who were co-authors. All authors reviewed the manuscript.

8.1 Introduction

The operating temperature of the Li-ion batteries significantly affect their performance, lifespan, and safety [202–204]. It has been shown that the elevated temperatures accelerate the capacity fade of Li-ion batteries during storage and under cycling conditions [152,155,205,206]. In addition, lacking of a proper thermal management can give rise to the occurrence of thermal runaway in some extreme conditions such as harsh charging and discharging [207,208] and internal short circuit [209,210]. As a result, in order to prevent high temperatures and overcome overheating during battery operation, thermal management of Li-ion batteries is vital for their development.

There are mainly two main approaches in thermal management of Li-ion batteries: decreasing the heat generation inside the batteries, and improving the heat dissipation from the battery. In the first approach, the electrochemical performance of the cell is improved by reducing the internal resistance of the battery. Different methods such as altering the thickness of the electrodes [211,212], changing the active materials' particle size [213–215], and modifying the negative [216–218] and positive electrodes [219–222] are incorporated. In the second approach, the heat transfer from the battery to the environment is optimized in order to minimize the maximum temperature of the battery and

make its temperature distribution more uniform. To this end, four types of thermal management systems based on the air cooling [223–226], liquid cooling [227–230], heat pipe cooling [231–233], and phase-change-material cooling [234–237] are developed. In both thermal management approaches, however, developing the models capable of predicting the electrochemical-thermal behavior of Li-ion batteries is necessary. These models provide a framework to study the effect of each parameter on the thermal behavior of batteries without utilizing costly and time-consuming experimental tests. In addition, the modeling provides battery internal information that is not accessible from experiments.

Different mathematical models including equivalent circuit (EC) models [46,147] and physics-based one-dimensional models [89,109,238,239] are developed for battery simulations. However, it was discussed that in the case of large-sized Li-ion batteries and in extreme operating conditions, as might be required in EVs and PHEVs, the non-uniformities in electrochemical and thermal variable distributions cannot be ignored and three-dimensional models must be utilized [112]. In addition, the influence of tabs utilized in commercial batteries is not seen by these simple one-dimensional models. As an alternative approach, some researchers combine equivalent circuit models with the three-dimensional charge conservation and heat diffusion equations for three-dimensional modeling of batteries [240–242]. This type of models, however, have limited applicability due to the incorporated EC model [243]. Furthermore, Kwon et al. [55] developed a model to study the current and potential distributions in a lithium-polymer battery. In their model, the electrochemical modeling part is skipped and fitting parameters to the experimental data as a function of depth of discharge (DOD) is used to model the internal resistance of the battery layers. Kim et al [40,41,244] added a thermal model to the work done by Kwon et al. to determine the temperature distribution of the battery. The coupling between electrochemical and thermal models, however, is one way and the temperature distribution does not affect the electrochemical variables. In an attempt to couple the electrochemical and thermal models, Bandhauer et al. [245–247] use a series of fitted functions to the experimental data instead of electrochemical model. Although this modeling approach works well for studying different thermal management strategies, similar to EC models has limited applicability. To address the abovementioned issues, a variety of models have been developed in

literatures utilizing the physics-based electrochemical model instead of EC models and fitting approaches. Some of these models assume uniform kinetics all over the electrodes and incorporate a single physics-based one-dimensional model throughout the electrodes [144,248,249]. As a result, the distributions of electrochemical variables in the battery are neglected while the current and potential variations are solved three-dimensionally. To model the electrochemical variable distributions as well as the current and temperature variations, the other developed models utilize the physics-based one-dimensional models as a source term in the charge conservation and heat diffusion equations [22,23,112,130,138,250–252]. These models, however, have not usually been compared against the experimental data or the layered geometry of the battery is not resolved in their computational domain that may lead to inaccurate fitting parameters.

In this chapter, a coupled electrochemical-thermal model for a commercial 20 Ah prismatic cell is developed that considers all the electrochemical-geometrical details of the cell. In this model, the physics-based one-dimensional electrochemical models are combined with the charge conservation and heat diffusion equations throughout the battery domain in order to calculate the electrochemical variables, current, and temperature distributions. The utilized physics-based one-dimensional models accurately predict the behavior of the negative and positive electrodes considering the material phase-change inside the active electrode particles and the particle-size distribution observed in SEM images of electrodes. This approach provides the opportunity of precisely studying even the particle-level phenomena effects on the prismatic cell electrochemical-thermal behaviors. In addition, since many of the required model parameters are obtained from half-cell simulations, the estimated prismatic cell parameters are more physical. The developed model for the 20 Ah prismatic cell is compared against the experimental data for the operating voltage and temperature distribution on the surface of the prismatic cell during both charge and discharge. Good agreement between the simulation results and experimental data shows that the approach utilized in this chapter can also be implemented for the other battery materials and geometries.

8.2 Experimental

A prismatic Li-ion cell [253] is used to verify model results. The battery is held in the upright position by a two-clamp stand as shown in Figure 8-1(a) for all testing. Seven Omega brand HFS-4 thin-film Type-K thermocouples are used to gather temperature data from the battery surface. Temperatures are measured on only one side of the prismatic cell given its symmetric construction as described in Section 8.3. Heat flux sensors are used to measure the surface temperature and are attached to the pouch cell as shown in Figure 8-1. In addition, two additional individual Type-K TCs is attached to the battery terminals.

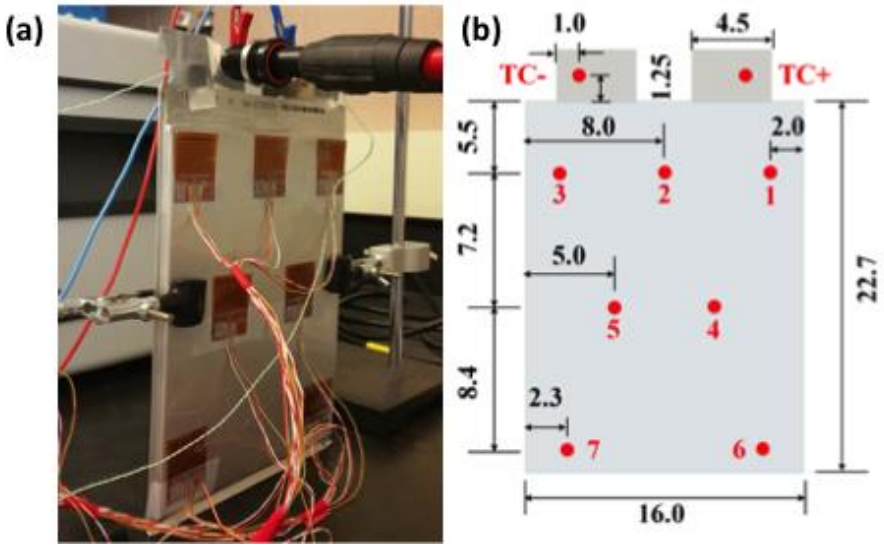

Figure 8-1: (a) Battery held in upright position with thermocouples attached. (b) Locations of thermocouples on battery, TC locations denoted by red '●' (all dimensions are in cm). TC_+ and TC_- are located on the negative and positive battery terminals, respectively.

Temperatures versus time measurements from the nine pairs of TC wires are obtained using a National Instruments DAQ 9171 and National Instruments LabVIEW software [254]. A BioLogic Science Instruments BCS-815 battery cycler with a CC8 8-channel current collector [255] is used to apply the required current to the battery. Using BioLogic Science's BT-Lab software, a charge/discharge profile was created using the following standard procedure: (i) first, charge the battery at the desired C-rate, that is at a constant current (CC), until the voltage reaches the higher cut-off voltage of 3.7 V, (ii) then continue to charge the battery at a constant voltage (CV) of 3.7 V

until the current drops below 200 mA, (iii) put the battery at its open circuit rest condition for 8 h, (iv) discharge the battery at the desired C-rate, constant current, until the voltage reaches the lower cut-off voltage of 2.4 V, (v) continue to discharge the battery at a constant voltage (CV) of 2.4 V until the current magnitude drops below 200 mA, and (vi) lastly, put the battery at its open circuit rest condition for 8 h. These 6 steps are repeated using C-rates of 1C, 2C, 3C, and 5C. Given the unknown state of the battery before the 1C discharge, an initial charge and discharge following the above procedure is first done for C/2.

8.3 Model Development

As seen in Figure 8-2, the studied prismatic cell includes a number of individual cells connected in parallel. Each cell contains a negative electrode, a separator, and a positive electrode, surrounded on either side by the current collectors. In the prismatic cell studied in this paper the negative and positive electrodes active materials are made from graphite and LiFePO4, respectively. Copper is used as the negative current collector and aluminum as the positive current collector (Figure 8-2). This cell includes 48 individual cells resulting in a 20 Ah nominal capacity. In order to decrease the material demand and reduce the electrical losses, current collectors are covered by electrode materials on both sides. Therefore, the number of aluminum current collectors for 48 cells is 24, while there are 25 copper collectors since copper collectors are on each end of the stack like that shown in Figure 8-2 for a 6 cell stack. All the layers are then enclosed in a separator sheet and a casing covers all.

To capture the current flow in the prismatic cell, the method used in Chapter 5 to describe the three-dimensional current distribution in a single cell is expanded here to multiple cells. The current flowing to the prismatic cell is first divided between all 48 cells and then enters the current collectors using tabs. The current entering the collectors distributes inside the current collectors' plate and then crosses active materials as explained in Chapter 5. Due to the much higher electrical conductivity of metallic collectors compared to the active material layers, and also due to the thinness of active material layers, it is assumed that the current flow in the active material layers is effectively one-dimensional, i.e., perpendicular to the current collectors' plate. However, it should be noted that in

spite of the very low electrical resistance of metallic collectors, the conductor resistance cannot be ignored since it is the source of the three-dimensional distribution of the current crossing the active material layers. Figure 8-3 displays the explained current distribution in the current collectors and between the layers during discharge. As seen, current from the current collectors goes into the active material layers on either side of the collector.

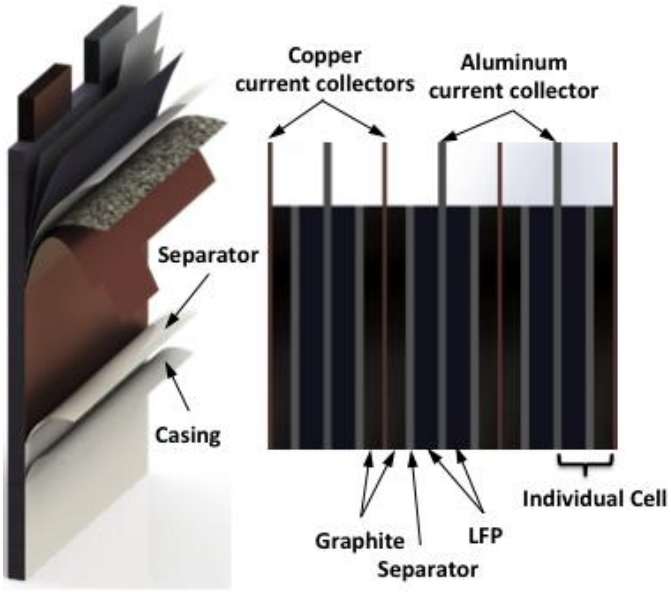

Figure 8-2: Structure of the multi-cell Li-ion prismatic cell.

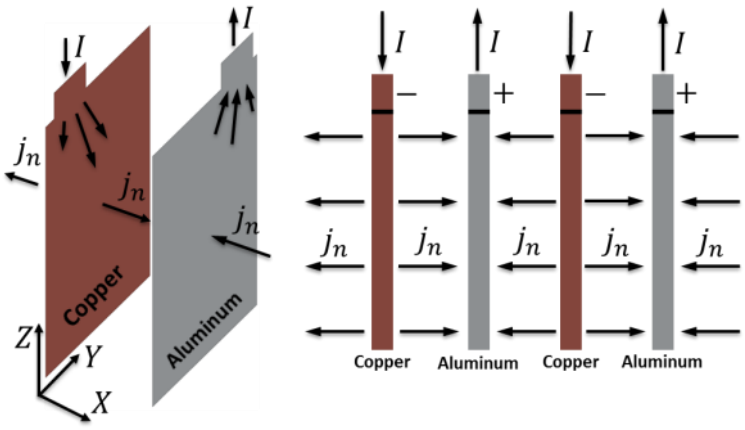

Figure 8-3: Current and current density distribution in the Li-ion battery electrodes during the discharge.

8.3.1 Electrochemical Model

8.3.1.1 One-Dimensional Electrochemical Model

The one-dimensional electrochemical model is already explained in Chapter 4 and Chapter 5 where the Li-ion battery contains a lithium foil negative electrode. In commercial batteries, however, the graphite is usually used as the negative electrode. Utilizing the porous graphite electrode changes the one-dimensional model governing equations given in Chapter 4 and Chapter 5. Therefore, these governing equations for a Li-ion battery containing the graphite as the negative and $LiFePO_4$ as the positive electrode are listed in Table 8-1. It should be mentioned that the given equations are for the homogenous pseudo-two-dimensional (HP2D) model showing the best computational performance. The input to the one-dimensional model is the local normal current density, j_n, and the output is the potential variation across the active material layers, $\nabla\phi_{lay}$, calculated from Equation (8-1):

$$\nabla\phi_{lay} = \phi_s|_{x=L} - \phi_s|_{x=0} - R_c j_n \tag{8-1}$$

where ϕ_s is the solid-phase potential of the electrodes, L is the cell thickness of active material layers (separator plus the electrodes), and R_c is the contact resistance between current collectors and electrodes.

8.3.1.2 Prismatic Battery Cell Electrochemical Model

To calculate the current and voltage distribution in the prismatic cell the model presented in Chapter 5, which is applicable to only one individual cell, is expanded here. In the model explained in Chapter 5, the charge conservation equation is applied to the current collectors, and one-dimensional electrochemical models relate the local normal current densities and the potential variation across the active material layers. Noting the current flow shown in Figure 8-3, in order to expand the model to a prismatic cell, the current flow from both sides of the current collectors has to be taken into the account except for the two copper collectors at each end of the Li-ion prismatic cell. The charge conservation equation that applies to each current collector is thus arranged as follows, with the two copper collectors on the ends of the Li-ion prismatic cell having one of the right hand side terms set to zero:

Table 8-1: The governing equations and corresponding boundary conditions of the homogenous pseudo-two-dimensional (HP2D) model.

Particle-level governing equations	
Anode/Cathode active materials	Boundary and initial conditions
$\frac{\partial c_{s,k}}{\partial t} = \frac{1}{r_k^2}\frac{\partial}{\partial r_k}\left(r_k^2 \alpha_k \mathcal{D} \frac{\partial c_{s,k}}{\partial r_k}\right)$ $\alpha_k = -\frac{F}{RT} y_k (1-y_k) \frac{\partial U_k}{\partial y_k}, y_k = c_{s,k}/c_s^{max}$ $i_{n,k} = 2i_k^0 \left[\exp\left(\frac{(1-\beta)F}{RT}\eta_k\right) - \exp\left(\frac{-\beta F}{RT}\eta_k\right)\right]$ $j_n = L_i \sum a_k i_{n,k}$ $\eta_k = \phi_s - \phi_e - U_k, a_k = 3\varepsilon_k / R_{p,k}$ $i_k^0 = F k^0 {c_e}^{1-\beta} c_s^{max} (1-y_k)^{1-\beta} y_k^{\beta}$	$\frac{\partial c_{s,k}}{\partial r_k}\|_{r_k=0} = 0$ $\alpha_k \mathcal{D} \frac{\partial c_{s,k}}{\partial r_k}\|_{r_k=R_{p,k}} = \frac{i_{n,k}}{F}$ $c_{s,k}\|_{t=0} = c_{s,k}^0$
Electrode-level governing equations	
Battery layers	Boundary and initial conditions
$\nabla.\left(\sigma_i^{eff} \nabla \phi_s\right) = H_i, i = a, c$ $\sigma_i^{eff} = \sigma_i (1-\varepsilon_i)^{\gamma}$ $\nabla.\left(-\kappa_i^{eff} \nabla \phi_e\right) + \nabla.\left(\kappa_{D,i}^{eff} \nabla \ln c_e\right) = H_i, i = a, s, c$ $\kappa_i^{eff} = \kappa_i \varepsilon_i^{\gamma}, \kappa_{D,i}^{eff} = \frac{2RT\kappa_i^{eff}}{F}(1-t_+^0)\left(1 + \frac{d \ln f_{\pm}}{d \ln c_e}\right)$ $H_a = \frac{j_n}{L_a}, H_s = 0, H_c = -\frac{j_n}{L_c}$ $\frac{\partial(\varepsilon_i c_e)}{\partial t} = \nabla.\left(D_{e,i}^{eff} \nabla c_e\right) + \frac{1-t_+^0}{F} H_i, i = a, s, c$ $D_{e,i}^{eff} = D_e \varepsilon_i^{\gamma}$	$\sigma_a^{eff} \nabla \phi_s\|_{x=L_a} = \sigma_c^{eff} \nabla \phi_s\|_{x=L_a+L_s} = 0$ $\sigma_c^{eff} \nabla \phi_s\|_{x=L} = j_n$ $\phi_s\|_{x=0} = 0$ $\kappa_a^{eff} \nabla \phi_e\|_{x=0} = \kappa_c^{eff} \nabla \phi_e\|_{x=L} = 0$ continuity at $x = L_a$ and $x = L_a + L_s$ $D_{e,a}^{eff} \nabla c_e\|_{x=0} = D_{e,c}^{eff} \nabla c_e\|_{x=L} = 0$ continuity at $x = L_a$ and $x = L_a + L_s$ $c_e\|_{t=0} = c_e^0$

$$\sigma_i \frac{\partial^2 \Phi_i}{\partial Y^2} + \sigma_i \frac{\partial^2 \Phi_i}{\partial Z^2} = \frac{j_{n,i-1}}{L_i} + \frac{j_{n,i+1}}{L_i} \tag{8-2}$$

where $j_{n,i-1}$ is the normal outward current density flowing between the i^{th} and $(i-1)^{th}$ current collectors and $j_{n,i+1}$ is the normal outward current density flowing between the i^{th} and $(i+1)^{th}$ current collectors.

The material and geometrical properties of the current collectors are known. Similar to the method presented in Chapter 5 [256], the normal current densities are replaced by the following linear relation:

$$j_n = a \nabla \phi_{lay} + b \tag{8-3}$$

where a and b are space varying linear relation coefficients, and $\nabla\phi_{lay}$ is the potential gradient between the corresponding nodes on the positive and negative current collectors calculated using Equation (8-1). In contrast to the approach used in Refs. [146,178] that ignores the potential gradient along the current collectors, the coupling utilized here between the current and potential distributions yields calculating these two variables simultaneously at each time step.

The boundary conditions for Equation (8-2) are the zero reference potential for all negative current collector tabs and an equal but varying electrical potential for all positive tabs. It is also assumed that the current, I_i, at the top surface area of a positive current collector tab is evenly distributed spatially, but the current is allowed to be different for each tab. The total current through all positive current collector tabs sums to the total applied prismatic cell current, I_{app}, as follows:

$$I_1 + I_2 + \cdots + I_{23} + I_{24} = I_{app} \tag{8-4}$$

A zero flux condition is considered for the remaining current collector boundaries.

Utilizing the above boundary conditions, as well as Equation (8-3), the charge conservation equation (Equation (8-2)) can be solved for the voltage distribution in the prismatic cell. Equation (8-3) is then used to calculate the normal current density distribution. By knowing the current density distribution, new values for the one-dimensional model variables (electrochemical variables) can be determined. This process is repeated for the next time step to update the voltage distribution, normal current density distribution, and electrochemical variables until the lower cut-off voltage of the prismatic cell (2.4 V) during the discharge or higher cut-off voltage (3.7 V) during the charge is reached.

8.3.2 Thermal Model

After calculating the current density and electrochemical variable distributions in the prismatic cell, a thermal model is used to determine the temperature distribution. This model is actually a heat conduction equation with appropriate heat generation terms, material properties, and boundary conditions. Following the presentation of the governing equation and boundary conditions, the equations used to calculate the heat generation in the active material layers and the current collectors

are presented. Finally, the approach used to determine material properties for use in Equation (5) is presented.

8.3.2.1 Energy Balance

The energy balance for the prismatic cell is given by the heat diffusion equation:

$$\rho C_P \frac{\partial T}{\partial t} = \frac{\partial}{\partial X}\left(k_X \frac{\partial T}{\partial X}\right) + \frac{\partial}{\partial Y}\left(k_Y \frac{\partial T}{\partial Y}\right) + \frac{\partial}{\partial Z}\left(k_Z \frac{\partial T}{\partial Z}\right) + \dot{q}_{gen} \quad (8\text{-}5)$$

where ρ is the density, C_p is the specific heat, k is the thermal conductivity, T is the local temperature, t is the time, and $\dot{q}_{gen}$ is the heat generation rate per unit volume. Equation (8-5) is separately applied to the active material layers, current collectors, and outside layer (the separator and casing) of the prismatic cell. Note that the active material layers are treated as a single layer whose local temperature gradient normal to the current collector plates is negligible given the thinness of these layers and relatively high thermal conductivity of the contained materials [26].

The thermal model considers both convective and radiative heat transfers to the surrounding. These heat transfers are treated as the boundary conditions for Equation (8-5) and are expressed as follows:

$$\dot{q}_{conv} = h\left(T_{surf} - T_{amb}\right), \quad (8\text{-}6)$$

$$\dot{q}_{rad} = \sigma E\left(T_{surf}^4 - T_{amb}^4\right), \quad (8\text{-}7)$$

where $\dot{q}$ is the heat transfer rate per unit area of the prismatic cell, h is the convective heat transfer coefficient, T_{surf} is the local temperature on the surface of the prismatic cell, T_{amb} is the ambient temperature, σ is the Stefan-Boltzmann constant, and E is the emissivity.

8.3.2.2 Heat Generation

Heat generation in prismatic cells comes from two different sources: heat generation in active material layers, and heat generation in the current collectors. Each of these heat sources has to be separately calculated. The local heat generation rate in the active material layers, $\dot{q}_{gen,lay}$, is revised from [25,52] for HP2D model to reflect the homogeneity of the electrochemical reaction rate across the electrodes and is expressed as follows:

$$\dot{q}_{gen,lay} = \sum_{l=n,p}\sum_{k} a_{k,l} i_{n,k,l} T \frac{\partial U_{k,l}}{\partial T} + \sum_{l=n,p}\sum_{k} a_{k,l} i_{n,k,l}\left(\phi_s - \phi_e - U_{k,l}\right) + \frac{1}{L}\int \left(\sigma^{eff}\left(\frac{\partial \phi_s}{\partial x}\right)^2 + \kappa^{eff}\left(\frac{\partial \phi_e}{\partial x}\right)^2 + \kappa_D^{eff}\left(\frac{\partial \ln c_e}{\partial x}\right)\left(\frac{\partial \phi_e}{\partial x}\right) \right) dx + \frac{R_c}{L} j_n^2 \quad (8\text{-}8)$$

where a is the specific surface area of the active particles, i_n is the reaction current density at the surface of active particles, T is the local temperature of the active material layers, U is the equilibrium potential of active particles, L is the thickness of the active material layers (separator plus the electrodes), ϕ_s and ϕ_e are the solid-phase and electrolyte potentials, respectively, σ^{eff} is the solid-phase effective electrical conductivity, κ^{eff} is the electrolyte effective ionic conductivity, and R_c is the contact resistance between current collectors and electrodes.

In Equation (8-8), the first term on the right-hand-side is reversible entropic heat generation while the remaining terms are irreversible heat generation terms. Specifically, the second term represents the reaction heat generated on the surface of the negative and positive electrodes' particle surfaces, while the third term represents Joule heating from movement of electrons and ions in the electrodes and electrolyte, respectively. Finally, the last term represents heat generated from contact resistance between the electrodes and current collectors. In contrast, the heat generated in the current collectors, $\dot{q}_{gen,cc,i}$, is only due to ohmic resistance in the current collectors and is formulated as follows [22,138]:

$$\dot{q}_{gen,cc,i} = \sigma_{cc,i}\left[\left(\frac{\partial \Phi_{\mathrm{i}}}{\partial Y}\right)^2 + \left(\frac{\partial \Phi_{\mathrm{i}}}{\partial Z}\right)^2\right] \quad (8\text{-}9)$$

where σ_{cc} is the current collector electrical conductivity, Φ is the its local potential, and i stands for negative or positive current collector.

8.3.2.3 Thermal Properties

When applying the energy balance equation to different layers of the prismatic cell, utilizing correct thermal properties (such as thermal conductivity, heat capacity, and density) is important. For the

current collectors, the known thermal properties of copper or aluminum are used. In contrast, the active material layers, and the outside layers, of the prismatic cell are non-homogeneous yet modelled as a single material for heat transfer purposes, consequently, an effective conductivity must be determined for these layered materials. Given the layered nature of the active materials two different effective conductivities are required, specifically, one effective conductivity, k_{ser}, in the direction perpendicular to the layers, and one effective conductivity, k_{par}, parallel to the layers. Figure 8-4 shows, for two active material layers, the series and parallel thermal circuits used for calculating effective conductivities based on thermal resistances. Similar parallel and series effective conductivities are also calculated for the prismatic cell outer layers.

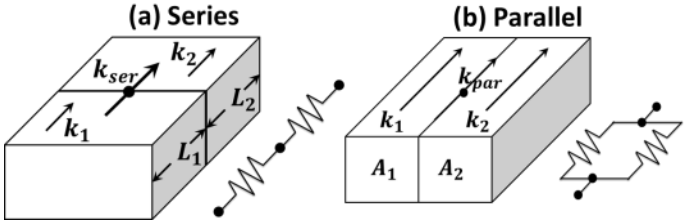

Figure 8-4: Schematic representation of the effective thermal conductivity estimation when the layers are connected in (a) series or (b) parallel (based on [39]).

Since the electrolyte fills the pores and gaps between the material particles and its thermal conductivity is comparable to that of particles, it is assumed that the contact resistance between the separator and electrodes in the active material layers, and between the separator and casing in the outside layer, is negligible. Therefore, whenever two layers are connected in a series configuration (Figure 8-4(a)), the thermal conductivity, k_{ser}, is determined by:

$$k_{ser} = \frac{L_1 + L_2}{\left(\frac{L_1}{k_1}\right) + \left(\frac{L_2}{k_2}\right)}, \tag{8-10}$$

and whenever the two layers are parallel (Figure 8-4(b)), the following equation provides the effective thermal conductivity, k_{par}:

$$k_{par} = \frac{A_1}{A_1 + A_2} k_1 + \frac{A_2}{A_1 + A_2} k_2 \tag{8-11}$$

where L is the layer length in the heat transfer direction and A is the layer cross-section normal to the heat transfer direction. In addition, since each layer is composed of different materials, such as conductive filler, polymer, and active material, the thermal conductivity of each layer, k_{layer}, is calculated based on the volume averaging as follows:

$$k_{layer} = \frac{\sum_i k_i V_i}{\sum_i V_i}, \tag{8-12}$$

where V is the volume of a specific component. In order to calculate the average product value of the heat capacity,C_P, and the density, ρ, the same volume weighted average method is used as in Equation (8-12) and is as follows:

$$\rho C_P = \frac{\sum_i \rho_i C_{P,i} V_i}{\sum_i V_i}. \tag{8-13}$$

8.3.3 Electrochemical-Thermal Coupling

In the case of prismatic cells, heat generation during their operation is large enough to noticeably change battery temperature. This temperature change affects the parameters required for electrochemical modeling such as the diffusion coefficients and electrochemical reaction rate constants. Therefore, the thermal and electrochemical models are highly coupled, and needs to be considered. To couple the thermal and electrochemical models, the method suggested by Song and Evan [50], which assumes a quasi-steady-state temperature at each time step, is adopted. By this assumption the electrochemical model is solved at a fixed temperature yielding the heat generation over the specified time step. The electrochemical heat generation and heat generated in the current collectors are then used in the thermal model to calculate a new temperature distribution in the prismatic cell. Finally, the new temperature distribution updates the electrochemical parameters utilized in the next time step electrochemical model. A schematic of this procedure is presented in Figure 8-5. Moreover, in order to make sure that the quasi-steady-state assumption holds throughout the simulation, the temperature variation along each time step is monitored. If the temperature variation at any point in the prismatic cell exceeds 1 ºC, that time step is halved and repeated.

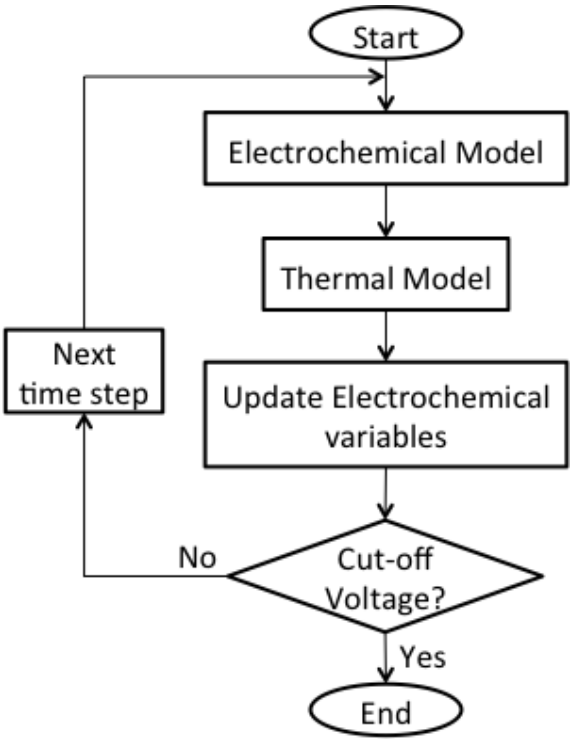

Figure 8-5: Schematic diagram showing the overall solution procedure and coupling between the electrochemical and thermal models.

8.4 Model Parameters

The required electrochemical parameters for the electrodes and separator are obtained from Li/graphite and Li/LFP half-cell simulations reported in Chapter 7. The low and high cut-off voltages for the prismatic cell are set to 2.4 V and 3.7 V, respectively (the 3.7 V limit is a manufacturer's recommendation, and the 2.4 V limit is an experimental apparatus limitation).

The temperature dependency of the electrodes' equilibrium potential is approximated using the data reported in the literature. Similar to Chapter 7, the data reported by Reynier et al. [197,198] is used for the graphite equilibrium potential temperature dependency and the data given by Dodd et al. [182,183] is utilized for the LFP equilibrium potential temperature dependency. These temperature dependencies are given in Figure 8-6(a) and Figure 8-6(b) for graphite and LFP electrodes, respectively. As explained in Chapter 7, for the temperature range studied in this paper, the

temperature dependency of the equilibrium potentials is negligible. However, they contribute significantly to the heat generation in active material layers as discussed in Section 8.3.2.2.

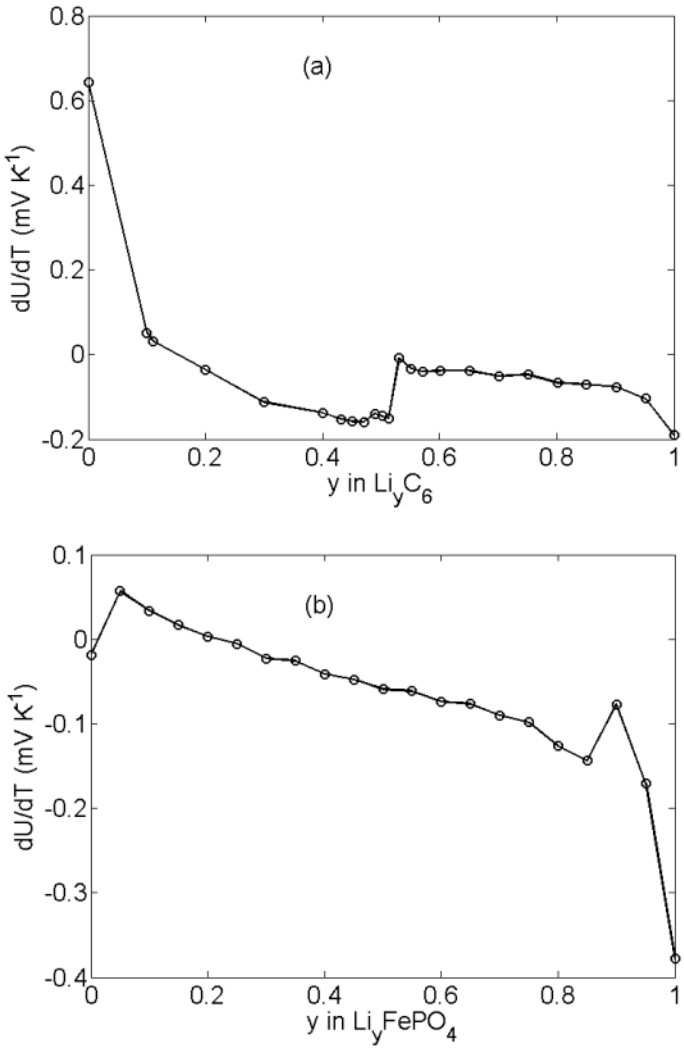

Figure 8-6: The equilibrium potential temperature dependency of the (a) graphite electrode [197,198] and (b) LFP electrode [182,183] as a function of lithium concentration.

In addition to the electrochemical parameters, the geometric parameters of the negative and positive double-sided electrodes in the prismatic cell are given in Figure 8-7. To measure these parameters the prismatic cell was cut and disassembled inside a glove box. The thickness of each layer in the prismatic cell is also given in Table 8-2. The separator and casing thicknesses were measured using a micrometer while the thicknesses of other layers are obtained from measurements

explained in Chapter 7. The parameters required for the thermal modeling of the prismatic cell include the density, heat capacity, and thermal conductivity of battery materials, as well as the electrical conductivity of current collectors, and are listed in Table 8-2. Finally, the electrical conductivities of the copper and aluminum current collectors in S cm-1 are given by Equations (8-14) and (8-15) [22]:

$$\sigma_{Cu} = -0.04889T^3 + 54.65T^2 - 21800T + 3.52 \times 10^6 \quad (8\text{-}14)$$

$$\sigma_{Al} = -0.0325T^3 + 37.07T^2 - 1500T + 2.408 \times 10^6 \quad (8\text{-}15)$$

where T is the local temperature of current collectors in K.

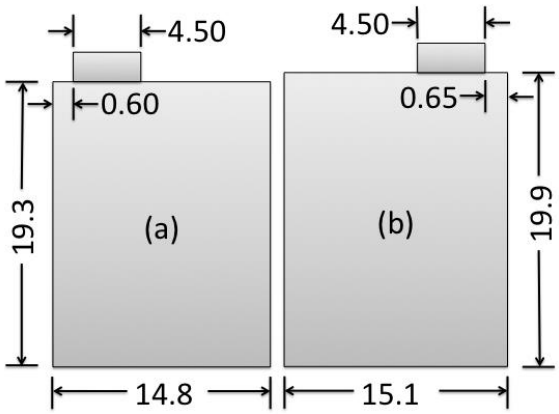

Figure 8-7: The geometric parameters of (a) the negative electrode and (b) the positive electrode. All dimensions are in cm.

Table 8-2: Thicknesses and thermal properties of battery components (m: measured, ma: Mastali et al. [257], li: Li et al. [238], ch: Chen et al. [39], ta: Taheri et al. [258]).

Material	Thickness, L, (μm)	Density, ρ, (kg m^{-3})	Heat capacity, C_p, (J kg^{-1} K^{-1})	Thermal conductivity, k, (W m^{-1} K^{-1})
Graphite	46 [ma]	2223 [li]	641 [li]	1.04 [li]
Separator	20 [m]	900 [li]	1883 [li]	0.5 [li]
LFP	59 [ma]	1500 [li]	800 [li]	1.48 [li]
Electrolyte		1210 [li]	1518 [li]	0.099 [li]
Copper	10 [ma]	8933 [ch]	385 [ch]	398 [ch]
Aluminum	19 [ma]	2702 [ch]	903 [ch]	238 [ch]
Casing	110 [m]	1150 [ta]	1900 [ta]	0.16 [ta]

8.4.1 Stoichiometry Window for Graphite and LFP Electrodes

Given the graphite and LFP electrochemical parameters from half-cell simulations as presented above, the two electrodes can now be combined to simulate a 20 Ah prismatic cell. To this end, however, the initial stoichiometries of the electrodes must first be estimated. When the prismatic cell is assembled for the first time, the LFP cathode is fully lithiated while the graphite (anode) is completely empty of lithium. During the first charge of the prismatic cell, a portion of the cathode lithium content forms a SEI layer on the surface of the graphite particles [259]. Since the exact amount of lithium consumed for SEI formation is unknown, the initial stoichiometry of the electrodes cannot be calculated. In addition, the stoichiometry window of each electrode during full charge/discharge depends on the capacity ratio of the electrodes [260].

To estimate the initial stoichiometries, the discharge/charge output voltage of the prismatic cell at a very slow rate of C/50 is simulated using the isothermal one-dimensional model presented in Section 8.3.1.1. The simulation of the prismatic cell using the one-dimensional model should be valid since the Ohmic losses in the current collectors, tabs, etc. are negligible at very low charge/discharge rates; thus, the normal current density distribution between current collectors is almost uniform. The temperature rise of the prismatic cell during operation is also insignificant at low C-rates, hence, the isothermal model is satisfactory for this simulation. Since the prismatic cell contains 48 cells, the measured electrode dimensions in Figure 8-7 yield a total surface area of 1.44 m^2 and 1.37 m^2 for the graphite and LFP electrodes, respectively. The graphite electrode is 5.1% greater in surface area compared to the LFP electrode for the purpose of preventing lithium plating at the edge of the graphite electrode [106,261,262]. This excess graphite area may be inactive, a suggestion that is tested next by allowing the ratio between the graphite and LFP electrode active surface areas to be treated as an adjustable parameter.

Referring to Figure 8-8, the initial stoichiometry of the LFP (graphite) electrode during discharge (charge) is estimated by fitting the model to the onset-of-discharge region of the prismatic cell voltage data. Similarly, the initial stoichiometry of the LFP (graphite) electrode during charge (discharge) is estimated by fitting the model to the end-of-discharge region voltage data. The initial

stoichiometries for discharge and charge are given in Table 8-3. Finally, the location of stage-2 graphite (Li_yC_{12}) voltage ramp region when fit to the model is used to evaluate the ratio between the graphite and LFP active surface areas. From this curve fit, the ratio between the graphite and LFP active electrode surface areas is determined to be 1.0 suggesting that the 5.1% greater physical surface area of the graphite electrode is inactive and solely exists for battery safety.

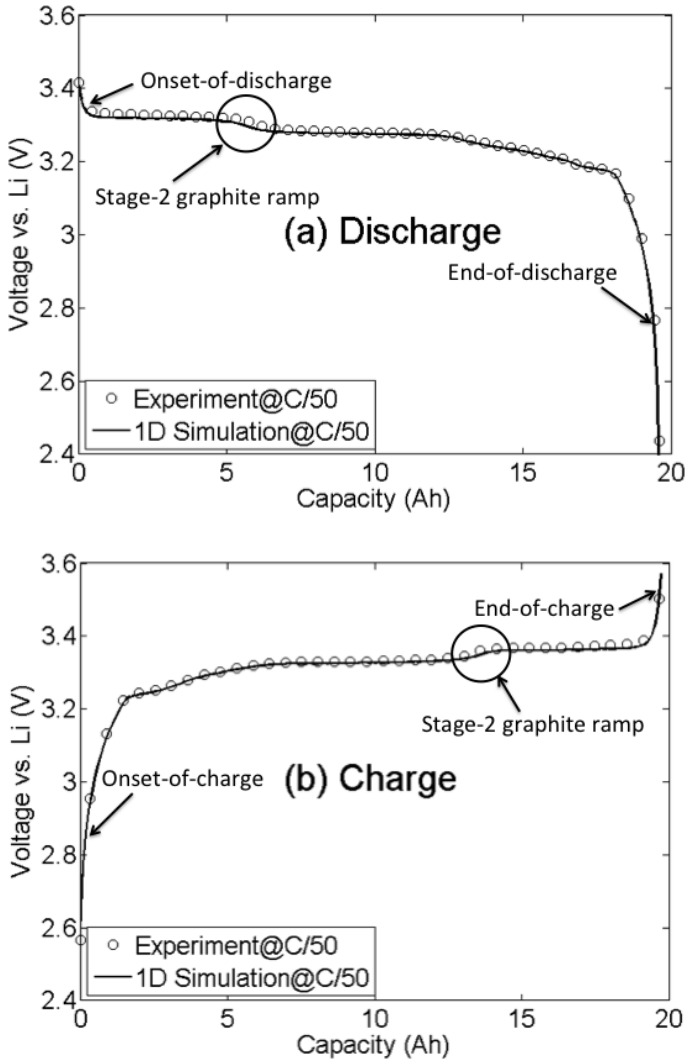

Figure 8-8: Fitting the experimental prismatic cell voltage curves at C/50 rate using the isothermal one-dimensional model at room temperature (24 ºC) during the (a) discharge and (b) charge process.

Table 8-3: The initial stoichiometry of electrodes in 20 Ah prismatic cells.

	Discharge	Charge
Graphite	0.816	0.003
LFP	0.012	0.941

8.5 Results and Discussions

This section presents the result of applying the developed model to a 20 Ah prismatic cell.

8.5.1 Model Implementation and Validation

As explained in Chapter 5, the equations described in Section 8.3 are finite volume discretized and implemented using an in-house Fortran code. To improve code convergence speed, a non-uniform structured grid is used as shown in Figure 8-9. This grid is finer in regions close to the tabs since the current densities and temperature gradients are larger in these locations. Moving further away from the tabs the grid becomes coarser as less sever gradients exist. It is important to note that the tabs are not included in the model, however, they still impact the thermal characteristics of the battery. To capture this impact the tabs are modelled as a heat source as explained later in the Figure 8-13. Specifically, a tab heats from Ohmic losses providing a heat source boundary condition at the tab/current collector interface.

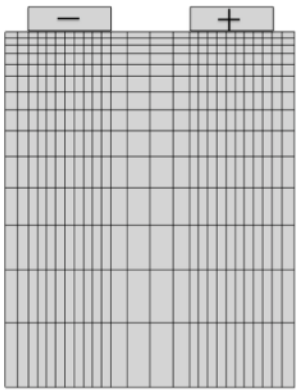

Figure 8-9: The non-uniform structured grid used for simulations.

Even with the model simplifications detailed above, computations are still intensive, more than 12 hours, for the 20 Ah prismatic cell when modelled with its 48 individual cells. Reviewing the few 48 cell prismatic cell computations it was observed that the current flowing through the current

collectors was virtually the same for all individual cells except for the two individual cells on either side of the prismatic cell. Since most of the model's computational time/cost is related to the current distribution calculation, the model is further simplified by considering only 6 individual cells for the current distribution calculation: the two individual cells on either side of the prismatic cell and two representative interior cells (see Figure 8-10). This simplification reduces maximum computation times to less than one hour. It is the one-dimensional electrochemical sub-routines that primarily slow the current distribution calculation. In contrast, the thermal calculations are fast and continue to use the full 48 individual cells.

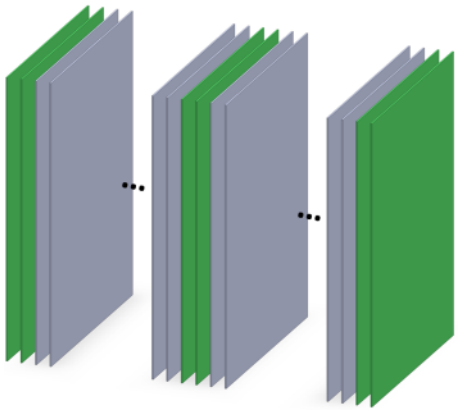

Figure 8-10: Shown in green are the six layers used for the current distribution calculations (two on each end, and two in the middle).

In order to validate the 20 Ah model, the measured operating voltage and temperature distribution on the surface of the prismatic cell are compared with the model voltage and temperature predictions. The experimental method and the temperature sensor locations are described in Section 8.2 and shown in Figure 8-1, respectively. Ambient temperature and initial prismatic cell temperature was 24 ºC. Experiment and simulation voltage curves during discharge and charge are compared in Figure 8-11 for charge and discharge rates ranging from 1C to 5C. The contact resistance between the current collectors and electrodes, R_c, as well as the total tab resistance are the only parameters adjusted to obtain these fits. The total tab resistance consists of the contact resistance that forms when joining the individual cell tabs into a single prismatic cell tab plus the Ohmic losses in the tab material itself. The individual cell tabs are joined together through a punch process. As explained in the following paragraphs, the current collector/electrode contact resistance

is estimated to be $1.5\times10^{-4}\ \Omega\ m^2$, and is determined by fitting the model to experiment surface temperatures. The total resistance for the tabs is also estimated to be $3\times10^{-4}\ \Omega$, and is determined by fitting model charge and discharge voltages where changing the total tab resistance shifts the voltage curves up or down. As expected, for an increasing tab resistance, the voltage curves shift down during discharge and up during charge. As seen in Figure 8-11, good agreement between the simulation results and experiment data is observed for all operating rates for charge and discharge.

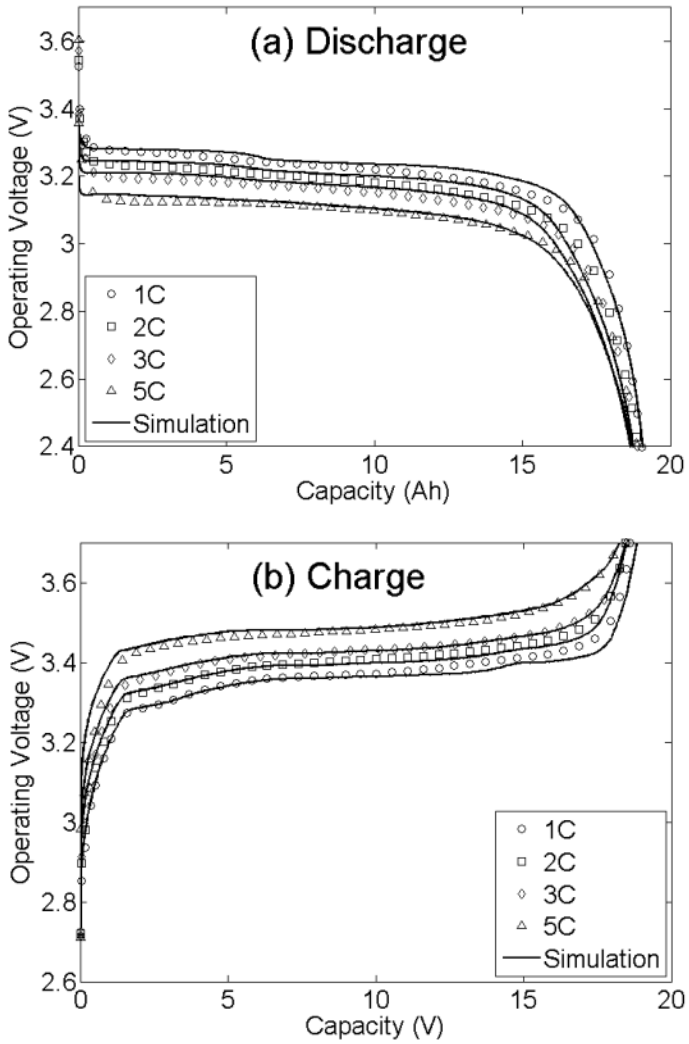

Figure 8-11: Comparison between the experimental operating voltages (markers) and simulation results (solid lines) at different (a) discharge and (b) charge rates (1C to 5C). Initial prismatic cell and ambient temperatures are 24 ºC.

In order to validate the thermal model used in this paper, the model predicted temperature distribution on the surface of the prismatic cell is compared to experimental data. However, it should first be noted that, as seen in Figure 8-1, for safety purposes, a safety flush-mounting plug (model ID/S6AR-N-S) [263] is used to connect the tabs to the cables carrying current from the battery cycler. These plugs are attached to the tabs using a nut and bolt connection that introduce a contact resistance between the cycler cables and the tabs. Referring to Figure 8-12, a close-up top view of the flush-mounting plugs is shown. Even though the tabs are not included in the model as has been noted above, they do experience Ohmic heating and therefore provide a heat flux boundary condition. This heat flux boundary condition is modelled as a heat source at the boundary of the current collector/tab interface. The importance of Figure 8-12 is to note that the total tab resistance is less than the resistance responsible for Ohmic heating of the tab, that is, the tab voltage is measured before the flush-mounting plug contact resistance. Consequently, in addition to the total tab resistance determined above, a heat generation resistance must be determined. The next paragraphs of this section explain how this heat generation resistance is determined.

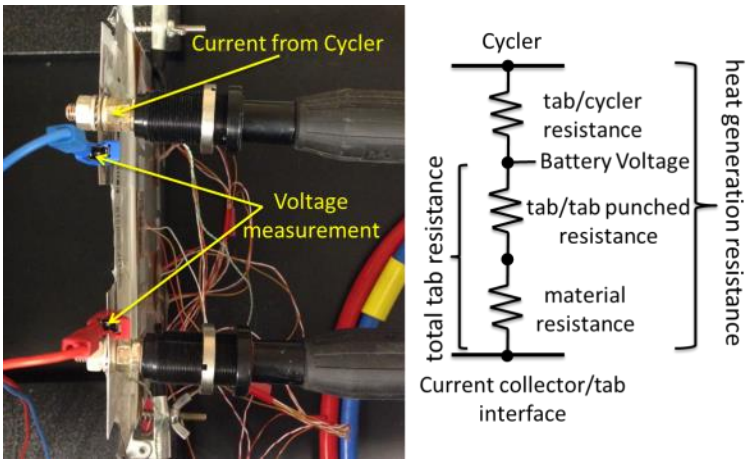

Figure 8-12: (left) the location of the voltage measurement as well as the nut and bolt connection utilized to attach the tabs to the battery cycler cables, and (right) the schematic of the total tab and heat generation resistances used in the developed model to validate the cell voltage and temperature distribution on the surface of the prismatic cell, respectively.

To have a better understanding about the heat transferred from the tabs toward the battery, two thermocouples are connected to the battery tabs and the recorded temperatures are compared with the prismatic cell surface temperatures at locations near the tabs. Figure 8-13, for instance, shows

this comparison during 5C charge/discharge rates. As seen, the tab temperatures are much higher compared to the points on the battery surface resulting in a significant heat transfer from the tabs toward the battery current collectors.

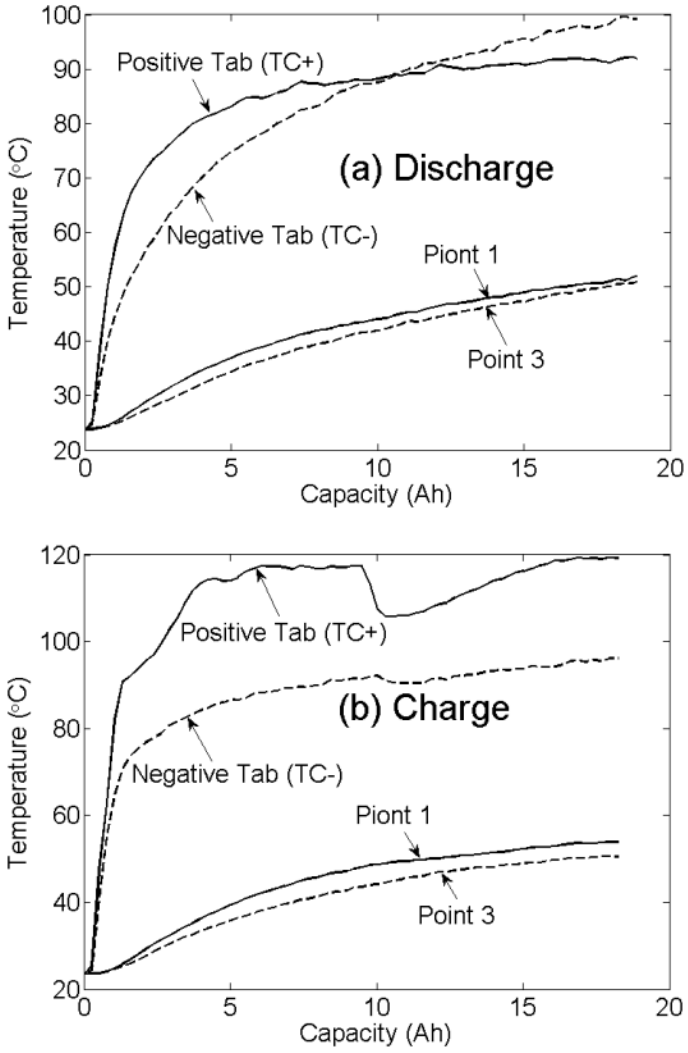

Figure 8-13: Comparison between the experimentally measured temperatures at the positive and negative tabs, and at the points closest to the tabs on the prismatic cell surface during (a) 5C discharge and (b) 5C charge rates. See Figure 1 for measurement locations.

In order to determine the heat generation resistances at the positive and negative tabs, the model predicted temperatures at the surface of the prismatic cell are fitted to the experiment data especially at locations closer to the tabs. In addition to these resistances, the contact resistance between the

electrodes and current collectors are obtained by fitting the measured temperatures at the cell surface, however, with more attention paid to the surface temperatures at the bottom of the prismatic cell. It should be mentioned that the values of 0.7 for emissivity and 2 W m^{-2} K^{-1} for convective heat transfer coefficient [264] are used to describe the heat transfer boundary condition at the battery surface. This fitting process, during the 5C discharge process yields the values of 5.0×10^{-4} Ω and 3.6×10^{-4} Ω for heat generation resistances at the positive and negative tabs, respectively. For 5C charge process, the values of 6.7×10^{-4} Ω and 4.8×10^{-4} Ω at positive and negative tabs are obtained, respectively. Higher values for the heat generation resistance at the positive tabs compared to the negative tabs as well as for the charge compared to the discharge is consistent with the higher recorded temperatures at the positive tabs and during the charge (Figure 8-13). Moreover, as expected the heat generation resistances are larger than the total tab resistances since they additionally include tab/cycler resistance (Figure 8-12). The contact resistance between the electrodes and corresponding current collectors is also estimated to be 1.5×10^{-4} Ω m^2. As shown in Figure 8-14 for 5C charge/discharge process, good agreement between the simulation results and experiment data is observed. Some discrepancy is observed between the simulation and experiment in the points 1, 2, and 3 (on top of the battery) that may be described by noting that constant heat generation resistances are utilized to model the time-variant heat transfer from the tabs.

The results of described fitting process at the charge/discharge rates ranging from 1C to 5C are given in Table 8-4. To show the accuracy of the results, the comparison between the model predicted temperatures at point 5 and experiment data are presented in Figure 8-15. Good agreement between the simulation results and experiment data is observed at all operating rates. As seen in Table 8-4, the estimated heat generation resistances vary with operating rates. This may be explained by noting that not all the heat generated in the tabs is conducted to the battery current collectors. The rest of this heat generation, actually, is lost to the surroundings and also conducted through the cycler cable. The smaller the transferred portion of the tabs' heat generation to the battery is, the smaller the heat generation resistance will be. In higher operating rates, since the tabs' temperatures are higher, a larger portion of the generated heat is lost to the environment leading to the lower heat generation resistances consistent with the results listed in Table 8-4. It may also be noted that the positive tab

heat generation resistances for 1C rate charge/discharge are more than one order of magnitude larger than the total tab resistance (1.5×10^{-4}), confirming the high resistance in the nut and bolt connection of the cycler to the tab.

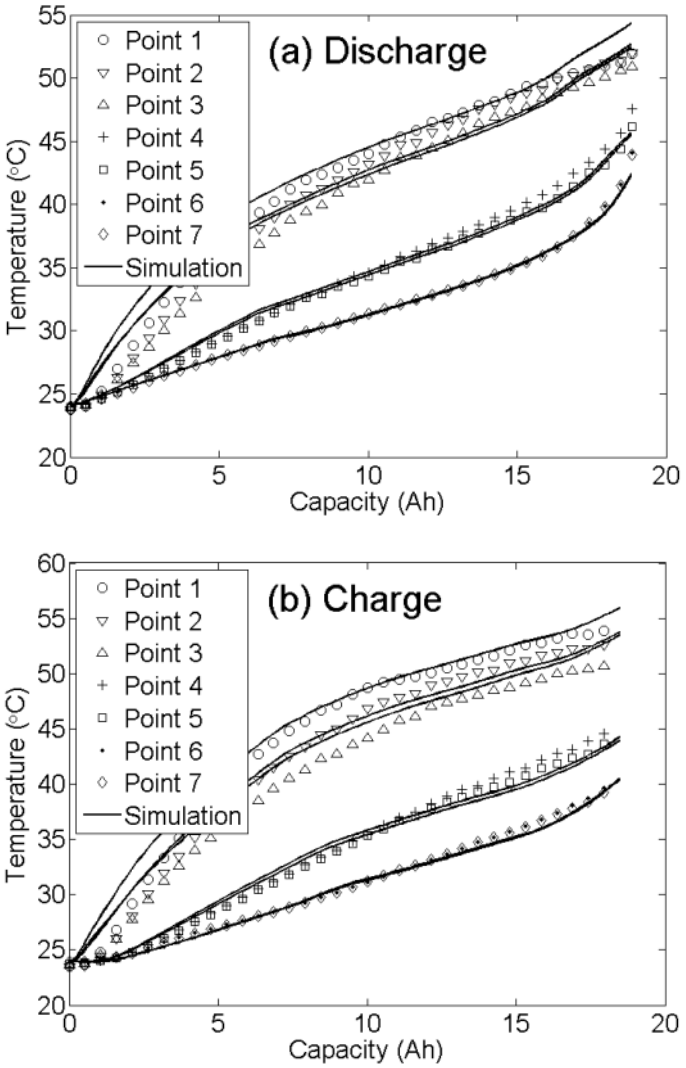

Figure 8-14: Comparison between the measured temperatures at different locations on the prismatic cell surface (markers) and simulation results (solid lines) at 5C (a) discharge and (b) charge rate. Initial prismatic cell and ambient temperatures are 24 ºC.

Table 8-4: The heat generation resistances at positive and negative tabs in Ω for different discharge and charge rates.

Tab	1C discharge	1C Charge	2C discharge	2C Charge	3C discharge	3C Charge	5C discharge	5C Charge
Positive	3.5×10^{-3}	4.2×10^{-3}	1.5×10^{-3}	1.8×10^{-3}	8.7×10^{-4}	1.3×10^{-3}	5.0×10^{-4}	6.7×10^{-4}
Negative	7.6×10^{-4}	7.6×10^{-4}	6.4×10^{-4}	7.6×10^{-4}	5.6×10^{-4}	9.2×10^{-4}	3.6×10^{-4}	4.8×10^{-4}

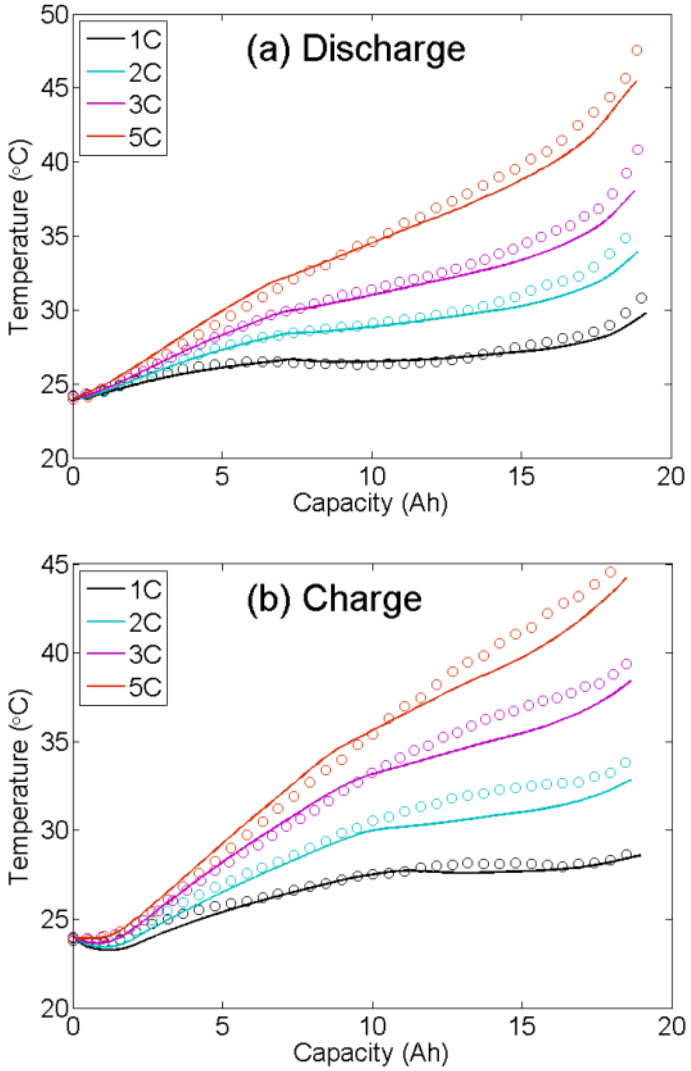

Figure 8-15: Comparison between the measured temperatures at the prismatic cell surface (markers) at point 5 (shown in Figure 8-1) and simulation results (solid lines) at different (a) discharge and (b) charge rates of 1C, 2C, 3C, and 5C with the initial cell and ambient temperatures of 24 °C.

8.5.2 Temperature Effect on the Prismatic Cell Performance

As shown in Figure 8-11, during both charge and discharge, the end capacities are almost independent of operating rate. According to the experiments presented in Ref. [257] for coin cells, this is not expected since the electrochemical performance of the electrodes decreases as operating rate increases. Safari and Delacourt [105,106] discussed that the better electrochemical performance of commercial cells compared to the coin cells is due to their higher uniaxial pressure. They suggested that increasing the pressure actually decreases the contact resistance between the LFP particles and conductive matrix yielding electrode performance improvement.

In this paper, another point of view based on the effect of temperature on electrochemical performance of batteries is presented. Isothermal simulations of the prismatic cell at 24 ºC and 5C Charge/discharge rates show that the cell capacity significantly decreases especially in the discharge process (Figure 8-16). Repeating the isothermal simulations at higher temperatures (45 ºC) and at the same 5C Charge/discharge rates, however, represents that the temperature rise increases the cell electrochemical performance and shifts the end capacities to the larger values. This effect is actually due to the temperature dependency of electrodes' kinetic and transport properties, especially the LFP electrode diffusion coefficient. Finally, the prismatic cell charge/discharge simulations at 5C Charge/discharge rates are given in Figure 8-16. These results show that at the beginning of 5C charge/discharge since the cell temperature is 24 ºC, the output voltages of the cell during both charge and discharge match the isothermal simulation predictions at 24 ºC. Upon charging/discharging the prismatic cell, however, the cell temperature increases and the operating voltage of the prismatic cell approaches toward the 45 ºC isothermal simulation results. This reveals that during the prismatic cell operation, the self-heating may be the reason for improving the electrochemical performance of the prismatic cell.

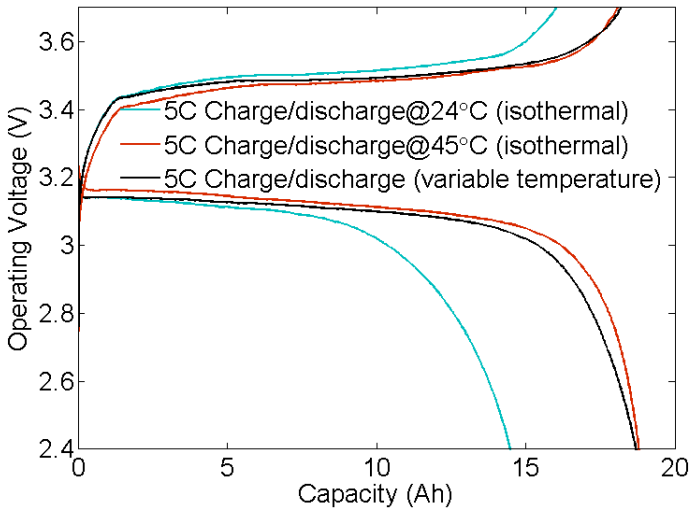

Figure 8-16: Investigating the effect of the discharge rate and temperature on the pouch cell end-capacity.

8.5.3 Temperature Distribution and Heat Generation

In this section, the temperature distribution and heat generation in the prismatic cell is discussed. Temperature distribution on the central cell of the prismatic cell (cell number 24) and temperature variation between the surface and center of the prismatic cell are discussed. Moreover, the heat generation in negative and positive current collectors as well as the heat generation in active material layers are displayed for a representative cell (central cell). All the studies are carried out at 5C rate since the heat generation is maximum during this rate and the highest temperatures are achieved; hence, gives the limitations of the battery operation. The effect of ambient temperature on prismatic cell behavior is not discussed and is left for future studies. In all simulations, the ambient temperature is considered to be the same as the lab actual temperature equal to 24 ºC.

The heat generated rate in the active material layers and current collectors of 24th cell of the prismatic cell are shown separately in Figure 8-17 and Figure 8-19, respectively. In the case of current collectors, since the current flowing inside the current collectors is almost constant with respect to time, the heat generation rate does not change during the battery operation. In addition, between the charge and discharge processes, only the current direction varies and its value remains constant. Therefore, the heat generation rate in the current collectors of the 24th cell is shown solely for the middle of the discharge process. Figure 8-17 illustrates that the heat generated close to the

current collectors' tab is larger compared to the other parts. Given that the heat generation in current collectors is the result of the resistance against electron movements, closer to the tabs where current density is higher, the heat generation rate is maximum. However, except that region, the heat generation rate in other current collector locations is insignificant. The main heat source in these locations is the heat generated in active material layers, as seen in Figure 8-19. Comparing Figure 8-17(a) and Figure 8-17(b) shows that the heat generation in both current collectors are similar since their electrical resistivity and current distribution are almost the same.

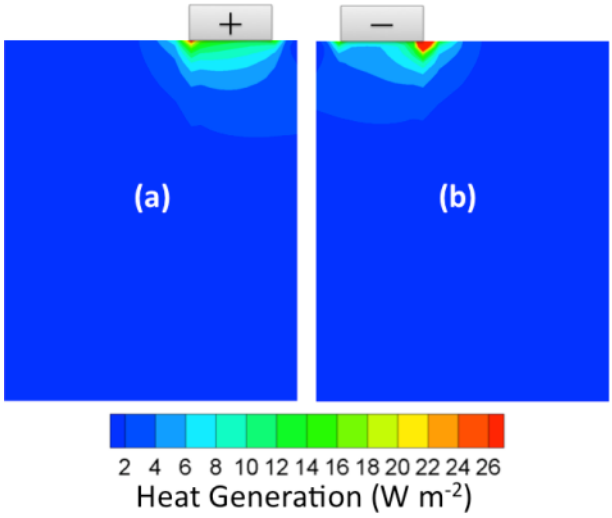

Figure 8-17: Heat generation in (a) positive and (b) negative current collectors of 24th cell of the prismatic cell in the middle of a 5C discharge rate with the initial cell and ambient temperatures of 24 °C.

In contrast to the current collector heat generation, the heat generated in the active material layers poses a very dynamic behavior depending on the normal current density crossing the layers, electrode material properties, and the prismatic cell local stat of the charge. In order to have a better idea about this heat generation, the normal current density in the 24th cell for three representative points at top, middle, and bottom of the cell during the 5C discharge and charge rates are shown in Figure 8-18. The locations of these points are already given in Figure 8-1. As seen in Figure 8-18, the normal current density at the top of the prismatic cell (closer to the tabs) is initially higher than the other parts and by moving to the bottom parts the normal current density is lowered. However, at the end of battery operation the distribution of the normal current density is reversed and the bottom parts shows higher normal current densities.

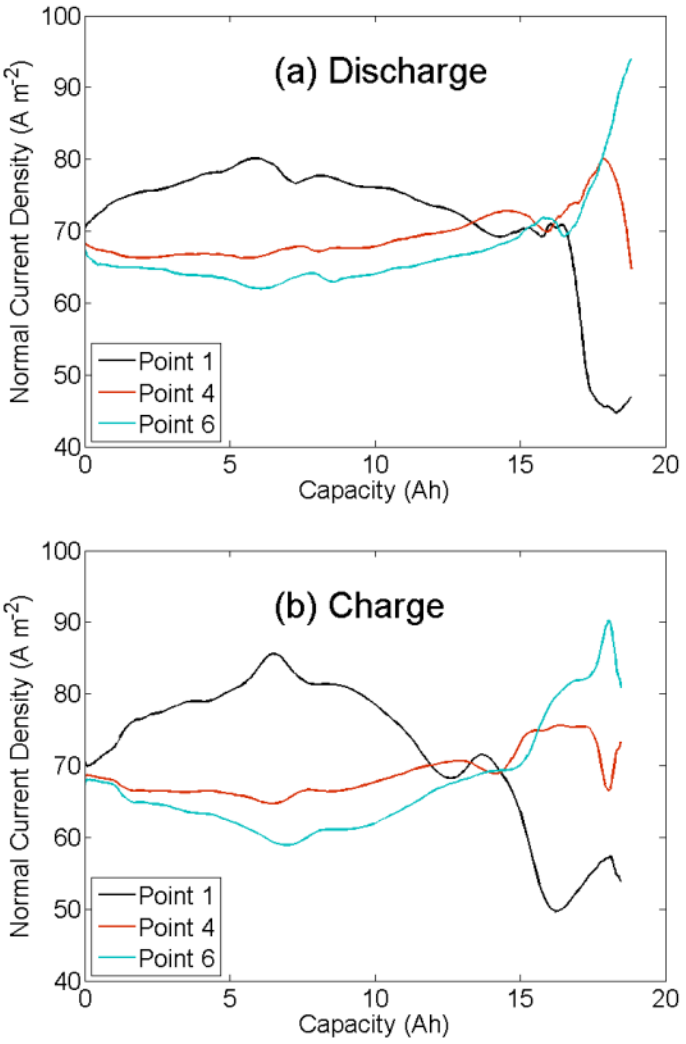

Figure 8-18: Normal current density crossing the active material layers in the 24th cell of the prismatic cell for three representative points on top, middle, and bottom of the cell during the 5C rate (a) discharge and (b) charge with the initial cell and ambient temperatures of 24 ºC.

Figure 8-19 presents heat generation rate in the same points. As seen, the heat generation rate is correlated with the normal current density. For example, at the end of the discharge, there is an increase in the heat generation at the bottom of the cell corresponding to the increase in the normal current density at that location. In addition, in the beginning of the battery operation when all locations are the same state of the charge, the top parts of the prismatic cell generate more heat compared to the lower parts since the normal current density is higher at those locations. Another important factor affecting the heat generation rate in battery active material layers is the entropic

heat generation [265]. For instance, it causes sharp increase in the heat generation rate at the end of especially discharge process. As seen, at the end of the discharge, the heat generation rate at point 1 (at the top of the prismatic cell) is increased even with decreasing the normal current density. In addition, the negative heat generation rate in the beginning of the charge is the result of entropic heat.

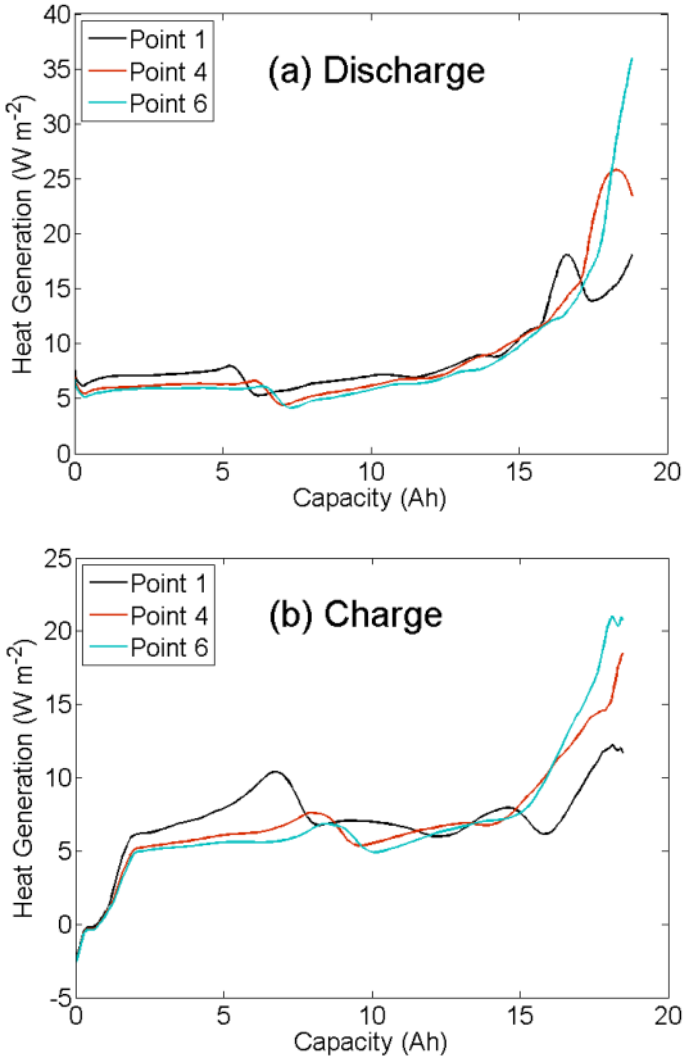

Figure 8-19: Heat generation in the 24th cell of the prismatic cell for three representative points on top, middle, and bottom of the cell during the 5C rate (a) discharge and (b) charge with the initial cell and ambient temperatures of 24 ºC.

Figure 8-20 shows the temperature distribution on the 24th cell of the prismatic cell in the middle and end of the 5C discharge and charge rates with the initial cell and ambient temperatures of 24 ºC. As seen, the temperatures close to the tabs are higher compared to those at other locations especially at the bottom of the cell. This is mostly attributed to the larger heat generation rates closer to the tabs in current collectors as well as the heat transferred from the tabs to the current collectors.

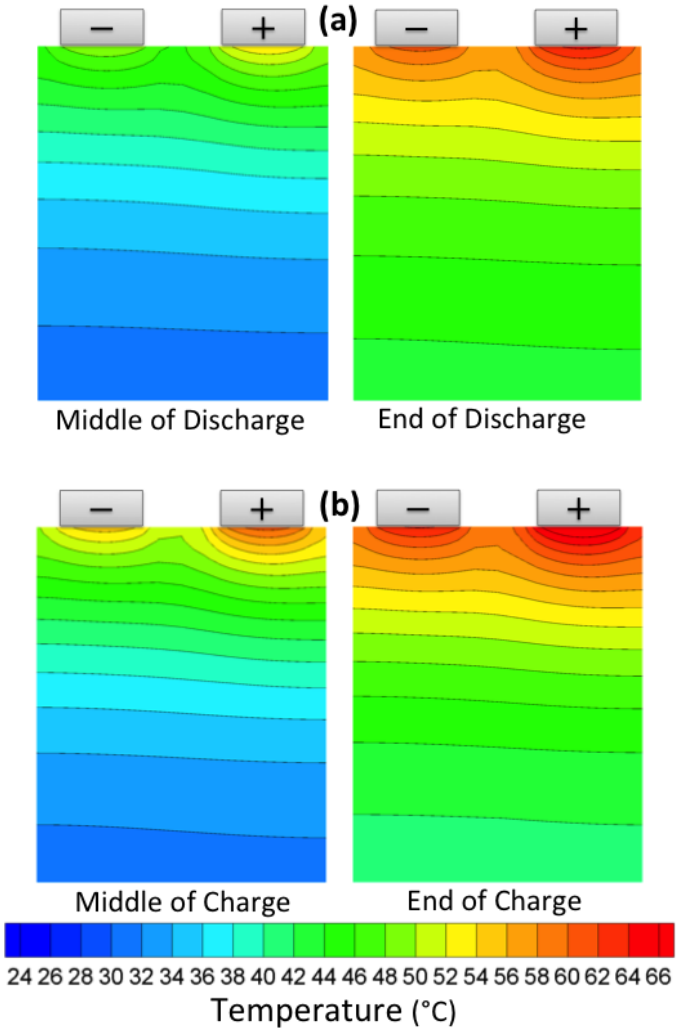

Figure 8-20: The temperature distribution on the 24th cell of the prismatic cell in the middle and end of 5C (a) discharge and (b) charge with the initial cell and ambient temperatures of 24 ºC.

Figure 8-21 shows the temperature at the center and surface of the prismatic cell for three representative points on the top, middle, and bottom of the cell (points 1, 4, and 6 in Figure 8-1,

respectively). The operating rate of these simulations is 5C and the initial cell and ambient temperatures are set 24 ºC. As expected, the temperature at the center is always higher than the temperature at the surface of the cell. This is more remarkable at locations closer to the top of the prismatic cell due to the larger heat generation rate in those locations as observed in Figure 8-17 and Figure 8-19. For the simulation presented in Figure 8-21, however, the temperature difference between the center and surface of the prismatic cell seems insignificant. For instance, it does not exceed 2 ºC at the end of both discharge and charge processes for point 1 located on the top of the cell. Repeating the simulation with larger convective heat transfer coefficients leads to larger temperature difference between the surface and center of the cell. However, this temperature difference even for a convective heat transfer coefficient as large as 20 W m^{-2} K^{-1} does not become greater than 3 ºC. It should be noted that this temperature differences are built up during a single battery charge or discharge process. However, when batteries are operating in an electric vehicle environment under continuous charge/discharge cycles, the temperature difference between their center and surface may reach the higher values. This is planned as future work.

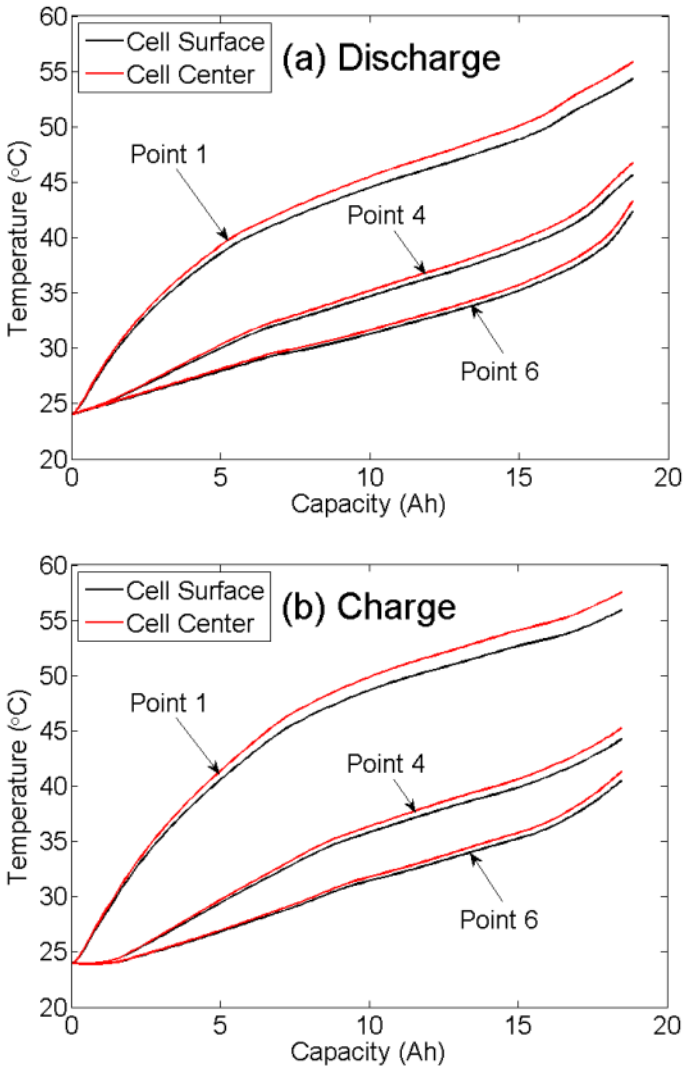

Figure 8-21: Comparing the temperatures at the center and surface of the prismatic cell for three representative points on top, middle, and bottom of the cell during the 5C (a) discharge and (b) charge with the initial cell and ambient temperatures of 24 ºC.

Chapter 9 Conclusions and Recommendations

9.1 Conclusions and Contributions

In this thesis, different one-dimensional, three-dimensional, and multi-layer three-dimensional electrochemical-thermal models for Li-ion batteries are developed and validated against experimental data. The models were developed, and represent a major step towards modeling vehicle battery packs including internal thermal heating. The next sections summarize the conclusion for the increasingly capable models developed.

9.1.1 Kalman Filtering

In Chapter 3, a method based on the Kalman filtering theory is developed to estimate SOC in a battery management system (BMS) for $LiFePO_4$ cells, and this method is applied to both cylindrical and prismatic cells. Three models are utilized to describe the battery dynamics in a hybrid electric (HEV) or plug-in hybrid electric vehicle (PHEV). It is found that the simple model presents a deviation even in the constant voltage charging periods, whereas the hysteresis-state model generates the best predictions in both dynamic and static environments. The zero-state hysteresis and hysteresis-state models are subsequently implemented in two types of Kalman filtering processes in order to estimate the SOC of the battery. The extended Kalman filter is used in the case of the fixed-parameter (zero-state hysteresis) model, and the dual extended Kalman filter is employed for the varying-parameter (hysteresis-state) model. In the dual method, the model parameters and the SOC of the battery are simultaneously estimated using Kalman filtering. The implementation of both filters is described in detail and then the results of the Kalman filtering are compared with experimental data. Good agreement (less than 4%) is observed between Kalman filtering methods and the experimental data, indicates that the proposed methods can properly predict the SOC of the battery under dynamic environments such as in a PHEV application. Accordingly, it can effectively be used in BMS. The method is also employed to predict the SOC of a prismatic cell, showing the filter capabilities to estimate the SOC for different types of batteries. Analysis of the parameters

calculated by the filter reveals that these values depend on the type of battery (e.g. geometrical factors varying their properties). However, these parameters can be quickly determined from an initial study of a specific cell configuration, and subsequently used for that cell type under other operating conditions. Although the method presented in this chapter estimates the states of the battery well, the estimated battery parameters may be not accurate due to the curve-fitting feature of this method. Therefore, the method lacks the predictive ability and cannot effectively be used for thermal modeling of batteries using the estimated parameters. As a result, the presented method in Chapter 3 is not followed in the next chapters. However, due to the different type of models (equivalent circuit models) developed in this chapter as well as valuable insights provided about battery states and parameters, Kalman filtering method is not excluded from this thesis.

9.1.2 Simplified One-Dimensional Model

In order to increase the computational efficiency in mathematical modeling of Li-ion batteries, two simple yet accurate multi-particle (SEMP and HP2D) models are developed and validated for a known commercial LFP electrode in Chapter 4 and Chapter 5. In the developed models, the Li insertion/deinsertion process into/out of LFP particles is modeled using the VSSD concept and four particle bins are considered to represent the apparent PSD of the cathode. In general, depending on the active materials used in the electrode and regardless of microscopic details of Li transport within the particles, including more than one particle bin with different intrinsic or geometric properties remains a common practice. The effect of the electrolyte is added in the SEMP model by incorporating a polynomial approximation method wherein the electrolyte variables are expressed as cubic and quadratic polynomials or solved analytically. In the HP2D model, however, the electrolyte effect is added by solving the electrolyte mass and charge conservation equations using the assumption of homogenous electrochemical reaction across the electrodes. It is shown that the one-dimensional SEMP and HP2D models can accurately predict the operating voltage of LFP half-cells with a maximum 2.5% and 1.5% error, respectively, compared to the standard Newman P2D model. In addition, the simple models are one order of magnitude faster than the P2D model and can safely replace the P2D model to increase the speed of the simulations.

9.1.3 Three-Dimensional Model

In Chapter 5, the developed one-dimensional models are expanded for three-dimensional simulations using two different approaches. In one approach, a combination of one-dimensional SEMP models is utilized; while in the second approach (three-dimensional HP2D model), except the solid-phase, the other regions were solved three-dimensionally. It has been indicated that not considering three-dimensional effects might be acceptable for calculation of the electrochemical current generation distribution, but it will introduce larger errors in predicting the heat generation of the battery. Finally, since the simulation times of both models are almost the same, it is suggested that the three-dimensional HP2D model is used as a reliable fast three-dimensional model with or without thermal effects being considered.

9.1.4 Parametric Study

As described in Chapter 6, reducing the non-uniformities in the cell can reduce battery ageing and hence effectively increases the durability of the cell. Therefore, the developed three-dimensional model in Chapter 5 is used to study the effect of two parameters (current collectors' thickness and the battery tab locations) on non-uniformity of the variables in the cell. It is observed that increasing the thickness of the current collectors make the distributions more uniform. In addition, it is shown that changing the tab configurations may positively alter the distribution of the electrochemical current generation in the cell. It is concluded that transferring tabs from the edges and the same side (common commercial design) to the center and opposite sides of the cell, and extending them as much as possible in width, can lower the non-uniformity variation in electrochemical current generation by 7%.

9.1.5 Parameter Characterization

Chapter 7 validates the simulated Li/LFP and Li/graphite half-cell voltages against experimental data and extends the application of the VSSD model to a broader range of charge/discharge rates and temperatures for both LFP and graphite electrodes. Fitting simulation results to experimental voltage data at various galvanostatic charge/discharge rates (C/5 to 5C) and temperatures (10 ºC, 23 ºC,

35 ºC, and 45 ºC) provides estimates of the kinetic and transport parameters of the electrode active materials in a wide range of operating conditions. As the result, the activation energies for diffusion in LFP and graphite particles are estimated to be 89 kJ mol^{-1} and 20 kJ mol^{-1}, respectively. Furthermore, the activation energies for charge-transfer reaction at the surface of LFP and graphite particles are 9 kJ mol^{-1} and 20 kJ mol^{-1}, respectively. The modeling/experimental framework pursued in this chapter proves more comprehensive methodology for estimating the transport and kinetic properties of LFP and graphite, and their temperature dependencies. Furthermore, this framework is general and can be applied to other battery active materials.

9.1.6 Prismatic Cell Model

In Chapter 8, an electrochemical-thermal model for a 20 Ah prismatic cell is developed and validated against the experimental data for charge/discharge rates varying from 1C to 5C. Physics-based one-dimensional electrochemical models are coupled with charge conservation and heat diffusion equations to describe the electrochemical and thermal variable distributions throughout the battery domain. The accuracy of the model in predicting the cell output voltage and the temperature distribution on the surface of the prismatic cell confirms the ability of the model to be incorporated for other battery materials and geometries. In this model, all the electrochemical properties of the graphite and $LiFePO_4$ electrodes are obtained from half-cell simulations performed on the same electrode materials. The rest of parameters are obtained from literatures or measurements, thus, the estimated parameters for prismatic cell are more physical.

Using the developed model, first, the temperature rise effect due to the 20 Ah prismatic cell self-heating on the cell electrochemical performance is discussed. It is shown that higher temperatures improve the kinetic and transport properties of the electrodes yielding the better electrochemical performance of the large-sized prismatic cell. Thereafter, the temperature and heat generation distributions of the prismatic cell during charge and discharge are discussed. Some important factors such as heat generation in the current collectors, the reversible entropic heat generation, and the effects of three-dimensional normal current density distribution on the heat generation are also explained in this chapter. Finally, the simulation results reveal that in the case of prismatic cells the

temperature gradient across the cell thickness is negligible. It is observed that even at high charge/discharge rates and with high heat transfer coefficients at the surface of the prismatic cell the temperature gradient across the cell does not exceeds 3 ºC and therefore might be neglected.

9.2 Recommendations

This thesis provides a solid framework for the electrochemical-thermal modeling of the Li-ion batteries. There are a number of potential extensions and recommendations that could be considered for future research:

- One problem associated with the Kalman filtering method introduced in this thesis is estimating non-physical parameters for the Li-ion battery. This problem may be overcome by replacing the equivalent circuit model used in the filter with a more physical model such as the averaged electrochemical model [62,266].
- Although the simplifying methods reported in this thesis highly reduce the simulation time of the Newman pseudo-two-dimensional model, there is still some rooms for the improvements. As explained in the thesis, the computational cost of the one-dimensional electrochemical model is mainly associated with solving the mass conservation equation inside the active material particles. In this thesis, simple numerical finite volume approach applied on a fixed numerical grid solves this equation. However, some methods such as adaptive grid generation based on the lithium concentration gradient at each time step may speed up this process [267]. Some analytical methods such as symmetry analysis or perturbation theory may also simplify or approximate mass balance equation in the active material particles [268,269]. In addition, analytical methods such as separation of variables can be incorporated for analytical solution of the mass and charge conservations in the electrolyte domain leading to reducing the simulation time [270,271].
- In the electrochemical-thermal model presented in this thesis, the same numerical grid is used for solving of the electrochemical and thermal equations. The grid used for electrochemical model may, however, be separated from the one used for thermal

modeling since accurate results can be obtained even by utilizing coarser grids for electrochemical model [113,178]. In addition adaptive grid generation methods can be used for both models to improve computational efficiency of the model [272].

- In the case of $LiFePO_4$ electrodes, a zero current hysteresis exits between the charge and discharge potentials [180,273]. This hysteresis is due to the entropic effects, mechanical stress, and microscopic distortions inside the active material particles during lithium insertion or extraction [274]. To include the hysteresis effect in Li-ion battery models, however, the involved phenomena are not usually added to the battery model. In Li-ion battery electric circuit models the OCV is considered as the sum of an averaged OCV and a hysteresis term [45,46,275,276]. The hysteresis term is then estimated using off-line approaches or as a battery state. In physics-based models, however, the hysteresis effect is included in the model by considering separate OCVs for charge and discharge [108,109]. It is explained in Chapter 7 and Chapter 8 that the same procedure of considering separate charge and discharge OCVs for each electrode is used in this thesis to account for the hysteresis effects. As a result, the developed model not only predicts the output voltage of the coin and prismatic Li-ion cells during galvanostatic charge and discharge processes, but also simulates the behavior of the Li-ion battery under dynamic charge and discharge cycles such as those observed in electric vehicles. It is recommended that the developed model to be used for simulating the battery output voltage, and current and temperature distributions under different drive cycles. In this way, the battery design and thermal management system of the battery can be optimized in order to prevent the battery overheating and also improve the uniformity of temperature and current distributions.
- In this thesis, the electrochemical-thermal model is simulating up to the prismatic cell. This model can easily be extended to simulate a module or even a pack. However, since the computational time of a prismatic cell is in the order of an hour, extending this work to higher levels consisting of even 100 individual prismatic cells may result in very long

simulation times. Some more simplifications in this case are suggested such as neglecting the electrochemical variable distribution on the active layers.

- The developed electrochemical-thermal model in this thesis has not been used to study the effect of different parameters on the electrochemical and thermal behavior of the prismatic cell. Since the developed model includes length scales ranging from nano-sized particles to multi centimeters cells, the mutual effects of different phenomena at different length scales can be studies using this model. For example, the effect of size and chemistry of the active material particles on the thermal behavior of the prismatic cell can easily be studied using the developed model.

References

[1] WWF CLIMATE CHANGE AND ENERGY PROGR AM, Greenhouse Gas Reduction Potential of Electric Vehicles : 2025 Outlook Report, 2012.

[2] F.R. Kalhammer, B.M. Kopf, D.H. Swan, V.P. Roan, M.P. Walsh, Status and Prospects for Zero Emissions Vehicle Technology, 2007.

[3] D. Linden, T.B. Reddy, eds., Handbook of Batteries, 2nd ed., McGraw-Hill, New York, 2002.

[4] Cadex Electronics, Http://batteryuniversity.com/ (2011).

[5] R. Spotnitz, in:, Adv. Lithium Ion Batter., Kluwer Academic / Plenum Publishers, New York, 2002, pp. 433–458.

[6] A. Dinger, R. Martin, X. Mosquet, M. Rabl, D. Rizoulis, M.R. And, G. Sticher, Batteries for Electric Cars, Challenges, Opportunities, and the Outlook to 2020, The Boston Consulting Group, 2010.

[7] A.A. Pesaran, G.-H.K. And, M. Keyser, in:, EVS24, Stavanger, Norw., 2009.

[8] F. V. Conte, J. Elektrotechnik Informationstechnik 123 (2006) 424.

[9] B.L. Ellis, K.T. Lee, L.F. Nazar, Chem. Mater. 22 (2010) 691.

[10] T.L. Kulova, Russ. J. Electrochem. 49 (2013) 1.

[11] S.R. Alavi-Soltani, T.S. Ravigururajan, M. Rezac, in:, Mater. Nondestruct. Eval. Press. Vessel. Piping, Chicago, Illinois, 2006.

[12] T.M. Bandhauer, S. Garimella, T.F. Fuller, J. Electrochem. Soc. 158 (2011) R1.

[13] M. Broussely, in:, Adv. Lithium-Ion Batter., Kluwer Academic / Plenum Publishers, New York, 2002, pp. 393–432.

[14] M. Broussely, P. Biensan, F. Bonhomme, P. Blanchard, S. Herreyre, K. Nechev, R.J.

Staniewicz, J. Power Sources 146 (2005) 90.

[15] H. Yang, S. Amiruddin, H.J. Bang, Y.-K. Sun, J. Prakash, J. Ind. Enginieering Chem. 12 (2006) 12.

[16] G.-H. Kim, A. Pesaran, R. Spotnitz, J. Power Sources 170 (2007) 476.

[17] C.R. Pals, J. Newman, J. Electrochem. Soc. 142 (1995) 3274.

[18] J. Fan, S. Tan, J. Electrochem. Soc. 153 (2006) A1081.

[19] M. Doyle, T.F. Fuller, J. Newman, J. Electrochem. Soc. 140 (1993) 1526.

[20] T.F. Fuller, M. Doyle, J. Newman, J. Electrochem. Soc. 141 (1994) 1.

[21] K. Thomas, J. Newman, and R. Darlin, in:, Adv. Lithium-Ion Batter., Kluwer Academic / Plenum Publishers, New York, 2002, pp. 345–392.

[22] R.E. Gerver, J.P. Meyers, J. Electrochem. Soc. 158 (2011) A835.

[23] G.-H. Kim, K. Smith, K.-J. Lee, S. Santhanagopalan, A. Pesaran, J. Electrochem. Soc. 158 (2011) A955.

[24] D. Bernardi, E. Pawlikowski, J. Newman, J. Electrochem. Soc. 132 (1985) 5.

[25] L. Rao, J. Newman, J. Electrochem. Soc. 144 (1997) 2697.

[26] K.E. Thomas, J. Newman, J. Electrochem. Soc. 150 (2003) A176.

[27] J. Hong, H. Maleki, S. Al Hallaj, L. Redey, J.R. Selman, J. Electrochem. Soc. 145 (1998) 1489.

[28] S. Al Hallaj, J. Prakash, J.. Selman, J. Electrochem. Soc. 87 (2000) 186.

[29] S. Al Hallaj, R. Venkatachalapathy, J. Prakash, J.R. Selman, J. Electrochem. Soc. 147 (2000) 2432.

[30] Y. Saito, K. Takano, K. Kanari, A. Negishi, K. Nozaki, K. Kato, J. Power Sources 97-98 (2001) 688.

[31] K. Onda, H. Kameyama, T. Hanamoto, K. Ito, J. Electrochem. Soc. 150 (2003) A285.

[32] H. Bang, H. Yang, Y.K. Sun, J. Prakash, J. Electrochem. Soc. 152 (2005) A421.

[33] W. Lu, I. Belharouak, D. Vissers, K. Amine, J. Electrochem. Soc. 153 (2006) A2147.

[34] J. Newman, W. Tiedemann, J. Electrochem. Soc. 142 (1995) 1054.

[35] P. Taheri, M. Bahrami, SAE Int. J. Passeng. Cars - Electron. Electr. Syst. doi10.4271/2012-01-0334 5 (2012).

[36] M. Ozisik, Boundary Value Problems of Heat Conduction, Dover Publications Inc., New York, 2002.

[37] Y. Chen, J.W. Evans, J. Electrochem. Soc. 140 (1993) 1833.

[38] Y. Chen, J.W. Evans, J. Electrochem. Soc. 141 (1994) 2947.

[39] S.C. Chen, C.C. Wan, Y.Y. Wang, J. Power Sources 140 (2005) 111.

[40] U.S. Kim, C.B. Shin, C.-S. Kim, J. Power Sources 180 (2008) 909.

[41] U.S. Kim, J. Yi, C.B. Shin, T. Han, S. Park, J. Electrochem. Soc. 158 (2011) A611.

[42] H. Sun, X. Wang, B. Tossan, R. Dixon, J. Power Sources 206 (2012) 349.

[43] K. Yeow, H. Teng, M. Thelliez, and E. Tan, SAE Tech. Pap. 2012-01-0331, Doi 10.4271/2012-01-0331 (2012).

[44] G. Karimi, X. Li, Int. J. Energy Res. 37 (2012) 13.

[45] G.L. Plett, J. Power Sources 134 (2004) 262.

[46] M. Mastali, J. Vazquez-Arenas, R. Fraser, M. Fowler, S. Afshar, M. Stevens, J. Power Sources 239 (2013) 294.

[47] V. Srinivasan, C.Y. Wang, J. Electrochem. Soc. 150 (2003) A98.

[48] M.W. Verbrugge, AIChE 41 (1995) 1550.

[49] C.R. Pals, J. Newman, J. Electrochem. Soc. 142 (1995) 3282.

[50] L. Song, J.W. Evans, J. Electrochem. Soc. 147 (2000) 2086.

[51] K. Smith, C.-Y. Wang, J. Power Sources 160 (2006) 662.

[52] W. Fang, O.J. Kwon, C. Wang, Int. J. Energy Res. 34 (2010) 107.

[53] K. Kumaresan, G. Sikha, R.E. White, J. Electrochem. Soc. 155 (2008) A164.

[54] W.B. Gu, C.Y. Wang, J. Electrochem. Soc. 147 (2000) 2910.

[55] K.H. Kwon, C.B. Shin, T.H. Kang, C.-S. Kim, J. Power Sources 163 (2006) 151.

[56] K. Kumaresan, Theoretical Analysis of the Discharge Performance of Lithium Ion and Lithium/sulfur Cells, University of South Carolina, 2008.

[57] J. Zhang, J. Lee, J. Power Sources 196 (2011) 6007.

[58] Y. Barsukov, in:, Texas Instrum. Workb., 2004.

[59] G.L. Plett, J. Power Sources 134 (2004) 252.

[60] S. Pang, J. Farrell, J. Due, M. Barth, in:, Proceeding Am. Control Conf., Arlington, VA, 2001, pp. 25–27.

[61] K.A. Smith, C.D. Rahn, C.-Y. Wang, in:, 2008 IEEE Int. Conf. Control Appl., IEEE, 2008, pp. 714–719.

[62] D. Di Domenico, A. Stefanopoulou, G. Fiengo, J. Dyn. Syst. Meas. Control 132 (2010) 061302.

[63] S. Lee, J. Kim, J. Lee, B.H. Cho, J. Power Sources 185 (2008) 1367.

[64] G.L. Plett, J. Power Sources 134 (2004) 277.

[65] G.L. Plett, J. Power Sources 161 (2006) 1356.

[66] G.L. Plett, J. Power Sources 161 (2006) 1369.

[67] D. Andre, C. Appel, T. Soczka-Guth, D.U. Sauer, J. Power Sources 224 (2013) 20.

[68] W. He, N. Williard, C. Chen, M. Pecht, Microelectronic Reliability, 2013.

[69] S. Yuan, H. Wu, C. Yin, Energies 6 (2013) 444.

[70] S. Piller, M. Perrin, A. Jossen, J. Power Sources 96 (2001) 113.

[71] M. Stevens, Hybrid Fuel Cell Vehicle Powertrain Development Considering Power Source Degradation, University of Waterloo, 2008.

[72] S. Rodrigues, N. Munichandraiah, A.K. Shukla, J. Power Sources 87 (2000) 12.

[73] F. Huet, J. Power Sources 70 (1998) 59.

[74] S. Rodrigues, N. Munichandraiah, A. Shukla, J. Solid State Electrochem 3 (1999) 397.

[75] A. Zenati, P. Desprez, H. Razik, IECON Proc. (Industrial Electron. Conf. (2010) 1773.

[76] B. Saha, K. Goebel, "Battery Data Set", NASA Ames Prognostics Data Repository, n.d.

[77] N. Watrin, B. Blunier, A. Miraoui, 2012 IEEE Transp. Electrif. Conf. Expo, ITEC 2012 (2012).

[78] M.Wahlstrom, Design of a Battery State Estimator Using a Dual Extended Kalman Filter, University of Waterloo, 2010.

[79] Http://www.a123systems.com/, (2016).

[80] S. Santhanagopalan, R.E. White, J. Power Sources 161 (2006) 1346.

[81] S.K. Rahimian, S. Rayman, R.E. White, J. Electrochem. Soc. 159 (2012) A860.

[82] D. Simon, Optimal State Estimation: Kalman, H-Infinity, and Nonlinear Approaches, John Wiley & Sons, 2006.

[83] G.L. Plett, No Title, Patent No.: US 7,593,821 B2, 2009.

[84] E.A. Wan, A.T. Nelson, Kalman Filtering and Neural Networks, John Wiley & Sons, 2001.

[85] A. Nelson, No Title, Oregon Graduate Institute of Science and Technology, 2000.

[86] W.B. Gu, C.Y. Wang, Electrochem. Soc. Proc. Ser. PV 99-25 (1999) 748.

[87] W.A. van Schalkwijk, B. Scrosati, No Title, Kluwer Academic Publishers, New York, 2002.

[88] V. Srinivasan, J. Newman, J. Electrochem. Soc. 151 (2004) A1530.

[89] M. Mastali Majdabadi, S. Farhad, M. Farkhondeh, R.A. Fraser, M. Fowler, J. Power Sources 275 (2015) 633.

[90] A.K. Padhi, K.S. Nanjundaswamy, J.B. Goodenough, J. Electrochem. Soc. 144 (1997) 1188.

[91] J. B. Goodenough, A.K. Padhi, K.S. Nanjundaswamy, C. Masquelier, US Patent, 5, 910, 382, 1999.

[92] S.-Y. Chung, J.T. Bloking, Y.-M. Chiang, Nat. Mater. 1 (2002) 123.

[93] N. Ravet, J.B. Goodenough, S. Besner, M. Simoneau, P. Hovington, M. Armand, in:, 196th Meet. Electrochem. Soc. Abstr. # 127 Hawai, 1999.

[94] N. Ravet, Y. Chouinard, J.F. Magnan, S. Besner, M. Gauthier, M. Armand, J. Power Sources 97-98 (2001) 503.

[95] B. Kang, G. Ceder, Nature 458 (2009) 190.

[96] A. Yamada, S.C. Chung, K. Hinokuma, J. Electrochem. Soc. 148 (2001) A224.

[97] C. Delacourt, P. Poizot, S. Levasseur, C. Masquelier, Electrochem. Solid-State Lett. 9 (2006) A352.

[98] V. Srinivasan, J. Newman, J. Electrochem. Soc. 151 (2004) A1517.

[99] U.S. Kasavajjula, C. Wang, P.E. Arce, J. Electrochem. Soc. 155 (2008) A866.

[100] S. Dargaville, T.W. Farrell, J. Electrochem. Soc. 157 (2010) A830.

[101] G.K. Singh, G. Ceder, M.Z. Bazant, Electrochim. Acta 53 (2008) 7599.

[102] D. Burch, G. Singh, G. Ceder, M.Z. Bazant, Solid State Phenom. 139 (2008) 95.

[103] D. Burch, M.Z. Bazant, Nano Lett. 9 (2009) 3795.

[104] K.E. Thomas-Alyea, ECS Trans. 16 (2008) 155.

[105] M. Safari, C. Delacourt, J. Electrochem. Soc. 158 (2011) A63.

[106] M. Safari, C. Delacourt, J. Electrochem. Soc. 158 (2011) A562.

[107] I. V. Thorat, Understanding Performance-Limiting Mechanisms in Li-Ion Batteries for High-Rate Applications, Brigham Young University, 2009.

[108] M. Farkhondeh, C. Delacourt, J. Electrochem. Soc. 159 (2012) A177.

[109] M. Farkhondeh, M. Safari, M. Pritzker, M. Fowler, T. Han, J. Wang, C. Delacourt, J. Electrochem. Soc. 161 (2013) A201.

[110] R. Klein, N. a. Chaturvedi, J. Christensen, J. Ahmed, R. Findeisen, A. Kojic, IEEE Trans. Control Syst. Technol. 21 (2013) 289.

[111] S.J. Moura, N. a. Chaturvedi, M. Krstić, J. Dyn. Syst. Meas. Control 136 (2013) 011015.

[112] M. Guo, R.E. White, J. Power Sources 221 (2013) 334.

[113] N. Baba, H. Yoshida, M. Nagaoka, C. Okuda, S. Kawauchi, J. Power Sources 252 (2014) 214.

[114] S. Atlung, K. West, T. Jacobsen, J. Electrochem. Soc. 126 (1979) 1311.

[115] S. Santhanagopalan, Q. Guo, P. Ramadass, R.E. White, J. Power Sources 156 (2006) 620.

[116] V.R. Subramanian, V. Boovaragavan, V.D. Diwakar, Electrochem. Solid-State Lett. 10 (2007) A255.

[117] V.R. Subramanian, V. Boovaragavan, V. Ramadesigan, M. Arabandi, J. Electrochem. Soc. 156 (2009) A260.

[118] K. a. Smith, C.D. Rahn, C.-Y. Wang, J. Dyn. Syst. Meas. Control 130 (2008) 011012.

[119] L. Cai, R.E. White, J. Electrochem. Soc. 156 (2009) A154.

[120] L. Cai, R.E. White, J. Electrochem. Soc. 157 (2010) A1188.

[121] T.-S. Dao, C.P. Vyasarayani, J. McPhee, J. Power Sources 198 (2012) 329.

[122] S. Khaleghi Rahimian, S. Rayman, R.E. White, J. Power Sources 224 (2013) 180.

[123] W. Luo, C. Lyu, L. Wang, L. Zhang, J. Power Sources 241 (2013) 295.

[124] J. Newman, K.E. Thomas-Alyea, Electrochemical Systems, 2004.

[125] M. Ender, A. Weber, E. Ivers-Tiffée, Electrochem. Commun. 34 (2013) 130.

[126] COMSOL Multiphysics, User's Guide, Version 4.4, COMSOL Inc., 2015.

[127] C. Delacourt, M. Safari, Electrochim. Acta 56 (2011) 5222.

[128] M. Safari, M. Farkhondeh, M. Pritzker, M. Fowler, T. Han, S. Chen, Electrochim. Acta 115 (2014) 352.

[129] M. Mastali, E. Samadani, S. Farhad, R.A. Fraser, M. Fowler, Electrochim. Acta 190 (2016) 574.

[130] M. Mastali, E. Samadani, S. Farhad, R.A. Fraser, M. Fowler, in:, SAE Tech. Pap. 2015-01-1182, 2015, Doi 10.4271/2015-01-1182, 2015, pp. 1–9.

[131] G. Karimi, A.R. Dehghan, Int. J. Energy Res. 38 (2014) 1793.

[132] A. Awarke, M. Jaeger, O. Oezdemir, S. Pischinger, Int. J. Energy Res. 37 (2013) 617.

[133] H.S. Hamut, I. Dincer, G.F. Naterer, Int. J. Energy Res. 37 (2013) 1.

[134] M. Shadman Rad, D.L. Danilov, M. Baghalha, M. Kazemeini, P.H.L. Notten, Electrochim. Acta 102 (2013) 183.

[135] J. Wang, P. Liu, J. Hicks-Garner, E. Sherman, S. Soukiazian, M. Verbrugge, H. Tataria, J. Musser, P. Finamore, J. Power Sources 196 (2011) 3942.

[136] I. Bloom, B.. Cole, J.. Sohn, S.. Jones, E.. Polzin, V.. Battaglia, G.. Henriksen, C. Motloch, R. Richardson, T. Unkelhaeuser, D. Ingersoll, H.. Case, J. Power Sources 101 (2001) 238.

[137] J.R. Belt, C.D. Ho, C.G. Motloch, T.J. Miller, T.Q. Duong, J. Power Sources 123 (2003) 241.

[138] D. a. H. McCleary, J.P. Meyers, B. Kim, J. Electrochem. Soc. 160 (2013) A1931.

[139] M. Guo, G.-H. Kim, R.E. White, J. Power Sources 240 (2013) 80.

[140] M. Guo, G. Sikha, R.E. White, J. Electrochem. Soc. 158 (2011) A122.

[141] L. Cai, R.E. White, J. Power Sources 196 (2011) 5985.

[142] J. Newman, K.E. Thomas-Alyea, Electrochemical Systems, 3rd ed., Wiley-IEEE, 2004.

[143] P. Taheri, A. Mansouri, M. Yazdanpour, M. Bahrami, Electrochim. Acta 133 (2014) 197.

[144] A. Tourani, P. White, P. Ivey, J. Power Sources 255 (2014) 360.

[145] J. Yi, U.S. Kim, C.B. Shin, T. Han, S. Park, J. Electrochem. Soc. 160 (2013) A437.

[146] S.U. Kim, P. Albertus, D. Cook, C.W. Monroe, J. Christensen, J. Power Sources 268 (2014) 625.

[147] E. Samadani, S. Farhad, W. Scott, M. Mastali, L.E. Gimenez, M. Fowler, R. a. Fraser, Electrochim. Acta 160 (2015) 169.

[148] P. Taheri, A. Mansouri, B. Schweitzer, M. Yazdanpour, M. Bahrami, J. Electrochem. Soc. 160 (2013) A1731.

[149] Technology Roadmap Electric and Plug-in Hybrid Electric Vehicles, 2011.

[150] Electric Vehicle Technology Roadmap for Canada, 2010.

[151] B. Scrosati, J. Garche, J. Power Sources 195 (2010) 2419.

[152] M. Safari, C. Delacourt, J. Electrochem. Soc. 158 (2011) A1436.

[153] E. Prada, D. Di Domenico, Y. Creff, J. Bernard, V. Sauvant-Moynot, F. Huet, J. Electrochem. Soc. 159 (2012) A1508.

[154] Y.-T. Cheng, M.W. Verbrugge, J. Appl. Phys. 104 (2008) 083521.

[155] M. Safari, C. Delacourt, J. Electrochem. Soc. 158 (2011) A1123.

[156] H. Buqa, D. Goers, M. Holzapfel, M.E. Spahr, P. Novak, J. Electrochem. Soc. 152 (2005) A474.

[157] M. Heß, P. Novák, Electrochim. Acta 106 (2013) 149.

[158] J.R. Dahn, Phys. Rev. B 44 (1991) 9170.

[159] N. Takami, A. Satoh, M. Hara, T. Ohsaki, J. Electrochem. Soc. 142 (1995) 371.

[160] T. Ohzuku, J. Electrochem. Soc. 140 (1993) 2490.

[161] R. Yazami, A. Martinent, Y. Reynier, in:, I. V. Barsukov, C.S. Johnson, J.E. Doninger, V.Z. Barsukov (Eds.), New Carbon Based Mater. Electrochem. Energy Storage Syst., Springer, 2006, pp. 245–258.

[162] R. Yazami, Y. Reynier, J. Power Sources 153 (2006) 312.

[163] M.W. Verbrugge, B.J. Koch, J. Electrochem. Soc. 150 (2003) A374.

[164] Q. Zhang, Q. Guo, R.E. White, J. Electrochem. Soc. 153 (2006) A301.

[165] D.M. Bernardi, J.-Y. Go, J. Power Sources 196 (2011) 412.

[166] K.G. Gallagher, D.W. Dees, A.N. Jansen, D.P. Abraham, S.-H. Kang, J. Electrochem. Soc. 159 (2012) A2029.

[167] D.K. Karthikeyan, G. Sikha, R.E. White, J. Power Sources 185 (2008) 1398.

[168] D.R. Baker, M.W. Verbrugge, J. Electrochem. Soc. 159 (2012) A1341.

[169] E. Tatsukawa, K. Tamura, Electrochim. Acta 115 (2014) 75.

[170] M. Takahashi, S. Tobishima, K. Takei, Y. Sakurai, Solid State Ionics 148 (2002) 283.

[171] D.Y.W. Yu, C. Fietzek, W. Weydanz, K. Donoue, T. Inoue, H. Kurokawa, S. Fujitani, J. Electrochem. Soc. 154 (2007) A253.

[172] F. Jiang, P. Peng, Y. Sun, J. Power Sources 243 (2013) 181.

[173] T.L. Kulova, a. M. Skundin, E. a. Nizhnikovskii, a. V. Fesenko, Russ. J. Electrochem. 42 (2006) 259.

[174] G.Y. Cho, J.W. Choi, J.H. Park, S.W. Cha, Int. J. Automot. Technol. 15 (2014) 795.

[175] G.G. Botte, B.A. Johnson, R.E. White, J. Electrochem. Soc. 146 (1999) 914.

[176] O.Y. Egorkina, a. M. Skundin, J. Solid State Electrochem. 2 (1998) 216.

[177] P.W.C. Northrop, V. Ramadesigan, S. De, V.R. Subramanian, J. Electrochem. Soc. 158 (2011) A1461.

[178] J. Christensen, D. Cook, P. Albertus, J. Electrochem. Soc. 160 (2013) A2258.

[179] MATLAB, Curve Fitting ToolboxTM User's Guide, 2015.

[180] W. Dreyer, J. Jamnik, C. Guhlke, R. Huth, J. Moskon, M. Gaberscek, Nat. Mater. 9 (2010) 448.

[181] M. Farkhondeh, M. Pritzker, M. Fowler, M. Safari, C. Delacourt, Phys. Chem. Chem. Phys. 16 (2014) 22555.

[182] J.L. Dodd, Phase Composition and Dynamical Studies of Lithium Iron Phosphate, California Institute of Technology, 2007.

[183] J.L. Dodd, S. Nishimura, R. Yazami, A. Yamada, B. Fultz, 210th ECS Meet. , Abstr. #179 (2006).

[184] A. Yamada, H. Koizumi, S.-I. Nishimura, N. Sonoyama, R. Kanno, M. Yonemura, T. Nakamura, Y. Kobayashi, Nat. Mater. 5 (2006) 357.

[185] K. Jalkanen, T. Aho, K. Vuorilehto, J. Power Sources 243 (2013) 354.

[186] D.R. Baker, M.W. Verbrugge, J. Electrochem. Soc. 159 (2012) A1341.

[187] L.O. Valøen, J.N. Reimers, J. Electrochem. Soc. 152 (2005) A882.

[188] Y. Li, S. Meyer, J. Lim, S.C. Lee, W.E. Gent, S. Marchesini, H. Krishnan, T. Tyliszczak, D. Shapiro, A.L.D. Kilcoyne, W.C. Chueh, Adv. Mater. 27 (2015) 6591.

[189] Celgard LLC, CELGARD 2500 Prod. Inf. (2015).

[190] M. Doyle, J. Newman, A.S. Gozdz, C.N. Schmulz, J.-M. Tarascon, J. Electrochem. Soc. 143 (1996) 1890.

[191] E. Prada, D. Di Domenico, Y. Creff, J. Bernard, V. Sauvant-Moynot, F. Huet, J.

Electrochem. Soc. 159 (2012) A1508.

[192] V. Srinivasan, J. Newman, Electrochem. Solid-State Lett. 9 (2006) A110.

[193] D. Morgan, a. Van der Ven, G. Ceder, Electrochem. Solid-State Lett. 7 (2004) A30.

[194] H.C. Shin, K.Y. Chung, W.S. Min, D.J. Byun, H. Jang, B.W. Cho, Electrochem. Commun. 10 (2008) 536.

[195] A.V. Churikov, A.V. Ivanishchev, I.A. Ivanishcheva, V.O. Sycheva, N.R. Khasanova, E.V. Antipov, Electrochim. Acta 55 (2010) 2939.

[196] H. Matsui, T. Nakamura, Y. Kobayashi, M. Tabuchi, Y. Yamada, J. Power Sources 195 (2010) 6879.

[197] Y. Reynier, R. Yazami, B. Fultz, J. Power Sources 119-121 (2003) 850.

[198] Y.F. Reynier, R. Yazami, B. Fultz, J. Electrochem. Soc. 151 (2004) A422.

[199] K.E. Thomas, J. Newman, J. Power Sources 119-121 (2003) 844.

[200] R.E. Williford, V. V. Viswanathan, J.-G. Zhang, J. Power Sources 189 (2009) 101.

[201] M. Alias, O. Crosnier, I. Sandu, G. Jestin, A. Papadimopoulos, F. Le Cras, D.M. Schleich, T. Brousse, J. Power Sources 174 (2007) 900.

[202] D. Doughty, E.P. Roth, Electrochem. Soc. Interface 21 (2012) 37.

[203] T. Waldmann, M. Wilka, M. Kasper, M. Fleischhammer, M. Wohlfahrt-Mehrens, J. Power Sources 262 (2014) 129.

[204] E. Samadani, M. Mastali, S. Farhad, R.A. Fraser, M. Fowler, Int. J. Energy Res. (2015).

[205] P. Ramadass, B. Haran, R. White, B.N. Popov, J. Power Sources 112 (2002) 614.

[206] L. Tan, L. Zhang, Q. Sun, M. Shen, Q. Qu, H. Zheng, Electrochim. Acta 111 (2013) 802.

[207] R.A. Leising, M.J. Palazzo, E.S. Takeuchi, K.J. Takeuchi, J. Power Sources 97-98 (2001) 681.

[208] Y. Zeng, K. Wu, D. Wang, Z. Wang, L. Chen, J. Power Sources 160 (2006) 1302.

[209] W. Cai, H. Wang, H. Maleki, J. Howard, E. Lara-Curzio, J. Power Sources 196 (2011) 7779.

[210] J. Lamb, C.J. Orendorff, L.A.M. Steele, S.W. Spangler, J. Power Sources 283 (2014) 517.

[211] H. Zheng, J. Li, X. Song, G. Liu, V.S. Battaglia, Electrochim. Acta 71 (2012) 258.

[212] R. Zhao, J. Liu, J. Gu, Appl. Energy 139 (2015) 220.

[213] S.P. Sheu, C.Y. Yao, J.M. Chen, Y.C. Chiou, J. Power Sources 68 (1997) 533.

[214] M. Okubo, E. Hosono, J. Kim, M. Enomoto, N. Kojima, T. Kudo, H. Zhou, I. Honma, J. Am. Chem. Soc. 129 (2007) 7444.

[215] W. Du, A. Gupta, X. Zhang, A.M. Sastry, W. Shyy, Int. J. Heat Mass Transf. 53 (2010) 3552.

[216] L. Jabbour, M. Destro, D. Chaussy, C. Gerbaldi, S. Bodoardo, N. Penazzi, D. Beneventi, Compos. Sci. Technol. 87 (2013) 232.

[217] X. He, D. Hubble, R. Calzada, A. Ashtamkar, D. Bhatia, S. Cartagena, P. Mukherjee, H. Liang, J. Power Sources 275 (2015) 688.

[218] Y. Han, L. Dong, J. Feng, D. Li, X. Li, S. Liu, Electrochim. Acta 167 (2015) 246.

[219] H. Shu, X. Wang, W. Wen, Q. Liang, X. Yang, Q. Wei, B. Hu, L. Liu, X. Liu, Y. Song, M. Zho, Y. Bai, L. Jiang, M. Chen, S. Yang, J. Tan, Y. Liao, H. Jiang, Electrochim. Acta 89 (2013) 479.

[220] D. Zhao, Y.L. Feng, Y.G. Wang, Y.Y. Xia, Electrochim. Acta 88 (2013) 632.

[221] H. Shu, X. Wang, Q. Wu, B. Hu, X. Yang, Q. Wei, Q. Liang, Y. Bai, M. Zhou, C. Wu, M. Chen, A. Wang, L. Jiang, J. Power Sources 237 (2013) 149.

[222] D. Baster, K. Zheng, W. Zajac, K. Swierczek, J. Molenda, Electrochim. Acta 92 (2013) 79.

[223] R. Mahamud, C. Park, J. Power Sources 196 (2011) 5685.

[224] H. Park, J. Power Sources 239 (2013) 30.

[225] L. Fan, J.M. Khodadadi, A.A. Pesaran, J. Power Sources 238 (2013) 301.

[226] H. Sun, R. Dixon, J. Power Sources 272 (2014) 404.

[227] T.M. Bandhauer, S. Garimella, Appl. Therm. Eng. 61 (2013) 756.

[228] A. Jarrett, I.Y. Kim, J. Power Sources 245 (2014) 644.

[229] N. Nieto, L. Díaz, J. Gastelurrutia, F. Blanco, J.C. Ramos, A. Rivas, J. Power Sources 272 (2014) 291.

[230] W. Tong, K. Somasundaram, E. Birgersson, A.S. Mujumdar, C. Yap, Int. J. Therm. Sci. 94 (2015) 259.

[231] A. Greco, D. Cao, X. Jiang, H. Yang, J. Power Sources 257 (2014) 344.

[232] Q. Wang, B. Jiang, Q.F. Xue, H.L. Sun, B. Li, H.M. Zou, Y.Y. Yan, Appl. Therm. Eng. (2014) 1.

[233] R. Zhao, J. Gu, J. Liu, J. Power Sources 273 (2015) 1089.

[234] N. Javani, I. Dincer, G.F. Naterer, B.S. Yilbas, Int. J. Heat Mass Transf. 72 (2014) 690.

[235] N. Javani, I. Dincer, G.F. Naterer, G.L. Rohrauer, Appl. Therm. Eng. 73 (2014) 305.

[236] Z.G. Qu, W.Q. Li, W.Q. Tao, Int. J. Hydrogen Energy 39 (2014) 3904.

[237] C. Lin, S. Xu, G. Chang, J. Liu, J. Power Sources 275 (2015) 742.

[238] J. Li, Y. Cheng, M. Jia, Y. Tang, Y. Lin, Z. Zhang, Y. Liu, J. Power Sources 255 (2014) 130.

[239] P. Amiribavandpour, W. Shen, D. Mu, A. Kapoor, J. Power Sources 284 (2015) 328.

[240] S. Jung, D. Kang, J. Power Sources 248 (2014) 498.

[241] N.A. Samad, J.B. Siegel, A.G. Stefanopoulou, in:, Proc. ASME 2014 Dyn. Syst. Control Conf., San Antonio, 2014, pp. 1–9.

[242] C. Veth, D. Dragicevic, R. Pfister, S. Arakkan, C. Merten, J. Electrochem. Soc. 161 (2014) A1943.

[243] N.A. Chaturvedi, J. Christensen, J. Ahmed, IEEE Control Syst. Mag. (2010) 49.

[244] U.S. Kim, C.B. Shin, C.-S. Kim, J. Power Sources 189 (2009) 841.

[245] T. Bandhauer, S. Garimella, T.F. Fuller, J. Electrochem. Soc. 162 (2014) A125.

[246] T. Bandhauer, S. Garimella, T.F. Fuller, J. Electrochem. Soc. 162 (2014) A137.

[247] H. Lundgren, P. Svens, H. Ekström, C. Tengstedt, J. Lindström, M. Behm, G. Lindbergh, Submitt. to J. Electrochem. Soc. 163 (2015) 309.

[248] Y. Lai, S. Du, L. Ai, L. Ai, Y. Cheng, Y. Tang, M. Jia, Int. J. Hydrogen Energy 40 (2015) 13039.

[249] W. Huo, H. He, F. Sun, RSC Adv. 5 (2015) 57599.

[250] M. Xu, Z. Zhang, X. Wang, L. Jia, L. Yang, Energy 80 (2015) 303.

[251] J. Li, Y. Cheng, L. Ai, M. Jia, S. Du, B. Yin, S. Woo, H. Zhang, J. Power Sources 293 (2015) 993.

[252] K.-J. Lee, K. Smith, A. Pesaran, G.-H. Kim, J. Power Sources 241 (2013) 20.

[253] E. Samadani, J. Lo, M. Fowler, R.A. Fraser, L. Gimenez, (2013).

[254] LabVIEW Syst. Des. Softw. - Natl. Instruments, Http//www.ni.com/labview/ (2016).

[255] BCS-815 Batter. Cycl. Syst. - Bio-Logic - Sci. Instruments, Http//www.bio-Logic.info/instruments/battery-Cycling-Bcs-815/ (2016).

[256] M. Yazdanpour, P. Taheri, A. Mansouri, M. Bahrami, J. Electrochem. Soc. 161 (2014) A1953.

[257] M. Mstali, M. Farkhondeh, S. Farhad, R. Fraser, M. Fowler, Submitt. to J. Chem. Soc. (2016).

[258] P. Taheri, M. Yazdanpour, M. Bahrami, J. Power Sources 243 (2013) 280.

[259] P. Arora, R. White, M. Doyle, J. Electrochem. Soc. 145 (1998) 3647.

[260] J. Christensen, J. Newman, J. Electrochem. Soc. 152 (2005) A818.

[261] K. Kumaresan, Q. Guo, P. Ramadass, R.E. White, J. Power Sources 158 (2006) 679.

[262] M. Tang, P. Albertus, J. Newman, J. Electrochem. Soc. 156 (2009) A390.

[263] Multi-Contact.com (2016).

[264] S. Turns, Thermal-Fluid Sciences, Cambridge University Press, 2006.

[265] R. Zhao, J. Gu, J. Liu, J. Power Sources 266 (2014) 422.

[266] D. Di Domenico, G. Fiengo, A. Stefanopoulou, Control Appl. 2008. CCA 2008. IEEE Int. Conf. (2008) 702.

[267] J.F. Thompson, Z.U. Warsi, C.W. Mastin, Numerical Grid Generation: Foundations and Applications, Amsterdam: North-holland, 1985.

[268] P.J. Olver, Equivalence, Invariants and Symmetry, Cambridge University Press, 1995.

[269] J.A. Murdock, Perturbations: Theory and Methods, Vol. 27. Siam, 1999.

[270] V.R. Subramanian, R.E. White, 96 (2001) 385.

[271] A. Guduru, P.W.C. Northrop, S. Jain, A.C. Crothers, T.R. Marchant, V.R. Subramanian, J. Appl. Electrochem. 42 (2012) 189.

[272] R. Deiterding, in:, ESAIM Proc., 2011, p. Vol. 34, p. 97–150.

[273] Y. Zhu, C. Wang, J. Power Sources 196 (2011) 1442.

[274] M. a. Roscher, O. Bohlen, J. Vetter, Int. J. Electrochem. 2011 (2011) 1.

[275] F. Baronti, W. Zamboni, N. Femia, R. Roncella, R. Saletti, IECON Proc. (Industrial Electron. Conf. (2013) 6728.

[276] F. Baronti, N. Femia, R. Saletti, C. Visone, W. Zamboni, IEEE Trans. Magn. 50 (2014) 1.

[277] D.R. Lide, ed., CRC Handbook of Chemistry and Physics, Section 12, Properties of Solids; Electrical Resistivity of Pure Metals, 84th Editi, CRC Press. Boca Raton, Florida, 2003.

Appendix-A

Battery properties used in simulations of Chapter 4, Chapter 5, and Chapter 6

Table A-1: List of the battery cell parameters used in both one-dimensional electrochemical and electric current and potential models a: assumed; c: CRC [277]; e: estimated; f: Farkhondeh et al. [109]; g: Gerver and Meyers [22]; s1: Safari and Delacourt [106]; s2: Safari and Delacourt [152].

Parameter	Symbol	Value
Anode charge-transfer coefficient	β_a	0.5[a]
Cathode charge-transfer coefficient	β_c	0.5[a]
Li foil charge-transfer coefficient	β_f & β_{Li}	0.5[a]
Bruggeman exponent	γ	1.5[a]
Initial salt concentration in the electrolyte (mol m^{-3})	c_e^0	1000[f]
Maximum Li concentration in the Gr particles (mol m^{-3})	$c_{s,a}^{max}$	31370[s1]
Maximum Li concentration in the LFP particles (mol m^{-3})	$c_{s,c}^{max}$	22806[s1]
Solid-state binary diffusion coefficient in Gr (m^2 s^{-1})	$\mathcal{D}_a$	2×10^{-14}[s1]
Solid-state binary diffusion coefficient in LFP (m^2 s^{-1})	$\mathcal{D}_c$	5×10^{-19}[f]
Diffusion coefficient of the electrolyte (m^2 s^{-1})	D_e	5.2×10^{-10}[f]
Porosity of the anode	ε_a	0.4024[e]
Porosity of the separator	ε_s	0.6[f]
Porosity of the cathode	ε_c	0.5[f]
Thermodynamic factor of the anode	α_a	1[sd1]
Total active material volume fraction of the anode	$\varepsilon_{t,a}$	0.565[s2]
Total active material volume fraction of the cathode	$\varepsilon_{t,c}$	0.351[f]
Reaction rate constant for anode (mol m^{-2} s^{-1} (mol m^{-3})$^{-1.5}$)	k_a^0	8.19×10^{-12}[s1]
Reaction rate constant for cathode (mol m^{-2} s^{-1} (mol m^{-3})$^{-1.5}$)	k_c^0	2.5×10^{-13}[f]
Li foil exchange current density (A m^{-2})	i_f^0	19[f]
Anode thickness (μm)	L_a	39[e]
Separator thickness (μm)	L_s	675[f]
Cathode thickness (μm)	L_c	80[f]
Bulk ionic conductivity of electrolyte (S m^{-1})	κ	1.3[f]
Li^+ ion transference number	t_+^0	0.363[f]
Temperature (K)	T	298.15[a]
Lithium foil thickness (μm)	L_{Li}	35[a]
Cupper negative current collector thickness (μm)	L_{Cu}	6.2[g]
Aluminum positive current collector thickness (μm)	L_{Al}	10[g]
Width of the cell (cm)	L_Y	20[a]
Height of the cell (cm)	L_Z	30[a]
Negative tab width (cm)	L_{NT}	4[a]
Positive tab width (cm)	L_{PT}	4[a]
Lithium electrical conductivity (S m^{-1})	σ_{Li}	1.056×10^{7}[c]
Cupper negative current collector conductivity (S m^{-1})	σ_{Cu}	5.96×10^{7}[g]

Aluminum positive current collector conductivity (S m^{-1})	σ_{Al}	3.70×10^{7}[g]
Lower cut-off voltage (V)	V_{cut}^{min}	2.5[f]
Upper cut-off voltage (V)	V_{cut}^{max}	4.1[f]
Arbitrary point on the cathode	$x_{c,a}$	0.22[e]
Graphite node equilibrium potential [s1 †]: $U_a = 0.6379 + 0.5416\exp(-305.5309y_a) + 0.044\tanh\left(-\frac{y_a-0.1958}{0.1088}\right) - 0.1978\tanh\left(\frac{y_a-1.0571}{0.0854}\right) - 0.6875\tanh\left(\frac{y_a-0.0117}{0.0529}\right) - 0.0175\tanh\left(\frac{y_a-0.5692}{0.0875}\right)$		
LFP cathode equilibrium potential [f, †]: $U_{k,c} = 3.4277 - 2.0269\times10^{-2}y_{k,c} + 0.5087\exp\left(-81.163y_{k,c}^{1.0138}\right) + 7.6445\times10^{-8}\exp\left(25.361y_{k,c}^{3.2983}\right) - 8.4410\times10^{-8}\exp\left(25.262y_{k,c}^{3.3111}\right)$		

† used in Chapter 6.

Table A-2: The particle size distribution and their corresponding volume fraction used in the models [109].

Particle bin	Radius of particles (nm)	Volume fraction, $\boldsymbol{\varepsilon_k/\varepsilon_t}$
1	22	0.36
2	36	0.42
3	62	0.12
4	169	0.10

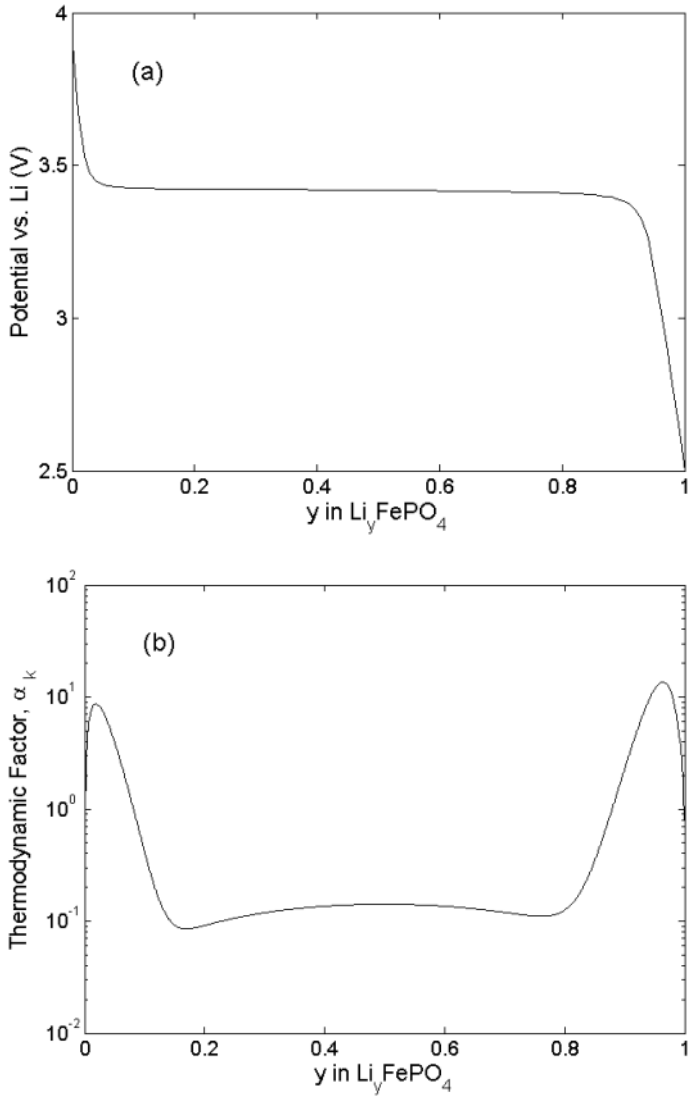

Figure A-1: (a) The equilibrium potential and (b) the thermodynamic factor, α_k, of the LFP cathode particles as a function of the Li mole fraction [109] (used in Chapter 4 and Chapter 5).

Appendix-B

The solid-phase potential across the electrode

In order to show the validity of ignoring the solid-phase potential gradient across the cathode, a simple calculation is present here. By considering constant reaction current density across the cathode, the Ohm's law is written as follows:

$$\frac{\partial}{\partial x_c}\left(\sigma_c^{eff}\frac{\partial \phi_{s,c}}{\partial x_c}\right) = L_c j_n \tag{B-1}$$

and the corresponding boundary conditions are:

$$\frac{\partial \phi_{s,c}}{\partial x_c}|_{x_c=0} = 0 \tag{B-2}$$

$$\frac{\partial \phi_{s,c}}{\partial x_c}|_{x_c=1} = \frac{L_c j_n}{\sigma_c^{eff}} \tag{B-3}$$

This assumption enables us to perform a simple dimensional analysis without getting involved with complicated mathematical formulation. Solution of Equation (B-1) using its boundary conditions results in:

$$\phi_{s,c} = \frac{L_c j_n}{2\sigma_c^{eff}} x_c^2 + C \tag{B-4}$$

where C is the an arbitrary unknown whose value can be obtained using the averaged potential of the cathode.

$$C = \phi_{s,c}^{avg} - \frac{L_c j_n}{6\sigma_c^{eff}} \tag{B-5}$$

By replacing C in the relation for ϕ_s, the final form of the cathode potential distribution is:

$$\phi_{s,c} = \frac{L_c j_n}{\sigma_c^{eff}}\left(\frac{x_c^2}{2} - \frac{1}{6}\right) + \phi_{s,c}^{avg} \tag{B-6}$$

By noting the final form of the solid-phase potential distribution on the cathode and incorporating the parameter values from the Appendix A ($L_c = 80 \times 10^{-6}\ m$ and $\sigma_c^{eff} = 6.75\ S\ m^{-1}$), it is seen

that the first two terms are of an order of $O(10^{-5} j_n)$. On the other hand, the third term, average solid-phase potential, is of an order of $O(1)$. As a result, to alter the solid-phase potential across the cathode, j_n has to take very large values. Therefore, the assumption of constant solid-phase potential across the cathode seems to be verified for the objective application of the electric vehicles.